Radio Pulsar Search and Timing

A Thesis

Submitted to the
Tata Institute of Fundamental Research, Mumbai
for the degree of Doctor of Philosophy
in Physics

by

Mayuresh Surnis

National Centre for Radio Astrophysics
Tata Institute of Fundamental Research, Pune

January 2017

To Aditi, my dear wife ...

"A giant leap for a man; a tiny, insignificant step for mankind !"

"Piled Higher and Deeper" by Jorge Cham

www.phdcomics.com

Contents

Acknowledgements xiii

Declaration xv

Synopsis xvii

List of Figures xxxii

List of Tables xxxvii

Glossary of Acronyms xxxix

1 Introduction 1
- 1.1 What Are Pulsars? . . . 1
- 1.2 Important Properties of Radio Pulsars . . . 2
  - 1.2.1 Integrated Profiles . . . 2
  - 1.2.2 Flux Densities and Spectra . . . 4
  - 1.2.3 Effects of the Interstellar Medium . . . 8
    - 1.2.3.1 Dispersion . . . 8
    - 1.2.3.2 Scattering and Scintillation . . . 10
  - 1.2.4 The Pulsar Population . . . 12
- 1.3 Pulsars as Physical Tools . . . 14
  - 1.3.1 High Precision Timing and Pulsar Time . . . 15
  - 1.3.2 Testing Theories of Gravity . . . 15
  - 1.3.3 Extrasolar Planets . . . 16
  - 1.3.4 Galactic Structure . . . 16
  - 1.3.5 Condensed Matter Physics . . . 17
  - 1.3.6 Pulsar Timing Array . . . 17

2 Literature Review 19
- 2.1 Why Search for Pulsars ? . . . 19
- 2.2 A Short History of Blind Pulsar Searches . . . 20
  - 2.2.1 Initial Pulsar Searches . . . 21
  - 2.2.2 The Parkes Multi-beam Pulsar Search . . . 24
  - 2.2.3 Modern Pulsar Searches . . . 25
- 2.3 Some Interesting Pulsar Systems . . . 28

2.4 Scope of the Thesis 29

3 Observations **33**
3.1 GMRT and ORT 33
3.1.1 The GMRT 33
3.1.1.1 Front End 35
3.1.1.2 Baseband System 37
3.1.2 The ORT 40
3.1.2.1 Modules 41
3.1.2.2 PONDER: The Pulsar Back-end 42
3.2 Blind Search Observations 44
3.2.1 Planning the Observations 44
3.2.2 A Typical Observing Session 46
3.2.3 Post Observation Work 48
3.3 Follow-up Timing Observations 49
3.3.1 Observations at the GMRT 50
3.3.1.1 Planning the Observations 51
3.3.1.2 A Typical Observing Session 51
3.3.1.3 Post Observation Work 52
3.3.2 Observations at the ORT 53
3.4 Targeted Search Observations 54
3.4.1 Planning the Observations 55
3.4.2 A Typical Observing Session 56
3.4.3 Post Observation Work 57

4 Data Analysis **59**
4.1 Blind Search 59
4.1.1 Radio Frequency Interference Mitigation 60
4.1.1.1 Narrow Band RFI 60
4.1.1.2 Broad Band RFI 62
4.1.2 Dedispersion 63
4.1.3 Harmonic Search 65
4.1.4 Folding and Diagnostic Plots 69
4.2 Targeted Search 72
4.2.1 HPC Search Pipeline 72
4.2.1.1 Phase I 73
4.2.1.2 Phase II 73
4.2.1.3 Phase III 74
4.2.2 Single Pulse Search 75
4.2.3 Broken Harmonic Search 77
4.2.4 Candidate Screening and Diagnostic Plots 79
4.2.4.1 Improving the Candidate Period and DM 80
4.3 Timing Analysis 86
4.3.1 Measuring Pulse TOA 86

4.3.1.1 Template Matching . . . 87
4.3.2 Time Standards . . . 89
4.3.3 Pulsar Timing Procedure . . . 89
4.3.4 TEMPO2 . . . 93
4.4 Imaging Analysis . . . 95
4.4.1 Fundamentals of Radio Interferometry . . . 96
4.4.2 Aperture Synthesis . . . 99
4.4.3 The Effect of Finite Sampling in U-V Plane . . . 99
4.4.4 Data Flagging . . . 100
4.4.5 Calibration . . . 101
4.4.5.1 Gain Calibration . . . 102
4.4.5.2 Bandpass Calibration . . . 104
4.4.6 FLAGCAL . . . 105
4.4.7 Imaging . . . 106
4.4.7.1 Högbom Algorithm . . . 108
4.4.7.2 Clark Algorithm . . . 109
4.4.8 Wide Field Imaging . . . 110
4.4.9 Self Calibration . . . 110

5 A Blind Pulsar Survey with the GMRT 115
5.1 Introduction . . . 115
5.2 Observations . . . 116
5.3 Data Analysis . . . 118
5.4 Results . . . 121
5.5 Discussion . . . 129

6 Discovery, Timing and Imaging of PSR J1838+1523 133
6.1 Introduction . . . 133
6.2 Discovery . . . 134
6.3 Initial Follow-up at GMRT . . . 135
6.4 Further follow-up at GMRT and ORT . . . 136
6.5 Data Analysis . . . 144
6.6 Results . . . 147
6.7 Discussion . . . 154

7 Follow-up Timing of Three GMRT Pulsars 161
7.1 Introduction . . . 161
7.2 Observations . . . 162
7.3 Data Analysis . . . 163
7.3.1 Local Search . . . 163
7.3.2 Timing Analysis . . . 165
7.3.3 Nulling Analysis for PSR J2208+5500 . . . 168
7.3.4 Modulation Index for PSR J2208+5500 . . . 170
7.3.5 Scattering Analysis for PSR J2217+5733 and J0026+6320 . 171
7.3.6 Imaging Analysis . . . 172

7.4 Results . . . 172
7.4.1 PSR B1937+21 . . . 173
7.4.2 PSR J2208+5500 . . . 178
7.4.3 PSR J2217+5733 . . . 185
7.4.4 PSR J0026+6320 . . . 190
7.5 Discussion . . . 197

8 Imaging Study of a Pulsar Field 199
8.1 Introduction . . . 199
8.2 Observations . . . 200
8.3 Data Analysis . . . 200
8.4 Results . . . 202
8.5 Discussion . . . 206

9 Radio Observations of HESS J1818–154/SNR G15.4+0.1 213
9.1 Introduction . . . 213
9.2 Observations . . . 216
9.3 Data Analysis . . . 217
9.4 Results . . . 222
9.5 Discussion . . . 223

10 Radio Pulsation Search in SGR Sources 227
10.1 Introduction . . . 227
10.2 SGR J1745–2900 . . . 229
10.2.1 Introduction . . . 229
10.2.2 Observations . . . 231
10.2.3 Data Analysis . . . 231
10.2.4 Results . . . 232
10.2.5 Discussion . . . 232
10.3 SGR J1935+2154 . . . 234
10.3.1 Introduction . . . 234
10.3.2 Observations . . . 235
10.3.3 Data Analysis . . . 236
10.3.4 Results . . . 238
10.3.5 Discussion . . . 239
10.4 SWIFT J174540.7–290015 . . . 245
10.4.1 Introduction . . . 245
10.4.2 Observations . . . 246
10.4.3 Data Analysis . . . 246
10.4.4 Results . . . 247
10.4.5 Discussion . . . 247
10.5 SGR J0755–2933 . . . 248
10.5.1 Introduction . . . 248
10.5.2 Observations . . . 248
10.5.3 Data Analysis . . . 249

10.5.4 Results 249
10.5.5 Discussion 249

11 Summary **251**
11.1 Main Results 251
11.2 Discussion 255
11.2.1 Blind Pulsar Survey with the GMRT 255
11.2.2 Discovery and Follow-up Timing of PSR J1838+1523 256
11.2.3 Follow-up of 3 GMRT pulsars 257
11.2.4 Imaging Study of a Known Pulsar Field 258
11.2.5 Pulsation Search towards HESS J1818–154 / G15.4+0.1 . . 258
11.2.6 Radio Pulsation Search towards Soft Gamma-ray Repeaters 259
11.3 Future Work 259

A The NCRA HPC **261**
A.1 Processor Performance 261
A.2 Disk Performance 262

Bibliography **265**

Acknowledgements

In today's world, haters are aplenty, lovers are few! Thus, when one finds them, it becomes mandatory to acknowledge them just because they want you to become better at whatever you do. This section is dedicated for those select few.

First and foremost is my advisor, Prof. B. C. Joshi. He has been my mentor in this field for eternity. He has provided me with every opportunity of learning and has supported me in everything I wanted to do. The gentle and caring ways of guiding accompanied with the much needed shouting routines for a laid-back person like me, have given me rich knowledge of pulsar physics and computational armoury required by any modern day researcher. He is and will always remain a fatherly figure in my life.

Next in line are the colleagues (read friends) at NCRA. I would like to thank Vishal Gajjar for all the help he has extended in my learning days as a graduate student. I would like to thank Abhishek Johri for sharing bits and pieces of wisdom and providing moral support on bad work days. I would like to mention Sambit Roychowdhury, Nissim Kanekar and Nirujmohan who are responsible for increasing my vocabulary in regards to making witty, sarcastic comments. I would like to thank Dipanjan Mitra and Divya Oberoi for the long personal interactions, which helped shape my views about my career in research. Special thanks are due to Ishwara Chandra and Ruta Kale for teaching me the nitty-gritties of imaging analysis. I am thankful to Manoharan, Krishnakumar and the ORT staff for essentially taking care of all the observational load at ORT, even without my intervention. I am indebted to Yogesh Maan, Kanhaiya Pande, Ruta Kale and Peter Kamphuis for insightful tea-time discussions involving random aspects of day-to-day life and life in general.

My thesis work involved loads of observations at the GMRT. I am eternally grateful to all the telescope operators at the GMRT, who are the source of all my information related to the working of the telescope. At NCRA, almost everything I know about linux as an operating system is because of (Late) Shekhar Bachal. He would have the answer to every question I had and it came without having to wait or browse the net. It was always there! Apart from him, VVS and Satpal Gole were always there to help whenever needed.

Next in line are the administrative staff, especially Reena and Hemant, the academic coordinators, who took care of the paperwork swiftly. I would also like to thank Mrs. Sabne and Mr. Barve from the accounts section for the help they have extended in filling up the umpteen reimbursement requests throughout my tenure.

During my Masters course at the University of Pune, Dr. Arun Banpurkar and Dr. Kiran Adhi (who was my advisor for the Masters thesis) provided support for keeping my research activities in flow.

During my Bachelors course at Fergusson College, Dr. Raka Dabhade was wholly responsible for keeping my contact with astronomy intact. She was the one, on whose personal recommendation, I was taken as a project student at NCRA, which really started it all! I would also like to mention Dr. Pushpa Ghalsasi, my science teacher in high school, for providing the initial impetus through stressing the importance of research and scientists in our society. This was the first real boost for my career ambition of becoming a scientist one day!

Last but not the least are my family members! My parents in law, Dr. Pramod Joglekar and Yashaprada Joglekar are responsible for providing me with resources and guidance, both professionally and personally. I would also like to thank Ajit Joglekar for lending his personal computer when I desperately needed it! My mother (Prerana Surnis) and father (Prakash Surnis) don't have a research background but they still believed in me and my chosen career path. I am grateful to them for not intervening much in my professional life.

Now comes the most important person in my life; my wife. In the last five years, I have realised that the words wife and life are much more deeply related than just the rhyming pronunciation. My wife, Aditi Joglekar is the sole reason for the progress I have made in my career so far. From doing things for her to doing things for myself, she has supported me through thick and thin, and has made me the person I am today. I don't think words are even distantly sufficient to describe her place in my life! This thesis is dedicated to her!

I would finally like to end this (very lengthy) section by thanking all the anonymous human beings who have indirectly taught me to conduct myself and helped me made my choices. I am a better person because of all of them!

Declaration

This thesis is a presentation of my original research work. Wherever contributions of others are involved, every effort is made to indicate this clearly, with due reference to the literature, and acknowledgement of collaborative research and discussions.

The work was done under the guidance of Professor B. C. Joshi, at the National Centre for Radio Astrophysics, Pune.

.....

Mayuresh Surnis

In my capacity as supervisor of the candidates thesis titled "Radio Pulsar Search and Timing", I certify that the above statements are true to the best of my knowledge.

.....

Prof. B. C. Joshi

Date: 04/07/2018

Synopsis

Thesis Title: Radio Pulsar Search and Timing
Mayuresh Surnis
Thesis Supervisor: Prof. B. C. Joshi

Introduction

Pulsating radio stars or *Pulsars* are *Neutron Stars*. They represent the end stages of the life cycle of massive stars. These are one of the many 'exotic objects' that can be observed in the sky. After the discovery of the first pulsar, PSR B1919+21 (Hewish et al. 1968), it was immediately realised that these objects could provide many interesting observational insights into different branches of physics. With more than 1.5 times the Solar mass compressed into a sphere of a radius of 10−20 km, pulsars form the most dense form of visible mass. They also have very high magnetic field strengths (10^8−10^{14} G). They are usually detectable via the coherent plasma emission that occurs due to the interaction between particles and their magnetic field. Pulsars are thus, very good laboratories for gravitational physics and plasma physics in extreme physical conditions. Pulsars are very stable rotators, allowing precise measurement of the rotation period (up to pico second accuracy) and in binaries, an exceptionally detailed description of the orbital parameters. Precise measurements of these parameters put a new discovery in its proper place in the pulsar population. Long term pulsar timing observations have the potential to reveal information about inherent characteristics like timing noise, glitches, nulling, mode changes and intermittency. These in turn provide observational constraints on current emission models and help us understand the physics much better. The precision pulsar timing observations enable pulsars to be used as useful physical tools. Pulsars are helpful in studying the interstellar medium (ISM) through dispersion, scattering and scintillation as seen in their signals when they travel through the ISM. Precise timing observations done on PSR B1257+12

helped discover the first ever extrasolar planetary system (Wolszczan and Frail 1992). Being highly compact objects, pulsars provide an opportunity to test the general relativity (GR) in the strong field regime. PSR B1913+16, the first binary pulsar system, showed the decay of orbit due to emission of gravitational waves at the expense of the orbital potential energy (Taylor and Weisberg 1989). This result was the most stringent test of GR in that time and it resulted in the Nobel prize being awarded to Russel Hulse and Joseph Taylor in 1993. The only known double pulsar binary system, PSR J0737−3039A/B has provided even more stringent tests of GR (Burgay et al. 2014). The most clever exploitation of the clock-like stability of pulsar rotation is implemented in the concept of a pulsar timing array (PTA; Foster and Backer 1990). This technique relies on correlated variations in the pulsar timing residuals as a function of the sky separation to directly detect the presence of gravitational wave background in the nHz frequency range. It is one of only two current experiments with the potential to make such a detection.

With so many interesting inherent phenomena and the possibility of exploring many more interesting physical phenomena, pulsars are one of the most enigmatic Galactic objects. In order to obtain a meaningful, statistical sample to be able to study their population properties, one has to observe a considerable number of pulsars across the Galaxy. The estimated total number of active pulsars in our Galaxy is about a million (Lorimer and Kramer 2005). Out of these, only about 2500 pulsars have been discovered to date[1]. This provides a very strong motivation to design more sensitive pulsar searches to try and detect as many of them as possible. The thrust of this thesis is pulsar search and timing of the discovered pulsars in order to characterize them. The search and timing work was performed in the radio frequency band with the Giant Metrewave Radio Telescope (GMRT) and Ooty Radio Telescope (ORT). During the course of the thesis, different types of observational efforts were put in. In the next few paragraphs, we will briefly describe these as well as the results obtained and their implications.

A Blind Pulsar Survey with the GMRT

Pulsar surveys are typically carried out with large single dish telescopes. Although such telescopes provide good sensitivity due to large collecting area, a small beam size makes them slow in sky coverage. A multi-element telescope like the GMRT

[1] www.atnf.csiro.au/people/pulsar/psrcat

offers a large collecting area of about 30,000 m^2 (Swarup et al. 1991) with a field of view of about 85' (Lal 2013) at 325 MHz, making it a sensitive pulsar survey instrument with a good survey speed. The only disadvantage at low radio frequencies is the large sky background due to non-thermal emission from the Galactic plane. Taking all these factors into account, we proposed a blind pulsar survey to cover the region between Galactic longitude $45° < l < 135°$ and Galactic latitude $1° < |b| < 10°$ with the GMRT at 325 MHz. This survey was titled "GMRT Galactic Plane Pulsar and Transient Survey (GMGPPTS)". Over two observation cycles of the GMRT, about 10% of the region was covered. The data were taken over a bandwidth of 32 MHz in incoherent array (IA) mode with a sampling time of 256 μs. The region to be observed was divided into circular 'pointings', each with a diameter of about 1°. Each pointing was observed for 1800 s and the data were recorded on magnetic tapes. The data analysis was done offline on a high performance cluster (HPC) at NCRA with a parallel processing pipeline using message passing interface (MPI). The actual analysis was done using the pulsar search package SIGPROC[2] and PRESTO[3]. Out of the 152 fields observed, data for 30 fields had to be ignored due to the presence of large amount of radio frequency interference (RFI). Based on the observed against expected signal to noise ratios (S/N) for known pulsars, the overall survey sensitivity was found to be a factor of 2 worse than the theoretical sensitivity. The overall survey sensitivity for harmonic search was found to be 2.7 mJy for an 8σ detection with a canonical pulse duty cycle of 10%. The sensitivity for single pulses was found to be 2.3 Jy for an 8σ detection and a burst duration of 10 ms. The survey analysis resulted in the detection of 27 out of 32 known pulsars in the observed region. The analysis also resulted in the discovery of a new pulsar, PSR J1838+1523. The simulated survey analysis using PSRPOP[4] using the post-analysis parameters resulted in the detection of 96 normal pulsars and no millisecond pulsars for the full survey region. Thus, the detection of 28 pulsars including the discovery of 1 new pulsar in the 10% region that was covered in a non-uniform manner, is consistent with the current population models.

Discovery and Follow-up Timing of PSR J1838+1523

[2]http://sigproc.sourceforge.net
[3]www.cv.nrao.edu/∼sransom/presto
[4]www.psrpop.phys.wvu.edu/index.php

PSR J1838+1523 was discovered as a strong candidate in the analysis of data taken in July 2009. Through follow-up observations done in May 2010, it was confirmed as a new pulsar. This pulsar has a period of 549 ms and a dispersion measure (DM) of 68 pc-cm^{-3}. Immediately after it was confirmed, we started doing follow-up timing observations. During the initial follow up timing observations, it was not detected for about 280 days. After it started being detected again, it showed random series of non-detections with durations of 1−2 months. The initial uncertainty on the position of the pulsar was about 1°. The long duration of non-detections followed by random detections and non-detections made it difficult to constrain the position using timing analysis. The position uncertainty was reduced in grid observations done using the ORT in December 2013. Thereafter, it was monitored daily at the ORT for two years. After getting a better estimate of the position from ORT timing analysis, we made radio maps using the imaging data obtained simultaneously during the timing observations done with the GMRT. This helped in identifying the continuum source associated with the pulsar. The maps indicated the presence of a continuum source even when the pulsations were not detectable in the time series data. When the time series data for all of the non-detections were folded using the timing solution, 15 out of 30 epochs at 325 MHz showed weak detections (S/N between 8−10). This makes a strong case for refractive interstellar scintillations (RISS) being the cause of the flux density going below the detection threshold, which resulted in the non-detections in the initial analysis.

Once the timing solution was obtained (and confirmed through a GBT detection at 820 MHz), multi-frequency timing observations were done at 610 and 1170 MHz. While the 1170 MHz observations resulted in non-detections, the flux densities measured through different means at 325 and 610 MHz are shown in Table 1.

Type of Measurement	Observing Frequency (MHz) 325	610
Time Series (GMRT)	4.0 ± 1.8 mJy	1.0 ± 0.4 mJy
Time Series (ORT)	4.2 ± 1.6 mJy	-
Imaging (GMRT)	4.7 ± 1.2 mJy	1.4 ± 0.7 mJy

Table 1: Mean flux densities of PSR J1838+1523 at different frequencies. The uncertainties come from the systematic variation across time rather than measurement uncertainties, which are smaller.

The mean flux density of PSR J1838+1523 was found to be 4.3 ± 1.8 mJy at 325 MHz and 1.2 ± 0.7 mJy at 610 MHz, implying a spectral index of −2. The non-detections at 1170 MHz are consistent with the expected flux density from the implied spectral index being lower than the detection limit at 1170 MHz. The discovery and follow-up analysis, along with full survey description is being written up and will be submitted to a journal soon.

Follow-up of 3 GMRT pulsars

Three new pulsars, PSR J2208+5500, J2217+5733 and J0026+6320 were discovered in an earlier survey carried out by Joshi et al. (2009) with the GMRT at 610 MHz. After the initial follow-up of about a year, they were not being followed-up. Out of these, PSR J2208+5500 was a suspected nulling pulsar. Given a low single pulse signal to noise ratio (S/N), Joshi et al. (2009) could only put a lower limit of 7.5% on its nulling fraction. The estimated spectral index of −2 implied that the single pulse S/N would be sufficient at 325 MHz for carrying out nulling analysis. The other two pulsars had high DMs and were located very close to the Galactic plane. This indicated a possibility of being able to estimate the scatter-broadening time scale at a lower radio frequency. In addition, the original timing observations were carried out at the frequencies of 610 and 1400 MHz. Thus, carrying out timing observations at 325 MHz in the phased array (PA) mode had scientific merit. With this motivation, we started the timing observations of these pulsars together with the newly discovered PSR J1838+1523. The observations were done at 325 MHz for over two years with a cadence of 2 weeks. Towards the end of the thesis work, we also performed a few timing observations at 610 and 1170 MHz in order to estimate spectral indices, scatter-broadening time scales ($\tau_{\rm sc}$) and much better DMs. While the GMRT observations were going on, we also started timing observations with the ORT at 326.5 MHz. In all of the observations, PSR B1937+21 was observed as a control pulsar. The timing analysis was performed using the pulsar timing package TEMPO2[5]. Only a coarse estimation of DMs was possible from the search observations for PSR J2217+5733 (162.75 pc-cm^{-3}) and J0026+6320 (230.31 pc-cm^{-3}) carried out by Joshi et al. (2009). Thus, coarse corrections were estimated through a search over local range of DMs. A much finer DM value was obtained later using multi-frequency timing analysis for all pulsars.

[5]http://www.atnf.csiro.au/research/pulsar/tempo2

PSR J2208+5500 showed clear nulling without apparent pulse drifting with an estimated nulling fraction of 50 ± 5% calculated over ten different observation epochs spread over three years. The phase averaged modulation index for this pulsar was estimated to be 2.5 ± 0.6. The DM for this pulsar was estimated to be 105.03 ± 0.02 pc-cm^{-3}, while the spectral index was estimated to be −2.4 ± 0.4. The DM for PSR J2217+5733 was estimated to be 131.54 ± 0.03 pc-cm^{-3} from timing analysis, while $\tau_{\rm sc}$ was found to be 9.7 ± 0.4 ms at 610 MHz and 61.9 ± 1.1 ms at 325 MHz. The spectral index for this pulsar was estimated to be −2.4 ± 0.3. For PSR J0026+6320, the DM was estimated to be 245.06 ± 0.06 pc-cm^{-3} from timing analysis, while $\tau_{\rm sc}$ was estimated to be 7.5 ± 0.9 ms at 610 MHz and 47.6 ± 0.2 ms at 325 MHz. The spectral index for this pulsar was estimated to be −0.9 ± 0.4. The values of $\tau_{\rm sc}$ obtained for PSR J2217+5733 and J0026+6320 are very different than the ones predicted by the NE2001 model of Cordes and Lazio (2002). The implied spectral indices of $\tau_{\rm sc}$ were found to be −2.9 (for PSR J2217+5733 and PSR J0026+6320), very different than a Kolmogorov spectrum. This indicates that both the pulsars lie in a region with significantly low scattering. All of these results are being put together in a paper, which is in a draft stage and will be submitted for publication soon.

Imaging Study of a Known Pulsar Field

The follow-up timing observations for PSR J1838+1523 at 325 MHz done with the GMRT spanned over three years with more or less uniform cadence of about two weeks. Each of the observation consisted of a 30 minute scan on the pulsar, allowing a snapshot image of the full field (about a degree across) to be made using the simultaneous imaging data. Due to multiple non-detections of PSR J1838+1523, the flux density of its continuum counterpart needed to be measured accurately. As the flux and phase calibration was done with multiple calibrator sources over the full data set, the consistency of the calibration across all the observations needed to be established. To do this, 29 point sources having a range of flux densities were selected from the field and their flux densities were also measured from images made in each epoch. This exercise gave rise to a unique data set, which allowed us to construct a flux density time series of all these sources and put stringent constraints on their flux variability. Out of these 29 sources, 4 sources had flux densities measured at other radio frequencies. This allowed us to estimate their spectral indices using flux density values estimated by us.

The spectral indices estimated including our measurements were consistent with earlier estimates. This established the accuracy of the measured flux densities. 12 of these sources were part of the 610 MHz primary beam. The flux density measurements for these sources provided spectral indices for 11 sources, which had measured flux densities at only one frequency prior to our study. Our variability analysis at 325 MHz revealed that out of the 29 sources, 2 sources, NVSS J183715+153015 (17%) and J183850+152214 (18%) were mildly variable, while 2 more sources, NVSS J183729+153210 (21%) and J183708+153141 (26%) were moderately variable. We also discovered that the source NVSS J183850+152214 was an essentially flat spectrum source. The variability and implied flat spectra together with the absence of counterparts at other electromagnetic bands makes us speculate that the two most variable sources along with the flat spectrum source NVSS J183850+152214 could be flat spectrum radio quasars (FSRQ). Currently, we are in the process of putting these results together for submission to a refereed journal.

Pulsation Search towards HESS J1818−154/G15.4+0.1

Many supernova remnants (SNRs) hosting a pulsar that powers a pulsar wind nebula (PWN), have been detected in very high energy (VHE) γ-rays (>100 GeV) with telescopes like HESS, MAGIC, VERITAS etc. Such SNRs are called composite SNRs. Detection/non-detection of the putative pulsar as well as making flux density measurements at low radio frequencies are critical in understanding the energetics as well as dynamical evolution of these sources. We had observed Galactic SNR G15.4+0.1 after VHE γ-ray emission was detected from its central part (the source was named HESS J1818−154) and a possible pulsar origin was suggested for the γ-ray emission (Hofverberg et al. 2011). The observations were done in May−June 2012 at 610 and 1420 MHz using the GMRT with 33 MHz bandwidth and a sampling time of 61 μs for pulsar mode and 16 s for imaging mode. These observations resulted in the first high resolution maps of this SNR at 610 and 1420 MHz, which were published in August 2013 (Castelletti G., Supan L., Dubner G., Joshi B. C., Surnis M. P., 2013, *A&A*, 557, 15). Our work on the HESS J1818−154/G15.4+0.1 pulsation search was recently accepted for publication. No associated pulsar was discovered in this search. The canonical duty cycle of 10% for the putative pulsar gives upper limits of 250 and 300 μJy at 610 and 1420 MHz, respectively, for the PA data, while the limits for IA data turn

out to be 700 and 500 μJy at 610 and 1420 MHz, respectively. These limits also rule out any un-associated pulsar along the line of sight at the same flux density levels. In addition, no point source or diffuse radio emission was detected in the continuum maps near the position of HESS J1818−154. Lack of radio pulsations together with the presence of molecular clouds and the broad band spectral energy distribution gives a plausibility argument for the VHE emission coming from the SNR to be hadronic in nature (Supan L., Castelletti G., Joshi B. C., Surnis M. P., Supanitsky D., 2015, *A&A*, 576, 81).

Radio Pulsation Search towards Soft Gamma-ray Repeaters

Soft Gamma-ray Repeaters (SGRs) are sources that produce repeating bursts of γ-rays and are usually discovered through either γ-ray or X-ray bursts followed by pulsations. Together with Anomalous X-ray Pulsars (AXPs), they form a rare, distinct class of pulsars which have transient, highly variable emission in the high energy electromagnetic band. In addition, a high energy burst from these sources is typically followed by radio pulsations. The radio emission usually fades away with the burst energy. Multi-frequency measurements of the flux density during the burst, may be useful in order to identify the mechanism of radio emission from these sources. In case the radio emission is detected at some radio frequencies and not at other frequencies or even otherwise, upper limits on the flux density are also useful inputs in the broad band spectral energy distribution. This makes SGRs with a on-going burst, very good candidates for targeted radio pulsation search at GMRT, as target of opportunity (TOO) observations. During the thesis period, we did TOO observations on four SGR sources. We describe them briefly below.

Pulsation Search towards SGR J1745−2900

We observed the Galactic centre magnetar SGR J1745−2900 to look for radio pulsations. The observations were carried out on 9$^{\rm th}$ May 2013 (ddtB086) with GMRT in the PA mode at 1 GHz with 33 MHz bandwidth and sampling time of 1 ms for 1 hour. We did not detect any significant pulsation with an 8σ upper limit, assuming 30% duty cycle, to be 0.4 mJy. The results were reported in Astronomer's Telegram (ATEL #5070).

Pulsation Search towards SGR J1935+2154

We observed SGR J1935+2154 to look for radio pulsations. The source was observed with ORT on July 9 and 14, 2014 at 326.5 MHz. The observations lasted for 4 and 3 hours respectively, and were done with 16 MHz bandwidth and 1 ms sampling time. The observations at GMRT were done on July 14 2014 (ddtB134) at 610 MHz using 15 antenna phased array, with 33 MHz bandwidth and 61 μs sampling, while the imaging data were recorded with a sampling time of 16 s. For the imaging observations, 3C48 and 1822−096 were observed as flux density and phase calibrator, respectively. We did not detect any significant pulsations with an 8σ upper limit of 0.4 mJy at 326.5 MHz and 0.2 mJy at 610 MHz assuming 10% pulse duty cycle. The results were reported in astronomer's telegram (ATEL #6376). We also did not detect significant bursts with 6σ upper limits on flux density (assuming 10 ms burst duration) of 0.5 Jy, and 63 mJy at 326.5, and 610 MHz, respectively. The corresponding flux density upper limits from GMRT IA data at 610 MHz are 0.8 mJy (8σ) for pulsed emission (with an assumed duty cycle of 10%), and 244 mJy (6σ) for isolated bursts (assuming 10 ms burst duration). We have made the first high resolution image of SNR G057.2+0.8 at 610 MHz. We did not detect any continuum emission from an associated point source at the position of SGR J1935+2154, with a 3σ upper limit of 1.2 mJy. No diffuse radio emission, associated with a putative wind nebula with an extent similar to the diffuse X-ray emission reported by Israel et al. (2016) (in radii of 15", and 70"), was detected with a 3σ flux density upper limit of about 4.5 mJy over a circular area with a radius of 70". From archival HI emission spectra, we have estimated a kinematic distance of 11.7 $\pm$ 2.8 kpc of SNR G057.2+0.8. From HI emission profile obtained in the direction of SGR J1935+2154, we calculate the HI column density in this line of sight to be $(1.1 \pm 0.1) \times 10^{22}$ cm^{-2}. A paper reporting these results has been accepted for publication in the *Astrophysical Journal*.

Pulsation Search towards SWIFT J174540.7−290015

We observed an SGR candidate, SWIFT J174540.7−290015 with the ORT on 10th February 2016 at 326.5 MHz in pulsar mode with a 16 MHz band spread over 1024 channels and a sampling time of 4 ms. The GMRT observations were carried out on 15th February 2016 at 1390 MHz with a 33 MHz band spread over 512 channels and a sampling time of 123 μs (ddtB210). The total integration time for ORT data was 3.5 hours, while the total integration time for GMRT observation was 2.7 hours. The analysis did not yield any significant pulsed or bursty radio emission in

both ORT and GMRT data. The 5σ flux density upper limits at 326.5 MHz were estimated to be 4.5 mJy (assuming 10% duty cycle) for harmonic search and 15 Jy (assuming a pulse width of 10 ms) for single pulse search. The corresponding limits at 1390 MHz were 70 μJy (assuming 10% duty cycle) and 0.2 Jy (assuming a pulse width of 10 ms), respectively. These results were posted on the astronomer's telegram (ATEL #8729).

Pulsation Search towards SGR J0755−2933

The observations at the ORT were performed on 17th March 2016 at 326.5 MHz with 8 ms sampling over a band of 16 MHz, spread over 1024 channels. The total integration time was 3 hours. The observations at the GMRT were performed on 25th March 2016 (ddtB216) at 1390 MHz wherein, the data were recorded simultaneously in imaging and PA mode, over a bandwidth of 33 MHz, spread over 512 channels. The PA data were recorded with a sampling time of 123 μs, while the imaging data were recorded with a sampling time of 16 s for a duration of 1 hour. For the imaging observations, 3C147 and 0828−375 were observed as flux density and phase calibrator, respectively. No significant pulsations were detected from either GMRT or ORT data. The 8 σ flux density upper limits at 326.5 MHz were estimated to be 0.89 mJy (assuming 10% duty cycle) for harmonic search and 2.8 Jy (assuming a width of 10 ms) for isolated bursts. Corresponding limits at 1390 MHz were estimated to be 0.12 mJy (assuming 10% duty cycle) for harmonic search and 220 mJy (assuming a width of 10 ms) for isolated bursts. From the radio maps, the absence of a continuum source implies a 3σ flux density upper limit of 0.3 mJy. These results were posted on the astronomer's telegram (ATEL #8943).

Organization of the Thesis

This thesis is divided into two parts. The first part describes the blind search observations followed by the timing observations and analysis. This part (majority of Chapters 3 and 4 and Chapters 5−8) gives details of the blind survey observations carried out with the GMRT as mentioned above. Chapter 3 outlines the observational effort put in the thesis work, while Chapter 4 gives details of the data analysis methods for different types of observations. Chapter 5 describes the GMGPPTS and its main results. This part also contains the description about the

discovery of a new pulsar, PSR J1838+1523 and the follow-up timing observations carried out thereafter, which are described in Chapter 6. The results from the follow-up timing observations for the pulsars discovered in the 610 MHz survey (mentioned above) are described in Chapter 7. In Chapter 8 we describe the variability study performed for the 29 point sources at 325 MHz using the snapshot images obtained from imaging mode data taken for PSR J1838+1523.

The second part contains Chapter 9 and 10. It contains the results obtained for targeted searches towards some promising radio pulsar candidates. Chapter 9 describes the pulsation search done at 610 and 1420 MHz with the GMRT towards the very high energy γ-ray source HESS J1818−154, which was associated with SNR G015.4+0.1 (Hofverberg et al. 2011). The observational constraints and considerations for this search are described in Chapter 3. This search was very different from traditional pulsar searches. Due to the constraints put by the requirement that the source be imaged properly, the search observations had to be broken into smaller scans (see Chapter 4 for details). This required the development of a new search pipeline as well as a diagnostic viewer. These are described in Chapter 4. The results obtained in the pulsation search as well as the other relevant material forms the subject matter of Chapter 9. Chapter 10 describes the observational efforts and results of the radio pulsation search for four SGR sources namely, SGR J1745−2900, SGR J1935+2154, SWIFT J174540.7−290015 and SGR J0755−2933. We summarize all the results and their implications in Chapter 11.

Conclusions

Part I: Blind Search and Follow-up Timing

The blind search carried out using the GMRT at 325 MHz resulted in the discovery of a new pulsar, PSR J1838+1523. A combination of daily timing observations carried out at the ORT and simultaneous imaging observations carried out at the GMRT provided a coherent timing solution, which is given in a table below

This pulsar showed a lot of flux density variations resulting in 15 non-detections during the follow-up observations. The primary reason for the variability appears to be interstellar scintillation. The mean flux density of this pulsar was estimated

TABLE 2: Timing solution obtained for PSR J1838+1523. For the measured quantities, numbers in brackets indicate 1σ errors in the last significant digit as reported by TEMPO2.

Fit and data-set	
Pulsar name	J1838+1523
MJD range	55770.6—57157.0
Data span (yr)	3.80
Number of TOAs	218
RMS timing residual (μs)	1656.5
Weighted fit	Y
Reduced χ^2	1.22
Measured Quantities	
Right ascension, α (hh:mm:ss)	18:38:46.78(1)
Declination, δ (dd:mm:ss)	+15:23:24.9(1)
Pulse frequency, ν (s^{-1})	1.82096092904(2)
First derivative of pulse frequency, $\dot{\nu}$ (s^{-2})	$-6.73(6)\times10^{-17}$
Dispersion measure, DM ($cm^{-3}pc$)	68.28(3)
Set Quantities	
Epoch (MJD)	56675
Derived Quantities	
$\log_{10}$(Characteristic age, yr)	8.63
$\log_{10}$(Surface magnetic field strength, G)	11.03
$\log_{10}$($\dot{E}$, ergs/s)	30.68
Assumptions	
Clock correction procedure	TT(TAI)
Solar system ephemeris model	DE405
Binary model	NONE
Model version number	5.00

to be 4.3 ± 1.8 mJy at 325 MHz and 1.2 ± 0.7 mJy at 610 MHz, implying a spectral index of −2.

Multi-frequency timing observations performed for the GMRT pulsars enabled their DMs to be measured with an accuracy of upto 0.4 pc-cm^{-3}, even with a cadence of 2 weeks and a few TOAs at high frequencies. Nulling analysis done over multi-epoch data for PSR J2208+5500 revealed a large nulling fraction of 50 ± 5%. The scatter-broadening estimates for PSR J2217+5733 and PSR J0026+6320 implied that despite being close to the Galactic plane, the regions containing these pulsars show significantly less scattering. Multi-frequency imaging data enabled the measurement of spectral indices as −2.4 ± 0.4 for PSR J2208+5500, −2.4 ± 0.3 for PSR J2217+5733 and −0.9 ± 0.4 for PSR J0026+6320.

The unique capability of the GMRT to provide simultaneous imaging data helped the calibrations to be verified based on the multi-epoch flux density measurements of 29 point sources at 325 MHz and 12 of them at 610 MHz, in the field of view of PSR J1838+1523. These unique data sets, obtained over more than three years, helped in constraining the spectral indices of 11 sources, while providing stringent limits on the variability of all the 29 sources at 325 MHz. It also helped in identifying NVSS J183729+153210, J183708+153141 and J183850+152214 as potential FSRQ sources in this field.

Part II: Targeted Search towards High Energy Sources

The high resolution images of SNR G15.4+0.1 were made for the first time at 610 and 1420 MHz by our collaborators. The study of molecular CO towards this SNR hinted towards a hadronic origin of the VHE γ-ray emission. Although the X-ray observations pointed towards a possible PWN connection, non-detection of radio pulsations as well as lack of point-like sources in the continuum maps made the hadronic scenario slightly more stronger. Better data obtained in the MeV$-$GeV energy range shall be useful to settle the issue once and for all.

The non-detections of radio pulsations towards SGR J1745$-$2900 and J1935+2154 in our observations were consistent with the expectations given the results at other radio frequencies. Simultaneous imaging data taken towards SGR J1935+2154 allowed us to make the first high resolution map of SNR G57.2+0.8 at 610 MHz. This map was consistent with the 1.4 GHz map made using archival VLA data. Non-detection of a continuum source associated with SGR J1935+2154 indicated that it may be radio quiet. Non-detection of radio pulsations and lack of pulsations even in high energy data from SWIFT J174540.7$-$290015 and SGR J0755$-$2933 make them unlikely SGR sources.

List of Publications

Refereed Journals:

1. Surnis M. P., Maan Y., Joshi B. C., Krishnakumar M. A., Manoharan P. K. & Naidu A. (2016), Radio Pulsation Search and Imaging Study of SGR J1935+2154, *ApJ accepted.*

2. Supan L., Castelletti G., Joshi B. C., Surnis M. P. & Supanitsky D. (2015, April). A complete radio study of SNR G15.4+0.1 from new GMRT observations. *A&A 576*, A81.

Conference Proceedings:

1. Castelletti G., Joshi B. C., Surnis M. P., Supan L. & Dubner G. (2014, January). GMRT Observations of SNR G15.4+0.1/HESS J1818−154. *IAUS 296*, 366.

2. Supan L., Joshi B. C., Castelletti G. & Surnis M. P. (2014). Deep Radio Study Towards the G22.7−0.2/HESS J1832−093 and G25.5−0.0/HESS J1837−069. *cosp 40*, E3237.

3. Surnis M. P., Joshi B. C., McLaughlin M. A. & Gajjar V. (2013, March). Discovery of an Intermittent Pulsar: PSR J1839+15. *IAUS 291*, 508.

4. Supan L., Castelletti G., Dubner G., Surnis M. P. & Joshi B. C. (2013). Molecular Gas Distribution Towards the SNR G15.4+0.1. *BAAA 56*, 315.

Others:

1. Surnis M. P., Maan Y., Joshi B. C. & Manoharan P. K. (2016, April). Upper limits on the pulsed radio emission from SGR candidate SGR 0755−2933. *The Astronomers Telegram 8943*, 1.

2. Maan Y., Surnis M. P., Krishnakumar M. A., Joshi B. C. & Manoharan P. K. (2016, February). Search for pulsed radio emission from SWIFT J174540.7−290015. *The Astronomers Telegram 8729*, 1.

3. Surnis M. P., Krishnakumar M. A., Maan Y., Joshi B. C. & Manoharan P. K. (2014, August). Upper limits on the pulsed radio emission of SGR 1935+2154 from the Ooty Radio Telescope and the Giant Meterwave Radio Telescope. *The Astronomer's Telegram 6376*, 1.

4. Surnis M. P., Joshi B. C. & Roy S. (2013, May). Search for pulsed radio emission from PSR J1745−2900 at 1 GHz with the GMRT. *The Astronomer's Telegram 5070*, 1.

In Preparation:

1. Surnis M. P. *et al.*, GMRT Galactic Plane Pulsar and Transient Survey, 2016.
2. Surnis M. P. *et al.*, Multi-frequency Timing Analysis of GMRT Pulsars, 2016.
3. Surnis M. P. *et al.*, Variability Study of Radio Sources in a Known Pulsar Field, 2016.

Unrelated Publications:

1. Castelletti G., Supan L., Dubner G., Joshi B. C. & Surnis M. P. (2013, September). A hadronic scenario for HESS J1818−154. *A&A 557*, L15.

List of Figures

1.1 Some pulse profiles observed at 1.4 GHz 3
1.2 Some pulse profiles observed at 10.7 GHz 5
1.3 Radius to frequency mapping in radio pulsars 6
1.4 Two major types of pulsar spectra 7
1.5 The known pulsar population represented in a $P-\dot{P}$ diagram 13

2.1 Beam positions for the four pointing strategy used in PMPS 25

3.1 The GMRT dishes 34
3.2 GMRT array configuration 35
3.3 The GMRT feed turret 36
3.4 Block diagram for GMRT front end and baseband system 37
3.5 The Ooty Radio Telescope 41
3.6 Block diagram of an ORT module 42
3.7 The region of sky proposed to be observed in GMGPPTS 46
3.8 Power band of GMRT antennae after power equalization 47

4.1 Histogram of RFI infected data 61
4.2 RFI seen in the GMRT 325 MHz band 62
4.3 The effect of whitening on spectrum of search data 67
4.4 Effect of pulse duty cycle on the FFT components 68
4.5 A diagnostic candidate plot for PSR J1838+1523 71
4.6 A Typical single pulse search plot 77
4.7 Example viewer plot for a broken search candidate 84
4.8 Observational set up for pulsar timing 87
4.9 The effect of some parameters on pulsar timing residuals 92
4.10 A screen shot showing plk interface 95

5.1 The region of sky observed in GMGPPTS 117
5.2 PRESTO plot showing the diagnostic plot for a strong candidate . . 119
5.3 Integrated profiles for the pulsars detected in GMGPPTS 122
5.4 Integrated profiles for the pulsars detected in GMGPPTS 123
5.5 Integrated profiles for the pulsars detected in GMGPPTS 124
5.6 Integrated profiles for the pulsars detected in GMGPPTS 125
5.7 S_{min} as a function of the pulse duty cycle 126
5.8 Single pulse search plot for GPT4208 129
5.9 Single pulse diagnostic plot with broad band RFI 131

5.10 Single pulse diagnostic plot after broad band RFI mitigation 132

6.1 Discovery plot for PSR J1838+1523 138
6.2 Average profiles of PSR J1838+1523 145
6.3 Average ON and OFF profiles of PSR J1838+1523 146
6.4 Confirmation plot for PSR J1838+1523 148
6.5 Post-fit timing residuals obtained for PSR J1838+1523 150
6.6 Image of PSR J1838+1523 in ON state at 325 MHz 151
6.7 Image of PSR J1838+1523 for a non-detection at 325 MHz 152
6.8 Image of PSR J1838+1523 at 610 MHz 153
6.9 Flux densities of PSR J1838+1523 measured at different epochs . . 154
6.10 Time series flux density histogram for PSR J1838+1523 at 325 MHz 155
6.11 Imaging flux density histogram for PSR J1838+1523 at 325 MHz . 156
6.12 Dynamic spectra obtained for PSR J1838+1523 from GBT data at 820 MHz 157
6.13 Dynamic spectra obtained for PSR J1838+1523 from ORT data at 326 MHz 158

7.1 Harmonic S/N as a function of trial DM 164
7.2 Clock jitter introducing timing irregularities for PSR B1937+21 . . 166
7.3 Average profiles for PSR J2208+5500 at different observing frequencies 169
7.4 Average profiles for PSR J2217+5733 at different observing frequencies 170
7.5 Average profiles for PSR J0026+6320 at different observing frequencies 171
7.6 Post-fit timing residuals obtained for PSR B1937+21 176
7.7 Spectrum of PSR B1937+21 177
7.8 Pulse nulling seen in PSR J2208+5500 at 325 MHz 178
7.9 Histograms of normalized pulse energies for PSR J2208+5500 . . . 179
7.10 Average phase resolved modulation index for PSR J2208+5500 . . . 180
7.11 Fluctuation spectrum of PSR J2208+5500 181
7.12 Post-fit timing residuals obtained for PSR J2208+5500 181
7.13 Image of PSR J2208+5500 at 325 MHz 183
7.14 Spectrum of PSR J2208+5500 184
7.15 Estimates of scatter-broadening in PSR J2217+5733 185
7.16 Post-fit timing residuals obtained for PSR J2217+5733 187
7.17 Image of PSR J2217+5733 at 325 MHz 188
7.18 Spectrum of PSR J2217+5733 189
7.19 Estimates of scatter-broadening in PSR J0026+6320 191
7.20 PRESTO plot showing a very faint detection of PSR J0026+6320 at 325 MHz 192
7.21 Post-fit timing residuals obtained for PSR J0026+6320 194
7.22 Image of PSR J0026+6320 at 325 MHz 195
7.23 Spectrum of PSR J0026+6320 196

8.1 Spectra of NVSS sources 209
8.2 Spectra of NVSS sources 210
8.3 Flux density variation as a function of source flux density 211
8.4 A histogram of systematic flux density variation 211

9.1 First high resolution image of SNR G15.4+0.1 at 1420 MHz 215
9.2 Diagnostic plot for known pulsar PSR J1901−0906 220
9.3 Flux density upper limits on a putative pulsar 223

10.1 GMRT Image of SNR G057.2+0.8 at 610 MHz 240
10.2 GMRT and VLA Image of SNR G057.2+0.8 at 610 MHz 241
10.3 Composite radio and X-ray image of SNR G057.2+0.8 242
10.4 HI emission and absorption profiles towards SNR G057.2+0.8 . . . 243

A.1 Cluster throughput for various array dimensions 262

List of Tables

2.1 Some important properties of major pulsar surveys 27

3.1 Important observational parameters for GMGPPTS 45
3.2 Important observational parameters for follow-up timing observations at the GMRT 52
3.3 Important observational parameters for follow-up timing observations at the ORT 54
3.4 Important observational parameters for G015.4+0.1 57

4.1 Some basic TEMPO2 parameters for isolated pulsars 94

5.1 Parameters for known pulsars in the region covered by GMGPPTS 127
5.2 Single pulse S/N for known pulsars detected in GMGPPTS 130

6.1 The flux density measurements for PSR J1838+1523 139
6.2 Timing solution obtained for PSR J1838+1523 149
6.3 Mean flux densities of PSR J1838+1523 at different frequencies . . 152

7.1 EFAC values for different telescopes and observing frequencies . . . 166
7.2 Timing solution obtained for PSR B1937+21 174
7.3 Timing solution for PSR B1937+21 from IPTA 175
7.4 Flux densities of the four observed pulsars at different observing frequencies 176
7.5 Timing solution obtained for PSR J2208+5500 182
7.6 Timing solution obtained for PSR J2217+5733 186
7.7 Timing solution obtained for PSR J0026+6320 193

8.1 The flux densities and uncertainties for the NVSS sources included in this study 203

9.1 Effective sampling time for various trial DM ranges at 610 MHz . . 218
9.2 Effective sampling time for various trial DM ranges at 1420 MHz . . 219

Glossary of Acronyms

ADC	**A**nalog to **D**igital **C**onverter
AGN	**A**ctive **G**alactic **N**ucleus
AIPS	**A**stronomical **I**mage **P**rocessing **S**ystem
ALFA	**A**recibo **L**-band **F**eed **A**rray
AMXP	**A**ccreting **M**illisecond **X**-ray **P**ulsar
API	**A**pplication **P**rogram **I**nterface
ASKAP	**A**ustralian **S**quare **K**ilometre **A**rray **P**athfinder
ATEL	**A**stronomer's **TEL**egram
ATNF	**A**ustralia **T**elescope **N**ational **F**acility
AXP	**A**nomalous **X**-ray **P**ulsar
BAT	**B**urst **A**lert **T**elescope
BIPM	**B**ureau **I**nternational des **P**oids et **M**esures
CASA	**C**ommon **A**stronomy **S**oftware **A**pplications
CCD	**C**harge **C**oupled **D**evice
CMB	**C**osmic **M**icrowave **B**ackground
DAS	**D**ata **A**cquisition **S**ystem
DDT	**D**irector's **D**escritionary **T**ime
DEC	**DEC**lination
DFT	**D**iscrete **F**ourier **T**ransform
DISS	**D**iffractive **I**nter-**S**tellar **S**cintillation
DM	**D**sipersion **M**easure
DoF	**D**egrees **o**f **F**reedom
EPIC	**E**uropean **P**hoton **I**maging **C**amera

EPTA	**E**uropean **P**ulsar **T**iming **A**rray
FAST	**F**ive-hundred-meter **A**perture **S**pherical **T**elescope
FFA	**F**ast **F**olding **A**lgorithm
FFT	**F**ast **F**ourier **T**ransform
FSRQ	**F**lat **S**pectrum **R**adio **Q**uasar
FWHM	**F**ull **W**idth at **H**alf **M**aximum
GAC	**G**MRT **A**rray **C**ombiner
GBNCC	**G**BT **N**orthern **C**elestial **C**ap pulsar survey
GBT	**G**reen **B**ank **T**elescope
GHB	**G**MRT **H**ardware **B**ackend
GHRSS	**G**MRT **H**igh **R**esolution **S**outhern **S**ky survey
GMGPPTS	**GM**RT **G**alactic **P**lane **P**ulsar and **T**ransient **S**urvey
GMRT	**G**iant **M**etrewave **R**adio **T**elescope
GPS	**G**lobal **P**ositioning **S**ystem
GPU	**G**raphical **P**rocessing **U**nit
GR	**G**eneral **R**elativity
GRB	**G**amma **R**ay **B**urst
GRS	**G**alactic **R**ing **S**urvey
GSB	**G**MRT **S**oftware **B**ackend
GUI	**G**raphical **U**ser **I**nterface
GUPPI	**G**BT **U**ltimate **P**ulsar **P**rocessing **I**nstrument
HESS	**H**igh **E**nergy **S**tereoscopic **S**ystem
HMXB	**H**igh **M**ass **X**-ray **B**inary
HPC	**H**igh **P**erformance **C**luster
HTRU	**H**igh **T**ime **R**esolution **U**niverse survey
IA	**I**ncoherent **A**rray
IB	**I**nfini**B**and
IERS	**I**nternational **E**arth **R**otation **S**ervice
IF	**I**ntermediate **F**requency
INTEGRAL	**INTE**rnational **G**amma-**R**ay **A**strophysics **L**aboratory
IP	**I**ntegrated **P**rofile

IPAC	**I**nfrared **P**rocessing and **A**nalysis **C**entre
IPS	**I**nter-**P**lanetary **S**cintillations
IPTA	**I**nternational **P**ulsar **T**iming **A**rray
ISM	**I**nter-**S**tellar **M**edium
JPL	**J**et **P**ropulsion **L**aboratory
LAB	**L**eiden **A**rgentine **B**onn
LAT	**L**arge **A**rea **T**elescope
LMXB	**L**ow **M**ass **X**-ray **B**inary
LNA	**L**ow **N**oise **A**mplifier
LO	**L**ocal **O**scillator
LOFAR	**LO**w **F**requency **AR**ray
LSF	**L**oad **S**haring **F**acility
MAD	**M**edian **A**bsolute **D**eviation
MAGIC	**M**ajor **A**tmospheric **G**amma **I**maging **C**herenkov Telescopes
MAGPIS	**M**ulti-**A**rray **G**alactic **P**lane **I**maging **S**urvey
MJD	**M**odified **J**ulian **D**ay
MPI	**M**essage **P**assing **I**nterface
MSP	**M**illi**S**econd **P**ulsar
NANOGrav	**N**orth **A**merican **N**anohertz **O**bservatory for **G**ravitational waves
NAS	**N**etwork **A**ttached **S**torage
NASA	**N**ational **A**eronautics and **S**pace **A**dministration
NCRA	**N**ational **C**enter for **R**adio **A**strophysics
NED	**N**ASA/IPAC **E**xtragalactic **D**atabase
NIST	US **N**ational **I**nstitute of **S**tandards and **T**echnology
NRAO	**N**ational **R**adio **A**stronomy **O**bservatory
NuSTAR	**Nu**clear **S**pectroscopic **T**elescope **AR**ray
NVSS	**N**RAO **V**LA **S**ky **S**urvey
ORT	**O**oty **R**adio **T**elescope
PA	**P**hased **A**rray
PALFA	**P**ulsar **A**recibo **L**-band **F**eed **A**rray survey
PMPS	**P**arkes **M**ulti-beam **P**ulsar **S**urvey

PONDER	**P**ulsar **O**oty radio telescope **N**ew **D**igital **E**fficient **R**eceiver
PPM	**P**ulse **P**er **M**inute
PPS	**P**ulse **P**er **S**econd
PPTA	**P**arkes **P**ulsar **T**iming **A**rray
PSR	**P**ulsating **S**ource of **R**adiation
PTA	**P**ulsar **T**iming **A**rray
PWN	**P**ulsar **W**ind **N**ebula
RA	**R**ight **A**scension
RAM	**R**andom **A**ccess **M**emory
RF	**R**adio **F**requency
RFI	**R**adio **F**requency **I**nterference
RFM	**R**adius to **F**requency **M**apping
RISS	**R**efractive **I**nter-**S**tellar **S**cintillation
RMS	**R**oot **M**ean **S**quare
RRAT	**R**otating **RA**dio **T**ransient
SED	**S**pectral **E**nergy **D**istribution
SGPS	**S**outhern **G**alactic **P**lane **S**urvey
SGR	**S**oft **G**amma-ray **R**epeater
SIMBAD	**S**et of **I**dentifications, **M**easurements and **B**ibliography for **A**stronomical **D**ata
SKA	**S**quare **K**ilometre **A**rray
SMART	**S**tretched **M**esh **A**ttached to **R**ope **T**russes
S/N	**S**ignal to **N**oise ratio
SNR	**S**uper**N**ova **R**emnant
SSB	**S**olar **S**ystem **B**arycenter
TAI	**I**nternational **A**tomic **T**ime
TGSS	**T**IFR **G**MRT **S**ky **S**urvey
TGSS ADR	**T**IFR **G**MRT **S**ky **S**urvey **A**lternate **D**ata **R**elease
TIFR	**T**ata **I**nstitute of **F**undamental **R**esearch
TOA	**T**ime **o**f **A**rrival
TOO	**T**arget **O**f **O**pportunity
TT	**T**errestrial **T**ime

UTC	**U**niversal **C**oordinated **T**ime
UVOT	**U**ltra**V**iolet **O**ptical **T**elescope
VERITAS	**V**ery **E**nergetic **R**adiation **I**maging **T**elescope **A**rray **S**ystem
VGPS	**V**LA **G**alactic **P**lane **S**urvey
VHE	**V**ery **H**igh **E**nergy
VLA	**V**ery **L**arge **A**rray
VLBI	**V**ery **L**ong **B**aseline **I**nterferometry
WSRT	**W**esterbork **S**ynthesis **R**adio **T**elescope
XMM	**X**-ray **M**ulti-mirror **M**ission
XRT	**X**-**R**ay **T**elescope

Chapter 1

Introduction

1.1 What Are Pulsars?

Pulsars are pulsating radio sources. They are rapidly rotating neutron stars possessing typical magnetic field strengths ranging between $10^8 - 10^{14}$ Gauss. They are detectable at radio frequencies through the beam of coherent radio emission from their magnetosphere. In landmark papers written in 1934, Walter Baade and Fritz Zwicky not only coined the term *supernova* (Baade and Zwicky 1934b) but also proposed a completely new type of stellar remnant, *neutron star* (Baade and Zwicky 1934a). In their words, "*With all reserve we advance the view that a super-nova represents the transition of an ordinary star into a neutron star, consisting mainly of neutrons. Such a star may possess a very small radius and an extremely high density.*" The idea was so ahead of its time that it took 33 years to get observational confirmation. In 1967, Jocelyn Bell, a doctoral student at the University of Cambridge, while determining angular sizes of compact radio sources using interplanetary scintillation (IPS), found a pulsating radio source. Once terrestrial radio frequency interference (RFI) was ruled out as a possibility, the frequency sweep of the radio pulsations indicated that the source was Galactic in origin and was either a white dwarf or a neutron star (Hewish et al. 1968). The pulses were thought to be originating from radial pulsations of the compact star

and were measured to be as stable as a few parts in 10^7. Gold (1968) attributed the remarkably stable pulsations to the rotation of neutron stars and proposed the so called "Lighthouse Effect" i.e. the beam being swept past our line of sight once per rotation, giving rise to the radio pulses.

1.2 Important Properties of Radio Pulsars

The word pulsar is an abbreviation of the phrase "Pulsating Star". Pulsars are characterised by their rotation periods. The rotation periods range from few milliseconds up to a few seconds. The most rapidly rotating pulsar is PSR J1748−2446ad with a period of only 1.4 ms (Hessels et al. 2006), while the slowest is PSR J2144−3933 with a period of 8.5 s (Young et al. 1999). These periods are usually very stable. Some of the pulse periods are as stable as a few parts in 10^{12} or more (Freire et al. 2003). On the basis of spin periods (P) and spin period derivatives ($\dot{P}$), radio pulsars are usually classified in two categories, namely normal pulsars ($P > 30$ ms and $\dot{P} \sim 10^{-15}$ s-s^{-1}) and millisecond pulsars or MSPs ($P < 30$ ms and $\dot{P} \sim 10^{-19}$ s-s^{-1}). Although they show many orders of magnitudes of difference in their properties, there are some properties which are common and are useful in the study of the pulsar population. We discuss some of them briefly in the next sections.

1.2.1 Integrated Profiles

Pulsars are weak radio sources. Thus, one needs to observe a few hundred pulses (Helfand et al. 1975) and fold the time series modulo the pulse period, to get what are called the *integrated profiles* (IP). Although, the individual pulses vary quite a lot in intensity, the integrated pulse profile is usually stable and is a unique feature of the particular pulsar. The IP, in fact, is a physical signature of the emission beam geometry and the angle made by our line of sight with the axis of the magnetic field. The typical duty cycles for pulsars are of the order of a few

percent but the pulse shapes as well as number of components vary widely. This has been shown for a few pulsars in Figure 1.1.

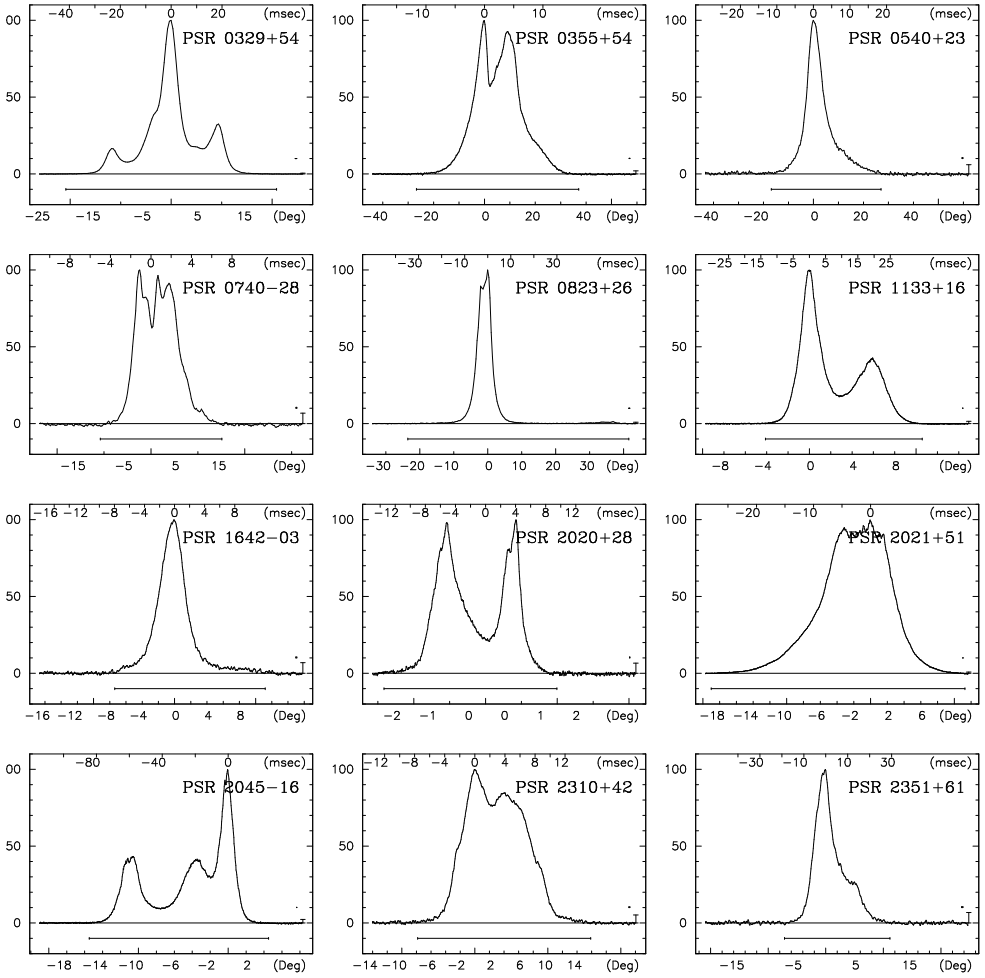

FIGURE 1.1: Some pulse profiles observed at 1.4 GHz. The X-axis shows pulse phase in degrees on the bottom scale and in time on the top scale. The profiles have been zoomed on the pulse area to show the structure in a better way. Figure taken from Seiradakis and Wielebinski (2004)

While the IP is unique to a pulsar (apart from the exceptions noted below), it does vary as a function of observing frequency. For some pulsars, the IPs also change as a function of time. The change in IPs over time can happen due to two major reasons. One of them is the precession in a binary system, which was seen as the decrease in the intensity of one of the two components in the profile for PSR B1913+16 (Weisberg et al. 1989). Another extreme example is that of pulsar B in the double pulsar system PSR J0747−3039A/B, which is not detectable any more because precession has made the emission beam of the pulsar to drift out

of our line of sight, making it non-detectable from the year 2008 (Burgay et al. 2014). The other reason for profile changes over time is due to a phenomenon called *mode changing*. The pulsars, which show mode changes, have two or three different stable profile shapes and shift abruptly into one of them. The extreme end of the mode change is that there is no detectable emission in the other mode. This phenomenon is called *nulling* and was first reported by Backer (1970). The current understanding about these phenomena is that the pulsar magnetosphere has more than one metastable states and each state gives rise to a slightly different beam geometry. Lyne et al. (2010) recently found out that the different configurations of the magnetosphere also correspond to different spin-down rates for the mode changing pulsars.

The integrated profiles of pulsars also differ in their shapes according to the observation frequency. One can compare Figure 1.1 and 1.2 to see that the profiles look very different at different observing frequencies. This effect is seen due to the radio emission mechanism, giving rise to emission at different radio frequencies at different heights from the pulsar surface. This so called radius to frequency mapping (RFM) is explained conceptually in Figure 1.3.

1.2.2 Flux Densities and Spectra

As was stated in the previous section, pulsars are weak radio sources. The typical pulsar flux densities at a frequency of 400 MHz[1] are a few to a few hundred mJy (1 Jansky = 1 Jy = 10^{-26} W-m^{-2}-Hz^{-1}). As pulsars have a small duty cycle, the flux densities of the pulsars are always converted into mean continuum flux densities by averaging the integrated pulse intensity over the rotation period. Pulsars are typically steep spectrum sources and their spectra can be represented to the first order by a single power law of the form

$$S_\nu \propto \nu^\alpha \tag{1.1}$$

[1]According to the Australia telescope national facility (ATNF) pulsar catalog. This catalog lists many pulsar properties and is available at www.atnf.csiro.au/people/pulsar/psrcat/

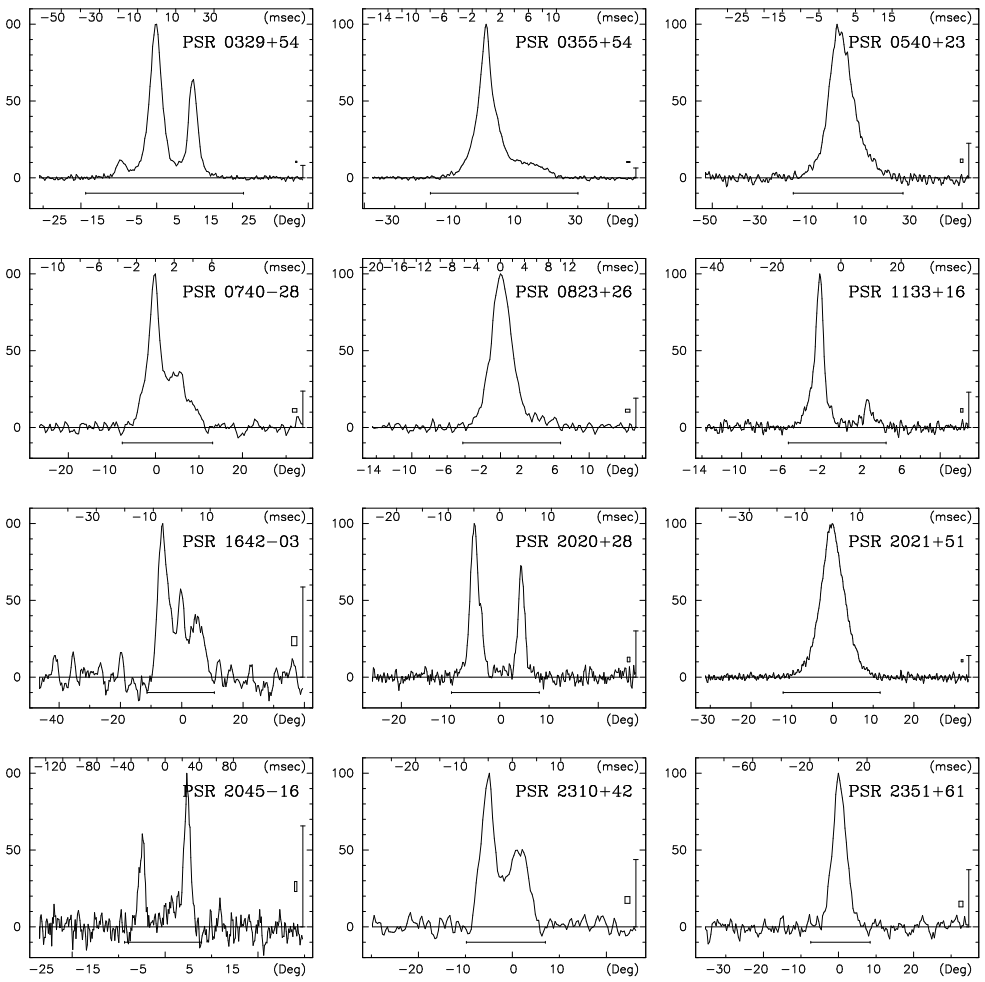

FIGURE 1.2: Pulse profiles for the same pulsars as in Figure 1.1 but observed at 10.7 GHz. Figure taken from Seiradakis and Wielebinski (2004)

The average value of α was recently estimated to be -1.41 ± 0.06 (Bates et al. 2013). Pulsars show different types of radio spectra. Apart from the usual power law spectra, some pulsars show broken spectra with two different power law slopes in low and high radio frequency ranges. An extreme example of this is the spectral turnover wherein, the power law slope becomes positive below some frequency. These spectral turnovers usually happen at around 100−300 MHz but there are some examples where the turnover frequency is much higher (Maron et al. 2000). Figure 1.4 shows representative spectra for a single and double power law type spectra. The average value of α as measured by Maron et al. (2000) was -1.8 ± 0.2. The recent value being slightly flatter means that there are many more flatter spectrum pulsars than previously known.

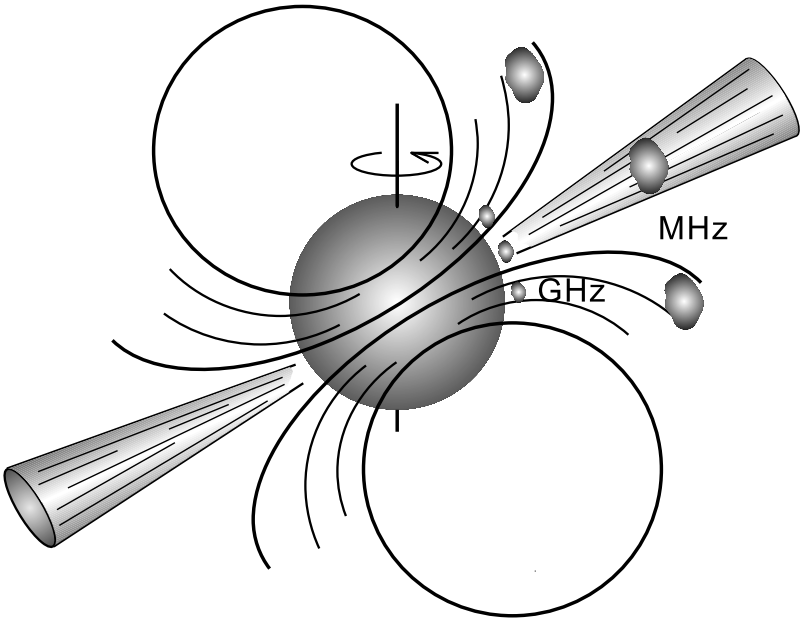

FIGURE 1.3: A model showing radius to frequency mapping in radio pulsars. The emission at high radio frequencies happens closer to the neutron star surface as compared to the emission at lower radio frequencies. This results into wider beams at low radio frequencies. Figure taken from Seiradakis and Wielebinski (2004)

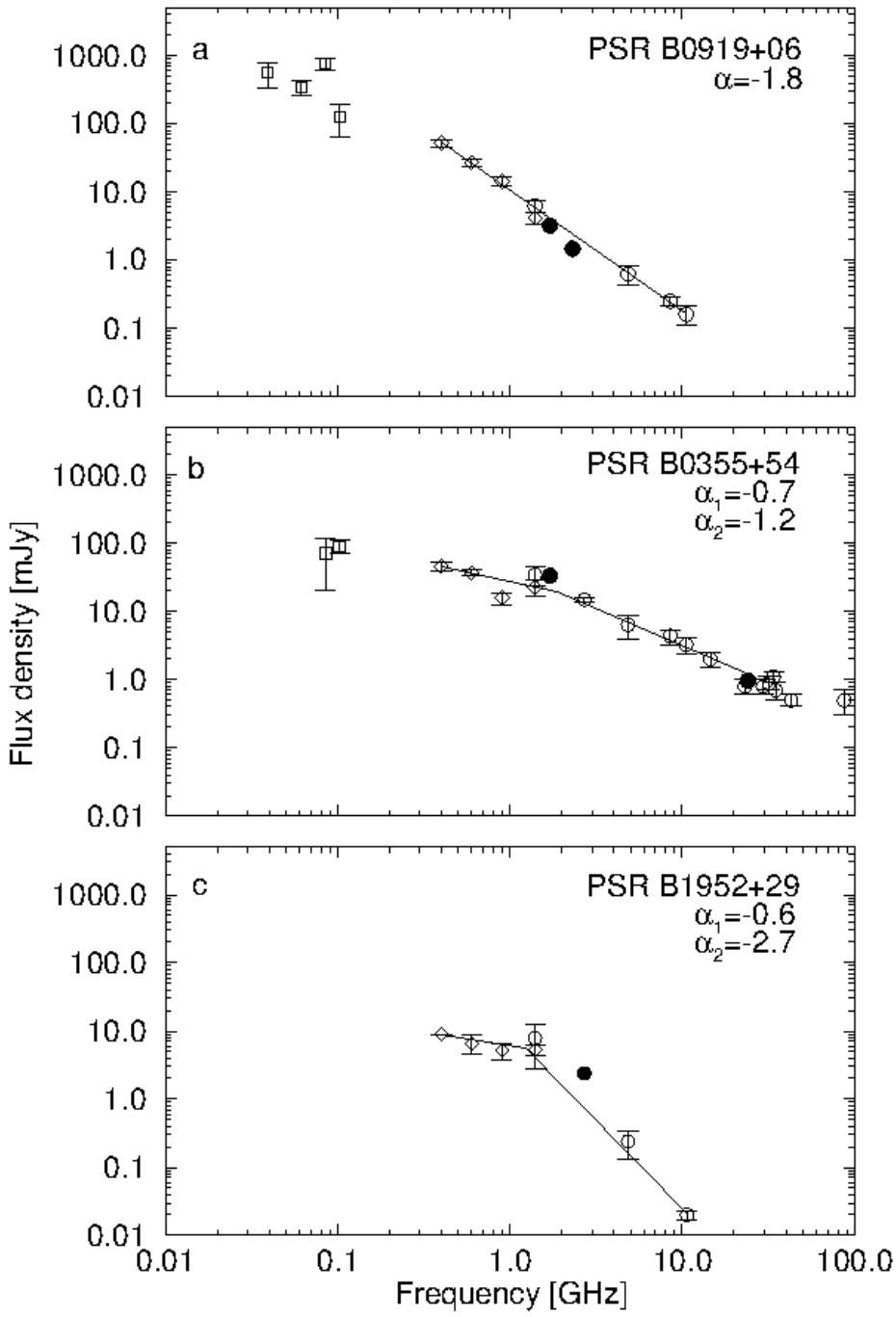

FIGURE 1.4: Two Major types of pulsar spectra. a) Typical power law spectrum with $\alpha = -1.8$, b) Two power law with smallest difference in slopes ($\alpha_1 = -0.7$ and $\alpha_2 = -1.2$), c) Two power law with largest difference in slopes ($\alpha_1 = -0.6$ and $\alpha_2 = -2.7$). Figure taken from Maron et al. (2000).

1.2.3 Effects of the Interstellar Medium

The interstellar medium (ISM), that spans the almost empty space between us and the pulsars in our Galaxy, consists of gas (like Hydrogen, Helium) and dust particles among other constituents. The gas can be either in the form of plasma or neutral atoms or even molecules. Dust particles mainly include aggregates of different molecules or atoms. As will be evident soon, the most influential part of the ISM for radio pulsar signals, is the plasma. Plasma produces many effects on the pulsar signal that passes through it. They are namely, *dispersion* (frequency dependent delays in the signal), *Faraday rotation* (rotation of the plane of polarization of the wave), *scattering* (delay produced due to multi-path propagation, resulting in an exponential tail in the integrated profile) and *scintillation* (occurs due to the fluctuations in the charge density in the ISM as well as the ionosphere of Earth. This introduces path differences and distorts wave fronts so that observed flux density varies randomly as a function of time). Apart from dispersion, all the other effects arise in specific cases where a longer term follow-up of some interesting pulsars is intended. In the sections below, we would discuss dispersion, scintillation and scattering in some more detail.

1.2.3.1 Dispersion

When the pulsar signal travels through cold plasma, it experiences a frequency dependent refractive index. The refractive index for a frequency f is given by

$$\mu = \sqrt{1 - \left(\frac{f_p}{f}\right)^2} \tag{1.2}$$

where f_p is the plasma frequency given by

$$f_p = \sqrt{\frac{e^2 n_e}{\pi m_e}} \simeq 8.5 \left(\frac{n_e}{cm^{-3}}\right)^{1/2} \text{ kHz} \tag{1.3}$$

where n_e is the electron number density in the plasma. A very crude estimate of the average value of n_e is about 0.03 cm^{-3} (Lorimer and Kramer 2005) implying f_p = 1.5 kHz. It is clear from Equation 1.2 that due to differential speed of the propagating wave, the pulse at a higher frequency will arrive earlier than that at a lower frequency. In fact, the group velocity of the propagating waves, $v_g = c\mu$ will always be less than c if $f > f_p$. As a consequence, the propagation of pulsar signal of frequency f to a distance d will be delayed in time with respect to a signal of infinite frequency by an amount

$$t = \left(\int_0^d \frac{dl}{v_g}\right) - \frac{d}{c} \tag{1.4}$$

Substituting for v_g and noting that $f_p \ll f$ we find

$$t \simeq \mathtt{D} \times \frac{DM}{f^2} \tag{1.5}$$

where *Dispersion Measure* (DM) i.e. integrated free electron density along the line of sight is given by

$$DM = \int_0^d n_e dl \tag{1.6}$$

and is usually expressed[2] in pc-cm^{-3} and the *Dispersion Constant* is

$$\mathtt{D} \equiv \frac{e^2}{2\pi m_e c} = (4.148808 \pm 0.000003) \times 10^3 \text{ MHz}^2\text{-pc}^{-1}\text{-cm}^3\text{-s} \tag{1.7}$$

The uncertainty in D is determined by the uncertainties in e and m_e. Now, the delay between two frequencies f_1 and f_2 (both in MHz) is given by

$$\triangle t \simeq 4.15 \times 10^6 \times (f_1^{-2} - f_2^{-2}) \times DM \text{ ms} \tag{1.8}$$

[2]Parsec (pc) is a unit of distance defined as the distance at which, the parallax of an object is 1 arc second as measured six months apart from earth. 1pc = 3.08×10^{16} m

From measurement of pulse arrival time for two different frequencies, the DM of pulsar can be inferred along the line of sight. Then according to Equation 1.6, the distance of pulsar can be estimated if $n_e(l)$ is known from standard models like the NE2001 model (Cordes and Lazio 2002). This is particularly useful in searching for new pulsars because the search algorithm is iterative in nature and uses an array of carefully chosen trial DM values, which act as proxy to distance from the Earth.

1.2.3.2 Scattering and Scintillation

Although the integrated pulse profiles for pulsars are relatively stable, there is a lot of variation in the pulse energy and shape for individual pulses. Sometimes, these variations are intrinsic to the pulsar (see Section 1.2.1). The flux density and pulse shapes of pulsars can also vary because of the change in the structure of the ionized medium lying between the pulsar and the Earth. Due to changes in the local free electron (or ion) density, the pulsar signal undergoes multi-path propagation instead of travelling in a straight line. This manifests either as intensity variations (scintillation) or stretching of the integrated pulse (scattering). The basic theory for these was given by Scheuer (1968). For simplicity, the density fluctuations are always modelled in the form of a thin screen present midway between the observer and the pulsar (the so called *thin screen approximation*). The fluctuations are also assumed to be Gaussian in nature, which implies that the quantities of interest are typically root mean square (RMS) values relating to the width of the Gaussian distribution. The repeated scattering of the pulsar signal produces a diffraction pattern at the location of the observer and the point source appears to be scatter-broadened. The angular broadening radius (θ_d) can be estimated to be (Scheuer 1968),

$$\theta_d \propto \sqrt{\frac{d}{a}} \frac{\triangle n_e}{f^2} \tag{1.9}$$

where d is the distance of the pulsar from Earth, a is the characteristic length scale of irregularities, $\triangle n_e$ is the RMS change in the free electron density and f is the observing frequency. Due to this angular broadening, the rays received by the observer at an angle θ with respect to an unperturbed ray are delayed by

$$\triangle t(\theta) = \frac{\theta^2 d}{c} \tag{1.10}$$

Williamson (1972) has shown that this introduces an exponential tail in time domain such that the observed intensity (I) in time is given by

$$I(t) \propto exp(-\triangle t/\tau_{sc}) \tag{1.11}$$

where τ_{sc} is the scatter-broadening time scale and is given by

$$\tau_{sc} = \frac{\theta_d^2 d}{c} \propto \frac{\triangle n_e^2}{a}\ d^2 f^{-4} \tag{1.12}$$

This implies that the pulsars having high DMs would show large scattering tails at low frequencies. This has been observationally verified (e. g. Krishnakumar et al. 2015). In the case of relative motion between the source, the observer and the scattering screen, the diffraction pattern would move and produce intensity fluctuations i. e. scintillation. The scintillation time scales also inherit the f^{-4} dependence. Based on the origin of the motion of the diffraction pattern, scintillations could either be diffractive [diffractive interstellar scintillation (DISS)] or refractive [refractive interstellar scintillation (RISS)]. For typical ISM velocities, the characteristic time scales for DISS are of the order of a few seconds to few hours, while the time scales for RISS are of the order of months at centimetre wavelengths.

1.2.4 The Pulsar Population

Given the very long lifetimes of pulsars (of the order of a few billion years), what one essentially does while studying pulsars is to look at a large number of them to do some population study to try and figure out how they form and evolve in different scenarios. Given the weak nature of their emission, the current pulsar population is very much Galactic in origin. Currently, the farthest known pulsars lie in the Magellanic clouds and they are 28 in number (Ridley et al. 2013). Out of the remaining, only 144 are located in Galactic globular and other clusters[3]. This means that out of about 2500 pulsars currently known, almost 93% pulsars reside in the Galactic disk. This implies that due to the ISM effects described in the previous section, there would be an observational bias against detecting highly scattered and weak, distant pulsars. Another bias is due to the narrow radio beam of the pulsars which means that there may be active radio pulsars not beaming towards the Earth. The estimated total number of active pulsars in our Galaxy is about a million (Lorimer and Kramer 2005). Now, like the optical stars, one can not construct an H-R diagram for radio pulsars. However, radio pulsars posses one unique property which enables us to construct a similar diagram for them. To a very rough approximation, pulsars emit radiation at the expense of their rotational kinetic energy. Thus, in the process of emission, the rotational kinetic energy decreases over time and in return, the pulsar slows down over time. This rate can be very precisely determined by doing pulsar timing measurements which are described in detail in Section 4.3. It is the rate of the slow-down or the period derivative ($\dot{P}$) which enables us to construct a diagram depicting the pulsar population. That diagram is called a $P-\dot{P}$ diagram.

In the $P-\dot{P}$ diagram plotted in Figure 1.5, the normal pulsars and MSPs show up as two different populations. The normal pulsars are clustered towards the center of the plot while, the MSPs form a cluster towards the bottom left of the plot. They have much smaller periods as well as period derivatives as compared to normal pulsars. Apart from the separation of different populations, simple

[3]www.naic.edu/∼pfreire/GCpsr.html

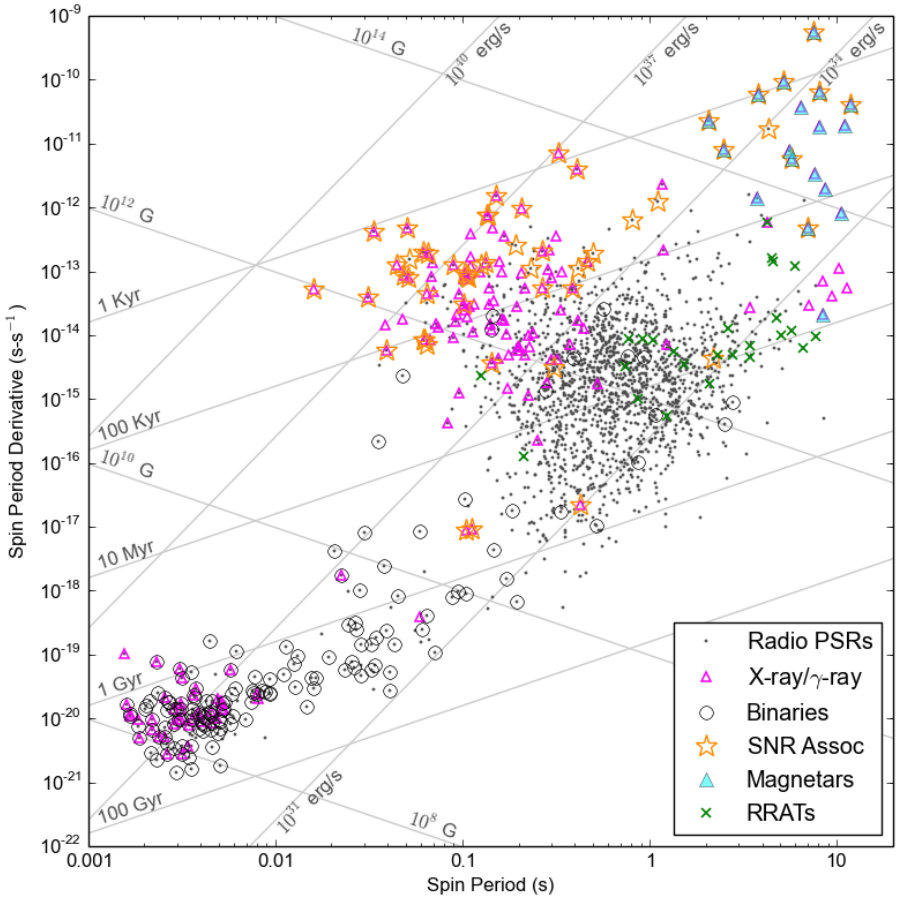

FIGURE 1.5: The known pulsar population represented in a P−$\dot{\text{P}}$ diagram. This diagram does not show the pulsars which are in globular clusters. Also shown in the plot, are the lines of constant surface magnetic field strength ($\text{B}_\text{S} \propto \sqrt{\text{P}\dot{\text{P}}}$), characteristic age ($\tau \propto \text{P}/\dot{\text{P}}$) and spin-down luminosity ($\dot{\text{E}} \propto \dot{\text{P}}/\text{P}^3$). Made by using the script `ppdot_plane_plot.py` in PRESTO[4].

dipole models of pulsar magnetosphere allow us to obtain an estimate for many more pulsar parameters like the surface magnetic field strength ($\text{B}_\text{S} \propto \sqrt{\text{P}\dot{\text{P}}}$), the characteristic or spin-down age ($\tau \propto \text{P}/\dot{\text{P}}$) and the spin-down luminosity of the pulsar ($\dot{\text{E}} \propto \dot{\text{P}}/\text{P}^3$). The lines of constant magnetic field strength, characteristic age and spin-down luminosity are also shown in the P−$\dot{\text{P}}$ diagram in Figure 1.5 . The region towards the bottom right of the plot, where no pulsar is seen is called the *death valley* region for radio pulsars. This region is separated by the *death*

[4]www.cv.nrao.edu/∼sransom/presto

line which is the line separating the neutron stars that can sustain radio emission from the ones that can not (Ruderman and Sutherland 1975). Although the exact spacing and nature of the death line is somewhat dependant on the emission model (Zhang et al. 2000), the death valley region is fairly well defined and as expected, not populated.

As can be clearly seen, MSPs are much older and have much lower magnetic fields as compared to the normal pulsars but are still almost as luminous. This lead to the conjecture that MSPs are born as normal pulsars and slowly fade away into the death valley. They are then recycled as MSPs through mass transfer from their binary companions (Bhattacharya and van den Heuvel 1991). Apart from MSPs, there are some more interesting types of pulsars sitting in the population. Magnetars or magnetic stars (denoted by filled cyan triangles in Figure 1.5), which are powered by their magnetic fields rather than rotational kinetic energy, form the top right island in the $P-\dot{P}$ plot. They have extremely high magnetic fields of the order of 10^{14} G. Rotating RAdio Transients (RRATs; denoted by green crosses in Figure 1.5) (McLaughlin et al. 2006) are transient pulse emitters and have slightly higher magnetic field strengths than normal pulsars. They were believed to form the bridge between normal pulsars and magnetars. This distinction appears to be less justified with a larger sample available now (Keane et al. 2011). Different types of extreme pulsars also exist and their position in the $P-\dot{P}$ diagram helps in assessing how the evolution of the neutron stars happens after the supernova explosion.

1.3 Pulsars as Physical Tools

With more than 1.5 $M_\odot$ packed into a sphere with a radius of about 10 km, pulsars are the most compact form of matter that can be detected directly through electromagnetic observations. This, combined with the ever so stable rotation that allows very precise measurements over long time scales, makes pulsars very fascinating objects for studying many different aspects of physics. In the next few

sections, we briefly discuss some of the extreme physics that can be studied using pulsars as physical tools.

1.3.1 High Precision Timing and Pulsar Time

Pulsars are very stable rotators. Their rotations can be monitored very precisely over a long time scale to obtain many important parameters. This is done usually by doing pulsar timing (described in detail in Section 4.3). MSPs show much more stability in their rotation as compared to that of the normal pulsars. This allows the prediction of the arrival time of a pulse just by using the timing model. Very stable MSPs thus, can become excellent clocks. The stability of MSPs as clocks is not very good over short time scales of a few years but after that, some of the most stable MSPs like PSR J0437−4715 shows better stability than atomic clocks (Lorimer and Kramer 2005). This fact points towards the possibility of establishing a pulsar time scale (albeit, with some caveats) which will be universal and would require dedicated timing observations of a handful of very stable MSPs (see Hobbs et al. 2012, for a recent account).

1.3.2 Testing Theories of Gravity

Although the Pound-Rebka experiment of gravitational red shift (Pound and Rebka 1959) provided a very stringent test of Einstein's theory of general relativity (GR), it was still in the weak field limit of the theory. In the classical limit, GR reduces to Newtonian gravity. Hence, the only place where the GR can be really put to test against alternate theories of gravity is in the strong field regime. Such a regime is readily provided by compact objects like neutron stars (Will 2014), especially binary neutron stars. In fact, the first indirect confirmation of the existence of gravitational waves was provided by precise timing measurements done on a double neutron star binary system PSR B1913+16, which showed the decay of orbit due to emission of gravitational waves at the expense of the orbital potential energy (Taylor and Weisberg 1989). The discovery of the double pulsar

system J0737−3039A/B (Burgay et al. 2003; Lyne et al. 2004) has lead to the most stringent tests of the GR to date.

1.3.3 Extrasolar Planets

The unprecedented precision afforded by pulsar timing, allowed Wolszczan and Frail (1992) to detect the presence of the first extrasolar planets; three of them, revolving around the MSP PSR B1257+12. Unlike the Jupiter-like planets detected using the optical telescopes, the timing analysis revealed the presence of one lunar mass and two Earth mass planets revolving around the pulsar. This level of precision is possible only due to the stable neutron star rotation. Although the origin of neutron stars (supernova explosion) does not typically allow such systems to sustain, pulsar timing is sensitive enough to detect such planets if they survive.

1.3.4 Galactic Structure

As stated in Section 1.2.3, the pulsar signal gets dispersed and the DM provides a handle on the integrated line of sight free electron density. An independent distance measurement for some pulsars can be obtained through optical parallax of its binary companion star (if any), an HI absorption line measurement, very long baseline interferometry (VLBI) based parallax measurement or associations with objects of known distance such as supernova remnant, globular cluster, star forming regions etc. Such measurements for a large number of pulsars across the Galaxy can be used to make a model of the free electron distribution. One such example is the NE2001 model (Cordes and Lazio 2002). This model, in turn, is used to estimate the distance to a pulsar once its DM is known with fair accuracy. In this sense, pulsar are useful tools to map out large scale structure of the Galaxy through DM measurements. A slight change in the DM value along the line of sight may indicate change in the free electron density. Long term monitoring of DM changes may reveal a lot about the dynamics of plasma along some few special lines of sight. In fact, the crab pulsar, PSR B0531+21, which is inside a pulsar wind

nebula, shows changes in the profile shape due to passage of filaments of plasma through the line of sight. Such measurements have helped in understanding the dynamics of plasma in the neighbourhood of this pulsar (Backer et al. 2000).

1.3.5 Condensed Matter Physics

The matter in the interior of neutron stars has a density, which is more than the nuclear density. Such super dense matter can not be created in any terrestrial laboratory. Naturally, it is difficult to predict the behaviour of such matter. The most fundamental quantity regarding such system is the equation of state of the matter i.e. a relation between pressure and density. There are many theories as to what kind of matter comprises the neutron star interior. Precise mass measurements in binary systems are very useful in ruling out some equations of state (Demorest et al. 2010).

1.3.6 Pulsar Timing Array

The clock-like stability of the MSPs makes them very useful tools for probing a very different aspect of gravitational physics. This requires an array of MSPs at different locations in the sky. Any passing gravitational wave will distort the space-time so that, one could detect very minor changes in the timing residuals (after subtracting timing model from the observed times of arrival) which will be correlated over many pulsars. This concept of the *pulsar timing array* (PTA) was first suggested by Foster and Backer (1990). The PTA would be sensitive to gravitational waves in the nano-Hertz frequency range, thus probing the gravitational wave background created by the merger of binary super-massive black holes. The RMS level of residuals required to be able to detect this background is of the order of 10 ns. Currently, there are only a handful of MSPs having the required level of residuals. The effort in the PTA has been initiated by three major PTAs worldwide. They are the Parkes Pulsar Timing Array (PPTA)[5], the European

[5] www.atnf.csiro.au/research/pulsar/ppta/

Pulsar Timing Array (EPTA)[6] and the North American Nanohertz Observatory for Gravitational waves (NANOGrav)[7]. Together, the effort is called the International Pulsar Timing Array (IPTA)[8]. Although there are not enough MSPs with the required residual levels, the IPTA and the individual PTAs are putting upper limits on the possible gravitational wave background amplitude (h_c), that are useful for understanding the evolution of the galaxies through mergers as they harbour super-massive black holes in their cores. The current upper limits on the gravitational wave background amplitude imposed by the NANOGrav, EPTA and PPTA stand at 1.5×10^{-15}, 3.0×10^{-15} and 1.0×10^{-15} with 95% confidence, at a frequency of 1 yr^{-1}, respectively (see Verbiest et al. 2016). The combined IPTA data set implies a limit of 1.7×10^{-15} with 95% confidence, at a frequency of 1 yr^{-1} (Verbiest et al. 2016). This limit implies a rejection of the standard galaxy evolution model used for the millennium simulation at 50% confidence limit (Shannon et al. 2013).

[6] www.epta.eu.org/
[7] www.nanograv.org/
[8] www.ipta4gw.org/

Chapter 2

Literature Review

As explained in Section 1.2.4, the study of pulsars as physical objects as well as their use as tools to understand physics in extreme limits, pertains to obtaining a good estimate of pulsars as a population. A good way to obtain a complete sample of pulsars is to keep searching for them with improved instruments and methods. Such quests are termed as pulsar searches. In this chapter, we take an overview of the past and ongoing blind pulsar searches carried out with different radio telescopes, using varied techniques.

2.1 Why Search for Pulsars ?

The discovery of the first pulsar, PSR B1919+21, by Jocelyn Bell (Hewish et al. 1968) was followed by an accurate association with a neutron star origin (Gold 1968). The fact that such extreme objects exist and are detectable by simple radio telescopes was recognised by astronomers. In early days of pulsar astronomy, the only property which was well known about pulsars was that their periods were very stable at the level of a few parts in 10^7 or better (Hewish et al. 1968). They were new, enigmatic and interesting radio sources. Thus, early motivations for pulsar searches were basically related to obtaining a meaningful, statistical sample to be able to study their population properties. After the discovery of PSR B1937+21,

the first MSP with a rotation period of only 1.5 ms, questions were raised about the origin and evolution of such sources (Backer et al. 1982). As the pulsar population started building, the motivation for finding new pulsars was augmented with many more aspects like trying to find more MSPs, constructing a luminosity function for pulsars, finding out the radial distributions of the pulsars in the Galaxy and trying to match the observed pulsar population to the predicted supernova rates relating directly to the evolution of our Galaxy (Lyne et al. 1985).

With the advent of advanced computing facilities as well as the availability of better hardware and software for data analysis, pulsar searches have become more fruitful in the modern era. The current population boasts of about 2500 known pulsars[1] with vastly different type of sources like normal pulsars, MSPs, RRATs, magnetars, low mass X-ray binaries (LMXBs), high mass X-ray binaries (HMXBs), accreting millisecond X-ray pulsars (AMXPs) and many more. The modern day motivation for pulsar searches is still basically trying to add to the existing population. In addition, with reference to the different types of pulsar studies as well as their use as tools for understanding many physical phenomena (as discussed in Sections 1.2 and 1.3), one needs to have as many sources of each different type to study the specific physics problem as well as understand the common origin with the later evolution into the different classes.

2.2 A Short History of Blind Pulsar Searches

It was clear from the beginning, that observable pulsars were mostly Galactic in origin. This meant that the density of pulsars would be highest near in the Galactic disk. Blind pulsar searches were thus, aimed primarily at the Galactic plane. One look at the history of pulsar searches reveals that the observing frequencies for pulsar searches went from 80 MHz to 1.4 GHz. The major mile stone in pulsar searches was achieved by the Parkes multi-beam pulsar survey (PMPS; Manchester et al. 2001), which doubled the number of pulsars known at that time. Due to

[1] www.atnf.csiro.au/people/pulsar/psrcat/

the remarkable feat achieved by the PMPS, pulsar search history can be divided in two sections namely, before PMPS and after PMPS. In the next sections, we describe these separately, while dedicating a special, short section to describing PMPS itself.

2.2.1 Initial Pulsar Searches

The discovery of the first pulsar, PSR B1919+21 was done at an observing frequency of 81.5 MHz (Hewish et al. 1968). The surveys those followed, were carried out at slightly higher frequencies of 110 and 408 MHz at National Radio Astronomy Observatory (NRAO) (Huguenin et al. 1968) and Molonglo (Turtle and Vaughan 1968), respectively. The initial surveys were basically performed with transit scanning instruments with very little steerability. This resulted in much shorter integrations and reduction in sensitivity. This can be related to the fact that the telescopes at Cambridge in the United Kingdom and Molonglo in Australia, were basically imaging instruments and were basically being used to map the radio emission in the observable part of the sky. The stationary nature of the telescope also reduced sensitivity due to non-uniform illumination at slightly higher zenith angles (Turtle and Vaughan 1968). The other limiting factor was the back-end, which was a pen and chart recorder which would produce a deflection proportional to the source intensity. The finest time resolution available was of the order of the order of a few ms (Large et al. 1968). The typical survey sampling was of the order of a few hundred ms (Turtle and Vaughan 1968) and a faster sampling was done only when a new source was suspected. Given that the instruments were not constructed for observing highly variable sources, there were limited means to correct for the frequency sweep produced by interstellar dispersion. In fact, Hewish et al. (1968) could figure out through carefully designed experiments, that the pulse dispersion has an inverse square dependence on frequency (as explained in Section 1.2.3.1) even in a band as small as 1 MHz. Burns and Clark (1969) have summarized the problems with using digital processing for pulsar detection and they point out that it is computationally expensive as well as low in yield. The

techniques discussed by Burns and Clark (1969) are basically fast folding analysis (FFA) and fast Fourier transforms (FFT) and they comment that given the time and frequency resolution, the search analysis is biased against weaker pulsars with periods not harmonically related to the sampling interval. Even with such coarse sampling, which was biased against short period pulsars and no way to correct for pulse dispersion, it is remarkable that they were able to detect and characterize about 30 new pulsars by the end of 1970. The survey started at the Jodrell Bank Mark I telescope at 408 MHz was the first to use an online computer for data processing (Davies and Large 1970). The offline analysis was carried out in real time and searched in DM space with a resolution of 20 pc-cm^{-3} over a range of 0−1100 pc-cm^{-3}. This survey was very successful and discovered 39 new pulsars (Davies and Large 1970; Davies et al. 1970, 1972, 1973).

The first pulsar survey at Arecibo telescope (Hulse and Taylor 1974) was conducted at 430 MHz with a dedicated pulsar back-end which performed online dedispersion using the tree dedispersion algorithm to produce 64 dedispersed time series streams with two different DM resolutions in the DM range 0−1240 pc-cm^{-3}. The offline processing, for the first time attempted a full search over the P−DM−duty cycle phase space by using the harmonic summation algorithm reported by Burns and Clark (1969). This survey was also very successful with the discovery of 40 new pulsars (Hulse and Taylor 1975a) including the much celebrated first binary pulsar, PSR B1913+16 (Hulse and Taylor 1975b). The Green bank survey described in Damashek et al. (1978) used similar search techniques to discover 11 more new pulsars. This survey was complementary to the survey undertaken at Molonglo by Manchester et al. (1978). This was the first time when low noise amplifiers (LNA) were employed just after the feed in order to reduce the system noise by a factor of 2.5 (Manchester et al. 1978). This survey was the most successful till its time, discovering 155 pulsars as compared to 149 in all the surveys combined. It also made use of the multiple beams to compensate for the loss in sensitivity due to low gains at high zenith angles (Manchester et al. 1978). The Princeton−NRAO survey described in Dewey et al. (1985), was carried out at 390 MHz and discovered 34 new pulsars. They also note that the pulsar surveys were reaching sensitivities

to a level below which, the probability of finding new pulsars was getting lower and lower. The overall search sensitivities were coming down drastically by this time and were hovering around a few mJy for normal pulsars. None of the above quoted surveys, however, was sensitive to pulsars having periods below a few tens of ms. The discovery of the first MSP, PSR B1937+21 in 1982 (Backer et al. 1982) in a targeted search, opened the possibility of a completely new class of pulsars. The surveys those followed, tried to look specifically for MSPs (the name was not yet stuck). The continuation of the Princeton−NRAO survey (Stokes et al. 1985) at Green bank and a limited, targeted survey to look for pulsars associated with supernova remnants (SNRs) carried out for the first time at a high frequency of 1.4 GHz at Jodrell bank (Manchester et al. 1985) had a sampling time of 2 ms. Both of them did not detect any MSPs. First successful blind search discovery of an MSP, PSR B1855+09 came through the Arecibo telescope observing at 430 MHz (Stokes et al. 1986). By this time, it was realized that the extra scatter broadening and dispersive smearing could be responsible for the limited success of the new surveys at 400 MHz and the pulsar surveys at the Jodrell bank telescope had moved to 1.4 GHz. The Jodrell bank B survey (Manchester et al. 1985; Clifton and Lyne 1986; Clifton et al. 1992) discovered 40 new pulsars.

The first successful survey at 1.5 GHz was carried out by Johnston et al. (1992) using the Parkes telescope, a fully steerable 64 m diameter single dish, discovering 46 new pulsars. This was the first survey which had sampling times going into the sub millisecond regime. This survey discovered many young and distant pulsars. PSR B1259−63, first pulsar in a binary system with a stellar mass star was discovered in this survey (Johnston et al. 1992). Nice et al. (1993) discovered two new MSPs with Arecibo telescope in a blind survey carried out at 430 MHz. They used a supercomputer for doing the survey data analysis, which gave them freedom to choose the trial DM values which were not related to delays which were integral multiples of the sampling time. With finer sampling times, the Arecibo surveys carried out at 430 MHz had started detecting MSPs (Nice et al. 1995; Foster et al. 1995). It was also noted that the MSPs were much closer to the Sun

and hence, their distribution was much more isotropic as compared to normal pulsars. This meant that the MSP population, as known at that time, was relatively local (Foster et al. 1995). Given the limited success of high frequency surveys in finding MSPs, it was thought that higher frequencies may not be good for detecting MSPs due to their low luminosities as well as steep spectra (Manchester et al. 1996). This lead to a blind survey for MSPs using the Parkes telescope at 436 MHz. This survey detected 101 new pulsars including 17 new MSPs (Lyne et al. 1998). The population analysis done by Lyne et al. (1998) indicated that there should be about 30000 potentially observable pulsars. The newly detected MSPs had much larger DMs and the pulsar population now showed a significant bimodal period distribution (Lyne et al. 1998). Just when it seemed that major surveys were shifting again to low radio frequencies, in came the PMPS !

2.2.2 The Parkes Multi-beam Pulsar Search

Pulsar searches at low radio frequencies were preferred because of the steep spectra of pulsars. These surveys, however, suffer from many drawbacks. The dispersion smearing is inversely proportional to the square of the observing frequency (Section 1.2.3.1). The scatter broadening of the profile is more severe at low frequencies. In fact the scattering strength is proportional to $\nu^{-4.4}$ (Rickett 1977) which essentially suppresses the pulsed nature of radio emission for highly scattered pulsars. In addition, the background continuum emission from the Galaxy is very dominant at low frequencies. It follows a typical brightness temperature spectrum of $T_b \propto \nu^{-2.5}$ (Haslam et al. 1982). Thus, highly sensitive surveys at high radio frequencies have larger potential to detect high DM or highly scattered pulsars as compared to their lower frequency counterparts. The only drawback of surveys at high frequencies is the small field of view. This drawback was removed with the fabrication of the multi-beam feed (Staveley-Smith et al. 1996). This focal-plane array had 13 feeds arranged in a hexagonal grid. The feed positioning is such that a cluster of four pointings (as shown in Figure 2.1) would cover a region about 1.5° across.

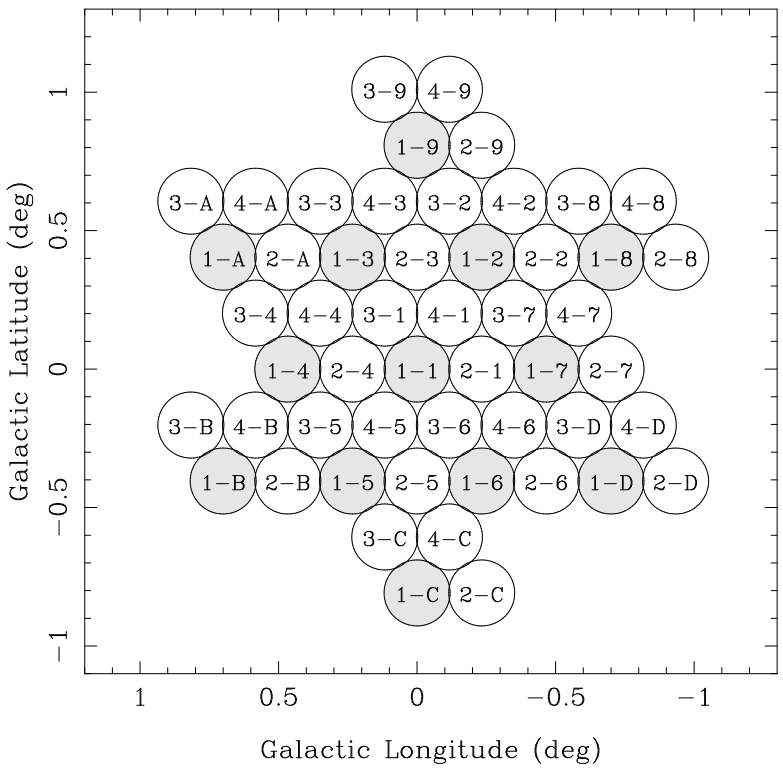

FIGURE 2.1: Beam positions for the four pointing strategy used in PMPS. The beams are labelled with pointing number followed by the hexadecimal feed number. The beam positions for the first pointing are shaded. Figure taken from Manchester et al. (2001)

A well organized survey strategy would provide good survey speed with uniform sensitivity (see Manchester et al. 2001, for details). With a cooled receiver resulting in a receiver temperature of 21 K and an unprecedented bandwidth of 300 MHz, the PMPS doubled the number of known pulsars. Not just the original processing but even reprocessing of the PMPS data has produced a lot of new pulsar discoveries of various types (e.g. McLaughlin et al. 2006; Eatough et al. 2013).

2.2.3 Modern Pulsar Searches

The PMPS revolutionized pulsar searches and paved way for many modern pulsar back-ends, resulting in more and more pulsar discoveries. So much so that, all the surveys including the PMPS discovered nearly 1500 pulsars in the 35 years following the discovery of pulsars, with later surveys discovering the remaining 1000

pulsars in only 12 years. Table 2.1 lists some important observational characteristics of major blind pulsar surveys to date. The multi-beam receiver at Parkes itself was used in many surveys like the Parkes high latitude (HL) survey (Burgay et al. 2006), the Swinburne intermediate-latitude pulsar survey (Edwards et al. 2001), the Perseus arm pulsar survey (Burgay et al. 2013) and the southern High Time Resolution Universe survey (HTRU; Keith et al. 2010). The multi-beam receiver idea itself was implemented at two of the premier radio telescopes. The Arecibo L-band Feed Array (ALFA), which has seven beams was constructed using Parkes multi-beam feed technology. This feed was used for the Pulsar ALFA survey (PALFA; Cordes et al. 2006). The Effelsberg telescope has a similar feed with seven beams and was used for the northern HTRU survey (Barr et al. 2013). With the advent of tera-flop level computer clusters and state of the art pulsar back-ends providing 61 μs sampling over 400 MHz bandwidth, the HTRU surveys will cover all the sky with an unprecedented sensitivity of 0.5 mJy and have already started making new exciting discoveries. These state of the art systems are paving the way for the next generation telescopes like the already constructed five-hundred-meter aperture spherical telescope (FAST)[2] in China and the upcoming square kilometre array (SKA)[3] with which, we expect to finally complete the Galactic census of pulsars while also detecting even the first and hopefully, many more extragalactic pulsars (Keane et al. 2015).

[2]www.fast.bao.ac.cn
[3]www.skatelescope.org

Survey Name	Observing Frequency (MHz)	Bandwidth (MHz)	Sampling Time (ms)	Dwell Time (s)	Field of View	Sky Coverage (deg^2)	No. Discovered	Reference(s)
Arecibo 1	430	8	5.6	137	10'	164	40	Hulse and Taylor (1975a)
Arecibo 2	430	0.96	0.3	39	10'	360	6	Stokes et al. (1986)
Arecibo 3	430	10	0.5	68	10'	260	24	Nice et al. (1995)
Arecibo 4*	430	8	0.2	33	10'	1428	91	Thorsett et al. (1993)
								Foster et al. (1995)
								Camilo et al. (1996)
PALFA	1420	100	0.064	134	10'	150	171	Cordes et al. (2006)
AO 327	327	57	0.125	60	10'	10000	71	Deneva et al. (2013)
Green Bank 1	400	16	16.7	144	36'	15400	31	Damashek et al. (1978)
Green Bank 2	390	16	16.7	138	36'	6500	34	Dewey et al. (1985)
Green Bank 3	390	16	2	132	36'	3700	20	Stokes et al. (1985)
Green Bank 4	370	40	0.256	134	81'	17400	8	Sayer et al. (1997)
GB350	350	50	0.082	140	36'	10000	71	Boyles et al. (2013)
GBNCC	350	100	0.082	120	36'	13500	75	Stovall et al. (2014)
GHRSS	325	33	0.031	1200	84'	2866	12	Bhattacharyya et al. (2016)
HTRUN	1360	240	0.054	1500	10'	20600	13	Barr et al. (2013)
HTRUS	1352	340	0.064	4200	14'	20600	171	Keith et al. (2010)
Jodrell Bank A	408	4	50	819	48'	276	39	Davies et al. (1970)
Jodrell Bank B	1400	40	2	540	10'	200	42	Clifton and Lyne (1986)
Molonglo 1	408	4	100	20	1'.45	4500	31	Turtle and Vaughan (1968)
Molonglo 2	408	4	10	45	4°.3 × 1'.4	15400	155	Manchester et al. (1978)
Parkes 1†	1434	80	0.3	79	14'	2000		
	1520	320	1.2	157	14'	2000	46	Johnston et al. (1992)
Parkes	436	32	0.3	157	45'	19400	101	Manchester et al. (1996)
Southern								Lyne et al. (1998)
Parkes HL	1374	288	0.125	265	14'	4800	18	Burgay et al. (2006)
Parkes MB	1374	288	0.25	2100	14'	1500	833	Manchester et al. (2001)
Parkes-Swinburne	1374	288	0.125	265	14'	4150	109	Edwards et al. (2001)
								Jacoby et al. (2009)
Parkes Perseus Arm	1374	288	0.125	2100	14'	600	14	Burgay et al. (2013)
Parkes NGP	1374	288	0.125	4200	14'	40	17	Lorimer et al. (2013)

* Many smaller surveys have been combined here. † The two systems available at the Parkes telescopes were simultaneously used.

TABLE 2.1: Some important properties of major pulsar surveys.

2.3 Some Interesting Pulsar Systems

Pulsars are one of the most enigmatic celestial objects. In over 47 years of discovery and observations of over 2500 pulsars, we have discovered many interesting systems which pushed the boundaries of our understanding by first befuddling us and then opening up new avenues of modern physics. Some of the important[4] systems are listed below.

- The first binary pulsar, PSR B1913+16, which was discovered by Hulse and Taylor (1975b). Follow-up timing analysis of this binary system led to the first indirect detection of gravitational waves (Taylor and Weisberg 1989), which culminated in the discoverers getting awarded by the Nobel prize in Physics in 1993[5].

- The first millisecond pulsar, PSR B1937+21, which was discovered by Backer et al. (1982). This 1.5 ms pulsar remained the fastest known pulsars for 24 years till Hessels et al. (2006) discovered PSR J1748−2446ad, a 1.4 ms pulsar which, to date, remains the known fastest spinning pulsar.

- The first extrasolar planetary system was discovered orbiting PSR B1257+12 (Wolszczan and Frail 1992). This system has one lunar mass planet and two Earth mass planets revolving around the pulsar.

- The slowest known radio loud pulsar, PSR J2144−3933, which was discovered by Young et al. (1999). This pulsar has a spin period of 8.5 s and it challenged all of the existing radio emission models at that time.

- The double pulsar system, PSR J0737−3039A/B, which was discovered by Burgay et al. (2003) and Lyne et al. (2004). This is the only double neutron star binary system wherein, both the neutron stars were seen as radio pulsars. It has provided the most stringent test of GR till date.

[4] as felt by this author
[5] http://www.nobelprize.org/nobel_prizes/physics/laureates/1993/

- The RRATs, which were discovered by McLaughlin et al. (2006). These transient pulsars emit very narrow, sporadic bursts and are still a matter of active research.

- The intermittent pulsars, PSR B1931+24 (Kramer et al. 2006), PSR J1841−0500 (Camilo et al. 2012) and PSR J1832+0029 (Lorimer et al. 2012). These pulsars randomly switch ON and OFF with no apparent reason and switch between two metastable magnetospheric configurations.

- A 2 $M_\odot$ neutron star, PSR J1614−2230, which was discovered by Demorest et al. (2010). This neutron star rules out most of the soft equations of state for neutron star matter.

- The binary MSP, PSR J1824−2452I, which was discovered by Papitto et al. (2013). This pulsar was seen to switch between accretion powered and rotation powered state, thus providing direct evidence for the evolution scenario for binary MSPs.

- The binary MSP, PSR J0337+1715, which was discovered by Ransom et al. (2014). This is a hierarchical triplet system wherein, the outer white dwarf accelerates the inner pulsar-white dwarf binary system. The study of this system will provide a stringent test of the strong equivalence principle.

2.4 Scope of the Thesis

Almost all of the major blind surveys for pulsars were and are being carried out with large single dish telescopes (see Table 2.1 for more details). As noted in Section 2.2 earlier, the initial pulsar surveys were carried out at low radio frequencies, while the modern surveys have mostly moved to a higher frequency of 1.4 GHz. Although single dish telescopes allow sensitive observations owing to their large collecting area, their beam widths are very narrow (refer to Table 2.1). This makes the survey speed a bit slow at high frequencies. This drawback has been, to some extent, removed by multi-beam receivers operating at Parkes (Manchester et al.

2001), Effelsberg (Barr et al. 2013) and Arecibo (Cordes et al. 2006) telescopes at 1.4 GHz. A multi-element telescope like the Giant Metrewave Radio Telescope (GMRT) provides a unique opportunity in this regard. At an observing frequency of 325 MHz, GMRT offers a large collecting area of about 30,000 m^2 (Swarup et al. 1991) with a field of view of about 85' (Lal 2013). Thus, observations made using the incoherent addition of signals of all GMRT antennae (incoherent array mode; Section 3.1.1.2) have good sensitivity as well as a wide field of view. Given the steep spectral index of -1.4 for pulsars (Bates et al. 2013), sensitive observations at low radio frequency has a higher potential of detecting pulsars. Major surveys like the PMPS employed high-pass filters to their data before digitization. This was done in order to remove the effect caused by slow variation of the telescope gain (Manchester et al. 2001). This meant that these surveys were not very sensitive to slow pulsars having periods greater than 1 s. Keeping this in mind, Joshi et al. (2009) carried out a pulsar survey with the GMRT at 610 MHz and discovered three new pulsars. The data taken during this survey did not employ any low-pass filtering. All of the new pulsars discovered in this survey have a high DM and two of them have long periods. This demonstrates the fact that long period pulsars can, in principle, be discovered at high DMs in sensitive surveys carried out at low frequencies. The area covered by this survey was between Galactic longitude $45° < l < 135°$ and Galactic latitude $|b| < 1°$. The success of the 610 MHz survey paved way for a follow-up survey proposed at 325 MHz. The frequency was chosen so as to optimize the trade-off between sensitivity and survey speed. With the choice of 325 MHz as the observing frequency, the survey was equally sensitive while being faster because of the wider field of view. The area coverage for this survey was between Galactic longitude $45° < l < 135°$ and Galactic latitude $1° < |b| < 10°$. The Galactic disc was not included in the survey area as the radio emission background at low frequencies is quite high at low radio frequencies (Haslam et al. 1982). The major thrust of this thesis was to carry out the observations as well as data analysis of this survey. In two observation cycles of the GMRT (proposal codes 16_282 and 17_092), we observed about 10% of the proposed survey region and discovered one new radio pulsar. This pulsar showed

some interesting characteristics (see Chapter 6 for details) and the later effort in the thesis was focused at obtaining more information about this source. At around the midway point of the thesis work, we also performed targeted searches on high energy sources which were promising candidates for being radio pulsars.

This thesis is divided into two parts. The first part, which contains majority of Chapters 3 and 4 with Chapters 5−8, gives details of the blind survey observations carried out with the GMRT as mentioned above. Chapter 3 outlines the observational effort put in for the thesis work, while Chapter 4 gives details of the data analysis methods for different types of observational efforts. This part also contains the description about the discovery of a new pulsar, PSR J1838+1523 in a blind pulsar survey with the GMRT (Chapter 5) and the follow-up timing observations carried out thereafter, which are described in Chapter 6. The results from the follow-up timing observations for the pulsars discovered in the 610 MHz survey (mentioned above) are described in Chapter 7. The unique feature of the GMRT is that it provides imaging data simultaneously with the time series data. This particular feature was very useful in determining the position of PSR J1838+1523. The regular follow-up timing observations for this pulsar spanned over three years with a cadence of two weeks in the initial stage and a month towards the last six months. This formed a unique imaging data set. The same field was observed regularly over three years. In order to check the consistency of the imaging calibration, 29 point sources were selected from the pulsar field and their flux densities were determined for each observation. In Chapter 8, we describe the variability study performed for these sources at 325 MHz using the snapshot images obtained from imaging data.

The second part contains Chapter 9 and 10. It contains the results obtained for targeted searches towards some promising radio pulsar candidates. Chapter 9 describes the pulsation search done at 610 and 1420 MHz with the GMRT towards the very high energy γ-ray source HESS J1818−154, which was associated with SNR G015.4+0.1 (Hofverberg et al. 2011). The observational constraints and considerations for this search are described in Chapter 3. This search was very different from traditional pulsar searches. Due to the constraints put by

the requirement that the source be imaged properly, the search observations had to be broken into smaller scans (see Chapter 4 for details). This required the development of a new search pipeline as well as a diagnostic viewer. These are described in Chapter 4. The results obtained in the pulsation search as well as the other relevant material forms the subject matter of Chapter 9. Chapter 10 describes the observational efforts and results of the radio pulsation search for four soft γ-ray repeater (SGR) sources namely, SGR J1745−2900, SGR J1935+2154, SWIFT J174540.7−290015 and SGR J0755−2933.

As is clear from the above description, the major goal of this thesis was towards searching for radio pulsations and follow-up timing of the radio pulsars discovered in blind surveys. The search observations themselves had both blind and targeted search components. In Chapter 11, we conclude the thesis. Here, we outline the major findings and discuss their impact on the current understanding of radio pulsars. We also discuss the possible ramifications of different types of surveys with an additional emphasis on using the simultaneous imaging mode data for faster pulsar localization, on future pulsar searches with the upcoming SKA.

Chapter 3

Observations

3.1 GMRT and ORT

As pulsars are very weak radio emitters, one needs very sensitive instruments in order to observe them. Majority of observations for the thesis work were performed at the Giant Metrewave Radio Telescope (GMRT) and the Ooty Radio Telescope (ORT).

3.1.1 The GMRT

The GMRT (Figure 3.1) is an interferometric array of 30 fully steerable, parabolic dishes, each of a diameter of 45 m, located approximately 80 km north of Pune (latitude: 19° 5' 47.46" N, longitude: 74° 2' 59.07" E, altitude: 588 m. Reference antenna: C02). Each dish uses a novel design called Stretched Mesh Attached to Rope Trusses (SMART; Swarup et al. 1991). In short, wire mesh is stretched over rope trusses to give the dish its parabolic shape. This design allows high fidelity without compromising sensitivity at a much lower price. The interferometer design has a hybrid configuration with 14 randomly placed dishes (C00 to C14 sans C07) in the central region of roughly 1 square km area (central square). The remaining 16 dishes form three roughly Y-shaped arms (Figure 3.2), namely East (E02 to

FIGURE 3.1: Some of the dishes from the central square of the GMRT. Photo credit: www.ncra.tifr.res.in/ncra/outreach/picture-gallery/gmrt/gmrt-dishes/019GMRTPune.jpg

E06), West (W01 to W06) and South (S01 to S06 sans S05), each with a length of roughly 14 km. The dishes themselves have an altitude-azimuth mount with a lower altitude limit of 17° resulting in a declination coverage of −53° to +90° (Lal 2013).

The longest baseline provided by this arrangement is about 25 km. The central square antennae provide a large number of relatively short baselines. This is very useful for imaging large extended sources, whose visibilities (see Section 4.4 for a detailed discussion on interferometric measurements) are concentrated near the origin of the UV plane. The arm antennae on the other hand are useful in imaging small sources, where high angular resolution is essential. A single GMRT observation hence yields information on a variety of angular scales. Additionally, the Y-shaped arm antennae allow a full aperture synthesis image in 8 hours as compared to 12 hours taken by linear arrays (Holdaway and Helfer 1999) like the Westerbork Synthesis Radio Telescope (WSRT). Currently, GMRT supports 5 observational bands centred at 153, 240, 325, 610 and 1420 MHz with a maximum instantaneous bandwidth of 33 MHz (Lal 2013). The unique feature of GMRT is its ability to provide simultaneous interferometric and beam mode data. There are different parts of the GMRT data acquisition system. The receiver chain

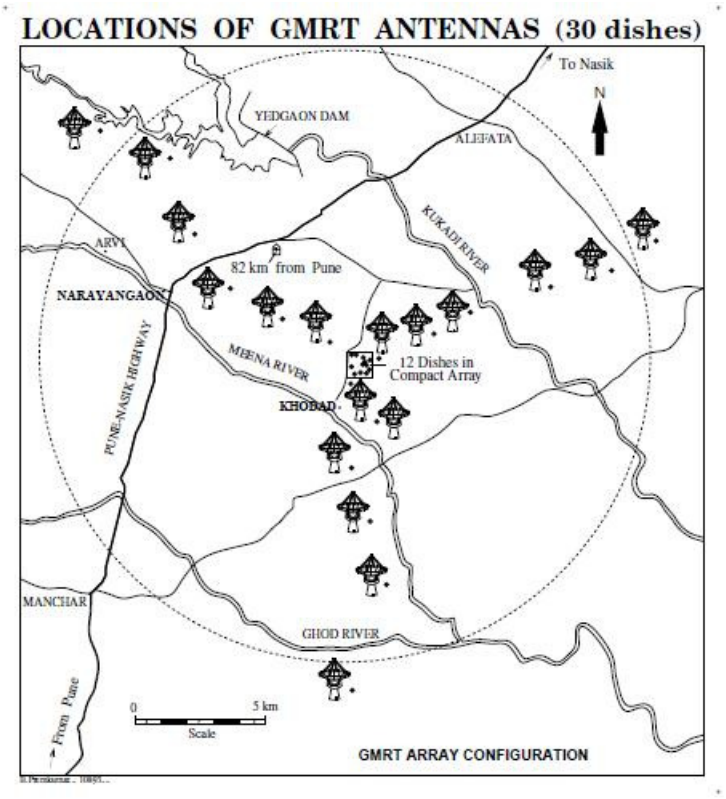

FIGURE 3.2: GMRT array configuration. Image credit: gmrt.ncra.tifr.res.in/gmrt_hpage/Users/doc /GMRT_specs_Dec09.pdf

begins from front end components like feed, LNA and goes through local oscillators (LO), fibre optics link, baseband converters and correlator and ends at the actual recording and controlling computers. These different parts are all working in tandem right from orienting the telescope towards the source to the acquisition of data. The receiver chain and signal flow in the GMRT is explained in the following sub-sections.

3.1.1.1 Front End

The front end consists of the feed, LNA and the solar attenuator. The solar attenuator is a damping circuit which suppresses the signal when the telescope is observing an area of sky very close to the Sun. The GMRT feed turret (Figure 3.3) is a complex structure which has 4 different sets of feeds. Each feed has 2 polarizations with an LNA attached to each. All the feeds convert linear polarization

signal into circular polarization using hybrid configuration, except the 1420 MHz feed. The 610 and 240 MHz feeds are co-axial, allowing simultaneous observations with a single polarization at each frequency.

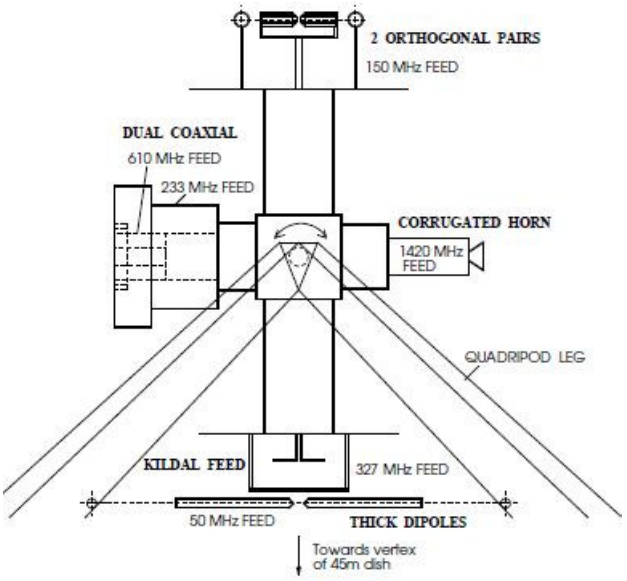

FIGURE 3.3: The GMRT feed turret. It has a motor to turn the feed for the correct feed to point towards the reflecting surface. It is supported by 4 mechanical legs connected to the rim of the dish. The image also shows a 50 MHz feed, which was present on an experimental basis in early days but no longer exists. Image credit: www.ncra.tifr.res.in/ncra/gmrt/gmrt-users/observing-help-for-gmrt-users/low-frequency-radio-astronomy/ch19.pdf

The feed probe detects electromagnetic fluctuations created due to the radiation coming from the source. This signal is at the radio frequency (RF). Astronomical radio sources are very weak emitters. The typical unit used to measure the power emitted per unit area per unit frequency (flux density) is Jansky (Jy). The typical source flux densities are of the order of a few to few hundreds of mJy. Thus, the signal needs to be amplified without adding a lot of noise, otherwise it will be swamped out by the noise generated by the receiver chain. This is achieved by the LNA. Once the signal is amplified, it needs to be transported to the central building for further processing. This is achieved by converting the signal to an intermediate frequency (IF) of 70 MHz by mixing it with a pure sinusoidal signal generated by the first LO. This signal is then again amplified by IF amplifiers and converted to 130 and 175 MHz, respectively for two different polarizations by

the second LO. This signal is then carried by the optical fibre cables from each antenna to the central electronics building. The signal flow from front end to IF is shown in Figure 3.4.

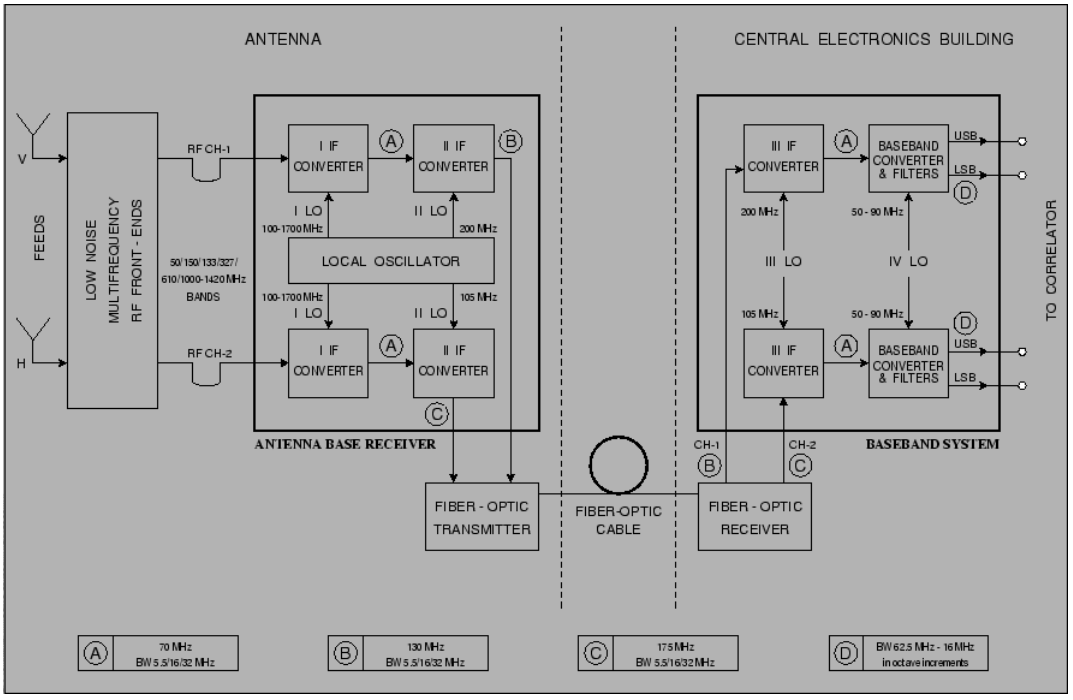

FIGURE 3.4: Block diagram for GMRT front end and baseband system. Image credit: www.ncra.tifr.res.in/ncra/gmrt/gmrt-users/observing-help-for-gmrt-users/low-frequency-radio-astronomy/ch21.pdf

3.1.1.2 Baseband System

The optical fibre cables bring all the signals to the central building, where they are converted back to 70 MHz through the third LO. The resultant 70 MHz signal is then converted to baseband by mixing with another 70 MHz signal. This is the fourth LO. This is followed by the baseband filter which selects different allowed final bandwidths, which are either the full IF band or a part of it for spectral line observations. In the old system, the baseband signal was created by adding and subtracting the fourth LO signal to create upper and lower side bands (designated USB and LSB in Figure 3.4) of 16 MHz each out of the maximum 32 MHz IF band. This would make the baseband from -16 to 16 MHz. In the new system, there is a fifth LO, which converts the full band from 0 to 33 MHz. Figure 3.4 shows the

block diagram for the front end and baseband system. The 60 signals (30 antennae $\times$ 2 polarizations) thus generated by the baseband system, are first digitized by an analog to digital converter (ADC) circuit into 16 bit integer samples. The resultant data samples can be combined by two different back-ends. They are the correlator and the beamformer.

1. Correlator: The GMRT correlator is an 'FX' correlator. It forms FFTs from the data from each antenna to form the spectrum. The final cross-correlation products are formed by cross correlating the spectra. The outputs from the baseband system are first digitized by an ADC circuit. This is followed by integral delay correction[1]. This is followed by an FFT stage and fractional delay correction. The spectra are then cross correlated. The cross spectra are then sent to the accumulator, where they are accumulated for some time (default is 16 s but 8 and 2 s integrations are also possible.) before they are finally written to disks.

2. Beamformer: The beamformer combines incoming antenna voltages to form simultaneous time series output. The voltage can be combined in two different ways which are described below:

   (a) Incoherent Array (IA): This time series output is formed by adding the power (voltage squared) output of each antenna. The signal chain has an FFT unit to form spectra. This unit is called a *filterbank*. This is followed by a self correlator to form spectral power for each polarization. This is followed by a combiner, which integrates the powers of all the antennae [which can be selected using a graphical user interface (GUI) called GMRT array combiner (GAC)] for each polarization separately followed by integrating the powers for both polarizations. This

[1]The individual antennae of an interferometer are present in geometrically different locations. Due to this, they do not sample the incoming electromagnetic wave front at the same phase. This introduces fringe patterns even without the presence of a source. In order to avoid this, the geometric delays are compensated for each antenna with respect to a reference antenna. This process is called delay correction. Due to digitization of the signal, this gets divided into an integral part and a fractional part.

is followed by an accumulator for time integration (the lowest time resolution allowed for 256 channel mode is 31.22 μs, while that for 512 channel mode is 61.44 μs, with post integration factors of 1, 2 and 4). This mode gives a field of view equivalent to the field of view of a single dish with sensitivity equal to the incoherent sum of individual antennae. If there are N antennae in the IA,

$$Sensitivity_{IA} = \sqrt{N} \times Sensitivity_{ant} \tag{3.1}$$

This mode is very useful for time domain surveys because of fast sky coverage provided by large field of view.

(b) Phased Array (PA): This time series output is formed by adding the voltage output of each antenna in phase after geometric and instrumental delay compensation. The signal chain has a integral delay compensation unit followed by the FFT and fractional delay compensation unit. Voltage spectra from each antenna for each polarization are then correlated to produce stokes I,Q,U and V parameters. This is followed by a combiner which integrates the powers for both polarizations for each antenna (which can be selected using the GAC), followed by integrating powers (or Stokes' I parameters) of both the polarizations and an accumulator for time integration (the lowest time resolution as well as integration factors are the same as IA mode). This mode gives a field of view equivalent to the field of view of the full array (λ/D_{max}, where D_{max} is the maximum baseline length), which means that it has the same resolution as the interferometer with sensitivity equal to the coherent sum of individual antennae. If there are N antennae in the PA,

$$Sensitivity_{PA} = N \times Sensitivity_{ant} \tag{3.2}$$

This mode is useful for studying compact objects (like pulsars) because it provides very high signal to noise ratio (S/N) time series data. For

very bright pulsars, this provides high S/N single pulses which is especially helpful in studying phenomena like nulling, giant pulse emission, pulse microstructure etc.

The PA data can be recorded either in Indian polar mode, which provides total intensity or full polar mode, which provides all four Stokes' parameters. The IA data provides only total intensity data.

The outputs of these back-ends are written to dedicated hard disks. The uniqueness of the GMRT is that the data for both the back-ends can be simultaneously recorded, thus providing high resolution imaging data with large field of view time series and high resolution and higher sensitivity time series at the same time. This makes GMRT a versatile instrument suitable for studying a large range of astronomical objects over a wide range of observing frequencies.

3.1.2 The ORT

The ORT is a single, large cylindrical paraboloid of length 530 m and width 30 m, located in the picturesque cardamom hills near Udhagamandalam (previously Ootacamund or Ooty. latitude: 11° 23' 00.25" N, longitude: 76° 39' 58.18" E, altitude: 2140 m.). The unique feature of ORT is that it is located on a hill, whose North-South slope is equal to the local latitude. It thus makes the long axis of the paraboloid parallel to the Earth's axis. The reflecting surface of ORT consists of 1100 steel wires parallel to the axis of the paraboloid. The cylindrical offset paraboloid shape of the ORT results in a fan shaped beam on the sky with a beam width of 2.3° in right ascension (RA) and 6' in declination (DEC). ORT operates at a central frequency of 326.5 MHz with a usable bandwidth of 15 MHz. The feed consists of 1056 dipoles receiving single linear polarization. The dipoles are clubbed into 22 modules of 48 dipoles each. These are supported by 24 parabolic frames as shown in Figure 3.5. The separation between two frames is 23 m. Unlike GMRT, ORT provides only time series data. The main components of the ORT receiver chain are described in the next sections.

FIGURE 3.5: The Ooty Radio Telescope. The tall structure seen in this image is the metal frame supporting the dipoles as well as carrying the front end electronics for a single module. Photo credit: rac.ncra.tifr.res.in/rac_images/ORT02.jpg

3.1.2.1 Modules

Each module of the ORT combines data from 48 dipoles. As is the case for all radio telescopes, each dipole is followed by its own LNA. This is followed by a phase shifter. It is introduced to change phases of the signal so that, multiple beams can be formed on the sky. These beams can also be steered on the plane of the sky as required using the phase shifter circuits. The voltages from four dipoles are then combined through a four way combiner (there are 12 such combiners per module). The signal from two such combiners is amplified by a stage-I amplifier (6 per module). The data from three stage-I amplifiers is combined by a three way combiner (2 per module) and then fed to stage-II amplifier, which is a wide band amplifier. The output of the two stage-II amplifiers is finally combined by a two way combiner and then fed to an RF amplifier. The RF amplifier output is converted to an IF of 30 MHz through a mixer and an LO. This signal goes through

an IF filter and amplifier. Thus, at the end of this stage, the voltages from 1056 dipoles are combined to form 22 module outputs at an IF of 30 MHz. These signals are then transported through co-axial cables to the electronics building where they are fed to the beamforming network. This combines data from 11 modules from the North and 11 from South into 2 data streams, which then feed the digital back-end. The signal flow for one such module is shown in Figure 3.6.

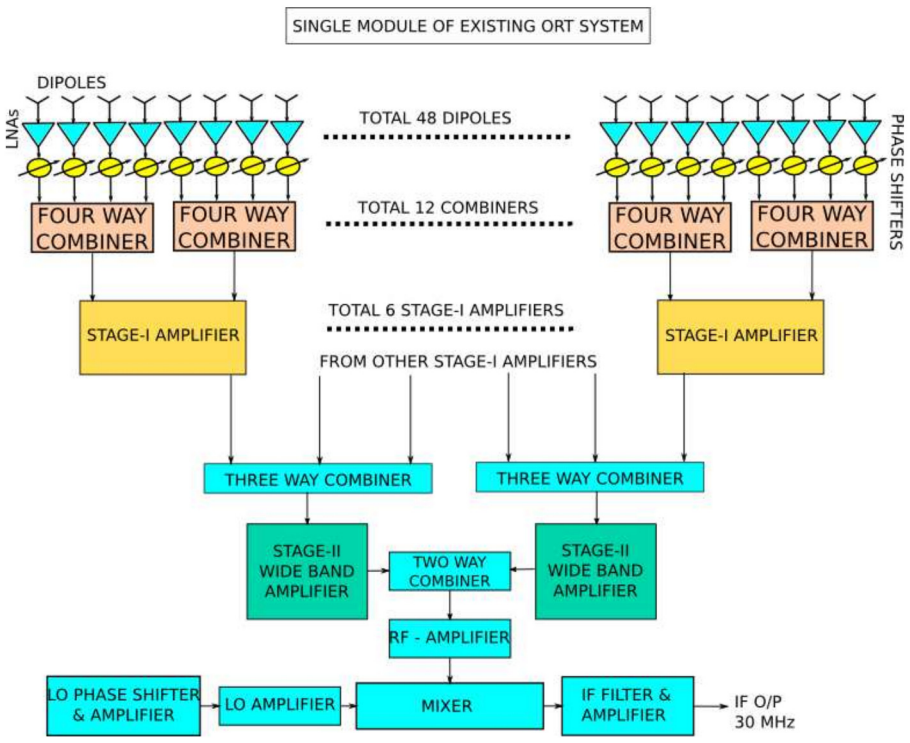

FIGURE 3.6: Block diagram depicting a single ORT module. Image taken from Naidu et al. (2015)

3.1.2.2 PONDER: The Pulsar Back-end

PONDER or Pulsar Ooty Radio Telescope New Digital Efficient Receiver is a real time versatile back-end, which can be used for high time resolution pulsar data, interplanetary scintillation measurements as well as very long baseline interferometry data. The design and capabilities of this back-end are described in detail in Naidu et al. (2015). Here we describe the pulsar mode, which was relevant for the present work. This back-end provides real time coherently dedispersed pulsar data

by using the computing power provided by graphical processing units (GPUs). It takes the data generated from both the halves. These are first amplified using a 30 dB amplifier. This IF data is then converted to baseband by mixing with a 38 MHz signal. The 16 MHz passband is recovered using a low pass filter. This is then fed to the ADC circuit. The output of the ADC can either be written to disk (as raw data) or processed further in a software module that adds the data from two halves in phase and performs an FFT to produce the spectrum. This produces the data in SIGPROC[2] filterbank format, which can either be written to disk or passed on to the dedispersion stage. This produces incoherently dedispersed time series, which can be written to disk or passed to the folding stage. The folding stage uses predictor files generated using pulsar timing package TEMPO2[3] to fold the time series modulo the predicted period for the pulsar being observed. The versatility of the back-end is reflected in the fact that the resultant data at each stage can be written to the data disk as well as can be passed on to the next stage. The filterbank file is particularly useful for search mode, time series files are useful for single pulse, nulling and scintillation studies, while the folded profiles are useful for mode change studies and pulsar timing. The capability of producing all these files in a single observing run is very unique. This back-end also has the capability to produce coherently dedispersed data using GPUs. The data products of this mode are time series as well as folded profile. This mode is particularly useful for studying giant pulses, pulse microstructure, scattering as well as high precision pulsar timing.

The thesis work involved using these telescopes in different configurations, serving different purposes. The observational effort consisted of blind search observations, follow-up imaging and timing observations as well as targeted search observations. In the following sections, we will motivate the particular set up and describe how each different type of observation was carried out with these telescopes.

[2] www.sigproc.sourceforge.net
[3] www.atnf.csiro.au/research/pulsar/tempo2

3.2 Blind Search Observations

Blind searches are surveys of large parts of the sky to look for a particular class of celestial objects. The basic idea is to observe a pre-selected part of the sky with high sensitivity while covering large area with good speed. The pulsar searches cater to data taken in the beam mode i.e. they look at time series data. Given that pulsars are steep spectrum sources (brighter at lower radio frequencies), searches done at high radio frequencies (1.4 GHz and above) may miss out on very steep spectrum pulsars, which may be very peculiar objects. Hence, it is better to carry out pulsar search observations at low radio frequencies. The disadvantage at low frequencies however, is that the sky background, scattering as well as scintillation are much more dominant, making it difficult to discover very short period pulsars such as MSPs. In this situation, GMRT provides a distinct advantage. It has a field of view of about 85' at 325 MHz in IA mode (Lal 2013), combined with a sensitive receiver. This provides rapid sky coverage with good sensitivity. The IA mode of GMRT is thus, the best suited mode for doing blind pulsar search observations. We had proposed a blind search for pulsars and transients along the Galactic plane covering the region between Galactic longitude $45° < l < 135°$ and Galactic latitude $1° < |b| < 10°$ with the GMRT[4]. It was named 'GMRT Galactic Plane Pulsar and Transient Survey'or GMGPPTS. Salient features of the survey observations are given in Table 3.1. In the following sections, we describe the planning, observations and post observational activities relevant to the blind search observations carried out with the GMRT.

3.2.1 Planning the Observations

While observing a large region of the sky for a blind pulsar search, one needs to have an observational strategy that depends on the amount of time spent per

[4]For observations related with the Milky Way Galaxy, it is better to use a coordinate system taking the plane of the Galaxy as the reference plane. Such a system with the plane of the Galaxy as its equatorial plane and the direction of the Galactic center from the Sun defining the reference line is called Galactic coordinate system. It is defined by Galactic longitude (l) and Galactic latitude (b), which are similar to longitudes and latitudes on Earth

Observing Mode	IA
Central Frequency	325 MHz
Receiver Bandwidth	16 MHz
Filterbank Channels	256
Sampling Time	256 μs
Sample Size	16 bit
Integration per Pointing	1800 s
Angular size of Pointing	$1.12^\circ \times 1.12^\circ$
Total Sky Area Observed	115 deg^2

TABLE 3.1: Important observational parameters for GMGPPTS.

observing session, availability of the observable region and incremental coverage of the same over time. The starting point is to divide the sky region to be observed into *pointings* (named GPT followed by a four digit pointing number) such that each pointing fits into the telescope beam[5]. This is shown in Figure 3.7, where each cross on the sky represents a single pointing. Once that is done, the next step is to create an observing plan for each session. This requires preparing special scripts for running the pulsar back-end as well as doing the data back up. The most important file is the source list which contains the field names and their RA and DEC coordinates in a fixed format. The next important file is the observational set up and break up of the observing time. This contains all the options for setting up the full receiver chain right from the front end (selecting and rotating the appropriate feed for the observing band) right upto the baseband (required bandwidth). The most important setting is to keep the automatic gain controller switched off for pulsar observations, which is on by default for interferometry observations. These files need to be given to the telescope operators, who do all the configuration for the data acquisition system of the GMRT. The other thing to keep in mind is the data size generated during an observing session. Looking at the specifications in Table 3.1, one can figure out that the data size would roughly be about 2 MB per second. One needs to check whether there is enough disk space available on the recording computer before starting the observations.

[5]Each telescope has a power pattern, which looks like a beam and the 'telescope beam' or field of view refers to the full width at half maximum (FWHM) of the power pattern.

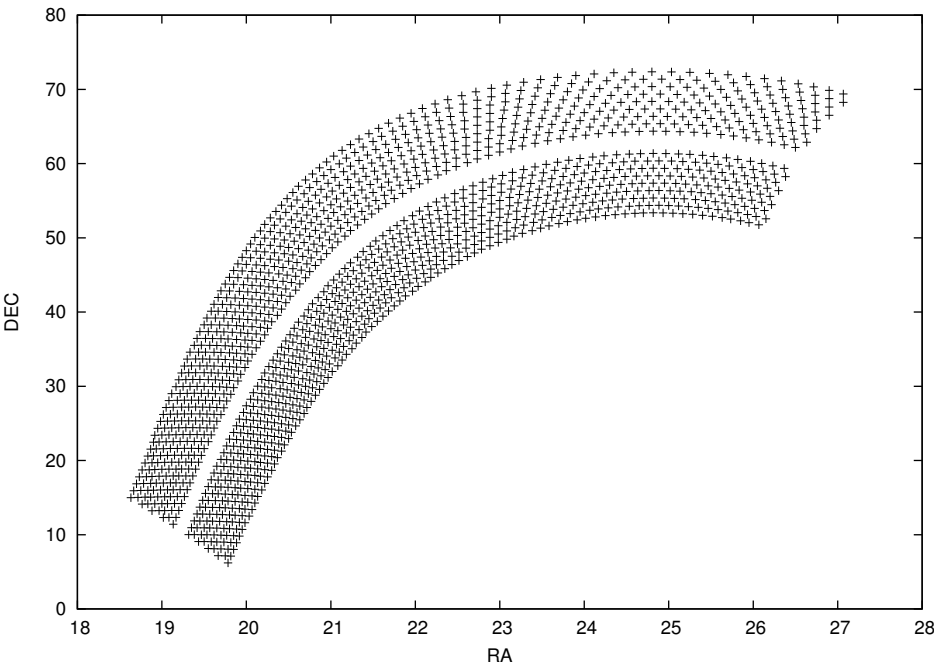

FIGURE 3.7: The region of sky proposed to be observed in GMGPPTS. RA is plotted in hours and DEC in degrees. Each small cross represents an individual pointing. The blank area is the Galactic plane.

3.2.2 A Typical Observing Session

The observing session starts with ensuring that the correct feed is facing the reflecting surface. If not, the feed needs to be rotated so that the required feed faces the reflecting surface. This is followed by running a script which calculates pointing offsets[6] by doing a raster scan on a strong point source calibrator. This procedure usually takes about 1 hour. After the pointing offsets are loaded, the actual set up starts. This involves setting the LO frequencies, followed by setting the final baseband bandwidth and gains of the amplifiers. This is followed by the most important step, *power equalization*. This process compares the power outputs from all the antennae and brings them to a same level by adjusting the gains of the respective amplifier. This exercise is absolutely necessary because, while adding power, we are also adding the noise at all the antennae. This noise is expected to be Gaussian distributed with zero mean. Power addition leads to

[6]There is always a difference between the origins of the celestial reference frame and the reference frame of the telescope. This is called pointing offset. This can be due to mechanical or geographical constraints. One needs to know this beforehand so that the telescope can be pointed to the proper sky coordinates.

addition of means. If $\bar{X}_i$ is the mean of ith antenna with n total antennae, the mean after addition ($\bar{X}$) is given by

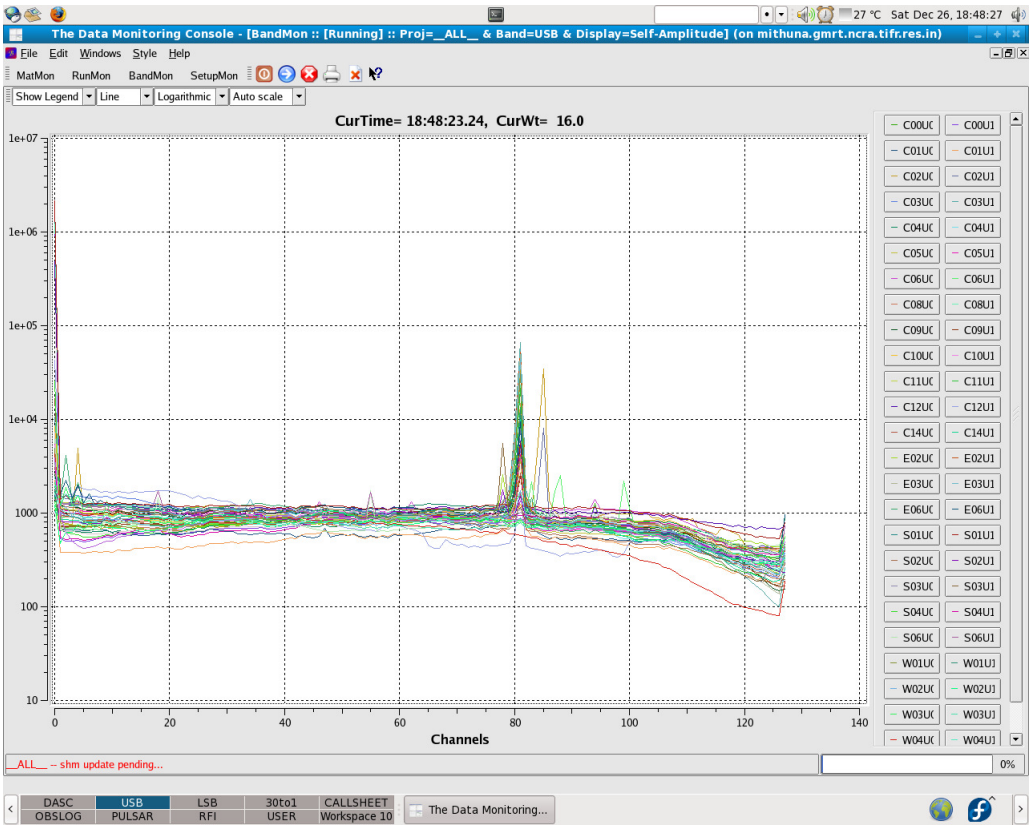

FIGURE 3.8: Power band of GMRT antennae after power equalization (see discussion in text). The frequency range is 325-341 MHz (divided into 128 channels) and equalized power level is 1000 (in machine counts). The plot shows power of all antennae with 2 polarizations per antenna. An RFI spike is also visible near channel 80.

$$\bar{X} = \bar{X}_1 + \bar{X}_2 + \bar{X}_3 + ... + \bar{X}_n \tag{3.3}$$

At the same time, if $\sigma^2_{X_i}$ is the standard deviation of ith antenna and $\sigma_{\bar{X}}$ is the resultant standard deviation, it is given by

$$\sigma^2_{\bar{X}} = \sigma^2_{X_1} + \sigma^2_{X_2} + \sigma^2_{X_3} + ... + \sigma^2_{X_n} \tag{3.4}$$

Thus if one antenna, lets say the nth antenna has a very high standard deviation due to RFI or other noise source, i.e. $\sigma^2_{X_n} \gg \sigma^2_{X_i}$ for all i $\neq$ n, this leads to

$\sigma^2_{\bar{X}} \approx \sigma^2_{X_n}$. Thus, the standard deviation and the RMS of the whole array is just the rms of a single antenna. This spoils the observations because of large amount of noise. This is avoided by doing power equalization. This ensures that the resultant noise of all the 30 (or whatever number is available) antennae is a Gaussian random variable with a standard deviation that is $\sqrt{n}$ times the standard deviation of each antenna (which is expected to be the same for all antennae after power equalization). The power equalized band shapes of all antennae are shown in Figure 3.8. If some antennae show fluctuation even after power equalization, they are not included in further data acquisition. Thus, this procedure not only helps in stabilising the data statistics but also helps in identifying potentially bad antennae. Once all the good antennae are identified, they are selected through the GAC. The next step is to configure specific back-end options like sampling time and data disk location. In the present case, the data were directly written to magnetic tapes. The time required for all of this was typically 30−40 minutes. The whole co-ordination between steering the telescope and writing out the data was done through an executable script which was generated before the observations. The data recording was started once proper timestamps were obtained through the global positioning system (GPS). During the observations, a careful log of the observing times as well as changes in the number of antennae (if any) was prepared. The only other job was to keep monitoring for problems like buffer loss or power failure in which case, the set up needs to be repeated once everything is restored to normal condition.

3.2.3 Post Observation Work

Once the observations are over, one needs to take care of the data backup that includes backing up the data files as well as all the auxiliary files such as time stamp files, header files, tape logs (if data were written to magnetic tapes) and observation logs. These files are very important as the data itself doesn't make any sense if it does not have this information associated with it. For this search, the tape logs were prepared at the time of writing data to tapes. The time stamp

and other files were also automatically created by the pulsar back-end programs. The only human made files were daily observation logs that listed all important file names and any problems encountered during the day's observations. The auxiliary files were sorted into different directories according to dates and they were also backed up onto magnetic tapes after the observations.

We observed 10% of the proposed sky region in 100 hours using the GMRT in 2 observing cycles. The first set of observations were carried out between 23−27 July 2009 and the second between 25−29 December 2009. The data were then taken to NCRA for offline analysis.

3.3 Follow-up Timing Observations

Once a new pulsar is discovered, it needs to be timed regularly to determine its period and period derivative accurately. This is helpful in putting the new discovery in terms of the overall population. This also helps to measure many more important parameters like the dipole magnetic field strength, characteristic age, width of the pulse, separation of components (if present). It also helps to classify the pulsar as normal or MSP or a high magnetic field pulsar etc. This in turn helps in putting the pulsar in its rightful position in the current population in the $P-\dot{P}$ diagram (Figure 1.5). This is what characterizes the pulsar as a useful physical tool to understand plasma physics, emission mechanisms etc. The follow-up timing observations for the newly discovered pulsar PSR J1838+1523 as well as known pulsars PSR B1937+21, PSR J2208+5500, PSR J2217+5733 and PSR J0026+6320, out of which, the last three are GMRT discoveries (Joshi et al. 2009), were carried out initially at GMRT and later, also at the ORT. PSR B1937+21 was chosen as a test pulsar as it is very well studied. Hence a good timing solution would always be available. In the timing analysis, this would provide confidence on the overall timing analysis and test the accuracy of the GMRT time stamps. The observations at the GMRT were done in pulsar as well as imaging mode, while

those at the ORT were just pulsar mode observations. We describe these in the next sections.

3.3.1 Observations at the GMRT

PSR J1838+1523 was discovered with the GMRT at 325 MHz using GMRT hardware back-end (GHB). Thus, 325 MHz was the most natural choice of observing frequency for initial follow up. As described in Section 3.2.1, the pointing covers $\sim$1° of sky, leaving a big uncertainty over the position of the pulsar. The initial follow up observations were used to localize the position by using a gridding method as described in Joshi et al. (2009). In our case, the gridding observations were done using the IA mode rather than PA mode because the 325 MHz IA beam is very wide and the widest PA beam with the closest central square antennae (C05, C06 and C09) was not sensitive enough to detect the pulsar as it was very weak. We also suspected that it was near the edge of the beam. Strangely, the pulsar was not detected after the first round of gridding observations, which left the position uncertainty of about 0.5°. Thereafter, we kept following up this pulsar as well as the three other GMRT pulsars with a cadence of two weeks. PSR J1838+1523 was detected again after 280 days. Thereafter, the follow up observations continued with the same cadence in the IA and imaging mode. The pulsar showed random ON and OFF states of 1−2 month duration till 27$^{\rm th}$ December 2013. At this epoch, we performed gridding observations at the ORT (see Section 3.3.2), which fixed the position within the PA beam extent of 200" (including only the central square antennae of the GMRT) at 325 MHz. Further observations were then carried out in the PA mode with the GMRT, giving more sensitive data. The pulsar was also observed with almost daily cadence with the ORT. The observations at the ORT were used to refine the pulsar position further. After the position was tied down to the point source detected in the maps made from the imaging data collected from all the previous observations, the GMRT follow up moved to 610 MHz (with ORT follow up continuing simultaneously at 325 MHz). These observations were carried at a cadence of 2 weeks for 3 years (with breaks when the observatory was

closed for maintenance between 2 cycles) from August 2011 and were continuing with a cadence of 1 month at the time of writing the thesis. Details of the set up and observing procedure for a typical GMRT observation are explained in the next section.

3.3.1.1 Planning the Observations

The data for all further observations were recorded using the much improved GMRT Software Back-end (GSB; Roy et al. 2010). This provided 33 MHz band as a single side band. Given that these observations were of much shorter durations (2−3 hours per session) and the additional requirement of being able to observe a flux and phase calibrator source (for phasing the array as well as for imaging calibrations) as well as the other three pulsars mentioned in Section 3.3 in the same session, observations had to be carefully planned. Once the required sources were fixed, a source list and a set up file (for the operator) were created. The last important file to be created was the command file which would send out tracking and data recording commands to the data acquisition system.

3.3.1.2 A Typical Observing Session

The session starts by getting the correct feed to face the reflecting surface and proceeds as is described in Section 3.2.2. The only additions are for the imaging and PA set up. In the GSB, the imaging back-end is set up simultaneously and the default sampling time is 16 s (data can also be recorded with sampling times of 8 and 2 s). The observatory default is to always record imaging data with 16 s sampling. The PA back-end requires the phases of the antennae to be made identical by calculating delays with respect to a user selected reference antenna. This is done by observing a point source phase calibrator nearby the target field which is sufficiently strong (>5 Jy at 325 MHz) and solving the phases for each antenna. These phase solutions, when subtracted from the data, will make the phases of all the antennae nearly equal. The whole set up for IA mode observations,

takes 30−40 minutes while for PA (or IA and PA) observations, it takes 40−50 minutes.

In an observing session, the phase calibrator was observed once every 35 minutes at 325 MHz and once every 45 minutes at 610 MHz, so that, the phase solutions could be interpolated in the imaging analysis. This is required because the density of free electrons and ions in Earth's ionosphere changes as a function of time and observing frequency. This introduces additional phase variations because of multi-path propagation within the ionosphere. The characteristic time over which, the signal from the different antennae decorrelates is smaller for higher frequencies. This implies that the point source phase calibrator can not be farther than a few degrees from the target source. During the follow up observations, Very Large Array (VLA) calibrators J1822−096, J1829+487, J1924+334, J1859+129 and J1830−360 were observed as phase calibrators. Flux density calibrators were observed once at the end of observation to establish the flux scale for imaging observations. To establish the calibration scale for pulsar data, the flux calibrator was observed in on source and off source (+5° in DEC) position in the same scan. VLA calibrators 3C48 and 3C286 were observed as flux density calibrators for all the observations. Some important observational parameters are listed in Table 3.2.

Observing Mode	IA and PA	Imaging
Central Frequency	325 (and 610) MHz	325 (and 610) MHz
Receiver Bandwidth	33 MHz	33 MHz
Filterbank Channels	512	512
Sampling Time	123 μs	16 s

TABLE 3.2: Important observational parameters for follow-up timing observations at the GMRT.

3.3.1.3 Post Observation Work

The imaging data were written to one of the server node and pulsar data were written on two compute nodes (node33 and node34) of the GSB cluster. With the choice of parameters indicated in Table 3.2, the typical data size for the pulsar

back-end was 0.5 GB per minute while that for imaging data was 1.5 GB for a 2 hour observing session. After the observing session was over, the data were copied to a common computer in the observatory. The data were then transferred directly to the computers in NCRA for offline analysis. Careful logs were prepared indicating any problems like antennae being removed, the names of the excluded antennae with reasons for each. The logs were also copied with the data.

3.3.2 Observations at the ORT

The follow-up observations at the ORT started from 27th December 2013. The ORT has a fan beam that is 2.3° wide in RA and 6' wide in DEC. In order to reduce the position uncertainty, a grid was set up in declination. PSR J1838+1523 was detected in only two of the grid pointings. This narrowed down the declination uncertainty to 4'. Once this was done, the follow-up timing observations were started daily and they were continuing at the time of writing this thesis. The observations at the ORT were very straightforward and did not require any elaborate set up. The typical session starts with the telescope being pointed in empty sky. The current levels in each of the module are then adjusted to get a value of 25 μA. This is the *power equalization*. Once that is done, the telescope goes on to a strong point source flux density calibrator. After power equalizing again, the telescope is calibrated. This calibration procedure is routinely carried out at the ORT once a week. Its effectiveness is judged by a number called "sensitivity". This number is defined as the S/N for a continuum source having flux density of 1 Jy. It is typically calculated from calibrator scans taken daily. In the follow up observations, 3C93 and 3C94 were used as flux density calibrators.

The ORT does not have North−South rotation. The beam can be steered using phase lags in the software beamformer network. Hence, the delays are always fixed for a particular orientation and they can be loaded instantly. The telescope is thus phased easily. The timing observations at the ORT consisted of 1800 s integration on PSR J1838+1523 and PSR J2208+5500 and 900 s integration on PSR B1937+21, to produce coherently dedispersed, folded profiles using the newly

developed pulsar back-end called PONDER (Naidu et al. 2015). These profiles were archived in a central storage disk. The data products at the end of each session were just three profiles. The important parameters for these observations are listed in table 3.3.

Observing Mode	Pulsar
Central Frequency	326.5 MHz
Receiver Bandwidth	16 MHz
Sampling Time	500 μs
Integration per session	1800 s

TABLE 3.3: Important observational parameters for follow-up timing observations at the ORT.

3.4 Targeted Search Observations

Pulsars are born in supernova explosions. Some of them are associated with SNRs but many are not. They have either left their SNRs or the remnants have faded away. Wherever there are associations, the presence of a Pulsar Wind Nebula (PWN) and measured values of $\dot{E}$ have enabled us to construct energy budgets which have proved vital in understanding how the energy is imparted by the explosion in the surrounding medium. This also helps in understanding the relevant emission mechanisms for electromagnetic radiation at different wavelengths. Recent detection of Very High Energy (VHE) γ-ray (>100 GeV) emission from many SNRs by High Energy Stereoscopic System (HESS) telescope hints at two different kinds of possible mechanisms, which are discussed in Section 9.1. A pulsation search in the direction of these sources (called composite SNRs) is useful because the detection of a putative pulsar will directly enable us to measure the $\dot{E}$ as well as flux density and construct the full energy budget of the high energy emission. Such class of observations for pulsation search are called targeted searches. Other examples of targeted searches are deep searches in globular clusters (see Manchester et al. 1991, for example), searches for radio pulsation in unidentified high energy point sources (see Hessels et al. 2011, for example). Targeted searches are

observationally easier because a small area of the sky is to observed. This allows deeper sensitive observations over a long period of time. The area observed usually fits in a single telescope beam. The targeted search observations performed for this thesis, were of composite SNRs with suspected association with PWNs. The typical SNR sizes are smaller than the IA beam of GMRT (∼85' at 325 MHz, ∼44' at 610 MHz and ∼15' at 1420 MHz) thus, making it easy to fit into a single beam. GMRT is an ideal instrument for doing such observations because of its ability to provide simultaneous imaging and pulsar mode data. This combined with the low radio frequency coverage allows the reconstruction of the full particle spectrum to discriminate between leptonic or hadronic origins of the emission. In the next sections, we describe the observations carried out on the source SNR G015.4+0.1 / HESS J1818−154, which was suspected to be a composite SNR.

3.4.1 Planning the Observations

The targeted observations towards HESS J1818−154 were performed at 610 and 1420 MHz. The intended science goals were to obtain a sensitive, high resolution radio image and search for radio pulsations. This required recording data simultaneously in all the possible modes on the GMRT at two frequencies. The imaging requirement was to have a good flux density calibrator in the beginning and in the end with a good phase calibrator all throughout the observation. The pulsation search required observing known radio pulsars for consistency checks as well as estimating sensitivity of the data. With all these in mind, it was decided to observe the source in two long slots per frequency. The two slots for a single frequency were scheduled on consecutive days. As with previous observations, the set up and source list files were prepared. The command file was split into three parts. The first and the last were made for the first and the last scans on the flux density calibrator as well as known control pulsars while the second file had a repeating block of the phase calibrator scan followed by the source scan and a phase calibrator scan for phasing the array and another for the imaging interpolation of phase solutions. This also implied that the time series observations

were non-contiguous, as these had to be broken for phasing and phase calibrator scans. This had certain implications on the search analysis, which are discussed in Section 4.2.3. As these were long observations, the expected data volumes were of the order of 600 GB per session per pulsar back-end (IA or PA) and about 10−15 GB for the imaging observations. Thus, one had to make sure that the data disks had sufficient capacity. A proper back up strategy had to be put in place to copy the data onto disks to be carried to the data processing site.

3.4.2 A Typical Observing Session

The observing session would go exactly as described in Section 3.3.1.2 except an array, using only the central square antennae and the first antenna from each arm of GMRT, was phased periodically to compensate the phase drift introduced by the ionosphere. The centroid of HESS J1818−154 (Hofverberg et al. 2011) was used as a phase centre of the PA as well as imaging mode. The observing run would begin with observing the flux density calibrator 3C286, followed by known pulsars PSR B1642−03 and PSR B1937+21. This was followed by repeat observations of the target source and phase calibrator J1822−096. The phase calibrator was observed for 4 minutes every 20 minutes to get good phase solutions. At the end, known pulsar PSR J1901−0906 was observed, followed by flux density calibrator 3C48. A careful log had to be prepared for these observations as the number of files recorded by the pulsar back-end would be of the order of 50−70. The file names would be some common thread name followed by numbers (1,2,3 ...). To make sure that the correct scan number corresponds to correct source, the scan numbers in the imaging and pulsar back-end were synchronized by recording all the scans simultaneously. Then the scan number to source mapping could be established by looking at the header of the lta (GMRT imaging data file format) file. Some important parameters for the said observations are listed in table 3.4.

Observing Mode	IA and PA	Imaging
Central Frequency	610 and 1420 MHz	610 and 1420 MHz
Receiver Bandwidth	33 MHz	33 MHz
Filterbank Channels	512	512
Sampling Time	61 μs	8 s

TABLE 3.4: Important observational parameters for targeted observation of SNR G015.4+0.1/HESS J1818−154 TeV source.

3.4.3 Post Observation Work

Once the observations were over, the data with all the logs were accumulated in a computer disk in the observatory. The data were then copied onto portable hard disks for further analysis.

Once all the data are accumulated, what remains is to analyse them to look for signatures created by the desired sources. How this was done, is a matter of the next chapter.

Chapter 4

Data Analysis

Different modes of observations require different data analysis methods on the same type of targets. However, raw data acquired with a telescope for any type of observation first needs to be reduced using similar data analysis methods. Three different types of observations are described in this thesis, viz., pulsar search, pulsar timing and imaging observations. In this chapter, we describe the preliminary data analysis techniques for reducing these different types of observations.

4.1 Blind Search

A typical blind pulsar search analysis looks at the data in a two parameter space of period and DM. The data analysis for the blind search observations was carried out using a software package called SIGPROC[1]. This package was implemented into a parallel model on a computer cluster having 64 dual core compute nodes, using open-mpi[2], which is an open source message passing interface (MPI) library for high performance computing. Following sections contain important details regarding each step followed during the data analysis.

[1] http://sigproc.sourceforge.net/
[2] http://www.open-mpi.org/

4.1.1 Radio Frequency Interference Mitigation

Almost all the radio data are corrupted to some extent by RFI. This RFI needs to be mitigated before doing any analysis on the search data. The two types of RFI typically encountered in the GMRT search data were narrow band (restricted to a few channels in the observing band) and broad band RFI (present in several tens of channels or even the full observing band). They require different methods for identification as well as mitigation. These are described in the following sections.

4.1.1.1 Narrow Band RFI

The raw data file is a 2 dimensional array of power in spectral channels and time. In order to identify narrow band RFI, this data file is fed to a program called `cliprfi`. In the first pass, after reading the input file, the program calculates an overall mean and RMS for each spectral channel. It also calculates a running mean every second and calculates overall RMS of the running mean subtracted data. At the end of this pass, it simply writes these out in a text file. In order to identify the narrow band RFI, one needs to understand what it does to the data RMS. The data without RFI (i.e. noise) is assumed to be a Gaussian random variable with a given mean ($\mu_{\rm n}$) and RMS ($\sigma_{\rm n}$). Now assume that RFI manifests as narrow (both in time and frequency) spikes whose level is much higher than $\mu_{\rm n}$. If the data with this kind of RFI were sampled every second and a time series was to be generated by collapsing all the spectral channels, it would have narrow, high spikes of RFI. They show up in a histogram as isolated points towards right end in Figure 4.1.

What these RFI spikes do is to increase $\mu_{\rm n}$ and $\sigma_{\rm n}$, resulting in a strictly non Gaussian distribution. This causes problems for detecting weak sources like pulsars that depend on the statistics of the noise being Gaussian. If the mean intensity of the source is $\mu_{\rm s}$ then, the S/N for the signal is defined as

$$S/N = \frac{\mu_s}{\sigma_n} \tag{4.1}$$

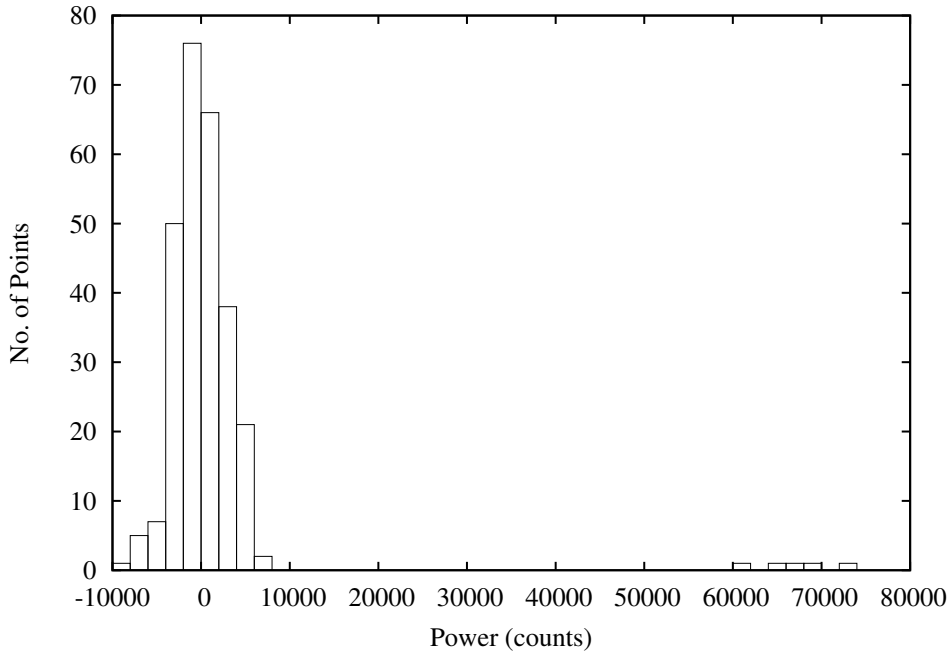

FIGURE 4.1: Histogram showing the distribution of intensities for an RFI affected time series. The data were integrated for 1 s and all the spectral channels were collapsed to produce the 0 DM time series (See Section 4.1.2 for a discussion on dedispersion). The histogram was then plotted after subtracting the mean from the data. The total duration of observation is 300 s.

The presence of RFI spikes thus, reduces the S/N for a source signal and depending on the detection threshold, may swamp out marginal detections. The knowledge that narrow band RFI increases data RMS is very helpful in identifying bad channels in the search data. As was previously stated, the program `cliprfi` produces RMS for each channel over the full observation span. One such plot showing RMS as a function of channel number is shown in Figure 4.2. It is clear even from the first look that some channels near channel number 50, 130, 250, 270, 350 and 400 are corrupted by narrow band RFI. These were identified manually and the flag for these channels were set to be 0 in the text file. In the second run, `cliprfi` clipped these channels so that, the data from those channels were not considered for further analysis.

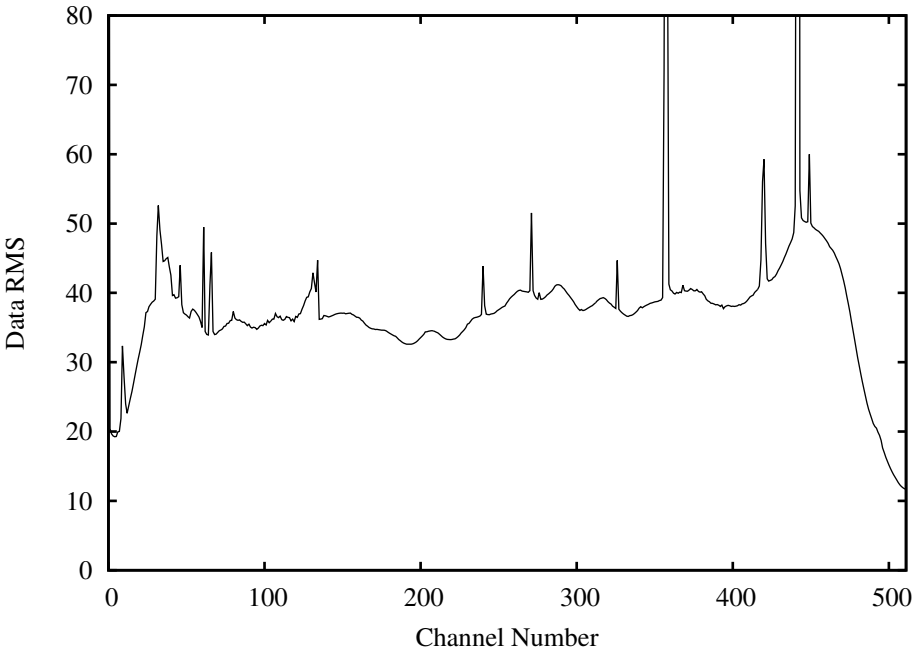

FIGURE 4.2: Narrow band RFI seen in the GMRT 325 MHz observing band. The average power level for the observing band is around 700 and the expected RMS level in the absence of broad band RFI is 5. The drop in RMS near the edges of the band is because of the filter response rather than cleaner data.

4.1.1.2 Broad Band RFI

Removal of broad band RFI was more complicated than narrow band RFI. Some times, all broad band RFI does is to elevate the baseline for those channels in which, it is present. The presence of broad band RFI is clearly evident in the plot shown in Figure 4.2. The observed level in the central band is around 35 whereas, the expected level is 5. Thus, the broad band RFI has elevated the RMS in each band in the central region by a factor of 7. In such cases, a second round of RFI mitigation using the zero DM filtering as described in Eatough et al. (2009) was implemented in addition to the manual clipping of RFI infected channels in the first round. Zero DM filtering is a simple minded RFI mitigating algorithm. It subtracts the mean of all frequency channels in each time sample. If there are N frequency channels then, the new values S'(f_i,t_j) are given by

$$S'(f_{\rm i}, t_{\rm j}) = S(f_{\rm i}, t_{\rm j}) - \frac{1}{N}\sum_{i=1}^{N} S(f_{\rm i}, t_{\rm j}) \tag{4.2}$$

This removes the broad band RFI present throughout the band and helps the pulsar signal stand out much better. In fact, if the pulsar is very strong, this subtraction will make most of the band negative. Although very simple and useful (reducing the RMS down to about a factor of 3 worse than the expected level), this method also fails sometimes when the broad band RFI is not present throughout the band or is present in less than 80% of the band. In such cases, one has to rely on identifying it based on manual scrutiny as described in the previous section.

This stage of the analysis was not a part of the high performance cluster (HPC) pipeline. The RFI mitigation stage was done manually for each field and the resultant data were then copied to the data directory in the network attached storage (NAS) disks in the HPC. This was followed by another stage, which converted the raw telescope data into SIGPROC filterbank format[3].

4.1.2 Dedispersion

Cold interstellar plasma delays lower frequency signal as compared to higher frequencies for radio waves. Hence, a proper delay has to be subtracted from the pulse arrival time at a lower frequency channel with respect to the highest frequency channel in the observing band before co-adding frequency channels. This process is called *dedispersion*. The pulsar search data is a two dimensional array of time samples and frequency channels. If the jth time sample of lth frequency channel is R_{jl} and there are N frequency channels, the jth time sample of the dedispersed time series, T_j is then,

$$T_j = \sum_{l=1}^{N} R_{j+k(l),l} \tag{4.3}$$

where k(l) is the nearest integer number of time samples corresponding to the dispersion delay of the lth frequency channel relative to the highest frequency in the observing band. If f_l is l^{th} frequency and f_1 is the reference frequency, then

[3]More information about the filterbank format can be found in SIGPROC documentation at http://sigproc.sourceforge.net/sigproc.pdf

k(l) in terms of trial DM, sampling time (t_{samp}) and frequencies is given as the nearest integer to,

$$k(l) = \left(\frac{t_{samp}}{4.15 \times 10^6 ms}\right)^{-1} \left(\frac{DM}{pc - cm^{-3}}\right) \left[\left(\frac{f_l}{MHz}\right)^{-2} - \left(\frac{f_1}{MHz}\right)^{-2}\right] \quad (4.4)$$

Here, the channel ordering is taken such that l = 1 corresponds to the highest frequency and frequency decreases with increasing l. If $\triangle$f is the bandwidth of a single filterbank channel, f_l is given by,

$$f_l = f_1 - (l - 1)\triangle f \quad (4.5)$$

The dedispersion process described above is called *incoherent dedispersion* as it simply subtracts proper time delay from the pulse arrival time for different frequencies in the time series, where phase information is lost. One such iteration provides a time series for only one trial DM value. In the search analysis, as the distance or DM of the pulsar is unknown, one needs to search over a large range of trial DM values. The choice of the DM step ($\triangle$DM) is very critical to reduce the computational time in this analysis. A very small DM step will result in producing redundant time series and wasting computing resources as well as time whereas, a large DM step will miss out pulsars due to reduced S/N at DMs different from the intrinsic DM of the pulsar. A sensible choice of $\triangle$DM may be obtained by setting the delay between the highest and lowest frequency channel to be equal to the sampling time. The ith trial DM in terms of total bandwidth $\triangle$f, center frequency f (MHz) and sampling time t_{samp} (ms) is,

$$DM_i = 1.205 \times 10^{-7}(i - 1)t_{samp}(f^3/\triangle f) \text{ pc-cm}^{-3} \quad (4.6)$$

The time series for i = 1 is the 'Zero DM' time series or is just the addition of signals without any delay. This time series is very important because it will contain

a lot of information about RFI which is terrestrial in origin and can thus serve as a very effective tool in identifying RFI signatures in the data. At i = N + 1 for a band of N channels, the so called 'Diagonal DM' is reached. Total delay across the whole band at this DM is just $n \times t_{samp}$ and broadening across each filterbank frequency channel is t_{samp}. Above the diagonal DM, effective time resolution is decided by broadening in individual filterbank channels. Usually when i = 2N or i = 3N, adjacent time samples are added together to reduce computational effort. This iterative dedispersion goes on until it reaches a desired maximum DM value. One look at the pulsar catalogue[4] reveals the fact that there is no known pulsar having a DM > 1000 and |b| > 1. Hence, the maximum DM was set at 1200 pc-cm^{-3}. Once the DM step and the maximum DM are decided, the next important detail is how to implement this in the HPC. The data for this search were analysed on the NCRA HPC, which had 64 compute nodes, each with an Intel® dual core processor. The data were copied to the NAS disks from where, they were copied onto the scratch area of each node. The full DM list was divided such that each participating node got equal number of DMs. The analysis from this point onwards was carried out in an *embarrassingly parallel model*, i.e., each node carried out the full analysis on its own copy of the data independent of the other nodes. Hence, for each field, the analysis was parallelised in the DM space as dedispersion is the costliest computing operation in the search analysis. The steps described in the following sections were carried out on the time series for each DM independently. The results were then copied back to the common disk for manual verification.

4.1.3 Harmonic Search

Once the dedispersed time series (T_j) is obtained, a Fourier transform is performed to get its power spectrum. Given that the time series is discretely sampled, the resultant transform is the discrete Fourier transform (DFT). If the time series has N distinct samples, the kth Fourier component (where $i = \sqrt{-1}$) is

[4] http://www.atnf.csiro.au/people/pulsar/psrcat/

$$F_k = \sum_{j=0}^{N-1} T_j exp(-2\pi ijk/N) \tag{4.7}$$

For a sampling time of t_{samp}, the frequency of the kth Fourier component would be

$$\nu_k = k/(Nt_{samp}) = k/T_{obs} \tag{4.8}$$

where T_{obs} is the length of the observation and $1 < k < N/2$. If each Fourier component is normalized by the factor $(N\bar{T_j^2})^{1/2}$, it is equal to the power at frequency ν_k (Lorimer and Kramer 2005). A periodic signal in time domain will show up as a peak at its corresponding frequency. Assuming that the noise in the data has a Gaussian distribution, its Fourier transform is *white*, i.e., the power is uniformly distributed over all frequencies. In practice however, the power spectrum does not have well behaved Gaussian noise. Fluctuations in the data acquisition system and/or receiver noise vary slowly over time, hence adding low frequency noise to the spectrum. RFI, as explained in Section 4.1.1, occurs sporadically over the observing span and hence, introduces high power at a large range of frequencies (especially broad band RFI). To counter this, the spectrum is first *whitened* by subtracting running median from different bands of the spectrum. The resultant spectrum is then normalized by subtracting the mean and dividing by its RMS so that the whitened spectrum then has zero mean and unit RMS. The effect of this whitening procedure is demonstrated in Figure 4.3.

Considering that the Fourier component at any frequency is just the power at that frequency, Equation 4.1 implies that the Fourier amplitude of a signal in the whitened spectrum is equal to it's S/N. This makes identifying candidate periodicities very easy. For example, if the threshold S/N is 8, any peak higher than 8 in the whitened spectrum is a candidate period with an S/N equal to its value.

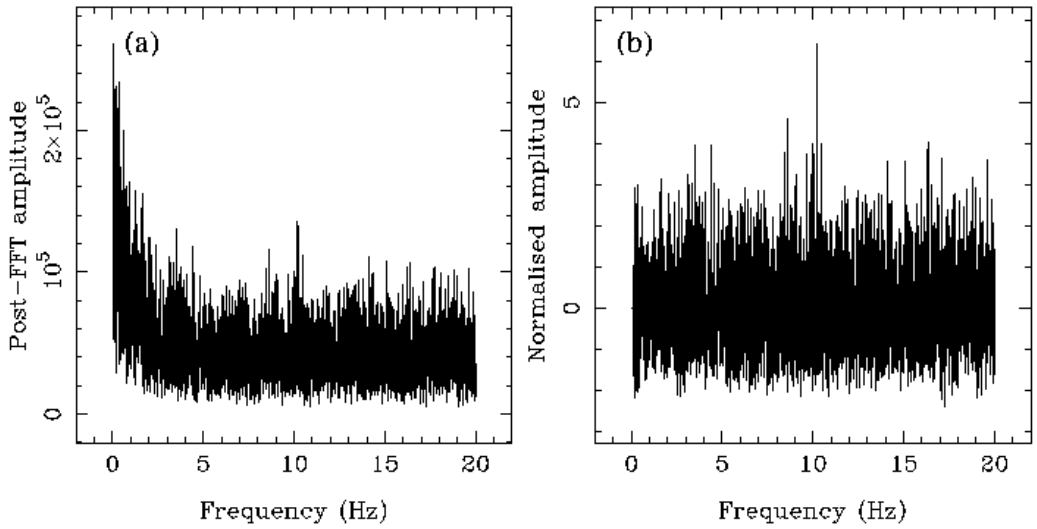

FIGURE 4.3: (a) Amplitude spectrum of the data collected using the Parkes telescope. (b) The same spectrum after whitening. The whitened spectrum is then normalized so as to have zero mean and unit RMS (see text for details). Image taken from Lorimer and Kramer (2005)

As explained earlier, the normalization factor in frequency domain is inversely proportional to the RMS of the data in time domain. This implies that the width of the signal in one Fourier domain is inversely proportional to its width in the corresponding Fourier domain. Pulsars typically have narrow duty cycle pulses. This results in the signal power being spread into many harmonics and sub harmonics in the frequency domain. The effect of pulse duty cycle on the spectrum is demonstrated in Figure 4.4. The spectra in the figure were derived from a simulated pulsar signal. The simulated signal was generated using a program `fake` from SIGPROC. The signal was generated for a pulsar of period 100 ms, DM of 10 pc-cm^{-3}, duty cycle of 5% (and 10%), with a single pulse S/N of 1. The simulated t_{samp} was 123 μs with T_{obs} of 10 s. Given that the single pulse S/N is 1, it is difficult to identify single pulses in the dedispersed time series and it looks like white noise (Figure 4.4a and 4.4c). What is clear from Figure 4.4b and 4.4d, is that narrower duty cycle pulse produces larger number of harmonics in the spectrum. The other notable difference is the relative strengths of the harmonics.

It is easy to identify strong pulsars from the FFT because the harmonics stand out from the noise, but for weaker pulsars, the peaks at the fundamental as well as

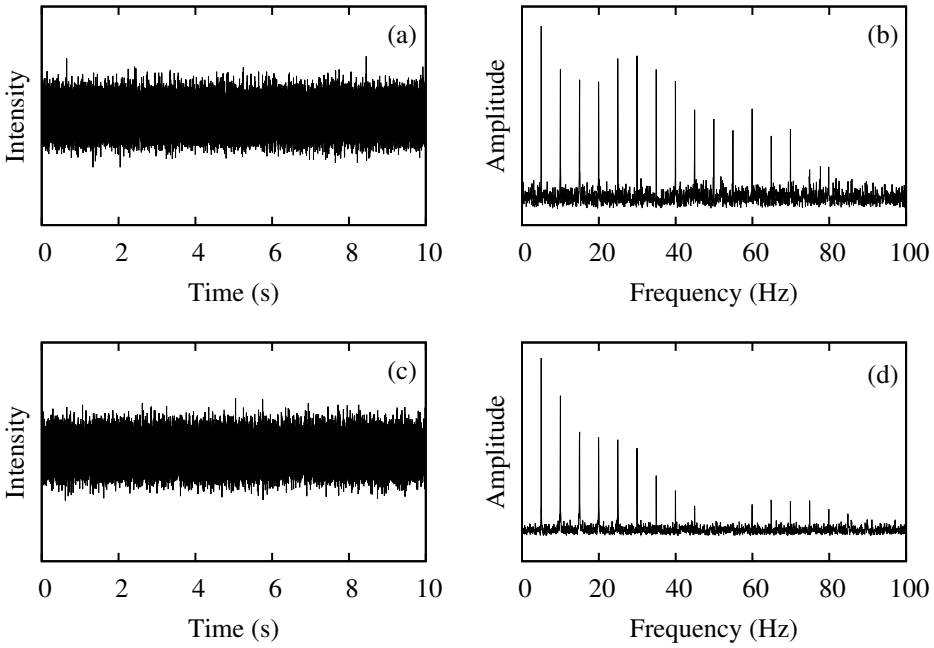

FIGURE 4.4: (a) Zero mean, dedispersed time series for a simulated pulsar signal with a period of 100 ms at a DM of 10 pc-cm^{-3} having a duty cycle of 5%. (b) Normalized FFT of the time series in (a). (c) Zero mean, dedispersed time series for the same simulated pulsar signal with a duty cycle of 10%. (d) Normalized FFT of the time series in (c). The signal was generated using a program `fake` from SIGPROC (see text for more details).

harmonics and subharmonics do not stand out as clearly as in Figure 4.4. Hence, before searching for significant peaks, the harmonics need to be added to the fundamentals. This is achieved through incoherent harmonic summing. In this technique, the original spectrum is stretched by an integer factor and added back to it to form a *harmonic sum*. The larger the number of harmonics added, the better will be the S/N. Figure 4.4 clearly demonstrates that narrow pulses have of the order of 10−15 harmonics in the data. The above discussion is applicable to pulses having single components. If the pulse has multiple components or if there are inter pulses, the number of harmonics may be suppressed. Thus, in reality, upto 16 harmonics are summed and each summed spectrum is searched individually for significant peaks. All the candidate periodicities with an S/N $>$ 8 are listed in a candidate file with S/N and the harmonic fold number. Although RFI usually appears as sporadic, narrow bursts in time and frequency, one kind of RFI actually produces periodic modulations in the time series data. This RFI is generated from

the power distribution network when there are loose contacts or gaps, which give rise to sparking. This produces RFI over a wide range of frequencies. The AC supply frequency in India is 50 Hz. Thus, sparking in the power distribution network produces a 20 ms modulation in the time series. Due to the high power at 50 Hz and its harmonics (and subharmonics), they may be wrongly identified as potential candidates. The blind search pipeline has a limited number of candidates that it stores. Thus, the false RFI periodicities (called *birdies*) actually occupy many places in the candidate files due to harmonic summing. To avoid this, the identified and confirmed RFI periodicities with typical number of harmonics are marked in a separate birdie file. Given a birdie period, number of harmonics and a bandwidth over which the observed frequency of the birdies changes, these particular frequency ranges can be zapped i.e. made zero during the harmonic search analysis.

4.1.4 Folding and Diagnostic Plots

Once the periodicity search creates a list of candidates, the dedispersed time series is folded modulo the candidate period in various ways to produce a diagnostic candidate viewer plot. In the HPC pipeline, each node created the viewer plots in their local area for all the DMs in their respective lists. At the end of the list, all the plots were copied to the common location under a directory by the field name. The diagnostic plot summarizes some important properties of the candidates, which help discriminate genuine candidates from false ones. One such example plot is presented in Figure 4.5. The figure shows a diagnostic plot for PSR J1838+1523, which was discovered during the analysis of the blind search data. This diagnostic plot contains 5 different parts. Each of these, from top to bottom (as in Figure 4.5), is explained in detail below.

- Header Text: It contains salient observational parameters such as the observation date, sampling time, folding period, DM and S/N of the folded profile.

- Time Series: This plot shows the zero mean, unit rms, dedispersed time series. This plot helps in identifying very strong RFI in time domain if it is present.

- Folded Frequency Sub-band Profile: This plot shows folded profile in frequency sub-bands. To make this plot, the observing band is divided into 8 sub-bands. Each subband is separately dedispersed with respect to a common reference frequency and the resultant time series is folded modulo the candidate period. This plot helps to identify DM signature of a true pulsar from RFI. Typical RFI candidates have a DM of 0 and will not show an aligned pulse at non-zero DMs.

- Folded Time Sub-integration Profile: This plot shows folded profile in time sub-integrations. To make this plot, the full dedispersed time series is divided into 8 sub-integrations and each one is independently folded modulo the candidate period. This plot helps in identifying period errors for true pulsars as well as clearly demarcating RFI candidates which will be present for a very short time and hence will not show up in all sub-integrations. This can then be mapped to the time series plot to correlate strong RFI instances to spurious candidates.

- Integrated Profile: This plot shows the full dedispersed time series folded modulo the pulsar period. If the two plots above show consistent signature, this plot should show a very high S/N which is reported in the header text.

  A true pulsar candidate can be differentiated from a spurious RFI candidate by looking for consistent signatures in all the plots.

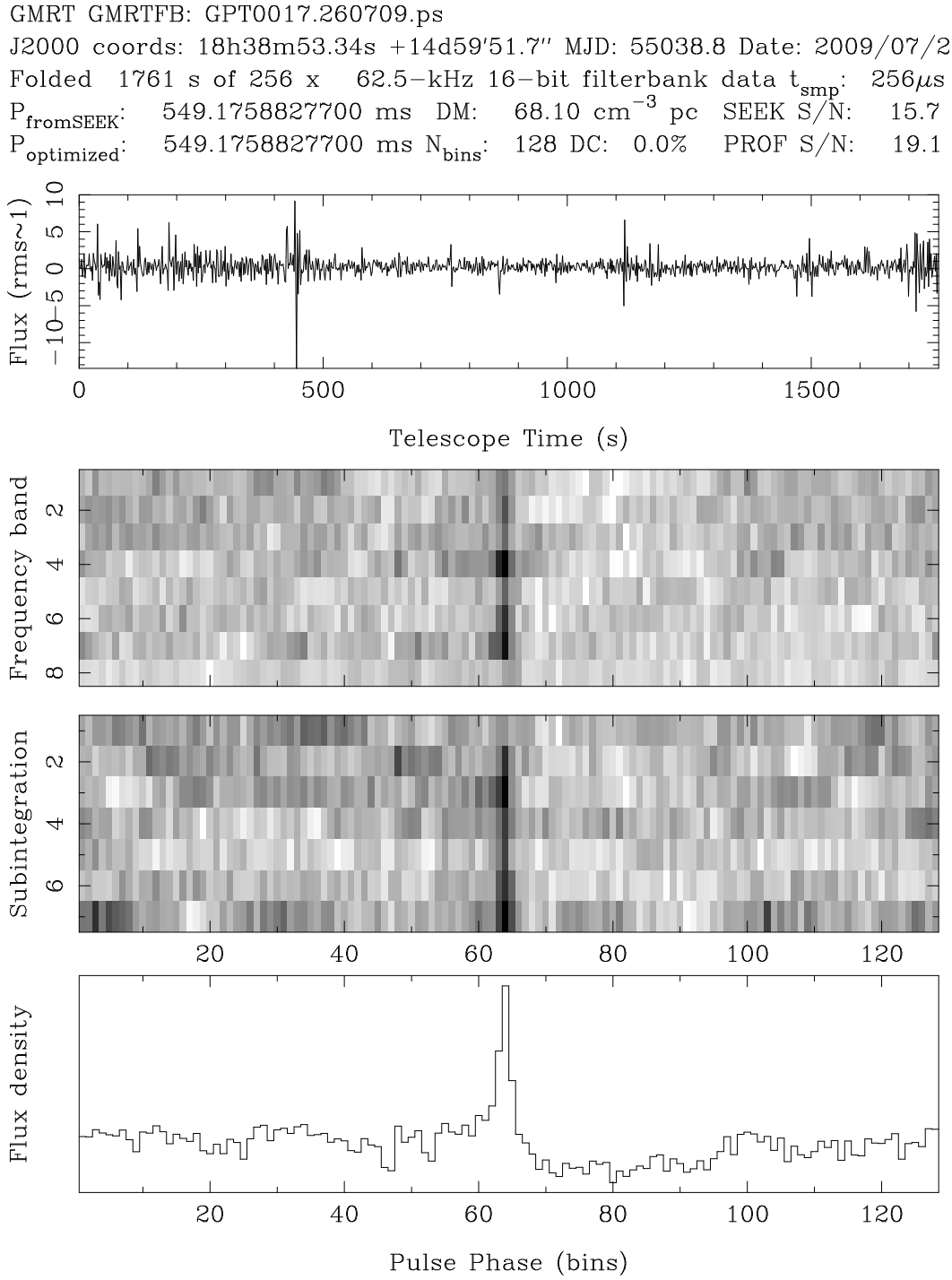

FIGURE 4.5: A diagnostic candidate plot for PSR J1838+1523. This is the discovery plot for this pulsar. See text for details.

4.2 Targeted Search

Targeted search analysis is similar to blind search analysis in the sense that it also looks at the data in P−DM space. Targeted search however, involves larger integrations over the same sky region. Thus, the data size per field (or pointing in blind search) is much larger. In classical searches, the observations are performed in a single stretch. Thus, the time series data are contiguous. As described in Section 3.4.1, the targeted search observations done with the GMRT involved intermediate scans on the phase calibrator source time and again. Thus, the time series data obtained from the telescope had breaks. The contiguous data spans were only of 20 minutes duration. In order to obtain the full expected sensitivity, all of these data needed to be joined together and then searched for periodic signal. This was done using a technique called *broken search*. The analysis pipeline was implemented using modified SIGPROC programs. It was run on the new HPC procured by NCRA in December 2012 (see Appendix A for more details about the HPC). In the following sections, we describe the analysis method and its implementation on the HPC.

4.2.1 HPC Search Pipeline

Though targeted search is very different from blind search observationally, the data analysis is very similar, especially when the distance estimate for the target is not available beforehand. This makes the basic stages of analysis similar i.e., RFI mitigation followed by dedispersion and harmonic search. The only difference here was the way harmonic search was implemented given the non-contiguous time domain data with an addition of single pulse search as well. The analysis pipeline was divided into three phases with two manual stages in between. It involved a batch mode MPI script written in C language. The actual implementation was done using `bsub`, which is a job submission program under the Platform LSF[5]. The use of `bsub` somewhat affected the working of the pipeline, which is explained

[5]LSF stands for load sharing facility, which is a workload managing platform for HPC environments

later. In the next sections, we describe the actual phases of the analysis and how they were implemented on the HPC.

4.2.1.1 Phase I

In this phase, the data were screened for RFI instances by using `cliprfi` to produce RMS values for each channel as described in Section 4.1.1.1. All the data files were kept in the NAS and each core ran the program on a separate data file independently. The text files containing final band shapes (as the one shown in Figure 4.2), were also stored in the same directory as the raw data files. The next stage was to manually flag bad channels, which had high RMS as compared to the overall RMS in the flatter part of the band.

4.2.1.2 Phase II

In this phase, the flagged frequency channels were blanked from the raw data files to produce RFI clipped data files. These were then converted to the filterbank format for actual search analysis. This was also done on the NAS disks with each core working independently on its own data file. The total free electron content along any line of sight depends on the distance to the source, and determines the DM value. The plasma content also determines the amount of scattering as well as pulse broadening. This increases the minimum detectable pulse period as a function of DM. Thus, one does not need to retain the same time resolution in the filterbank data. One look at the pulse broadening estimates from NE2001 model (Cordes and Lazio 2002) gives a good idea of how many adjacent samples could be safely integrated without losing sensitivity to short period pulsars. The criteria that was applied in the current search was to have at least 16 bins across the minimum detectable pulse period for DM larger than the diagonal DM. The phase II was thus, run to produce filterbank files with 2, 3, 4 etc. adjacent samples added together. The number of added samples was called *nadd*. Once the filterbank files were ready, another MPI script copied the files to local disks on each compute

node. This was done because there was no way to know which nodes will be participating in the analysis run before the job was submitted to `bsub`. At the end of this phase, each compute node had a local copy of all the data files to work on.

4.2.1.3 Phase III

This phase actually carried out the pulsar search on the data. This phase was run using a single MPI program written in C language. The very first thing that this script did was to get the total number of ranks[6] participating in the analysis and the nodes to which they belonged. It then divided the list of trial DMs equally into all the ranks. Each rank created its own results directory in the same local scratch disk with all the data. This directory had the trial DM list assigned to that particular rank. It would also have all the intermediate analysis products before they were copied on the NAS disk in the final result directory, which was created by the master rank (rank 0). Each rank directory also had a text file with the list of the names of filterbank files to be analysed. The list had to be in a chronological order with the names in a fixed format, which was desirable for later stages of analysis. In the next stage, each rank produced dedispersed time series files for their trial DMs for all the data files. This was followed by single pulse search to try and detect significant bursts of radio emission from RRATs. Finally, a harmonic search was carried out. These are described in more detail in Section 4.2.2 and 4.2.3, respectively. Once the harmonic search for a particular trial DM was finished, the resultant files were copied to the global result directory. The single pulse search result files needed to be appended for all the trial DMs. Hence, these were copied to the global result directory only at the end of the trial DM list. At the end of the search stage, a barrier prevented any rank from moving ahead. A master rank (rank 0) then concatenated the harmonic search candidates at all the trial DMs into one single candidate file. It also concatenated the single pulse search files into 4 groups of trial DMs such that each group contained equal number of trial DMs. The actual ranges were dependent on the DM range and

[6]In MPI terminology, rank refers to a particular process and has a unique number assigned to it when all processes are spawned by the MPI program.

steps. Although the harmonic search was done on combined data, single pulse search was run on individual files independently. The master rank then created the single pulse viewer plots using a SIGPROC program `plotpulses`. Harmonic search results were copied into one global directory, while dedispersed time series files and the single pulse files and viewer plots were copied in a different global directory. Thus, at the end of search, one directory had the candidate list for all trial DMs for harmonic search and the other result directory had time series files with 4 single pulse viewer plots per observation slot per field.

4.2.2 Single Pulse Search

McLaughlin et al. (2006) discovered a new class of rotating neutron stars, which emit sporadic bursts of radio emission every now and then. The so called RRATs could not be detected in the harmonic search because they do not emit regular periodic pulses like the normal radio pulsars motivating a simple minded single pulse search. The single pulse search is a time domain search and is run on the dedispersed time series. It is an exercise of matched filtering. It assumes a Gaussian distributed time series samples of known mean and standard deviation. As described in Cordes and McLaughlin (2003), the S/N for such narrow pulses having an amplitude S_{peak} and a width W, is given by

$$S/N = \frac{S_{peak}W}{S_{sys}}\sqrt{\frac{n_p \triangle f}{W}} \tag{4.9}$$

where S_{sys} is the system equivalent flux density, n_p is the number of polarizations summed and $\triangle$f is the receiver bandwidth. In order to get maximum S/N, the time series sampling time must match the pulse width. This is achieved by smoothing the time series by adding successive samples. As with all template matching techniques, false detection probability should be taken into consideration to apply a good threshold. As pointed out in Cordes and McLaughlin (2003), the probability of having a pulse of a given S/N by chance, decreases exponentially with S/N. Assuming pure Gaussian random noise yields a threshold of 3−4, but presence

of RFI makes the statistics distinctly non Gaussian. Thus, a threshold S/N of 6 is applied in real searches. The algorithm also improves the data statistics iteratively after removing detected significant pulses from further mean and RMS calculations. The resultant candidates are plotted in a diagnostic plot like the one shown in Figure 4.6. The plot has 4 different sub plots. They are described below.

- Top row left: This plot shows number of candidate pulses as a function of S/N. For random noise with RFI, it should show an exponential decay with isolated pulses indicating significant outliers. For a real pulsar signal, one should either see a bump in the distribution or an excess of very high S/N pulses. In Figure 4.6, there is a very slight bump near S/N of 25.

- Top row middle: This plot shows number of candidate pulses as a function of trial DM. In normal cases, there is a slight excess at low DMs due to RFI but otherwise, the plot is flat. For a real pulsar signal, one should see a clear peak at the DM of the pulsar. In Figure 4.6, this peak is suppressed by the low DM RFI pulses.

- Top row right: This plot shows S/N as a function of trial DM. In normal cases, it has a low DM excess due to RFI and an otherwise flat appearance. For a real pulsar signal like that present in Figure 4.6, we see a distinct peak at the pulsar's true DM.

- Bottom plot: This plot shows all candidate pulses as a function of trial DM marked as circles, with the radius of the circle proportional to the pulse S/N. In Figure 4.6, large RFI contamination at zero DM with some RFI stripes can be seen with strong, isolated single pulses at the true DM of the known pulsar PSR B2111+46. Incidentally, this pulsar was discovered in a single pulse search (Davies and Large 1970).

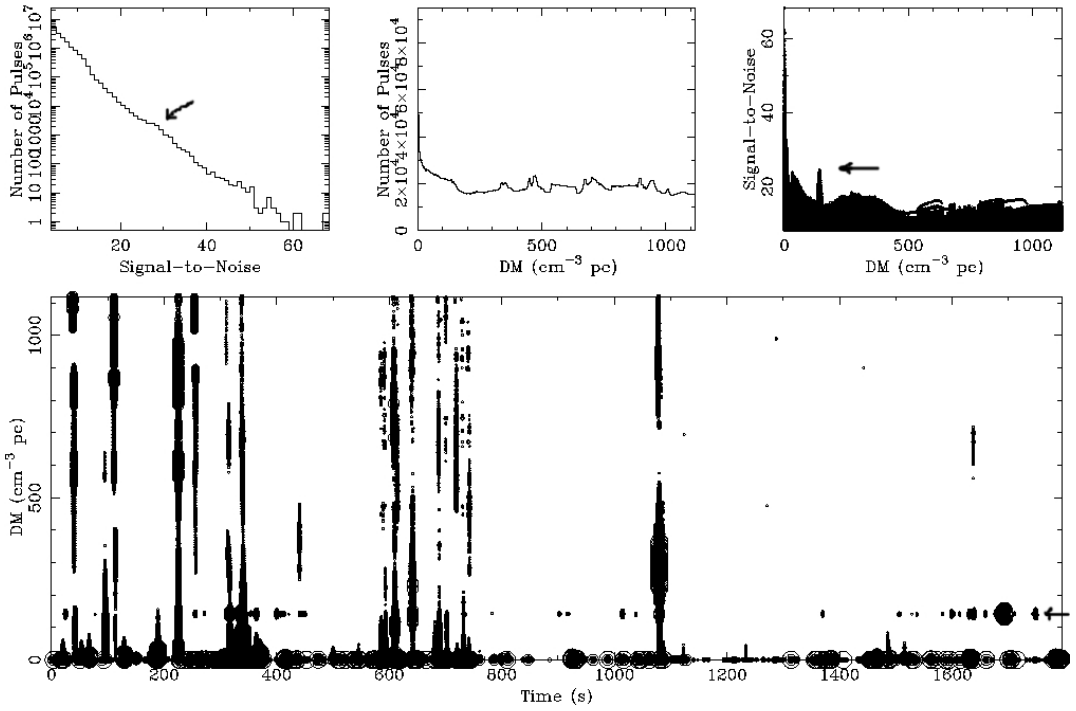

FIGURE 4.6: A Typical single pulse search plot. This particular plot shows single pulses from a known pulsar PSR B2111+46 which has a DM of 141.26 pc-cm^{-3} (marked by an arrow on the right in the bottom plot). See text for more details.

4.2.3 Broken Harmonic Search

As stated in Chapter 3, the targeted search observing strategy required that the target scans be non-contiguous. Pulsar search observations are usually done using single dish telescopes. Thus, while doing pulsar search, imaging is never an objective. This rules out observing calibrator sources during a search scan. Thus, all pulsar search data is always contiguous [7]. The only conceivable breaks are because of problems like power outage or parking due to high winds. Simultaneous imaging observations with search observations for our targeted search necessitated breaks in observations. Thus, a method for carrying out harmonic search on non-contiguous data was required. The standard harmonic search in SIGPROC is implemented through the program `seek`. In order for it to be able to work on non-contiguous data, it was augmented to create a new procedure called `seeknew`, which had the tweak required to make `seek` algorithm work on non-contiguous

[7] An exception is pulsar search in globular clusters such as 47 Tuc . Such searches are carried out over data spanning over more than a year (see Camilo et al. 2000)

time series data. The logic was simple. `seek` needs a single spectrum to work on, but we had multiple spectra, each corresponding to a single scan on the target source. In the new code, the time series files were read one by one. Their spectra were formed individually and all the resultant spectra were added *incoherently* to form the final spectrum. Thus, if $\mathrm{a_1}(\nu_\mathrm{k})$, $\mathrm{a_2}(\nu_\mathrm{k})$, $\mathrm{a_3}(\nu_\mathrm{k})$ $\ldots \mathrm{a_n}(\nu_\mathrm{k})$ are Fourier amplitudes of the spectra at a Fourier bin ν_k, the final amplitude will be given by

$$a(\nu_k) = a_1(\nu_k) + a_2(\nu_k) + a_3(\nu_k) \ldots + a_n(\nu_k) \tag{4.10}$$

The spectra were appropriately zero padded whenever required. The final spectrum was then searched for significant peaks by using the harmonic search algorithm as explained in Section 4.1.3. In order to estimate the improvement in noise statistics, let us assume that the noise in time (σ_t) as well as frequency domain (σ_ν) behaves as a Gaussian random variable in all the scans. Now from the definition of Fourier transform (see section 4.1.3), we have

$$\sigma_t \propto \frac{1}{\sigma_\nu} \tag{4.11}$$

If each scan lasts for time $\mathrm{T_{int}}$ and the total observation time is $\mathrm{T_{obs}}$ with n scans,

$$T_{obs} = nT_{int} \tag{4.12}$$

For a single scan in time domain, we have

$$\sigma_t \propto \sqrt{T_{int}} \tag{4.13}$$

The incoherent addition of n different spectra will give a $\sqrt{n}$ improvement in noise in the spectral domain. This implies that after the incoherent addition, the final noise level in the spectrum (σ) will be given by

$$\sigma = \frac{\sigma_\nu}{\sqrt{n}} \tag{4.14}$$

Substituting for σ_ν and n from the above equations, we get

$$\sigma \propto \frac{1}{\sqrt{T_{obs}}} \tag{4.15}$$

This corresponds to a $(\mathrm{T_{obs}})^{1/2}$ improvement in time domain and hence, one recovers the expected sensitivity equivalent of the total observing time. Note that the sensitivity is independent of the choice of integration time. Thus, one can choose as large an integration time as possible with number of scans limited by the observational constraints as mentioned above. In reality, RFI makes the noise non Gaussian in nature, which in turn affects the sensitivity. Even with this practical constraint on the sensitivity, once a candidate is detected, a fully coherent addition is possible and is discussed in the next section.

4.2.4 Candidate Screening and Diagnostic Plots

Once the search pipeline produced harmonic search candidates, the known *birdies* that survived the zapping, were removed from the candidate list. The list was further pruned by removing sub-millisecond candidates[8] and the periodicities which were smaller than the effective sampling time at higher DMs. The remaining candidates were considered for further analysis. The candidate viewer plots were then produced using another MPI script, which used the approximate period and DM from the search pipeline. Both these estimates were then improved by using a finer search in the time domain. This procedure is explained in detail below.

[8]Sub-millisecond period pulsars would have a large rotational kinetic energy, which will cause the neutron star to break at its equator due to large centrifugal force. This makes the existence of sub-millisecond pulsars unlikely. However, it can not be ruled out completely.

4.2.4.1 Improving the Candidate Period and DM

As explained in Section 4.1, pulsar search is done in the P−DM parameter space. The search pipeline always provides an approximate estimate of the candidate P and DM. A sparse DM sampling, especially at DMs higher than diagonal DM, may result in a DM estimate which is slightly offset from the true DM. Binning as well as smoothing in the Fourier space may result in an estimate of the period, which is slightly offset from the true period. Out of the two, an offset period estimate is usually a more severe limitation because the pulse peaks at a range of DMs but the peak in period is fairly narrow (as can be seen in the second panel from top in the left column in Figure 4.7), consequentially reducing S/N substantially. Also, one does not need a very accurate estimate of DM in the early follow-up of a new pulsar. It can be refined further using multi-frequency pulsar timing observations. One does not require high precision DM measurement unless there is an intended study of DM variations. Thus, the dedispersed time series files already saved in the global result directory were used. The parallelization was done on the DM space again with each rank running the fine period search on its designated list of trial DMs. In order to do a finer period search, the choice of period step is important, thus retaining full resolution afforded by the binning in the folded profile. This was decided such that the accumulated period error across one continuous integration was equal to time corresponding to one bin in the folded profile. For a rough search period P, folded with n_{bins} bins across observation time of T_{int}, with a period error dP, this gives,

$$\frac{P}{n_{bins}} = \frac{T_{int} dP}{P} \tag{4.16}$$

or

$$dP = \frac{P^2}{n_{bins} T_{int}} \tag{4.17}$$

This gave n_{bins} trial periods with the rough search period at its midpoint. The figure of merit for the goodness of a folded profile, was taken to be reduced χ^2 assuming the profile mean (no signal) as the null hypothesis (H_0). Thus, a sharp profile with high S/N would give a high value of reduced χ^2 as compared to just noise (for which, reduced χ^2 would be 1). This so called P−DM search generated a 2 dimensional array of reduced χ^2 values. The peak of this array provided the refined period and DM for the candidate. One example of this array is plotted in gray scale in the second panel from top in the left column of Figure 4.7.

The search observations were spread over a time span of two days. Any further error in the refined period could be removed by using a much finer search which involved a period step calculated using Equation 4.17 with T_{int} replaced by the time span of the observations, T_{obs}. Given that the observing time for a single scan was 20 minutes as compared to the full extent of 10−15 scans over a few days, this could give an order of magnitude improvement in the candidate period. Assuming that the measured period P_{mes} (and corresponding frequency ν_{mes}) is different than the true period P_{true} (and corresponding frequency ν_{true}) by an amount δP ($\delta\nu$) then,

$$P_{true} = P_{mes} + \delta P \tag{4.18}$$

or

$$\nu_{true} = \nu_{mes} + \delta\nu \tag{4.19}$$

Assuming that the rotation period of the pulsar changes by a perceivable amount only due to the inherent slow-down, we get the true rotation frequency at any given time with respect to some reference time (t_0) as

$$\nu_{true}(t) = \nu_{true}(t_0) + \dot{\nu}_{true}(t_0)[t - t_0] \tag{4.20}$$

Noting that rotation frequency is nothing but the rate of change of pulse number (N), the expected pulse number at any time (t) can be expressed in terms of ν_{true} as follows

$$N(t) = N(t_0) + \nu_{true}(t_0)[t - t_0] \tag{4.21}$$

Now, assuming that the times t_0 as well as all t in the above equation are measured values of pulse time of arrival and the reference point for the measurement is taken as the peak of the pulse, all the measured values of N for different observations at t_1, t_2, t_3, ..., t_n should be exact integers. Given that the measured period is slightly different as compared to the true period, there would be an additional fractional pulse number accumulated over time. This number (pulse phase) will have values between 0 and 1 and is denoted by $\delta\phi$. If we substitute Equation 4.19 in Equation 4.21 and subtract out the integer part of the pulse number, we get

$$\delta\phi(t) = \delta\nu(t_0)[t - t_0] \tag{4.22}$$

the corresponding equation in terms of the error in period (δP) is given by,

$$\delta\phi = \frac{-\delta P(t - t_0)}{P^2} \tag{4.23}$$

where t_0 is the time of arrival of the pulse in the first scan and t is the time of arrival of the pulse an any scan thereafter. The values of $\delta\phi_1$, $\delta\phi_2$, $\delta\phi_3$, ..., $\delta\phi_n$ can be easily measured by producing folded profiles in individual scans with the period provided by P−DM search. This was done in two steps. In the first step, folded profiles were produced by skipping the time from start of observation, required to get rid of the integral part of pulse number, assuming that the P−DM period was correct. The measured values for $\delta\phi$ were then obtained by calculating the phase shift by performing a cross-correlation between the observed profile and the reference profile, which was the folded profile for the first scan. Each time,

the next profile was added to the first profile by aligning, to get a better template for the next cross-correlation. The measured values of $\delta\phi$ were then converted to values between -0.5 and 0.5 by subtracting 1 when the value exceeded 0.5. Using the observation time span (T_{obs}) in Equation 4.17, instead of T_{int}, an array of very finely separated trial periods was generated around the P−DM period. The range of periods to be searched for, was determined as the width of the peak in the reduced χ^2 versus P−DM trial period (as shown in the left plot adjoining the P−DM gray scale in Figure 4.7) at 80% of its peak value. Simulated $\delta\phi$ values were then generated for each trial period using Equation 4.23. The simulated set was treated as a set of plausible models for the measured values of $\delta\phi$. A further refined period estimate was then obtained by comparing the measured values of $\delta\phi$ with the simulated values and searching for the trial period, which minimized the RMS error obtained after subtracting the model from the measured values. One such example plot is shown in the bottom panel in the left column in Figure 4.7. The above mentioned procedure is similar to pulsar timing analysis done over a time range of the order of 5−10 days. Pulsar timing analysis is further explained in Section 4.3. Given that this kind of analysis is suitable only for a stable rotator, this procedure naturally discriminates against RFI, which is only sporadic. This ensures that the candidate surviving this analysis is most probably a real pulsar. Such a unique candidate discriminant was a notable feature of broken time series observations spread over a few days.

Given the peculiar nature of observations and candidate screening applied in the search analysis, the resultant candidates could not be visualised properly using the in built viewer in SIGPROC (as shown in Figure 4.5). Hence, a new viewer was designed in order to visualise broken search harmonic candidates. One example of the diagnostic plot is shown in Figure 4.7. As is seen, the viewer plot is divided into three parts, the data header on the top and two columns having various diagnostic plots below. We describe in detail what each panel represents from the candidate analysis below (in a given column, the panels are numbered in increasing order from top to bottom).

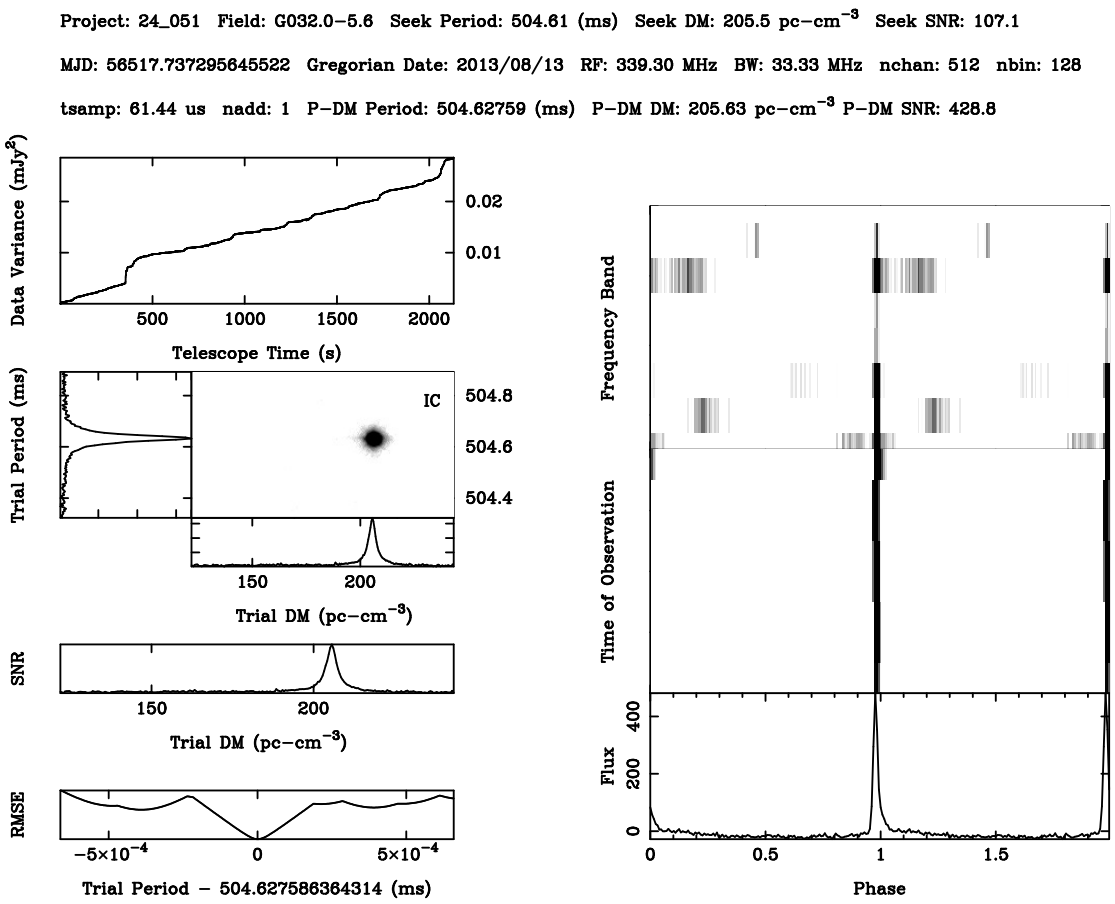

FIGURE 4.7: Example viewer plot for a broken search candidate. This particular field had a known pulsar PSR B1907–03. This plot represents the analysis done over 5 scans, each of a duration of 1800 s. The large improvement in the estimated candidate period as well as the overall profile S/N (designated as SNR in the plot) due to coherent addition of individual profiles is evident.

- Left column, panel 1: This panel shows a plot of the cumulative variance of the dedispersed time series as a function of observing time. In order to produce this plot, the individual scans were dedispersed to 0 DM. They were then appended to produce a single, dedispersed time series representing the whole integration time (T_{obs}). Data variance was then calculated over 1 s chunks of data in a cumulative manner. The variance was then rescaled to mJy^2 by using the radiometer equation [c.f. Appendix 1, Section A1.4 in Lorimer and Kramer (2005)]. In case of pure Gaussian random noise, the data variance should increase linearly with number of samples (or observing time). RFI spikes will produce sudden jumps in this overall linear trend and

can be marked clearly. One such jump can be seen at around 400 s in Figure 4.7.

- Left column, panel 2: This panel shows a zoomed part of the 2 dimensional P-DM plot in gray scale. In Figure 4.7, there is a clear sharp peak showing the detection of PSR B1907−03. The bottom plot shows reduced χ^2 as a function of trial DM at the peak period and the left plot shows reduced χ^2 as a function of trial period at the peak DM.

- Left column, panel 3: This panel shows pulse S/N (designated as SNR in Figure 4.7) as a function of trial DM at the peak period.

- Left column, panel 4: This panel shows RMS error as a function of trial period in the second stage of period estimation using pulse arrival times. It shows a clear dip and a unique minimum in Figure 4.7, indicating a more precise measurement of the pulsar period.

- Right column, panel 1: This panel shows a gray scale plot of the final profile in 8 frequency sub-bands. The frequency increases from top to bottom. The final profile was produced after adding the individual profiles by aligning them using the correct period estimate. The profile is repeated to show 2 rotations for clarity, which is also the case for the subsequent panels.

- Right column, panel 2: This panel shows folded profiles in individual scans. The chronological order is from top to bottom. The profiles were aligned by skipping appropriate time from start of observation, which is equivalent to the accumulated pulse phase due to slow-down. This phase was calculated using Equation 4.21 with respect to the start time of the first scan. Thus, skipping appropriate time from the scan start, the starting phase of each folded profile was the same.

- Right column, panel 3: This panel shows the accumulated profile produced by adding all the profiles in the previous panels. The resultant increase in S/N due to coherent addition of profiles is evident from the increased S/N (428 as compared to 107 in single scan).

4.3 Timing Analysis

Pulsars are very stable rotators. Their rotation periods can be measured with very high precision (up to nano seconds or pico seconds for some pulsars). This clock-like stability of pulsar rotation allows us to do pulsar timing which helps in the study of many phenomena associated with the radio pulse propagation as well as intrinsic variations in the pulse properties due to changes in the pulsar magnetosphere. This is usually done by measuring what is called *time of arrival* (TOA) of a pulse. Careful pulsar timing analysis reveals very useful information about phenomena like *timing noise* (irregularities in the pulse arrival times) and *glitches* (sudden increase in the pulsar rotation frequency followed by exponential recovery) that are very important towards understanding intrinsic pulsar properties. In this section, we discuss the main techniques and methodology of pulsar timing analysis in order to extract maximum information using the radio pulses emitted by these sources.

4.3.1 Measuring Pulse TOA

The most important step in pulsar timing is to measure the pulse TOA. This is the time of arrival of the average pulse from the start of observation (the time reference actually varies. Sometimes, it is also taken as middle of the observation. Whatever the time reference, it should be consistent throughout the timing analysis). The dedispersed time series is folded modulo the pulsar period to form the integrated pulse profile. TOA is measured for a *fiducial point* on the profile (usually its peak). The typical observational set up for pulsar timing observations is shown in Figure 4.8.

Once the integrated profile is formed, what remains is to accurately determine the pulse TOA. The precision afforded by the folded profile is many a times not sufficient. This depends on the strength of pulsar emission, sampling time as well as pulse S/N which in turn, constrains the number of bins across the profile. Even with optimum set up and folding parameters, some pulsars are very weak

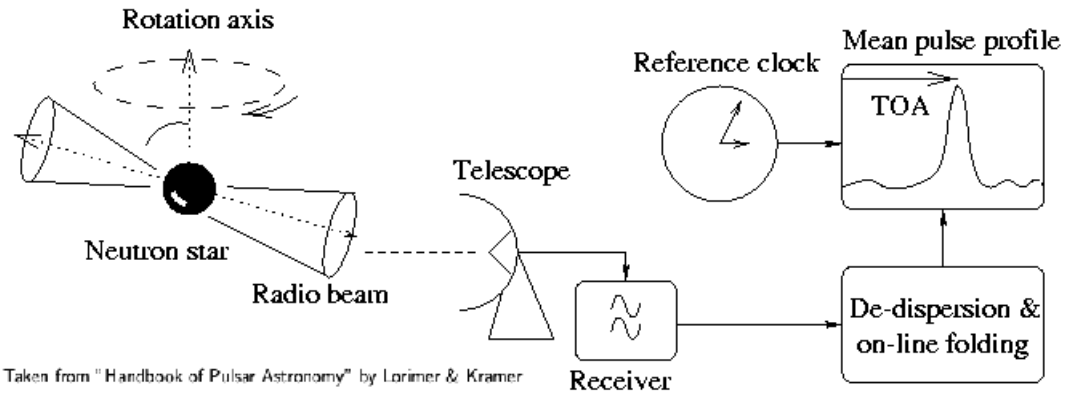

FIGURE 4.8: Observational set up for pulsar timing. Taken from Lorimer and Kramer (2005).

and hence have a low profile S/N. Thus, one uses a technique called template matching, in order to get a much more accurate TOA.

4.3.1.1 Template Matching

This technique was first described by Taylor (1992). It basically involves cross correlating the observed profile with a very high S/N template profile to get the position of the fiducial point in the observed profile. The template profile for a given observing frequency is generated from many individual profiles. In order to do this, the profiles are first added coherently. The accumulated profile is then passed through a low pass filter (or smoothed) to form an almost noise free, high S/N and/or noise free template profile. Now, both the template as well as observed profile are discretely sampled. Assuming that the observed profile $P(t_j)$ is a scaled and phase shifted version of the template profile $T(t_j)$ with additional Gaussian random noise $N(t_j)$, such that

$$P(t_j) = a + bT(t_j - \tau) + N(t_j) \tag{4.24}$$

where a is an arbitrary offset and b is the scaling factor. The value of τ yields the TOA relative to the fiducial point of the template and start of the observation. The cross correlation is usually calculated in the frequency domain after doing a

DFT on the profile as well as the template. If there are N bins in the profile and template,

$$p_k exp(i\theta_k) = \sum_{j=0}^{N-1} P_j exp(-2\pi ijk/N) \tag{4.25}$$

$$t_k exp(i\phi_k) = \sum_{j=0}^{N-1} T_j exp(-2\pi ijk/N) \tag{4.26}$$

Where p_k and t_k are the Fourier amplitudes and θ_k and ϕ_k are the phases of the profile and the template, respectively. The time offset τ in time domain (Equation 4.24) appears as a phase ramp $k\tau$ in the frequency domain owing to the shift theorem (Bracewell 1965). The scaling factor b and the desired TOA (in terms of τ) can be obtained by doing a χ^2 minimization to obtain (Taylor 1992),

$$\frac{\partial \chi^2}{\partial \tau} = 2b\sigma^{-2} \sum_{k=1}^{N/2} kp_k t_k sin(\phi_k - \theta_k + k\tau) = 0 \tag{4.27}$$

which can be solved for τ by using Brent's method (see Press et al. 1986). The value of b can then be obtained by (Taylor 1992),

$$b = \frac{\sum_{k=1}^{N/2} p_k t_k cos(\phi_k - \theta_k + k\tau)}{\sum_{k=1}^{N/2} t_k} \tag{4.28}$$

Uncertainty in the value of τ can be obtained by calculating the variation in the value of τ that leads to the variation of χ^2 by 1. This gives (Taylor 1992),

$$\sigma_\tau^2 = \left(\frac{\partial \chi^2}{\partial \tau^2}\right)^{-1} = \frac{\sigma}{2b\sum_{k=1}^{N/2} k^2 p_k t_k cos(\phi_k - \theta_k + k\tau)} \tag{4.29}$$

The noteworthy fact that arises from these equations [see Taylor (1992) for a detailed discussion] is that the accuracy of the measurement of τ is independent of the bin size of the profile. In fact, the assumption that p_k and t_k fall off rapidly, only depends on the S/N of the profiles in the time domain. Thus, one can, in

principle, decrease the number of bins on a profile to get a better S/N and hence, a better estimate of the TOA as compared to the time domain method which critically depends on the bin size.

4.3.2 Time Standards

The TOAs measured thus far, have a time stamp according the GPS, which gives a clock pulse every minute giving accurate Coordinated Universal Time (UTC) as measured by US National Institute of Standards and Technology (NIST). This, finally has to be converted to International Atomic Time (TAI) maintained as an average of large number of atomic clocks based at Bureau International des Poids et Mesures (BIPM). As the Earth does not rotate uniformly, leap seconds have to be added to UTC to keep it within 0.9 s from the actual Earth rotation time UT1. Thus, UTC is always an integral number of seconds away from TAI (TAI = UTC + δT). This time is then converted to a smooth running time standard called Terrestrial Time (TT). The final timing analysis uses TOAs converted to TT.

4.3.3 Pulsar Timing Procedure

In order to monitor the pulse arrival times and connect them to pulsar rotation, we need to find an expression for the pulsar rotation in its co-moving frame. Assuming a Taylor's series expansion we get,

$$\nu(t) = \nu_0 + \dot{\nu_0}(t - t_0) + \frac{1}{2}\ddot{\nu_0}(t - t_0)^2 + \dots \tag{4.30}$$

where $\nu_0 = \nu(\mathrm{t}_0)$ is the spin frequency and $\dot{\nu_0} = \dot{\nu}(\mathrm{t}_0)$ and $\ddot{\nu_0} = \ddot{\nu}(\mathrm{t}_0)$ are the time derivatives at some reference epoch t_0. $\dot{\nu}$ is the pulsar spin down rate corresponding to the period derivative ($\dot{\mathrm{P}}$). For solitary pulsars, $\ddot{\nu}$ is usually too small to be measured (apart from very young pulsars). Timing noise may result in time varying $\dot{\nu}$ or a finite $\ddot{\nu}$. Hence, care should be taken while fitting as well as interpreting

the value of $\ddot{\nu}$. Now, the spin frequency ν is the rate of change of pulse number. From Equation 4.30, we get

$$N(t) = N_0 + \nu_0(t - t_0) + \frac{1}{2}\dot{\nu}_0(t - t_0)^2 + \frac{1}{6}\ddot{\nu}_0(t - t_0)^3 + \dots \tag{4.31}$$

The above equation also tells us that if we set t_0 as a TOA of some pulse (N_0) and the pulsar spin down is accurately known, we should observe a pulse at every integral value of N from an inertial frame. Our frame at the observatory is far from inertial. The TOAs measured at the observatory or the topocentric TOAs have to be transferred to the Solar System Barycentre (SSB) frame, which, to a good approximation, is an inertial frame. These arrival times are called *barycentric arrival times*. This transformation takes care of gravitational effects due to other masses present in the solar system. It is also effective because the barycentric TOAs are independent of the observatory position as well as observation time. This allows one to combine TOAs calculated at different observatories at different times. The transformation from topocentric TOA (t_{topo}) to barycentric TOA (t_{SSB}) for an isolated pulsar can be summarised in the following equation (Lorimer and Kramer 2005).

$$t_{SSB} = t_{topo} + t_{corr} - \triangle D/f^2 + \triangle_{R\odot} + \triangle_{S\odot} + \triangle_{E\odot} \tag{4.32}$$

These terms are briefly explained below [see (Hobbs et al. 2006) for a more detailed discussion].

- Clock Correction (t_{corr}): This term takes care of the transformation of the local observatory time to TT.
- Frequency Correction ($\triangle$ D/f^2): This term takes care of the interstellar dispersion. It converts the TOA to infinite frequency; hence removing the dispersion in the data. $\triangle$D = `D` $\times$ DM, where `D` is the dispersion constant defined in Equation 1.7, DM is in the units of pc-cm^{-3} and f is the observation frequency (highest frequency in the observation band) in MHz.

- Römer delay ($\triangle_{R\odot}$): This delay is the classical light travel time between the phase centre of the telescope and the SSB. Calculating this delay requires accurate ephemeris of the solar system. They are published by Jet Propulsion Laboratory (JPL) [see Folkner et al. (2014) for the latest ephemerides and a detailed discussion]. These calculations also require accurate UT1 corrections published by International Earth Rotation Service (IERS)[9].

- Shapiro Delay ($\triangle_{S\odot}$): This is a relativistic delay caused by the curvature of space-time due to masses present in the solar system. The largest delay ($\sim$120 μs) is caused by the solar limb while Jupiter can cause a delay upto 200 ns (Lorimer and Kramer 2005). Usually, considering Sun and Jupiter is enough.

- Einstein Delay ($\triangle_{E\odot}$): This delay occurs due to the time dilation caused by the combined effect of all the solar system bodies. This takes care of the corrections in the atomic clocks due to the Earth's rotation in the gravitational potential of all the remaining solar system objects.

Once the TOAs are converted to barycentric frame, pulsar rotation parameters can be determined by doing a least square fit with respect to pulse number observed at the observation time. The χ^2 statistic for the problem can be defined as

$$\chi^2 = \sum_i \left(\frac{N(t_i) - n_i}{\sigma_i} \right)^2 \tag{4.33}$$

where $\mathrm{n_i}$ is the nearest integer to $\mathrm{N(t_i)}$ and σ_i is the uncertainty in the TOA in units of pulse period (turns). The aim of this whole exercise is to obtain a phase coherent solution that accounts for every pulsar rotation between any two observations. Initial solutions start with few TOAs spaced very close so that the accumulated TOA uncertainties do not exceed one pulsar period. If the fit is successful, the resultant post-fit residuals should have a Gaussian distribution with zero mean and RMS comparable to TOA uncertainties. This solution is then

[9] www.hpiers.obspm.fr

expanded to include all observations maintaining phase coherence. First few days require only period and pulse phase for fitting. After this, parameters like period derivative and position, slowly come into play as the time baseline of the timing observations increases. While including more and more parameters in the timing model fit, one needs to be careful about the nature and time scales of the effects caused by these parameters. For example, a wrong period causes a linear variation in the residuals, wrong $\dot{P}$ causes a parabolic variation over a few months, while a wrong position causes sinusoidal variation with a periodicity of a year. This is shown in Figure 4.9 for a known pulsar PSR J2208+5500, observed at the ORT at 325 MHz.

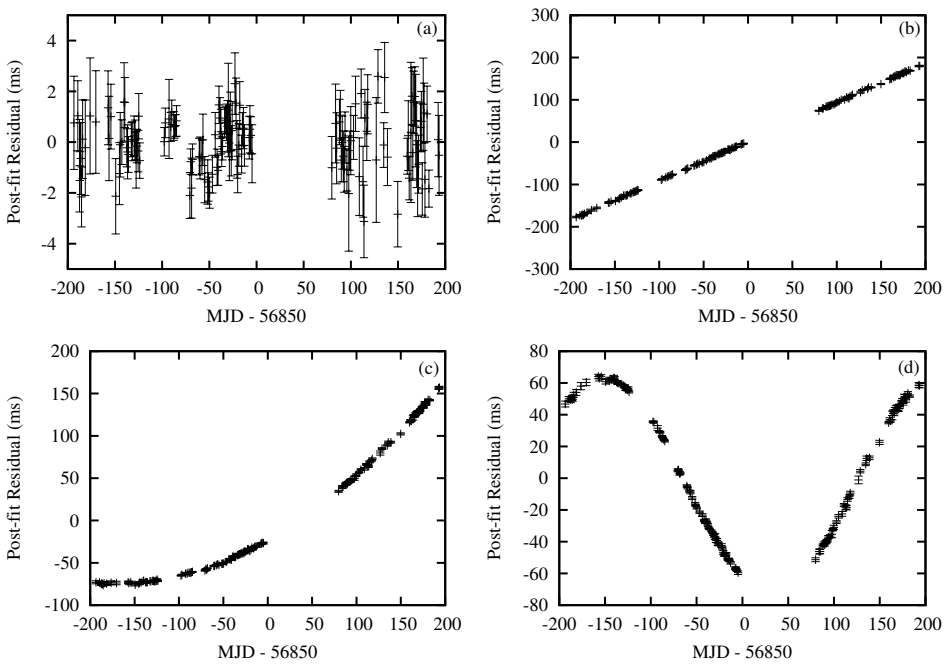

FIGURE 4.9: The effect of some parameters on pulsar timing residuals. The residuals were formed for PSR J2208+5500, which has a period of 933 ms, by using timing observations done with the ORT. (a) A good timing model results in Gaussian random residuals. (b) If the assumed period is lower by 10 ns than the true period, we get linearly increasing residuals. (c) If the assumed $\dot{P}$ is lower by 6.25 % than the true $\dot{P}$, we get parabolic increase in the residuals. (d) If the declination of the source is in error by 30", we get sinusoidal residuals with a period of 365 days. Note the progressively decreasing amplitudes of the variations and their different time scales.

The uncertainties in the fitted parameters are obtained from the coherence matrix of the least square fit (see Press et al. 1986). Sometimes, even after obtaining

an optimal fit, the resultant residuals do not go below a certain level. This slow variation of timing residuals is intrinsic to the pulsar and is called as *timing noise*. Some pulsars are intrinsically good rotators resulting in very small timing noise whereas some are 'noisy' rotators resulting in considerable timing noise. Typically, millisecond pulsars are more stable rotators as compared to normal pulsars. Changing pulse shape due to scatter broadening or intrinsic jitter may also contribute to timing noise. Thus, timing noise may, at times, indicate intrinsic pulsar properties (like mode changing).

4.3.4 TEMPO2

The pulsar timing techniques with all the required details are incorporated in an easy to use software package called TEMPO2[10] (Hobbs et al. 2006). It has all the propagation and other effects implemented at 1 ns level of precision. Apart from the different fitting routines, it also has various plugins to visualise data as well as make different kind of plots. In short, it provides a single interface to the multitude of pulsar timing techniques. In order to calculate the χ^2 as given in Equation 4.33, it needs the measured TOAs as well as the pulsar rotation parameters. This is achieved through two different files, a parameter file (the par file) and a file containing TOAs (the tim file). The parameter file contains the parameters to be used for calculating the timing model with their initial guess values and uncertainties. It also has other miscellaneous parameters, which denote epochs of some measurements, clock corrections, solar system ephemerides etc.

Table 4.1 shows some important parameters for isolated pulsars. TEMPO2 can calculate any number of spin frequency derivatives but usually, the first two are sufficient. It can also fit for DM if one has TOAs calculated at more than one observing frequency. The measurement epochs for period, DM and position are required when one wants to study their time evolution, while the zero residual parameters are useful for generating predictive polynomial coefficients, which provide the apparent period and pulse phase for any given modified Julian day (MJD).

[10] http://www.atnf.csiro.au/research/pulsar/tempo2

Parameter	Description	Symbol	Unit
RAJ	J2000 RA of the pulsar	α	hh:mm:ss.ss
DECJ	J2000 DEC of the pulsar	δ	dd:mm:ss.ss
F0	Spin frequency	ν	Hz
F1	First derivative of spin frequency	$\dot{\nu}$	Hz-s^{-1}
F2	Second derivative of spin frequency	$\ddot{\nu}$	Hz-s^{-2}
DM	Dispersion measure	DM	pc-cm^{-3}
PEPOCH	Epoch of measurement of ν	t_P	MJD
POSEPOCH	Epoch of measurement of position	t_{pos}	MJD
DMEPOCH	Epoch of measurement of DM	t_{DM}	MJD
TZRMJD	MJD of zero timing residual	–	MJD
TZRFRQ	Frequency of zero timing residual	–	MJD
TZRSITE	Telescope site of zero timing residual	–	MJD
CLK	Clock correction applied to get TT	–	–
EPHEM	Solar system ephemeris used	–	–

TABLE 4.1: Some basic TEMPO2 parameters for isolated pulsars.

The predictive polynomials are used basically, to do online folding of known pulsars when doing follow-up timing observations. The TOA file consists of observation frequency in MHz followed by the measured TOA in MJD (accurate upto 11 decimals), errors in TOAs in μs and the short code for the observatory. The observatory code needs to be present in a file 'observatories.dat' with the Earth-centric X,Y,Z coordinates which are used by TEMPO2 to convert the topocentric TOAs to barycentric frame. In order to visualise the pre-fit and post-fit residuals, TEMPO2 has a graphical plugin named `plk` (Hobbs et al. 2006). It is based on PGPLOT[11] and is useful for visualizing residuals as a function of MJD, date of year, hour angle etc (see Figure 4.10 for an example). Apart from this, it also allows the user to interactively select the parameters to be fit, particular sections of data for fitting as well as removing bad TOAs as well as add arbitrary phase jumps to align the residuals before fitting. It allows one to write out a new par file after the fit has converged. It also allows the plot to be printed as a postscript file as well as the data to be written to standard output for plotting in different ways. In all, it provides a user friendly, flexible interface for carrying out

[11]PGPLOT is a FORTRAN based set of subroutines used for data visualization as well a creating postscript files from the plots. (see http://www.astro.caltech.edu/~tjp/pgplot/)

basic timing analysis (even for multiple pulsars at the same time) and visualizing the results in various useful ways. In fact, this same interface was used to generate the data required to make the plots in Figure 4.9 (for more details, see www.atnf.csiro.au/research/pulsar/tempo2/index.php?n=Plugins.Plk).

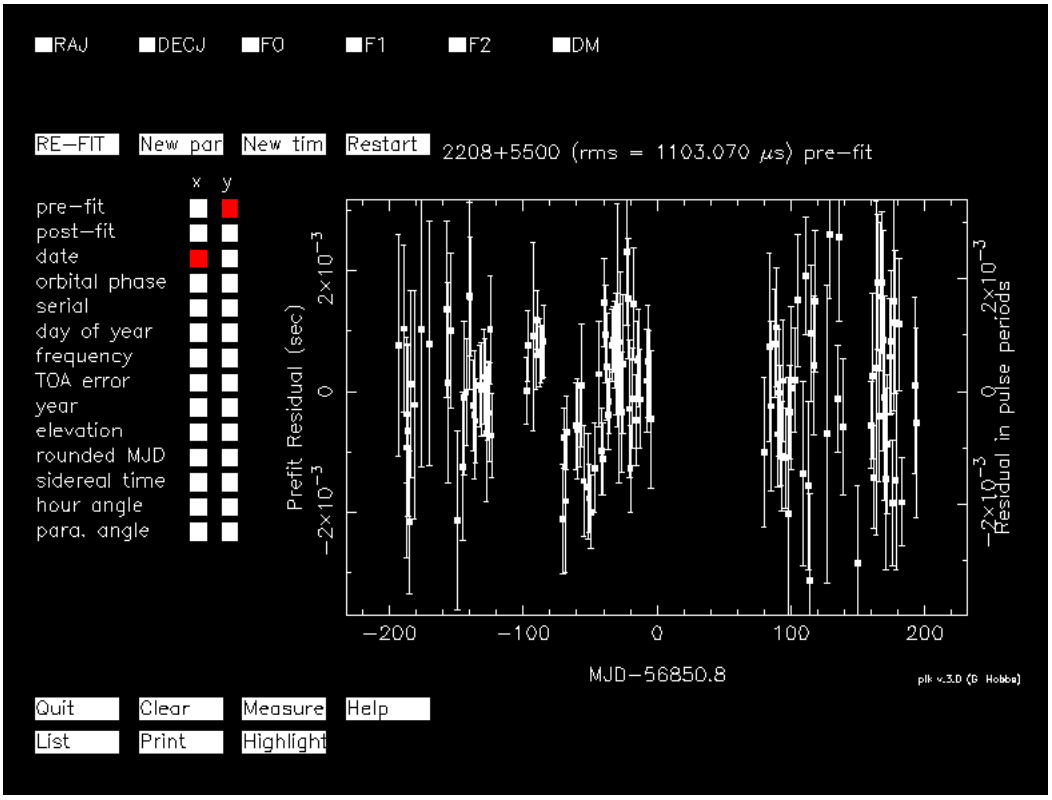

FIGURE 4.10: A screen shot showing `plk` (Hobbs et al. 2006) interface. The residuals were obtained from the ORT observations of PSR J2208+5500. The squares towards the top left corner are clickable to enable those parameters to be fitted. The list on the left allows the user to change the X and Y axes shown in the plot towards the right. See text for more details.

4.4 Imaging Analysis

During the analysis of time series data for the newly discovered pulsar PSR J1838+1523, it was discovered that the pulsar could not be detected for close to 280 days. This made the timing analysis difficult due to a large error on the pulsar position. This prompted the need to make images from the simultaneous interferometric data obtained from GMRT. In order to make an image, the bad

data needs to be flagged first. After this, it needs to be calibrated properly. The complex visibility function V(u,v) has two parts; an amplitude and a phase. Both of them need to be calibrated independently. The flagged and calibrated data is then Fourier transformed to get the final image. Although it seems fairly straight forward, in reality, it is much more complicated. In the following sections, we describe the process of obtaining the images in detail.

4.4.1 Fundamentals of Radio Interferometry

When we observe distant radio sources using interferometers, what we are measuring is really the spatial coherence function of the electric field of the electromagnetic radiation emitted by that source (Clark 1999). Assuming that the source of radiation lies on the surface of the celestial sphere[12] at $\mathbf{R}$ and the observer lies at $\mathbf{r}$ with respect to some origin, the quasi monochromatic electric field at $\mathbf{r}$ due to the source at $\mathbf{R}$ can be expressed as

$$E_\nu(\mathbf{r}) = \int \epsilon_\nu(\mathbf{R}) \frac{e^{(2\pi i\nu|\mathbf{R}-\mathbf{r}|/c)}}{|\mathbf{R}-\mathbf{r}|}\, dS \tag{4.34}$$

where $\epsilon_\nu(\mathbf{R})$ is the electric field and dS is the surface area element, respectively on the celestial sphere. Now, if we have two antenna elements at $\mathbf{r_1}$ and $\mathbf{r_2}$, the correlation of the electric field is defined as

$$V_\nu(\mathbf{r}_1, \mathbf{r}_2) = \langle \mathbf{E}_\nu(\mathbf{r}_1)\mathbf{E}^*_\nu(\mathbf{r_2})\rangle \tag{4.35}$$

This correlation function, in fact, represents the spatial coherence function of the radiation field (which is denoted by the electric field). Now, if we substitute for $E_\nu(\mathbf{r})$ from Equation 4.34 and write the product of two integrals as a double integral over two different dummy area elements dS_1 and dS_2, we get

[12]The imaginary sphere of infinite radius with the Earth at its centre. All celestial objects are assumed to lie on the surface of this sphere.

$$V_\nu(\mathbf{r_1},\mathbf{r_2}) = \left\langle \int\int \epsilon_\nu(\mathbf{R}_1)\epsilon^*_\nu(\mathbf{R}_2)\frac{e^{(2\pi i\nu|\mathbf{R}_1-\mathbf{r}_1|/c)}}{|\mathbf{R}_1-\mathbf{r}_1|}\frac{e^{(-2\pi i\nu|\mathbf{R}_2-\mathbf{r}_2|/c)}}{|\mathbf{R}_2-\mathbf{r}_2|}\ dS_1\ dS_2\right\rangle \quad (4.36)$$

now, assuming that the emission from astronomical objects is not spatially coherent, which means

$$\langle\epsilon_\nu(\mathbf{R}_1)\epsilon^*_\nu(\mathbf{R}_2)\rangle = 0 \text{ for } \mathbf{R}_1 \neq \mathbf{R}_2 \quad (4.37)$$

we can exchange integral and expectation with above mentioned assumption to get

$$V_\nu(\mathbf{r_1},\mathbf{r_2}) = \int \left\langle|\epsilon_\nu(\mathbf{R})|^2\right\rangle\left|\mathbf{R}^2\right|\frac{e^{(2\pi i\nu|\mathbf{R}-\mathbf{r}_1|/c)}}{|\mathbf{R}-\mathbf{r}_1|}\frac{e^{(-2\pi i\nu|\mathbf{R}-\mathbf{r}_2|/c)}}{|\mathbf{R}-\mathbf{r}_2|}\ dS \quad (4.38)$$

if we write $\mathbf{s}$ for $\mathbf{R}/|\mathbf{R}|$ and $\mathrm{I}_\nu(\mathbf{s})$ for the observed intensity $\left\langle|\epsilon_\nu(\mathbf{s})|^2\right\rangle\left|\mathbf{R}^2\right|$, then we can use the fact that the astronomical sources are at a very large distance to neglect terms of the order $|\mathbf{r}/\mathbf{R}|$ and replace the area element by $|\mathbf{R}|^2$ dΩ, we get

$$V_\nu(\mathbf{r_1},\mathbf{r_2}) \approx \int I_\nu(\mathbf{s})\ e^{-\{2\pi i\nu\mathbf{s}.(\mathbf{r}_1-\mathbf{r}_2)/c\}}\ d\Omega \quad (4.39)$$

This shows that the spatial coherence function just depends on the separation ($\mathbf{r}_1 - \mathbf{r}_2$) between the individual elements and not on their absolute placement. Thus, we can measure the spatial coherence function of the incoming electromagnetic radiation field by placing many such elements at different places. This concept is called interferometry. Now, if we assumed that the elements of this array are confined to a plane and the distance between two elements (or the baseline length) is measured in terms of wavelength (λ) of incoming radiation so that, $\mathbf{r}_1 - \mathbf{r}_2 = \lambda$(u,v,0). In this system, the coordinates of $\mathbf{s}$ are (l,m,$\sqrt{1-l^2-m^2}$). Now, Equation 4.39 becomes

$$V_\nu(u,v,w=0) = \int\int I_\nu(l,m)\frac{e^{-\{2\pi i(ul+vm)\}}}{\sqrt{1-l^2-m^2}}\ dl\ dm \tag{4.40}$$

now, if we assume that the area of the sky seen by the array at a given time is very small (which is true to a high degree), we have,

$$\mathbf{s} = \mathbf{s}_0 + \sigma \tag{4.41}$$

where σ has a small value and hence we can ignore second order terms. Now, $\mathbf{s}$ and $\mathbf{s}_0$ are both unit vectors. This implies

$$1 = \mathbf{s}.\mathbf{s} = \mathbf{s}_0.\mathbf{s}_0 + 2\mathbf{s}_0.\sigma + \sigma.\sigma \approx 1 + 2\mathbf{s}_0.\sigma \tag{4.42}$$

this implies that $\mathbf{s}_0$ and σ are perpendicular to each other. If we introduce a special coordinate system such that $\mathbf{s}_0$ = (0,0,1), Equation 4.39 then becomes

$$V_\nu^{'}(u,v,w) = e^{-(2\pi iw)}\int\int I_\nu(l,m)\ e^{-\{2\pi i(ul+vm)\}}\ dl\ dm \tag{4.43}$$

taking the constant exponential factor on the right will make it independent of w and we have

$$V_\nu(u,v) = \int\int I_\nu(l,m)\ e^{-\{2\pi i(ul+vm)\}}\ dl\ dm \tag{4.44}$$

which is clearly a Fourier transform relation. This enables us to define the reverse transform relation as

$$I_\nu(l,m) = \int\int V_\nu(u,v)\ e^{\{2\pi i(ul+vm)\}}\ du\ dv \tag{4.45}$$

this tells us that the so called visibility function V_ν(u,v) and the intensity in the sky plane I_ν(l,m) form a Fourier pair [see (Clark 1999) for more detailed discussion]

4.4.2 Aperture Synthesis

Equation 4.44 implies that the sky intensity distribution can be faithfully reproduced if we have continuous measurements in the U-V plane. In practice however, the interferometric arrays have fixed number of elements placed at fixed coordinates in the U-V plane. Thankfully, the radio sky does not change very rapidly and the Fourier components need not be measured at the same time. This allows for a brilliant technique which was envisioned by Ryle et al. (1959). The idea is fairly simple. The first step is to construct an array of smaller telescopes with fixed (or slightly flexible) positions. Now as the Earth rotates, the positions of the array elements change with respect to the source. This means, they form tracks on the U-V plane. This process synthesizes a much bigger telescope aperture than each of the array element. In fact, the resultant aperture is equivalent to a single dish of diameter equal to the largest baseline length. This provides very high resolution with better sensitivity. This technique is called Earth rotation aperture synthesis. All the current large interferometers like the VLA, WSRT, GMRT, Low Frequency Array (LOFAR) and SKA (in future) work using the same principle.

4.4.3 The Effect of Finite Sampling in U-V Plane

As described in the previous section, the interferometric arrays usually have a fixed number of elements. The aperture synthesis helps in filling up the U-V plane but the final result is far from continuous. This effect can be represented in terms of a sampling function S(u,v) whose value is 1 where there is a measurement and 0 otherwise. With this definition, we can define the measured intensity distribution as (Clark 1999)

$$I_\nu^D(l,m) = \int\int V_\nu(u,v)\ S_\nu(u,v)\ e^{\{2\pi i(ul+vm)\}}\ du\ dv \tag{4.46}$$

modified by a function, which is called the *dirty beam*. The measured brightness distribution is represented as a convolution between the real sky distribution I(l,m) and a function B(l,m) such that

$$B_\nu(l,m) = \int\int S_\nu(u,v)\ e^{\{2\pi i(ul+vm)\}}\ du\ dv \tag{4.47}$$

which is the *synthesized beam* or *point spread function* of the interferometric array. Thus the dirty beam (or dirty image) is given by

$$I_\nu^D(l,m) = I_\nu(l,m) * B_\nu(l,m) \tag{4.48}$$

In order to obtain the actual image from the measured visibilities, one has to de-convolve the dirty beam. This will be discussed in later sections.

4.4.4 Data Flagging

In typical interferometric observations, the array measures raw voltages, which are corrected for a geometric delay (τ_{g}) due to different positions of the individual elements. These are then correlated in the correlator to form the visibilities for all possible baselines. These are the data that are to be reduced to a radio image (or map). As stated in Section 4.1.1, radio observations are usually corrupted by RFI. One needs to identify bad data using some robust statistic and flag it so that it is not considered for further analysis. Such a robust statistic is provided by the median absolute deviation (MAD). For a univariate data set, it is defined as the median of the absolute deviations from the median of the data. If the data set is given as X_1, X_2, X_3, ..., X_n, then the MAD is given as

$$MAD = median_i\{|X_i - median_j(X_j)|\} \tag{4.49}$$

MAD is a very robust estimator of the variability of the data set. Thus, if we assume that the visibilities measured by a given baseline are a smooth function of space, time and frequency for a real astrophysical source, one can identify outliers (which are likely RFI instances) using the MAD filter. For example, one can treat any sample that has an amplitude more than, say six times MAD away from the median of the data, as an outlier and flag it as RFI. The beauty of this method is that it can be implemented iteratively. Thus, very strong RFI gets flagged in the first iteration, while in the next iteration, MAD can then be estimated by eliminating the outliers found in the first iteration. This provides a much stricter filter for bad data and the multiplier for identifying bad data (which was six in the first iteration), can be reduced further to remove low level RFI from the next iterations. This method is implemented by a package FLAGCAL[13] (Chengalur 2013), which was written specifically for GMRT data.

4.4.5 Calibration

What the interferometer measures is cross correlation counts across multiple baselines over a finite bandwidth over the full observation time. In order to make sense out of the counts, one needs to obtain a conversion factor (the so called gain factor), which converts the counts to sky intensity. In addition, instrumental phase corrupts the measured visibility phases. These need to be estimated (Thompson et al. 2001) and compensated for. The process through which one obtains the amplitude scaling factor and instrumental phases is called calibration. Although conceptually it is easy to understand, in practice, it is not so straightforward. In practice, a few simplifying assumptions are applied to simplify it somewhat. A typical radio observation happens over time and frequency across multiple baselines. The first simplifying assumption is that the time and frequency dependant gain factors are independent of each other and they can be separated into a product. If the gain function is of the form F(ν,t) then

[13]see http://ncralib1.ncra.tifr.res.in:8080/jspui/handle/2301/581 for more details

$$F(\nu, t) = G(t)H(\nu) \tag{4.50}$$

The calibration in time domain is loosely referred to as gain calibration, while that in frequency domain is usually called bandpass calibration. In the sections below, we discuss the methods to obtain both of these, in detail.

4.4.5.1 Gain Calibration

If we denote true visibility as V_{ij} and V'_{ij} as the measured visibility by two antennae i and j forming a single baseline,

$$V'_{ij}(t) \propto V_{ij}(t) \tag{4.51}$$

the process through which, one finds out all the proportionality constants in Equation 4.51, is called calibration. In order to achieve this, we assume that the antenna and array designs are made such that the whole system is linear. This allows us to write Equation 4.51 as (Fomalont and Perley 1999)

$$V'_{ij}(t) = G_{ij}(t)V_{ij}(t) + \epsilon_{ij}(t) + n_{ij}(t) \tag{4.52}$$

where $G_{ij}(t)$ is the time dependant gain factor, ϵ_{ij} is the offset and $n_{ij}(t)$ is the complex noise. As is clear from the notation, all these terms are baseline based. Out of these, the offset is taken care of by doing gain equalization and assuming that it is stable for a given observation. We then assume that the correlator does not produce any gain variations across time and frequency. This is a valid assumption for well balanced receiver systems and it allows us to express the baseline-based terms in Equation 4.52 in terms of antenna-based terms as,

$$V'_{ij}(t) = g_i(t)g^*_j(t)V_{ij}(t) + n_{ij}(t) \tag{4.53}$$

the problem of finding the baseline-based constants of proportionality has now reduced to finding out two antenna-based complex quantities, $g_i(t)$ and $g_j(t)$. They can further be divided into amplitude and phase parts to get

$$G_{ij}(t) = g_i(t)g_j^*(t) = a_i(t)a_j(t)e^{i\{\phi_i(t)-\phi_j(t)\}} \tag{4.54}$$

In order to estimate $G_{ij}(t)$, one usually observes a strong point source calibrator. The source is chosen to be such that it is at the phase center and the noise term in Equation 4.53 can be neglected. If we now replace $V_{ij}(t)$ by $A_{ij}(t)e^{i\Phi_{ij}}$ and $V'_{ij}(t)$ by $A'_{ij}(t)e^{i\Phi'_{ij}}$, we have

$$A'_{ij}(t) = a_i(t)a_j(t)A_{ij}(t) \tag{4.55}$$

and

$$\Phi'_{ij}(t) = [\phi_i(t) - \phi_j(t)]\Phi_{ij}(t) = 0 \tag{4.56}$$

Now, if the strength of the calibrator source is S and its position is at the phase center[14], we get

$$A'_{ij}(t) = a_i(t)a_j(t)S \tag{4.57}$$

and

$$\Phi'_{ij}(t) = \phi_i(t) - \phi_j(t) \tag{4.58}$$

[14]This is the position in sky where, after compensating for geometric delays, the phases for all antennae should identically be zero, i.e. the telescope is "pointing" in this direction.

If the interferometric array has N elements, we get N(N − 1)/2 baselines and the above equations can be easily solved using least squares method to get the calibration constants. This technique was developed for GMRT by Sanjay Bhatnagar and is implemented in a program called `antsol`[15] Notice that in Equation 4.58, what is important is the phase difference between a pair of antennae. In order to solve this, one typically assumes that the phases for a specific 'good ' antenna are zero. This is then taken as the *reference antenna* and all the phases are then solved with respect to this antenna. In typical observing conditions, the ionosphere is turbulent at radio frequencies. This means that the time and spacial scales of turbulence vary across the sky. This introduces additional variations in the phases estimated using the primary flux calibrator source. To counter this, one usually observes a secondary calibrator source repeatedly in a calibrator-target-calibrator sequence, during an observing session. This source is chosen such that it is sufficiently strong, essentially unresolved and less than 20° away from the target source (for more details, see the complex gain sub-section in the calibrator summary section at https://science.nrao.edu/facilities/vla/docs/manuals/obsguide/calibration). The calibration then usually works the following way. The amplitude gain factor is calculated using the primary calibrator or the flux calibrator. This converts the visibility from counts to Jy. The phase solutions are then calculated individually for each scan on the secondary or the phase calibrator and they are then interpolated across the target source to get a much better estimate of the phase variations in the antennae.

4.4.5.2 Bandpass Calibration

Once the gains are calibrated for antenna based variations, the data for each frequency channel is independently calibrated. As can be seen in Figure 4.2, the response of the instrument is not constant across the whole observing band. This happens due to the roll-off of the filter producing the final bandpass. Apart from the roll over at the edges, the bandpass may not be exactly stable over the full observation. In order to reduce the effects due to the variations across channels,

[15] http://www.aoc.nrao.edu/∼sbhatnag/GMRT_Offline/antsol/antsol.html

one typically selects either a very good single channel or a range of good channels after gain calibration to produce a good channel. This channel is called channel zero. Once the channel zero is obtained, all the channels are normalized to the value given by this channel zero using an appropriate scaling factor [see (Fomalont and Perley 1999) for more details]. After the bandpass calibration is applied, the bandpass essentially becomes constant over the observable frequency range. The bandpass calibration is usually done over a strong flux calibrator whose spectrum is very well known over a very wide frequency range (much larger than the observable band). Bandpass calibration is usually done once for a full synthesis observation (8 hours at GMRT) for a normal imaging observation. It is very critical for spectral line observations and needs to be done once every three hours or so.

4.4.6 FLAGCAL

As explained in Section 4.4.4, the package FLAGCAL was used for doing flagging and calibration on GMRT imaging data. In this section we elaborate more on how it actually does the flagging and calibration. It basically works on the assumption that the visibilities for a true astronomical source will vary smoothly but RFI will be very short and intrinsically very high as compared to everything else. The MAD filter is thus employed to identify very bad data. However, the true nature of bad data can never be revealed unless it is calibrated, but the calibration itself will suffer if bad data is included. FLAGCAL takes an iterative approach in order to optimize the effort. It first flags raw data very lightly, such that very bad data is flagged. It then calibrates this data. In the second round, the calibrated data is then flagged much more stringently and is then calibrated again. While the calibration is done by following the prescription given in the previous section, the flagging is much more complicated. It is usually done at various levels. These are antenna-baseline-channels-time records-visibilities in the same order. It recognises different kinds of sources and has identifiers for them. They are:

- F: Flux calibrator

- B: Bandpass calibrator
- P: Phase calibrator
- T: Target source

In order to identify the type of sources, it needs a file with two columns. The first column is the source name and the second is the source type as described above. A typical FLAGCAL run then happens as follows:

1. Initialize all the basic parameters.
2. Make a template of the output file.
3. Read calibrator data and flag it.
4. Calculate gain and bandpass calibration and write the data.
5. Calculate phase calibration and write the data.
6. Read the target source data and calibrate it.
7. Flag the target source data.
8. Calibrate the target source data again and write the data.

The output data is the flagged and calibrated version of the input data, which can be directly used for making images.

4.4.7 Imaging

Once the data is flagged and calibrated properly, we can, in principle, use Equation 4.45 to make an image of the astronomical source. In practice, however, the sampling function is discrete. This makes the continuous Fourier transform into a discrete one. With the incomplete sampling in the U-V plane, we can not fully reconstruct I(l,m). Thus, we need a model $\hat{I}$ having finite parameters such that,

with proper interpolation, it can very well approximate I(l,m). The model sky intensity $\hat{I}$(p$\triangle$l,q$\triangle$m) is thus, a two dimensional δ-function with intensities at the point where measurements exist and can take any value at other points. If we have N_l and N_m pixels along the sky axes, the model visibilities take the form from Equation 4.44 as (Briggs et al. 1999),

$$\hat{V}(u,v) = \sum_{p=1}^{N_l} \sum_{q=1}^{N_m} \hat{I}(p\triangle l, q\triangle m)\ e^{\{-2\pi i(pu\triangle l + qv\triangle m)\}} \tag{4.59}$$

Given that the sampling function is not uniform as well, it needs to be re-sampled and interpolated such that it becomes a uniform grid over the U-V plane. Usually, the grid spacings are such that $\triangle$l = $\triangle$m. Nyquist sampling theorem requires that

$$\triangle l = \triangle m = 1/2D_{max} \tag{4.60}$$

where D_{max} is the maximum baseline length. This ensures that the model sky intensity represents the true distribution with good accuracy. In practice, the pixel size in image plane is taken to be at least three times less then the Nyquist condition to ensure closure. The uniform gridding is achieved by convolving the visibilities with an appropriate gridding function. Before gridding, the visibilities are usually weighted by using a two dimensional Gaussian taper function. This is done to ensure that the inner region of the U-V plane with a more dense sampling gets higher weights than the longer U-V baselines where, the sampling is much more sparse. This ensures that the interpolation while gridding works much better at modelling the true sky intensity distribution. The Gaussian taper naturally also controls the synthesized beam parameters (Briggs et al. 1999). The resultant modified visibility function is thus, uniformly sampled and properly weighted. If we denote the weighting function as W(u_k,v_k), it can be represented as,

$$W(u_k, v_k) = \sum_k W_k \delta(u - u_k, v - v_k) \tag{4.61}$$

The dirty image can then be represented as

$$I^D(p\triangle l, q\triangle m) = \sum_k W(u_k, v_k)\ Re\left(V(u_k, v_k)\ e^{\{2\pi i(pu_k\triangle l + qv_k\triangle m)\}}\right) \tag{4.62}$$

where the synthesized beam is given by,

$$B(p\triangle l, q\triangle m) = \sum_k W(u_k, v_k)\ Re\left(e^{\{2\pi i(pu_k\triangle l + qv_k\triangle m)\}}\right) \tag{4.63}$$

The Hermitian nature of the visibility is utilized in taking only the real part of the transform in the above equations. In order to produce the model sky distribution (or the image), one needs to de-convolve the synthesized beam from the visibilities. This is usually achieved by using an algorithm called CLEAN, devised by Högbom (1974). The basic idea is to model any source a collection of many point sources in an otherwise empty field of view[16]. The algorithm iteratively finds the strengths and relative positions of these sources. The final CLEAN image is then formed by summing these point sources and convolving them with an appropriate CLEAN beam, which is usually chosen to be Gaussian, to reduce the effect of the spuriously interpolated large baselines. There are currently two main variants of this algorithm which are widely used. We describe them below.

4.4.7.1 Högbom Algorithm

1. Find the strength and relative position of the peak in the dirty image. This peak search can be limited by using visually specified CLEAN boxes.

2. Subtract the peak multiplied by dirty beam multiplied by a factor (called CLEAN loop gain) at its position in the dirty image.

3. Record the strength and relative position of the subtracted peak in a model.

[16]Field of view for an interferometer is usually equivalent to the half power beam width of a single antenna. For a wavelength λ and an antenna of diameter D (both in m), the field of view (in radian) is given by λ/D

4. Check for any more peaks above the user specified level. If yes, go to (1), else, proceed.

5. Convolve the accumulated point source model $\hat{I}$(p$\triangle$l,q$\triangle$m) with a CLEAN beam (which is usually an elliptical Gaussian fitted to the central lobe of the dirty beam).

6. Add the residuals of the dirty image to the CLEAN image formed in (5).

4.4.7.2 Clark Algorithm

Clark (1980) described an efficient method to implement the Högbom algorithm, which reduced a lot of computational effort. The CLEAN algorithm involves a lot of scaling and shifting of the dirty beam in order to fit for multiple point sources. This amounts to a convolution, which could be done more efficiently in the Fourier domain. This algorithm is thus, FFT based and it searches for peaks using only a small patch of the dirty beam in the Fourier domain. In practice, the Clark CLEAN has two cycles, a major and a minor cycle. The minor cycle goes on as

1. Select a beam patch (a part of the discrete representation of the dirty beam) to include the highest exterior side lobe.

2. Select peaks if the multiplication product of their strength and the loop gain is more than the side lobe strength.

3. Perform a Högbom CLEAN based on the list compiled and the beam patch. Keep doing till no more points will be selected by (2) in the residual dirty image.

The algorithm then goes into the major cycle where the point source model is transformed by FFT, multiplied by the weighted sampling function (inverse transform of the dirty beam), transformed back in image domain and is then subtracted from the dirty image. The errors introduced by selecting the beam patch instead of the full beam in the minor cycle, are corrected in further minor cycles. This is

the default CLEAN algorithm used in the imaging software packages such as Astronomical Image Processing System (AIPS)[17] and Common Astronomy Software Applications (CASA)[18]. [see (Briggs et al. 1999) for more detailed discussion]

4.4.8 Wide Field Imaging

The assumption used in getting Equation 4.44 is that the measurements in the baseline domain are limited to a plane. This puts an upper limit on the area of sky, where the assumption that $\mathbf{S_0}$ and σ are perpendicular to each other, holds. At high radio frequencies ($>$ 1 GHz), this assumption usually holds true over the full field of view (or primary beam area). At low radio frequencies, however, this assumption does not hold over all the primary beam (given that primary beam size $\propto$ λ). Equation 4.44 thus, becomes an incomplete description of the true sky distribution of the source intensity. In this case, the primary beam is subdivided into many smaller *facets*. The imaging then proceeds for each facet semi-independently with each facet having its own phase centre. Once the deconvolution is finished, each facet produces its own CLEAN image. These images can then be combined by applying proper phase shifts to correct the phase centre to the pointing centre of the beam. This approach is called multi-facet or wide field imaging and is routinely used in making radio images at observing frequencies below 1 GHz.

4.4.9 Self Calibration

As we saw in Section 4.4.5.1, the observed visibilities are proportional to the true visibilities with an additional noise term (see Equation 4.53). The usual approach to solve for the antenna based gains $\mathrm{g_i(t)}$ using a good phase calibrator source assumes that the ionospheric contribution to the phases of the incoming radiation is similar for the source and the calibrator. This assumption is based

[17]http://www.aips.nrao.edu/index.shtml
[18]http://casa.nrao.edu/

on expectations such as the source being very close to the target field, sufficiently strong and necessarily unresolved. In practice, one may not get all of these qualities in a single source or for some particular lines of sight, there may not be any good phase calibrator source sufficiently nearby. In any case, the phase calibrator is observed for a short period of time between target source scans. The actual phase solutions are always calculated for the calibrator source and interpolated on the target source scans. This is many times not sufficient to produce good phase solutions for antenna based gains for various reasons. The main reason is the failure of the assumption that the ionosphere in the direction of the phase calibrator behaves in the same manner as the one in the direction of the target source. This brings many un-modelled errors in the final image produced with normal phase calibration. The technique usually employed in order to reduce the effect of this, is called self calibration. In principle, it is just another method like CLEAN where the main aim is to improve the model sky intensity distribution $\hat{I}$(p$\triangle$l,q$\triangle$m), the Fourier transform of which, when corrected for gain variations, produces the observed visibilities within reasonable noise limits. In case of self calibration, this model is constructed from the CLEAN image itself (Cornwell and Fomalont 1999). In this approach, the point source model is constructed by adding the strong point sources above a specified intensity level provided by the user and a suitable model is constructed from it. The real crux of this algorithm is to treat the gains themselves as free parameters and try to minimize

$$S = \sum_{k} \sum_{i,j}^{i \neq j} w_{ij}(t_k) \left| V'_{ij}(t_k) - g_i(t_k) g^*_j(t_k) \hat{V}_{ij}(t_k) \right|^2 \tag{4.64}$$

where $w_{ij}(t_k)$ are the data weights. The time over which the gains should be kept constant, depends on the signal to noise ratio and the variability of the atmosphere. The above equation can be expressed as (Cornwell and Fomalont 1999)

$$S = \sum_{k} \sum_{i,j}^{i \neq j} w_{ij}(t_k) \left| \hat{V}_{ij}(t_k) \right|^2 \left| X_{ij}(t_k) - g_i(t_k) g^*_j(t_k) \right|^2 \tag{4.65}$$

where

$$X_{ij}(t_k) = \frac{V'_{ij}(t_k)}{\hat{V}_{ij}(t_k)} \tag{4.66}$$

Division by model visibilities transforms the object being imaged, into a pseudo-point source. The self calibration then is equivalent to normal calibration with this modified object as the calibrator source. This particular aspect makes this approach more useful in that, it can be used iteratively to improve the image quality as follows

1. Make an initial source model using the clean image generated from the normal calibration.
2. Divide the data by the model visibilities to create the point source model.
3. Solve for complex gains.
4. Calculate the corrected visibilities using the gain solutions.
5. Generate another image using the corrected visibilities.
6. Repeat (1) − (5) till the image RMS improves.

This can be worked out very easily using the tools already available in the standard imaging analysis packages. The procedure actually works but has no rigorous proof (Cornwell and Fomalont 1999). There are two main qualitative reasons why it works

1. For interferometric arrays with large number of elements (N), the ratio of constraints to unknown gains is (N − 2) / 2, for phases. This increases without bound as N and making some of the gains as parameters amounts to very little loss of information.

2. Radio sources are usually simple and can be represented by a few degrees of freedom (like strength and relative position as in CLEAN). Given the large number of U-V samples due to large number of baselines in interferometric arrays (GMRT, with all antennae, provides 435 of them), even with more number of degrees of freedom with the gains, the sources are effectively always oversampled and hence the minimization scheme works [see (Cornwell and Fomalont 1999) for more detailed discussion].

Chapter 5

A Blind Pulsar Survey with the GMRT

5.1 Introduction

Known pulsars are mostly Galactic sources. The active pulsar population in our Galaxy has been estimated to be about a million (Lorimer and Kramer 2005), while the number of currently known pulsars is only about 2500[1]. Considering that pulsars have a small emission beam, there should still be about 30,000 pulsars visible to us. This provides a very strong motivation to keep carrying out sensitive pulsar searches to discover as many of them as possible. On top of that, the observed pulsar emission shows a lot of temporal variations that range from nulling (Backer 1970), which lasts a few periods through transient bursts shown by RRATs (McLaughlin et al. 2006), which show few bursts over time scales of hours, to the extreme ON-OFF states shown by intermittent pulsars (Kramer et al. 2006; Camilo et al. 2012; Lorimer et al. 2012) over days to months. This makes repeated pulsar searches more fruitful in discovering these interesting objects. Blind pulsar searches scan a large area of sky with good sensitivity. This makes them relatively unbiased towards discovering any particular type of objects. This also imparts

[1] http://www.atnf.csiro.au/people/pulsar/psrcat/

blind searches with a possibility of serendipitous discoveries of exotic objects like the double pulsar (Burgay et al. 2003; Lyne et al. 2004). In addition to enhancing our knowledge of extreme physics, every new discovery adds to the population and helps to make better population models and study possible evolutionary scenarios.

As was mentioned in Chapter 2, majority of past and current pulsar surveys have used large single dish telescopes and high observing frequencies with shorter integration times as a trade off between sky background (which reduces the sensitivity at low frequencies) and survey speed (low at high frequencies). A multi-element telescope like the GMRT provides large collecting area of the order of 30,000 m^2 with a field of view of about 1° at 325 MHz (Swarup et al. 1991). This makes it a sensitive pulsar search instrument for rapid surveys. In fact, a pulsar survey carried out with the GMRT at 325 MHz would prove to be complimentary to high frequency pulsar surveys in providing a complete coverage of pulsar parameters. Low frequency surveys are also more sensitive to longer period pulsars, which would be missed by the low pass filtering employed in the PMPS (Manchester et al. 2001). This led us to propose a blind pulsar search with the GMRT at 325 MHz.

5.2 Observations

Majority of the known pulsars are concentrated near the Galactic plane. Thus, blind pulsar surveys typically observe previously un-searched parts of the Galactic plane with deeper integrations and better search strategies. Taking into consideration the relatively less explored higher Galactic latitude regions, we proposed to cover the region between Galactic longitude $45° < l < 135°$ and Galactic latitude $1° < |b| < 10°$ with the GMRT at 325 MHz. The survey was named "GMRT Galactic Plane Pulsar and Transient Survey" or GMGPPTS for brevity. The Galactic plane was not included in the survey due to very strong background emission, which makes blind searches ineffective at low frequencies. We acquired the data using the IA mode of the GMRT, which simply combines the power from

each antenna and gives the beamformed time series output. We acquired the data over a bandwidth of 32 MHz. Due to the hardware design, this bandwidth was divided into two side-bands of 16 MHz each (see Section 3.1.1.2 for details) and the data were recorded separately for each side-band. Taking into consideration the pulse smearing due to DM as well as increased scattering at low frequencies, we observed each side-band over 256 filterbank channels with a sampling time of 256 μs. The region to be observed was divided into circular fields with a diameter equal to the beam width (85') so as to form a hexagonal grid. This is shown in Figure 5.1, where each cross represents the position of the field center.

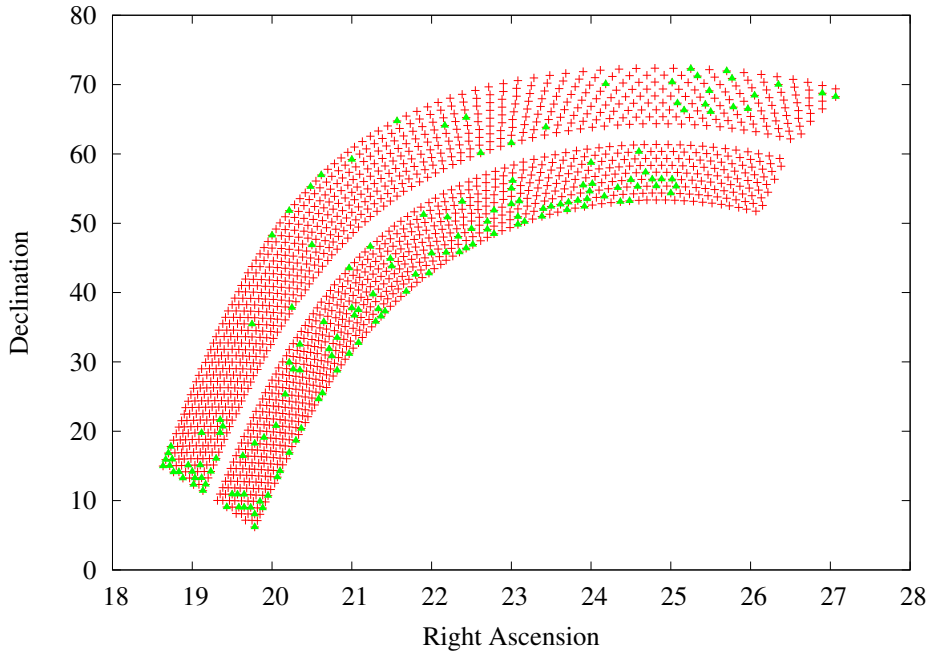

FIGURE 5.1: The region of sky observed in GMGPPTS. Right ascension is plotted in hours and declination in degrees. Each small cross represents an individual pointing. Green triangles indicate the observed fields. The blank area in between is the Galactic plane.

The survey observations were carried out in two sessions in two observing cycles of GMRT (16_282 & 17_092). Each session was 50 hours in duration and was divided into 5 sub-sessions of 10 hours each, which were carried out on consecutive days. The first set of observations were carried out between 23−27 July 2009, while the second set of observations were carried out between 25−29 December 2009. A total of 152 fields, covering an area of about 115 deg^2 were observed. They are indicated

by green crosses in Figure 5.1. The data were obtained in the IA mode and were recorded to storage disks as well as magnetic tapes. The detailed planning as well as the course of a typical observing session is explained in detail in Sections 3.2.1 and 3.2.2. Detailed observing logs were prepared for each sub-session and all the data were carefully backed up with all the auxiliary files containing time stamps.

5.3 Data Analysis

Pulsar search analysis looks at three different pulsar parameters. They are period, DM and pulse duty cycle (δ = W/P). For a blind search, there is no apriori information about any of these. Thus, one makes a set of some trial values and then the search runs over every possible combination of these parameters. In practice, the first step in the data analysis is to remove RFI from the acquired data. RFI reduces the survey sensitivity in general. But in some special cases, it may render some particular region of the phase space completely out of reach of the analysis pipeline. For the survey analysis, the RFI infected frequency channels were identified using data RMS as a function of channel number and flagging out the outliers from further analysis. This procedure is explained in more detail in Section 4.1.1. Remaining broad band RFI was removed using the zero DM filtering technique as described by Eatough et al. (2009). Once the amount of RFI in the data was reduced to an acceptable level, the actual search analysis commenced. The first loop of analysis ran over a range of trial DMs, wherein the data were dedispersed at that DM. The P$-\delta$ range was then covered by doing harmonic search (unlike the targeted search data, these data were contiguous). These methods are described in more detail in Sections 4.1.2 and 4.1.3, respectively. The search pipeline then produced diagnostic plots (like the one shown in Figure 5.2) for potential pulsar candidates, which were manually scrutinized and the candidates were appropriately classified into three categories from most promising to least promising. The search analysis was done using two pulsar search packages,

SIGPROC[2] and PRESTO[3]. The SIGPROC based pipeline was implemented in the HPC using open-mpi[4], wherein the parallelization was done so that each node did the search on its own set of trial DMs. The PRESTO based pipeline used subband dedispersion to reduce computational demand (Magro et al. 2011) and hence, could produce the full range of dedispersed time series files in a single node. The range of trial DMs was 0−1000 pc-cm^{-3} with a variable step size (see Section 4.1.2 for a discussion). In addition, PRESTO was used to perform acceleration search, which is useful for discovering binary pulsars. A single pulse search was also performed using the matched filtering technique as described by Cordes and McLaughlin (2003). At the end of the search analysis, all the results as well as diagnostic plots were copied into global result directories on the network mounted disks.

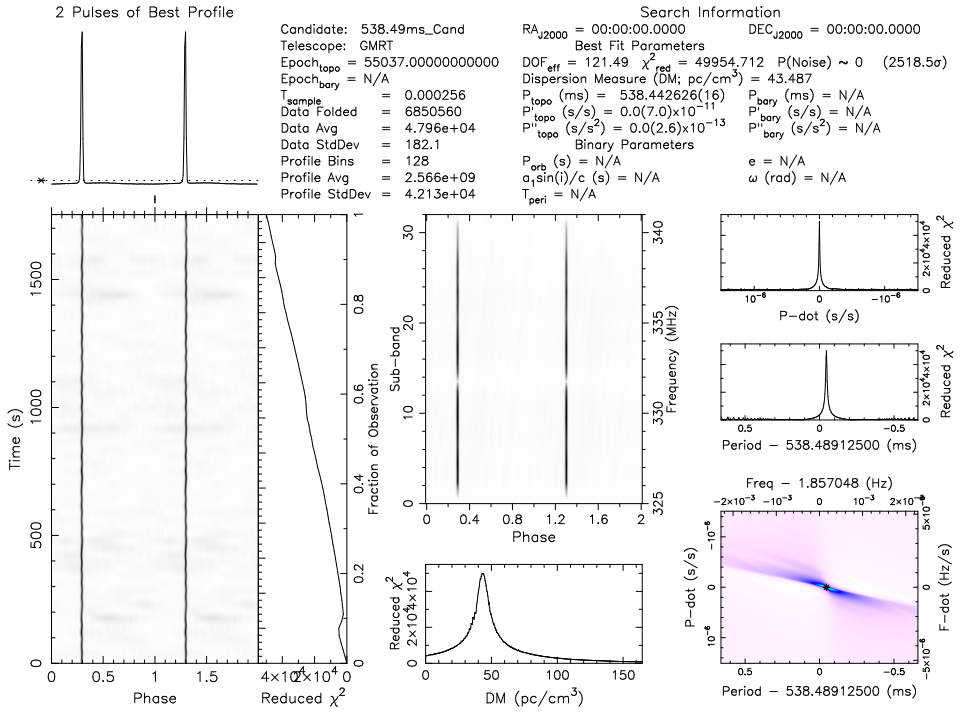

FIGURE 5.2: PRESTO plot showing the diagnostic plot for a strong candidate. The candidate was detected in the field GPT5102. The candidate happens to be a known pulsar PSR B2217+47, having a period of 538 ms and a DM of 43.5 pc-cm^{-3}.

[2]http://www.sigproc.sourceforge.net
[3]http://www.cv.nrao.edu/∼sransom/presto
[4]http://www.open-mpi.org

The overall survey sensitivity was calculated using the radiometer equation [c.f. Appendix 1, Section A1.4 in Lorimer and Kramer (2005)] assuming a system temperature of 190 K [receiver temperature of 66 K (Lal 2013) and sky background of 124 K (Haslam et al. 1982)], telescope gain (G) of 0.32 K/Jy for 25 GMRT antennae. In order to get a practical estimate, this number was multiplied by a degradation factor, which was given by the mean ratio of expected to observed profile S/N for known pulsars. The expected S/N were calculated using the above stated assumptions and the following equation (Lorimer and Kramer 2005)

$$S/N = \frac{S_{mean} G \sqrt{n_A n_p t_{obs} \triangle f}}{T_{sys}} \sqrt{\frac{P - W}{W}} \tag{5.1}$$

where S_{mean} is the pulse averaged flux density of the pulsar in mJy, G is the gain of the system in K/Jy, n_p is the number polarizations summed, n_A is number of antennae, t_{obs} is the integration time, $\triangle$f is the bandwidth in MHz, T_{sys} is the system temperature in K and P and W, both in s, are the period and pulse width at 10% of the peak. The mean flux densities of the known pulsars were scaled to the observing frequency using the available spectral indices from the pulsar catalog[5]. In cases where spectral index was not available, it was assumed to be −1.4 (Bates et al. 2013). The frequency scaled flux densities were further corrected for the beam response at 325 MHz. The pulse widths for detected pulsars were taken from their observed profiles, while the widths for undetected pulsars were scaled using the values given in the pulsar catalog. Whenever published pulse widths were not available, they were assumed to be 10% (including scatter-broadening and profile evolution) of the pulse period.

For the single pulse search, the sensitivity was determined by producing pulse energy streams in the ON and OFF pulse regions for known pulsars. In order to produce these, the dedispersed time series was folded modulo the pulsar period to produce a phase−time plot showing each pulse period. ON and OFF pulse widows of equal width were then manually chosen with the help of an interactive program (Joshi, private communication) to produce streams of pulse energies as

[5]http://www.atnf.csiro.au/people/pulsar/psrcat/

separate files. The observed single pulse S/N was calculated by taking a ratio of the mean of ON pulse energies to the RMS of the OFF pulse energies in an RFI-free region. The expected single pulse S/N was calculated using the radiometer equation with an integration time equal to the time corresponding to the width of the ON (or OFF) pulse widow. The ratio of the expected to observed S/N provided the degradation factor to be multiplied by the theoretical sensitivity to get a practical estimate. To get the degradation factor, only those pulsars were considered, wherein the observed S/N values were not very far from the expected values.

5.4 Results

The survey analysis resulted in the detection of 28 pulsars out of which, 2 were known MSPs and 1 was a new normal pulsar. The follow-up observations of this pulsar (PSR J1838+1523) and the results obtained are discussed in the next chapter. The observed profiles for all the pulsars detected in the survey are shown in Figures 5.3 to 5.6.

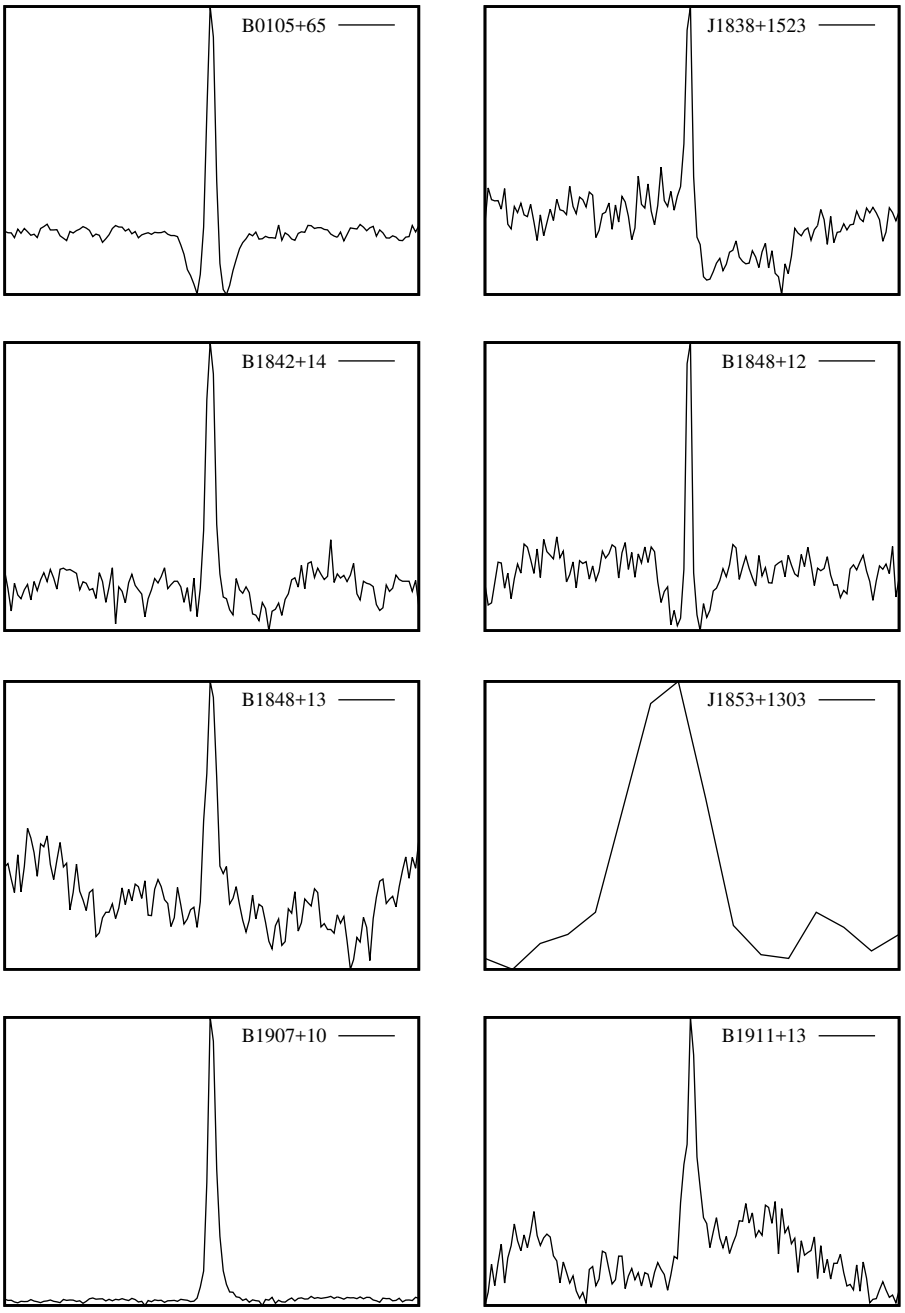

FIGURE 5.3: Integrated profiles for the pulsars detected in GMGPPTS.

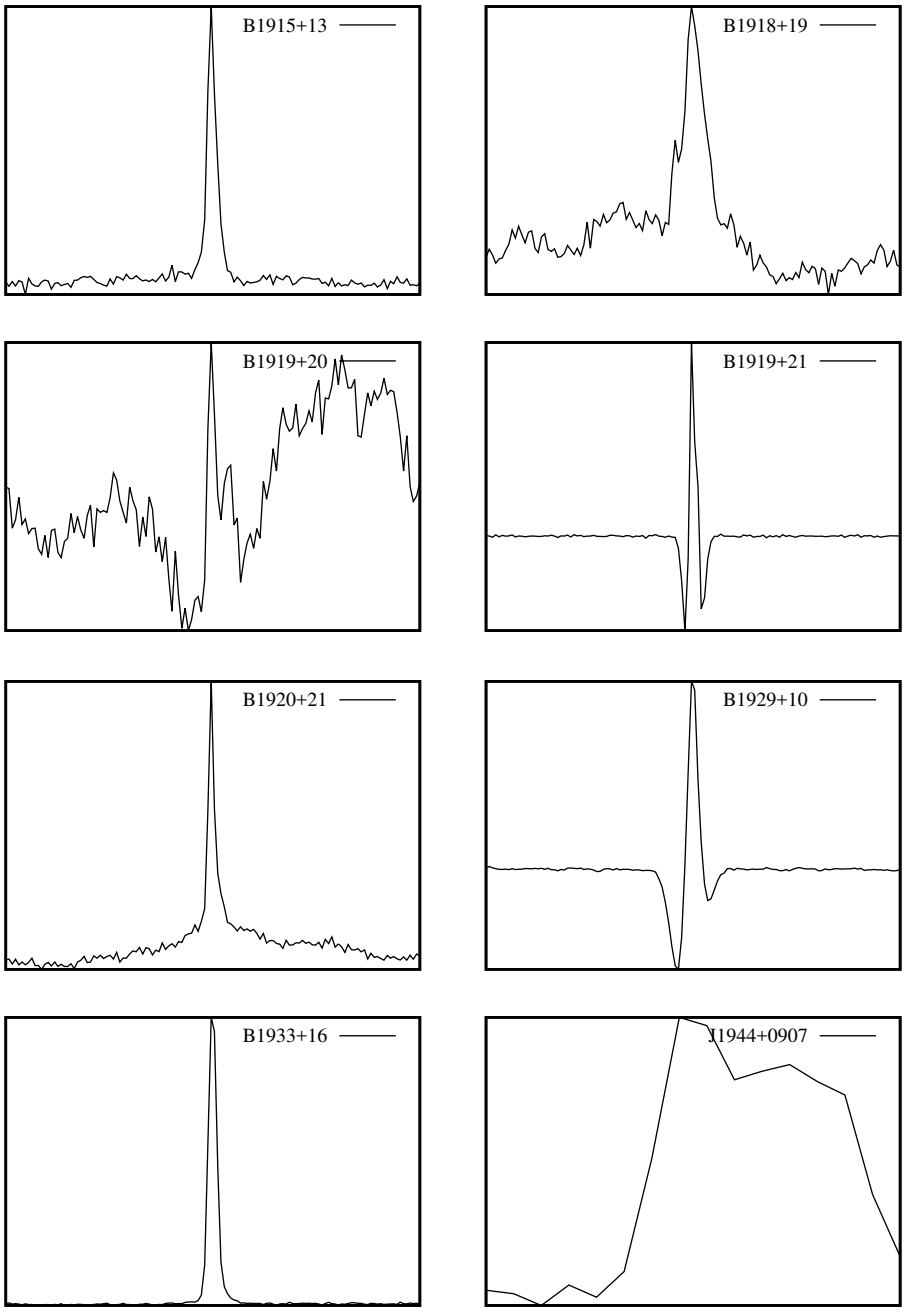

FIGURE 5.4: Integrated profiles for the pulsars detected in GMGPPTS.

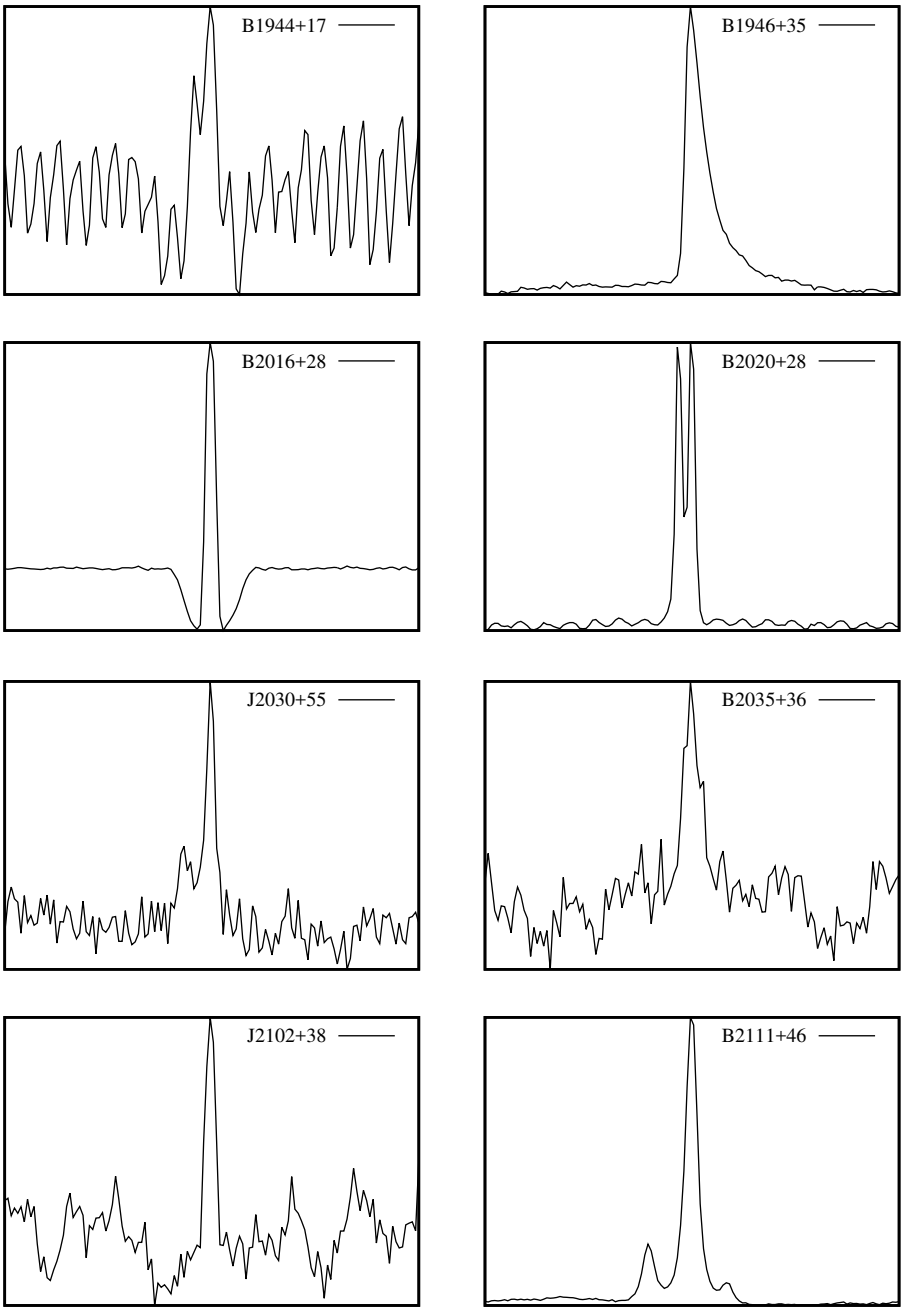

FIGURE 5.5: Integrated profiles for the pulsars detected in GMGPPTS.

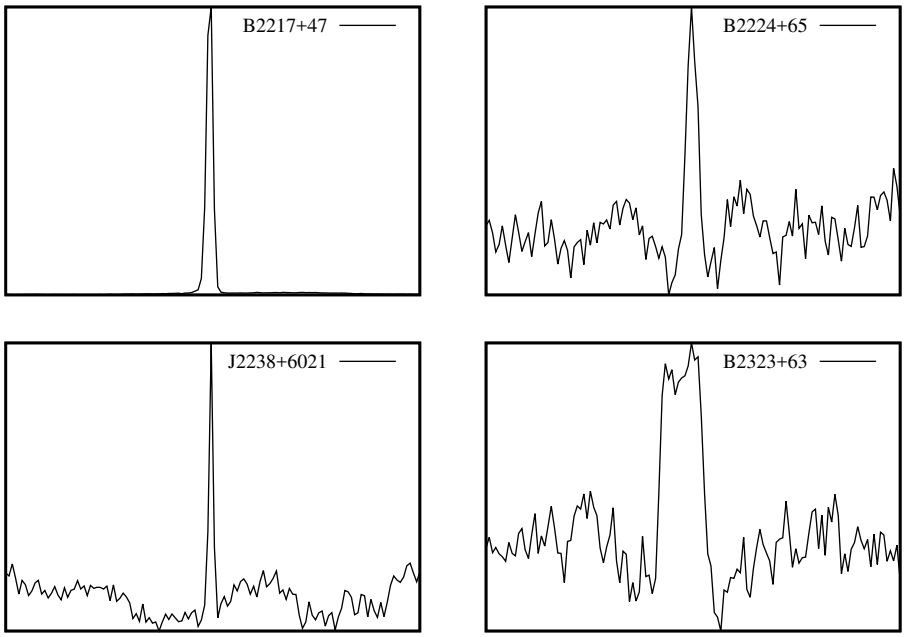

FIGURE 5.6: Integrated profiles for the pulsars detected in GMGPPTS.

The observed fields had 32 known pulsars, which could be detected in total. Table 5.1 lists the detected known pulsars with their parameters. The table also lists expected and observed profile S/N with appropriate remarks for non-detections. The expected theoretical sensitivity for an 8σ detection assuming a 10% pulse duty cycle was estimated to be 1.4 mJy. Excluding the pulsars, which showed either very low or very high observed S/N as compared to expected S/N (see Table 5.1 for more details), the mean degradation factor was found to be 1.9. Thus, the practical 8σ detection limit for a pulsar having 10% duty cycle was estimated to be 2.7 mJy. The detection limits for other duty cycles are plotted in Figure 5.7. The discovery of PSR J1838+1523 with a harmonic S/N of about 16, which has a mean flux density of 4.3 mJy at 325 MHz (see Chapter 6 for more details) provides a confirmation for this derived limit.

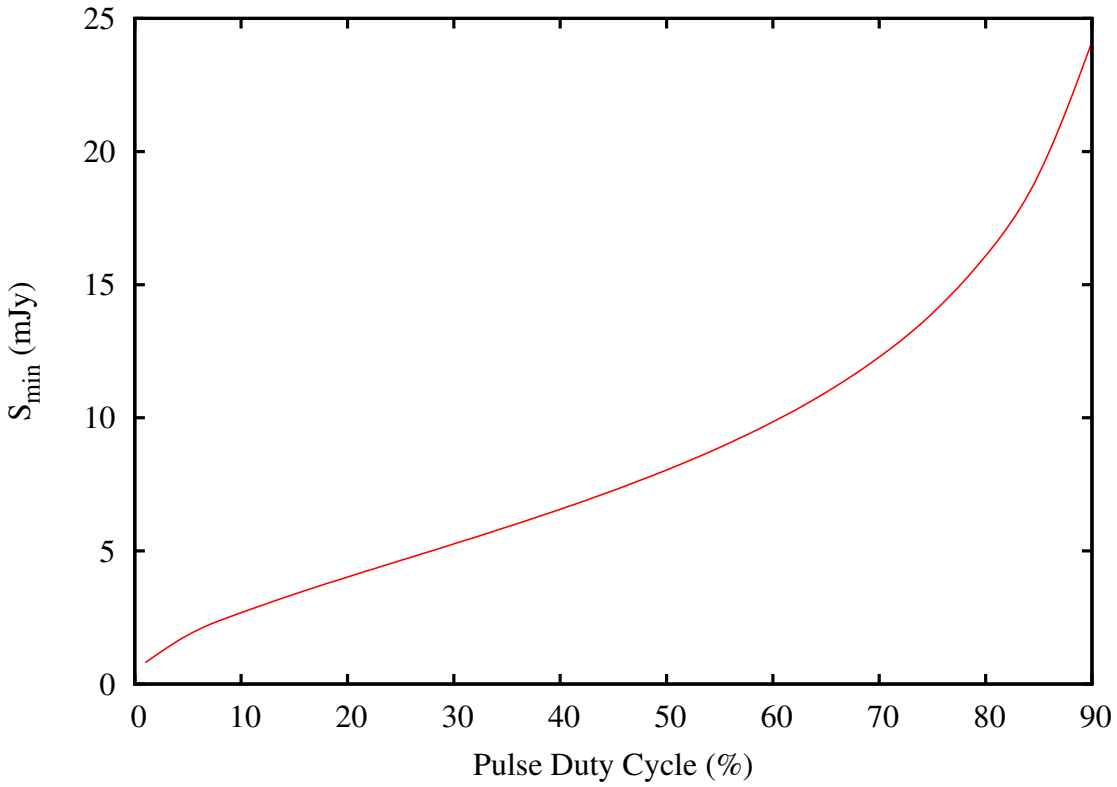

FIGURE 5.7: S_{min} as a function of the pulse duty cycle.

TABLE 5.1: Parameters for known pulsars in the region covered by GMGPPTS. The columns from left to right are, pulsar name, observed period, catalog period, observed DM, catalog DM, expected S/N, observed S/N, the distance of the pulsar from the field center, whether single pulses were detected and remarks for any discrepancies. The catalog period and DM as well as parameters for all un-detected pulsars were taken from the ATNF pulsar catalog (version 1.54).

Name	P_{obs} (ms)	P_{cat} (ms)	DM_{obs} pc-cm^{-3}	DM_{cat} pc-cm^{-3}	Expected S/N	Observed S/N	Distance (°)	Single Pulses Detected ?	Remarks
J0103+54	*	354.3	*	55.6	*	*	0.5	N	No flux measurements available
B0105+65	1283.7	1283.7	40.6	30.5	189	116	0.2	Y	Pulse distortion due to zero DM filtering
J0112+66	*	4301.2	*	112.0	98	*	0.2	N	Large position uncertainty
B1842+14	375.5	375.5	41.0	41.5	115	45	0.9	N	
B1848+12	1205.3	1205.3	71.6	70.6	110	25	0.6	N	Pulse distortion due to zero DM filtering
B1848+13	345.6	345.6	61.1	60.1	54	27	0.6	N	
J1853+1303	4.1	4.1	30.6	30.6	62	26	0.2	N	
B1907+10	283.6	283.6	150.4	150.0	724	422	0.5	Y	
B1907+12	*	1441.7	*	258.6	45	*	0.2	N	Scintillation time of 3000 s at 325 MHz
B1911+13	521.5	521.5	144.7	145.1	70	37	0.3	N	
B1915+13	194.6	194.6	94.7	94.5	222	159	0.9	N	
B1918+19	821.0	821.0	153.2	153.9	387	102	0.2	N	
B1919+20	380.3	760.7	97.4	101.0	31	15	0.3	N	
B1919+21	668.7	1337.3	8.2	12.4	1210	403	0.3	Y	Pulse distortion due to zero DM filtering
B1920+21	1078.0	1078.0	214.7	217.1	415	330	0.6	Y	
B1929+10	226.5	226.5	6.7	3.4	2635	578	0.7	Y	Pulse distortion due to zero DM filtering
B1933+16	358.7	358.7	158.6	158.5	2360	1376	0.6	Y	
J1944+0907	5.2	5.2	24.4	24.3	12	15	0.2	N	
B1944+17	440.6	440.6	17.3	16.2	446	14	0.2	N	Frequency close to 50 Hz harmonic
B1946+35	717.3	717.3	129.2	129.1	692	595	0.7	Y	
B2016+28	557.9	557.9	15.3	14.2	3066	672	0.7	Y	Pulse distortion due to zero DM filtering

Continued on next page

Table 5.1 – continued from previous page

Name	P_{obs} (ms)	P_{cat} (ms)	DM_{obs} pc-cm^{-3}	DM_{cat} pc-cm^{-3}	Expected S/N	Observed S/N	Distance (°)	Single Pulses Detected ?	Remarks
B2020+28	343.4	343.4	27.0	24.6	701	384	0.3	Y	
J2030+55	289.5	579.0	60.5	60.0	*	37	0.3	N	No flux measurements available
B2035+36	618.7	618.7	91.7	93.6	81	34	0.7	N	
J2102+38	1190.0	1189.9	85.7	85.0	*	26	0.4	N	No flux measurements available
B2111+46	1014.6	1014.7	144.2	141.3	609	893	0.3	Y	
J2137+64	*	1750.9	*	106.0	35	*	0.5	N	Large position uncertainty
B2217+47	538.4	538.5	46.4	43.5	1030	2446	0.2	Y	
B2224+65	682.5	682.5	38.0	36.1	478	26	0.4	N	Large amount of RFI
J2229+64	*	1893.1	*	194.0	21	*	0.4	N	Large position uncertainty
J2238+6021	1023.4	3070.2	185.7	182.0	2517	42	0.2	Y	Large position uncertainty
B2323+63	1436.2	1436.3	199.7	197.4	190	41	0.6	Y	Pulse distortion due to zero DM filtering

Single pulses were detected from 13 strong pulsars. Table 5.2 lists the single pulse properties of these pulsars. The diagnostic plot for PSR B2111+46 is shown in Figure 5.8. The indications of the presence of a true pulsar are marked by arrows in the figure.

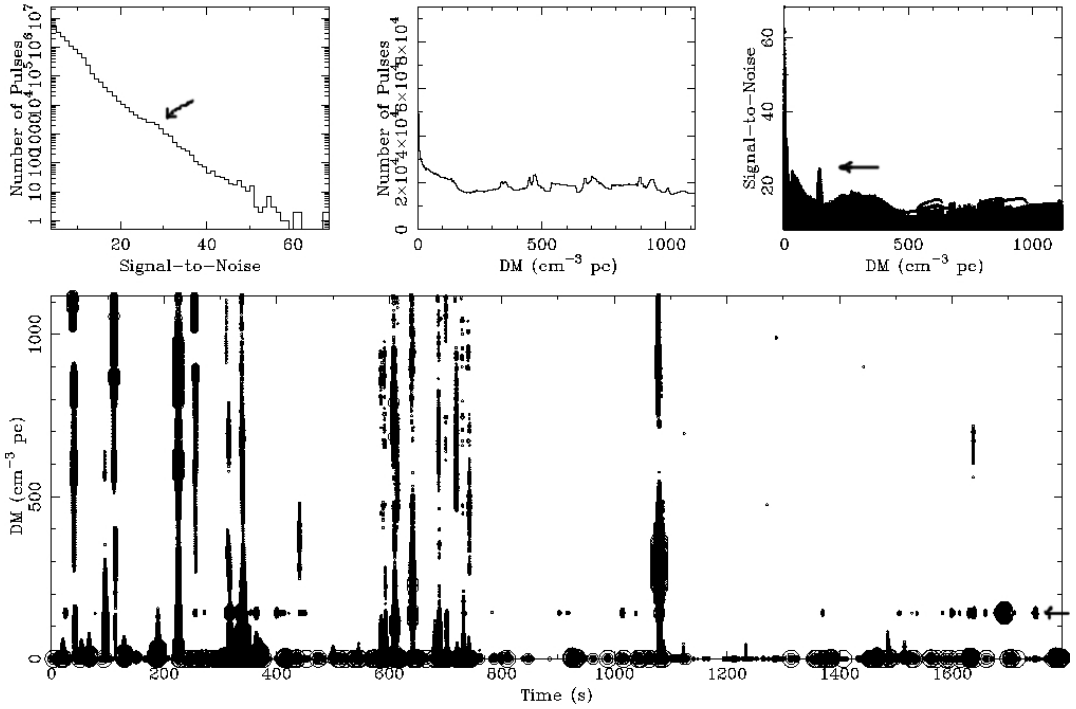

FIGURE 5.8: Single pulse search plot for the field GPT4208. This particular plot shows single pulses from a known pulsar PSR B2111+46, which has a DM of 141.26 pc-cm^{-3} (marked by an arrow on the right in the bottom plot). The bottom plot also shows a lot of vertical stripes, which are caused by broad band RFI.

The expected 8σ minimum detectable flux density for single pulse search (assuming a pulse width of 10 ms) was estimated to be 1.8 Jy, while the mean observed degradation factor was found to be 1.3. This implied a corrected value of 2.3 Jy or a fluence of 23 mJy-s.

5.5 Discussion

The simulated survey analysis using PSRPOP[6] with the post-analysis parameters indicates a detection of an average of 96 (actual numbers were between 91 and 101

[6]http://www.psrpop.phys.wvu.edu/index.php

Name	Expected Single pulse S/N	Observed Single pulse S/N	Largest Detected Single pulse S/N
B0105+65	0.7	2.6	18.2
B1907+10	1.4	3.3	10.6
B1919+21	3.8	9.6	25.1
B1920+21	1.4	3.7	12.6
B1929+10	4.6	3.6	17.0
B1933+16	4.7	3.5	9.2
B1946+35	3.2	2.3	12.9
B2016+28	8.3	3.4	13.1
B2020+28	1.8	2.3	19.7
B2111+46	2.8	4.6	36.8
B2217+47	2.3	11.5	39.4
J2238+6021	10.9	1.0	10.9
B2323+63	1.5	0.3	8.0

Table 5.2: Single pulse S/N for known pulsars detected in GMGPPTS. The S/N for the strongest detected single pulse is also shown.

for multiple simulations) normal pulsars and a maximum of 5 (actual numbers were between 0 and 5) MSPs (known plus new) for the full survey region. This region contains 72 normal pulsars and 3 MSPs that are already known. As can be seen in Figure 5.1, we could only cover 10% survey region, finally resulting in a very patchy sky coverage. We tried to obtain the detection rates for strips of 10% area along the Galactic latitude and longitude. This resulted in the detection of an average of 9 (actual numbers between 4 and 15) normal pulsars and a maximum of 2 (actual numbers between 0 and 2) MSPs. Even with the patchy coverage, the detection of 28 pulsars including 2 MSPs and the discovery of 1 new pulsar is encouraging. This indicates that the observed detection rate of normal pulsars is much higher than that predicted by population models, which were used in the simulations. It is clear from the number of known pulsars in the full survey region that almost half the known pulsars (30 normal pulsars and 2 MSPs) are contained in the region which we observed. This distinctly non-uniform survey coverage in terms of the distribution of known normal pulsars in this region may be responsible for the higher inferred detection rate. Another fact to be noted is that although the data were acquired over 32 MHz, the analysis was done only on data taken with one side-band, thus making the effective bandwidth 16 MHz. This was unavoidable because

the data files for the two sub-bands were written separately and combining these two to recover the full bandwidth was not possible as both the sub-bands were processed independently in the data acquisition system. Broad band RFI played a very important part in the survey analysis. The raw analysis without implementing zero DM filtering resulted in the detection of only 10 pulsars in harmonic search and 4 in single pulse search. After zero DM filtering, the degradation factor for harmonic search changed from about 2.5 to 1.9 accompanied with the detection of 18 more pulsars including 1 discovery, while the change for single pulse search was from 2.5 to 1.3 with the detection of 9 more pulsars. One example of how the removal of broad band RFI changes the detection threshold is shown in Figures 5.9 and 5.10. Although broad band RFI at low radio frequencies can not be completely removed by zero DM filtering, these figures demonstrate the need for doing good RFI mitigation for low frequency pulsar surveys.

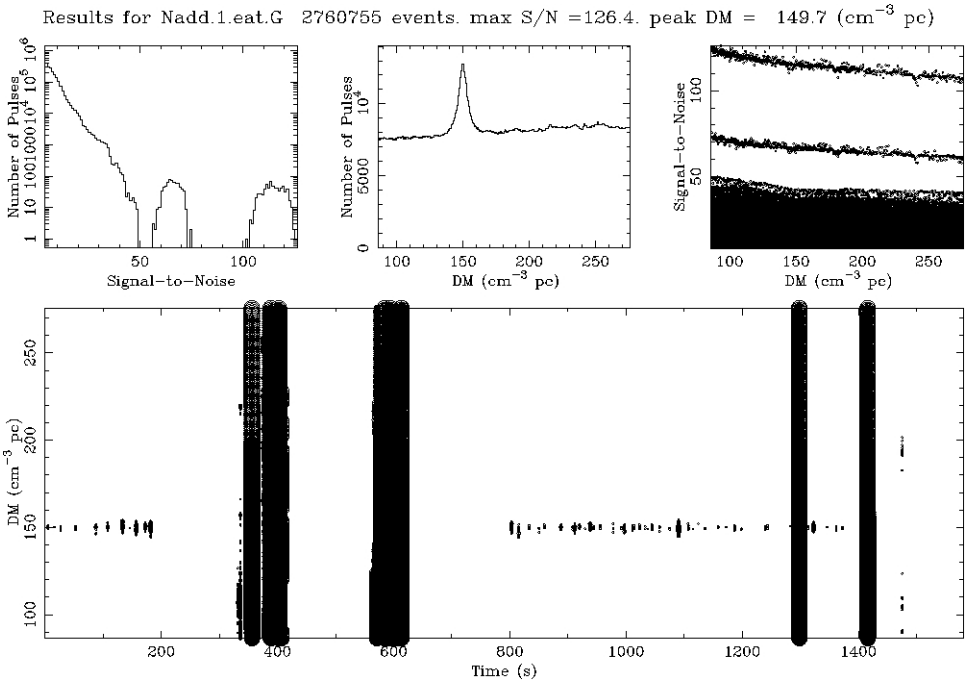

FIGURE 5.9: Single pulse diagnostic plot with broad band RFI. This field contained PSR B1907+10, which has a DM of 150 pc-cm^{-3}.

The GMGPPTS data were acquired with the old hardware back-end. The pulsar back-end, which is currently operational at GMRT, provides an instantaneous bandwidth of 33 MHz in a single side-band. With an improved system, future low frequency pulsar surveys with the GMRT would turn out to be much more

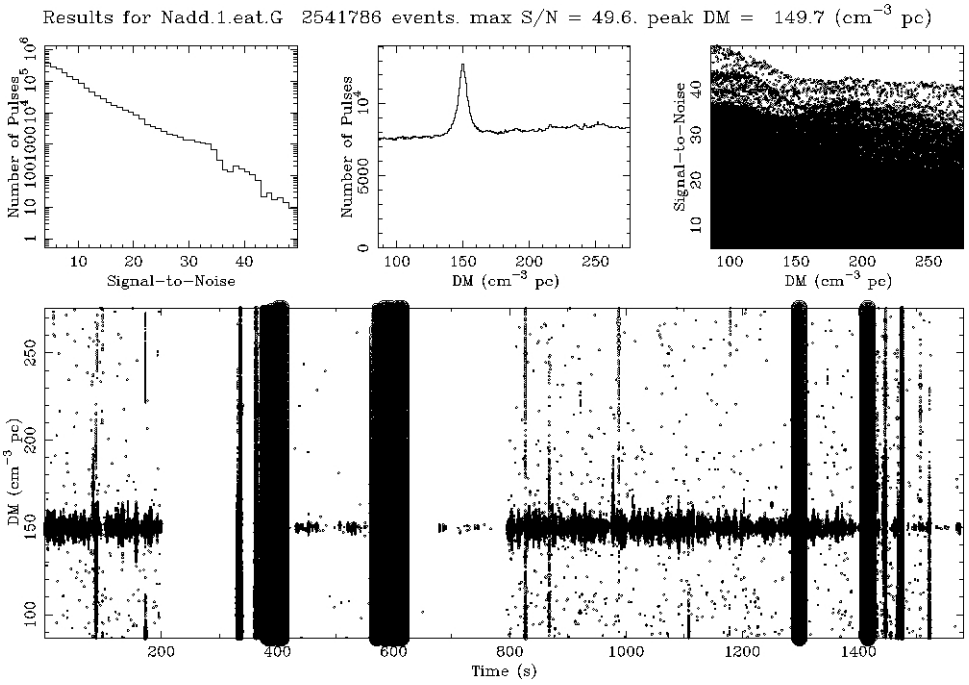

FIGURE 5.10: Single pulse diagnostic plot after broad band RFI mitigation. This field contained PSR B1907+10, which has a DM of 150 pc-cm^{-3}.

promising in terms of discovering pulsars and transients. The simultaneous imaging capability of the GMRT would augment the transient search by providing quick localization from the snapshot images of the survey region. In all, large area surveys combining imaging and time series data would prove to be highly efficient and successful.

Chapter 6

Discovery, Timing and Imaging of PSR J1838+1523

6.1 Introduction

Pulsars show a lot of temporal variation in their radio emission. This ranges from a few periods (nulling) to a few days (mode changes) to a few months (intermittency). Apart from these, there are also examples of neutron stars having temporal variations in between like the RRATs showing a few bursts within a few hours (McLaughlin et al. 2006) and SGRs showing radio emission during outbursts (see Chapter 10 for more details). Apart from these ON/OFF type of variations, the flux density of the pulsars can also vary due to the influence of the ISM. It typically manifests itself as either diffractive or refractive scintillations. Diffractive scintillations have time scales of a few seconds to a few minutes, while refractive scintillations may have time scales of a few days to a few months. Studying the different time scales reveals the physics behind different aspects of the pulsar's radio emission and helps in the understanding of how neutron stars emit electromagnetic radiation in various frequency ranges.

Although, the pulsed emission from pulsars is extensively studied, imaging studies are seldom carried out on pulsars because, no coherent, continuum emission is

expected to be observed in the OFF-pulse region. This perception changed when Basu et al. (2011) detected continuum, coherent radio emission in the OFF-pulse region of two pulsars, PSR B0525+21 and PSR B2045−16. They used a technique called gated imaging on simultaneous imaging data obtained using the GMRT. Another, indirect evidence of continuum, coherent radio emission was provided by PSR J2018+4232 (Navarro et al. 1995) for which, the continuum flux density was twice as much as the pulsed flux density. In this chapter, we describe the discovery and results of the multi-frequency radio follow-up studies performed on PSR J1838+1523, including imaging observations.

6.2 Discovery

PSR J1838+1523 was discovered in a blind survey along the Galactic plane conducted using the GMRT. The GMGPPTS (see Chapter 5 for more details) covered 10% of the region between Galactic longitude $45° < l < 135°$ and Galactic latitude $1° < |b| < 10°$. It was carried out at 325 MHz with a bandwidth of 16 MHz, divided into 256 filterbank channels. The observations were carried out using the IA mode of the GMRT. The data were written to magnetic tapes, which were later extracted to network storage disks of a high performance computing cluster having 64 dual core nodes. In the analysis done as described in detail in Section 4.1, PSR J1838+1523 emerged as a strong candidate (Figure 6.1). The survey observations were performed on 26 July 2009. After the discovery, a proposal was written for confirmation (DDTB003). The observation for confirming the pulsar were performed on 30 May 2010. The analysis of these observations and cross-matching with the pulsar catalog[1] confirmed this as a new pulsar.

[1]http://www.atnf.csiro.au/people/pulsar/psrcat

6.3 Initial Follow-up at GMRT

A newly discovered pulsar has to be observed regularly in order to construct a good timing model, which in turn, provides the estimates of many important parameters of the pulsar. The most important parameters are the spin period (P) of the pulsar and its time derivative ($\dot{\mathrm{P}}$). All the known pulsars are usually represented as a population by means of a P$-\dot{\mathrm{P}}$ diagram as the one shown in Figure 1.5. Apart from putting the new discovery in its proper place in the pulsar population, the measurement of P and $\dot{\mathrm{P}}$ allows determining other pulsar parameters like the characteristic age, surface magnetic field strength and spin-down luminosity. These are very important in understanding the properties of the pulsar magnetosphere, which is the origin of the electromagnetic emission from the pulsar.

As the survey observations were done using the IA mode, which has a beam width of about 1°, the position of this pulsar had a similar uncertainty. In order to reduce this uncertainty, a proposal was put right after its confirmation as a new pulsar (DDTB023). The procedure followed for reducing the position uncertainty involves observing six more nearby fields separated by half the beam width to form a compact hexagonal grid of pointings. Each of these pointings was observed with the exact same observational parameters as the search observations. The position refinement was obtained by using the S/N obtained for each pointing. This gridding procedure is explained in more detail in Joshi et al. (2009). This proposal also involved closely spaced timing observations, which would provide a good initial estimate of the barycentric period of the pulsar. With a better position constraint obtained from the gridding observations, these observations could help in constraining the timing solution over a period of one year.

The initial follow-up observations were done with the GMRT at 325 MHz. These spanned between MJD 55604−56745 with a cadence of roughly 2 weeks. They used the GMRT in simultaneous imaging and pulsar mode. These observations are described in detail in Section 3.3.1. The first set of gridding observations helped in constraining the pulsar position to within 0.5°. Four observing epochs, spaced

by one day each, followed this epoch. It is during this period that the first non-detection was encountered. In fact, the pulsar was detected on only one epoch out of the four. This meant that the timing solution could not be constrained with a large position uncertainty. This was followed by a series of non-detections between MJD 55802−56091. This was followed by a random sequence of non-detections over phases lasting 1−2 months (GMRT proposal ID numbers 21_054, 22_069, 23_063 & 24_028).

6.4 Further follow-up at GMRT and ORT

After a month long series of non-detections, PSR J1838+1523 was detected again on 27 December 2013 with the GMRT (25_043). This was followed-up by a gridding observation at the ORT with the grid points separated by 6' in declination and centred over the then best known position of the pulsar. In all, 15 separate points were observed. The pulsar was detected in three adjacent pointings and by using the S/N obtained, the pulsar position in declination was constrained to within $4'$. This meant that the ORT could be used for doing timing observations. These observations started from MJD 56657 (31 December 2013) with almost daily cadence and continued for almost two years. After this, the timing observations were continuing at the time of writing the thesis with a cadence of one week. These observations are described in more detail in Section 3.3.2. Using the refined position thus obtained, ORT TOAs obtained over a six month period were sufficient in obtaining a phase connected timing solution. The pulsar position thus obtained, was verified using one observing session at 820 MHz with the Green Bank Telescope (GBT) by our collaborator. This session was carried out on 11 September 2014 using the search mode with a bandwidth of 200 MHz and a sampling time of 82 μs. The data were recorded for 1800 s with the Green Bank Ultimate Pulsar Processing Instrument (GUPPI; DuPlain et al. 2008). The beam of the GBT has a diameter of $\sim 12'$ at 820 MHz. Thus, the detection with the GBT confirmed the pulsar position obtained from the ORT timing data. Once the pulsar position was identified correctly, we proposed to observe the pulsar at 1

GHz and 610 MHz with the GMRT, with simultaneous ORT observations at 325 MHz, in order to determine the spectral index of the pulsar (27_008). This project had total 5 observing sessions out of which, 2 were done at 1 GHz and 3 were done at 610 MHz at the GMRT. All further GMRT follow-up observations were carried out at 610 MHz in simultaneous PA and imaging mode with a cadence of about a month.

Given the closeness to detection limit and the flux density variation seen in this pulsar (see Table 6.1 and Figure 6.9), the first possible reason of non-detections could be DISS. From the NE2001 model (Cordes and Lazio 2002), the predicted scintillation bandwidth and time for this line of sight were 0.24 MHz and 232 s, respectively at 325 MHz. The typical observations were done with a bandwidth of 33 MHz with integration times of 1800 s. Thus, the only reason for getting non-detections was if the actual scintillation time scale was larger than the predicted time scale. In order to check this, dynamic spectra were obtained from the GBT observation. Another observation was performed at the ORT on 4 June 2015. The pulsar was observed continuously for 5 hours over a bandwidth of 16 MHz, spread over 1024 channels with a sampling time of 512 μs. This was done to achieve maximum frequency and time resolution of the dynamic spectra.

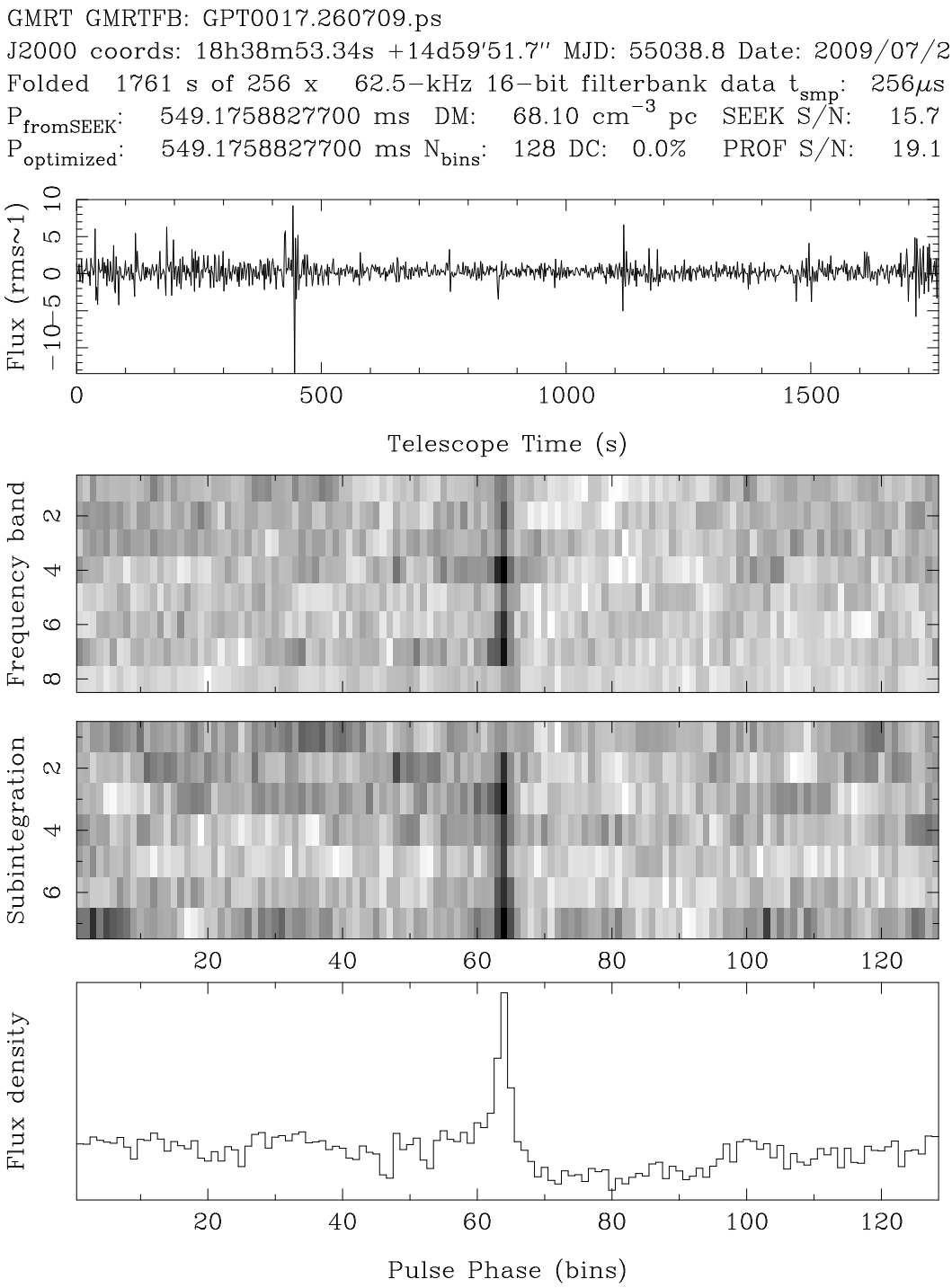

FIGURE 6.1: Discovery plot for PSR J1838+1523. The header text gives miscellaneous information about the observational parameters. Panels from top to bottom: First panel shows dedispersed, zero mean time series. Second panel shows grey scale plot of folded profile in 8 frequency sub-bands. Third panel shows grey scale plot of folded profile in 8 time sub-integrations. Fourth panel shows the centred, folded profile for the full bandwidth and observing time.

TABLE 6.1: The follow-up observations of PSR J1838+1523 with the flux densities measured from imaging (S_{im}) and time series (S_{ts}) observations with uncertainties. The remarks indicate about possible reasons for any discrepancies. The observations at 326 MHz were carried out with the ORT and the rest were carried out with the GMRT. All GMRT observations from MJD 56955 were done in PA mode and the rest were done in IA mode. Each GMRT observation had simultaneous imaging mode data.

Proposal ID	Observation Date (MJD)	Centre Frequency (MHz)	S_{im} (mJy)	σ_{im} (mJy)	S_{ts} (mJy)	σ_{ts} (mJy)	Remarks
ddtB023	55744.8	323	-	-	5.0	0.6	No Calibrator
ddtB023	55770.6	323	6.5	1.4	4.4	0.3	-
ddtB023	55774.5	323	-	-	8.2	0.4	No Calibrator
ddtB023	55789.5	323	4.9	1.5	3.0	0.3	-
ddtB023	55791.5	323	5.3	1.3	6.6	0.2	-
ddtB023	55796.7	323	4.3	0.9	2.6	0.2	-
ddtB023	55800.5	323	-	-	-	-	RFI
ddtB023	55801.5	323	4.3	1.8	-	-	-
ddtB023	55802.5	323	10.0	2.6	2.2	0.4	-
ddtB023	55803.5	323	3.3	1.0	-	-	-
21_054	55852.5	323	-	-	-	-	No Calibrator
21_054	55870.5	323	-	-	-	-	No Calibrator
21_054	55886.5	323	-	-	-	-	RFI in Phase Calibrator Data

Continued on next page

Table 6.1 – continued from previous page

Proposal ID	Observation Date (MJD)	Centre Frequency (MHz)	S_{im} (mJy)	σ_{im} (mJy)	S_{ts} (mJy)	σ_{ts} (mJy)	Remarks
21_054	55897.4	323	2.9	1.3	1.3	0.2	-
21_054	55911.5	323	-	-	1.5	0.2	Map RMS 1.2 mJy
21_054	55939.4	323	5.8	1.5	2.5	0.2	-
21_054	55960.3	323	5.3	1.6	-	-	-
21_054	55976.3	323	2.3	1.7	0.8	0.2	-
21_054	55997.2	323	3.5	0.8	1.0	0.2	-
22_069	56041.1	323	-	-	-	-	No Imaging Data
22_069	56051.1	323	4.6	1.6	-	-	-
22_069	56068.0	323	4.4	0.9	2.4	0.2	-
22_069	56081.0	323	6.2	1.7	1.5	0.3	-
22_069	56090.9	323	4.4	1.6	3.2	1.1	-
22_069	56108.7	323	-	-	3.7	0.8	RFI in Phase Calibrator Data
22_069	56118.1	323	-	-	3.8	0.3	Map RMS 3 mJy
22_069	56137.8	323	5.8	1.4	-	-	
22_069	56152.8	323	-	-	3.8	1.1	Map RMS 1.8 mJy
22_069	56172.8	323	4.4	1.9	-	-	-

Continued on next page

Table 6.1 – continued from previous page

Proposal ID	Observation Date (MJD)	Centre Frequency (MHz)	S_{im} (mJy)	σ_{im} (mJy)	S_{ts} (mJy)	σ_{ts} (mJy)	Remarks
23_063	56225.6	323	-	-	2.6	0.6	RFI in Phase Calibrator Data
23_063	56248.3	323	6.1	3.6	3.7	0.8	-
23_063	56262.5	323	5.2	1.3	8.2	1.3	-
23_063	56276.3	323	-	-	9.7	0.9	Map RMS 2 mJy
23_063	56298.5	323	3.8	1.4	2.5	0.3	-
23_063	56319.3	323	4.5	1.4	3.2	0.9	-
23_063	56339.3	323	-	-	0.7	0.2	Map RMS 1.4 mJy
23_063	56354.2	323	2.9	1.3	-	-	-
23_063	56367.2	323	6.4	2.8	1.0	0.2	-
23_063	56381.2	323	-	-	-	-	Imaging Non-detection
24_028	56401.1	323	3.2	1.1	1.0	0.2	-
24_028	56420.0	323	-	-	3.9	0.8	Map RMS 1.6 mJy
24_028	56441.0	323	-	-	8.7	0.8	Inconsistent fluxes
24_028	56464.0	323	-	-	8.1	1.0	Inconsistent fluxes
24_028	56489.9	323	3.5	1.2	0.8	0.2	-
24_028	56503.9	323	2.8	1.5	-	-	

Continued on next page

Table 6.1 – continued from previous page

Proposal ID	Observation Date (MJD)	Centre Frequency (MHz)	S_{im} (mJy)	σ_{im} (mJy)	S_{ts} (mJy)	σ_{ts} (mJy)	Remarks
24_028	56535.7	323	2.6	1.5	0.8	0.2	-
25_043	56550.7	323	-	-	-	-	Non-detection
25_043	56653.5	323	-	-	1.6	0.2	Map RMS 1.5 mJy
NA	56657−[a]	326.5	-	-	4.2	1.6	No Imaging Data
25_043	56663.1	323	3.6	1.1	4.8	0.9	-
25_043	56689.4	323	7.1	2.2	3.7	0.3	-
25_043	56704.3	323	7.4	2.6	4.6	0.4	-
25_043	56745.2	323	5.6	3.1	4.2	0.4	-
27_008	56955.6	608	-	-	-	-	Imaging Non-detection
27_008	56982.6	1168	-	-	-	-	Imaging Non-detection
ddtB055	57004.5	323	6.8	2.0	8.1	0.5	-
27_008	57012.5	608	1.5	0.7	1.0	0.2	-
27_008	57046.4	1168	-	-	-	-	Imaging Non-detection
27_008	57104.1	608	1.4	0.5	1.0	0.2	-
28_024	57140.0	608	1.3	0.6	0.9	0.2	-
28_023	57143.8	608	1.7	0.7	1.3	0.4	-

Continued on next page

Table 6.1 – continued from previous page

Proposal ID	Observation Date (MJD)	Centre Frequency (MHz)	S_{im} (mJy)	σ_{im} (mJy)	S_{ts} (mJy)	σ_{ts} (mJy)	Remarks
28_024	57156.9	608	1.2	0.5	0.8	0.2	-
28_024	57177.9	608	-	-	-	-	Imaging Non-detection
28_024	57198.9	608	-	-	-	-	Imaging Non-detection
28_024	57226.8	608	1.4	0.6	1.1	0.2	-
28_024	57255.7	608	-	-	-	-	Imaging Non-detection
28_024	57282.6	608	-	-	-	-	Imaging Non-detection

[a] The ORT observations are continuing till date.

6.5 Data Analysis

The data acquired for this project were of three different varieties. They were blind search, timing and imaging. Each of these had their own specific method of analysis. The blind search data were analysed by using the HPC analysis pipeline as described in detail in Section 4.1. The timing analyses were carried out using the pulsar timing package TEMPO2 (Hobbs et al. 2006). The details of timing analysis are given in Section 4.3. During the first series of non-detections, we also performed a local search for period (548−550 ms) and DM (50−80 pc-cm^{-3}), just to be sure that the non-detections were not due to slightly wrong pulsar parameters given by the search pipeline. After the full timing solution was obtained from the timing analysis of the ORT data, the time series data for all non-detections were folded using the period predicted using the timing solution. This resulted in 15 out of 30 non-detections at 325 MHz turning out to be weak detections. The average pulse profiles at different frequencies are shown in Figure 6.2. Figure 6.3 shows the comparison between the ON profile generated by coherently adding the profiles for all detections and the OFF profile generated by coherently adding the profiles for 9 out of the 15 non-detections at 325 MHz. The other profiles for non-detections were omitted because of presence of RFI. The profiles shown in Figure 6.2 were used as templates to generate the TOAs for the timing analysis. The template matching technique may underestimate TOA uncertainties at times. In order to compensate for this, the TOA uncertainties were multiplied by EFAC values (see Section 7.3.2 for more details). These were obtained for each telescope and frequency separately so as to obtain a reduced χ^2 value for timing residuals between 0.9−1.1. The EFAC values obtained for GMRT TOAs were 2.5 and 5.3 at 325 and 610 MHz, respectively. The value for the GBT TOAs was found to be 1.6, while that for ORT TOAs was found to be 2.7. In addition, constant phase offsets were also fit for different telescopes and frequencies. The method of estimation of these values and the results obtained are reported in Chapter 7. Due to the degeneracy between instrumental offsets and offsets due to DM delay, the systematic DM error was determined from the error in the estimates of different

offsets (see Section 7.3.2 for more details).

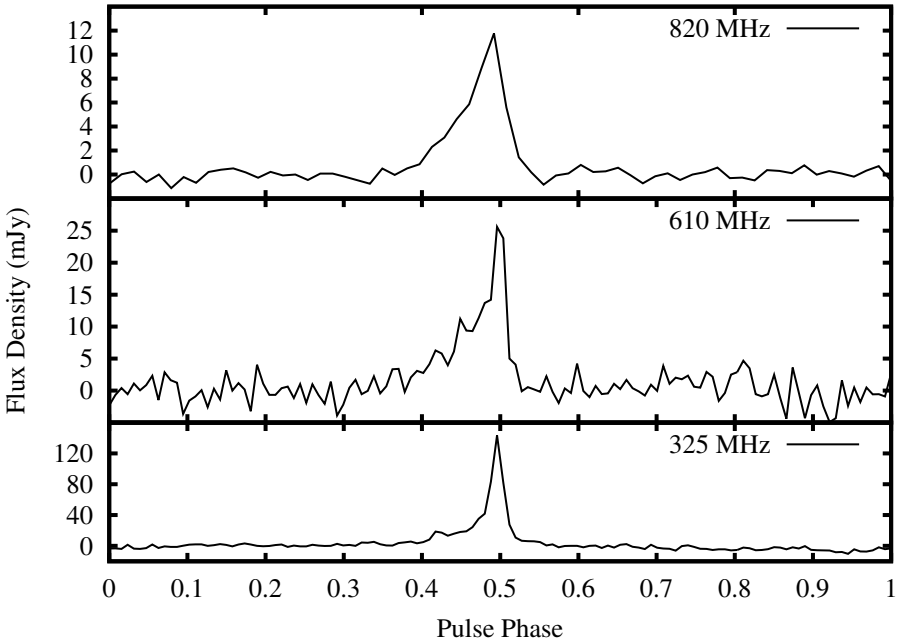

FIGURE 6.2: Average profiles of PSR J1838+1523 at different frequencies. The profiles at 325 and 610 MHz were scaled using actual measurements, while the 820 MHz GBT profile was scaled using extrapolated flux density assuming a spectral index of −2. The resolution of the GBT profile is also coarser than the other two profiles (64 bins against 128 bins).

The imaging data were flagged and calibrated using FLAGCAL (Chengalur 2013) and images were then generated using standard imaging procedure using AIPS, which included at least three rounds of phase self-calibration. The imaging analysis is described in detail in Section 4.4. In order to establish the change in the emission level of the pulsar, the time series data had to be calibrated and the mean flux density of the pulsar measured. The time series data at both ORT and GMRT, were calibrated by using ON and OFF scans on the flux density calibrators. The OFF source position used for the GMRT was +5° in DEC from the calibrator source. At ORT, the OFF source position was offset in RA towards East by 4.5−14°. The actual OFF source position was dependent on the calibrator source. The procedure followed for calibration was as follows:

1. Produce a 0 DM time series from the ON and OFF calibrator scans.

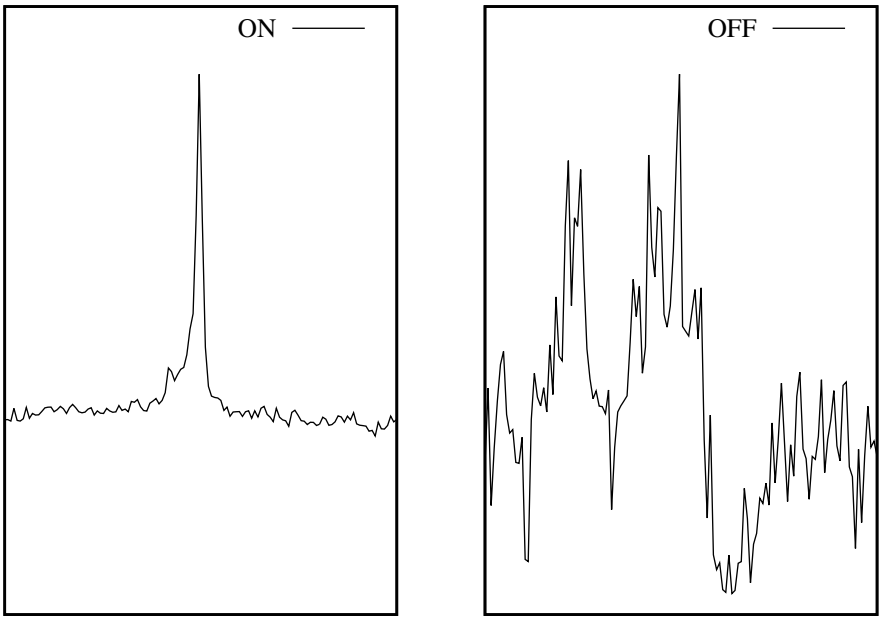

FIGURE 6.3: Average ON and OFF profiles of PSR J1838+1523 at 325 MHz. The OFF profile is an overage profile obtained from epochs when pulsed emission was not detected. The profiles were scaled just for comparison and the RMS in ON profile is 0.12 as compared to 0.31 in the OFF profile.

2. Fold both time series modulo the pulsar period to produce the ON and OFF calibrator profiles.

3. Obtain the ON−OFF value in counts, from the profiles.

4. Equate this to the flux density of the source, to get the scaling factor in Jy/counts.

5. Subtract OFF pulse mean from the pulsar profile and multiply by the scaling factor. The profile is now calibrated to Jy.

6. Add all the points in the pulse above 10% of the peak or 3 times the RMS level (whichever is higher) and divide by the total number of bins across the profile to get the mean flux density of the pulsed emission. This is equivalent to the flux density calculated from the continuum image.

After the images were obtained, continuum flux density measurements were made using the AIPS task JMFIT. A single elliptical Gaussian was used as a starting

model to fit the observed source. The major and minor axes of the post-fit position error ellipse obtained for all of the images, were comparable to the respective synthesized beam sizes. Thus, the continuum source, which was identified as the pulsar, is an unresolved (point) source and possesses no structure > 10" in size. The flux densities thus obtained are listed in Table 6.1. In order to make sure that there was no error in calibration due to very long duration gain variations, flux densities of 29 other unresolved continuum sources were also measured in each of the image. The data set created by these measurements is described in more detail in Chapter 8.

In order to generate dynamic spectra, the data were folded modulo the pulsar period by adding upto 100 pulses for each frequency channel separately. The ON pulse region was then identified and marked so as to include only the emission from the pulsar. Later on, the frequency channels were collapsed to obtain good S/N ratio and dynamic spectra were generated.

6.6 Results

The discovery plot for PSR J1838+1523 is shown in Figure 6.1, while the plot showing the confirmation detection is shown in Figure 6.4. The initial position of the pulsar was taken as the beam center of the pointing (RA: 18 h 38 m 53.34 s, DEC: +14° 59' 51.7"). After the first round of gridding observations, this was refined to RA: 18 h 40 m 15.59 s, DEC: +15° 11' 44". After the initial timing analysis, this was refined further to RA: 18 h 39 m 06.65 s, DEC: +15° 06' 58.97". The gridding observations at the ORT were useful in reducing the declination error and the refined position stood at RA: 18 h 39 m 06.65 s, DEC: +15° 21' 44". This estimate was very close to the actual position of the pulsar as was proven by the detection at the GBT. The full, coherent timing solution obtained after adding all the available TOAs at different radio frequencies is shown in Table 6.2. This solution contains TOAs from GMRT (325 and 610 MHz), ORT (326 MHz) and

GBT (820 MHz). The post-fit timing residuals thus obtained are shown in Figure 6.5.

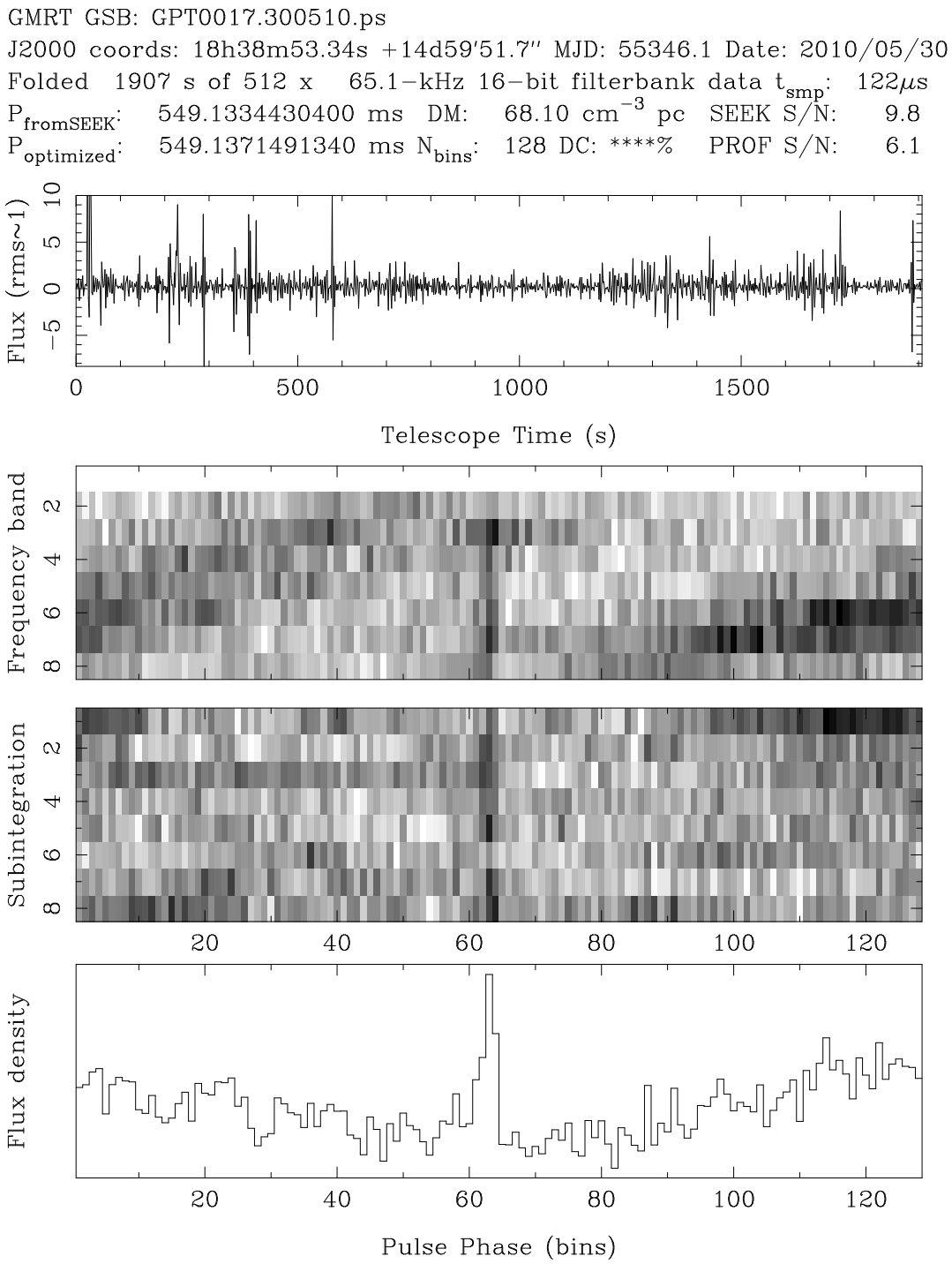

FIGURE 6.4: Confirmation plot for PSR J1838+1523. The panels are similar to the ones in Figure 6.1.

The radio maps made at 325 (Figure 6.6) and 610 MHz (Figure 6.8) showed two continuum sources within the PA beam centred on the best known position from

TABLE 6.2: Timing solution obtained for PSR J1838+1523. For the measured quantities, numbers in brackets indicate 1σ errors in the last significant digit as reported by TEMPO2.

Fit and data-set	
Pulsar name	J1838+1523
MJD range	55770.6—57157.0
Data span (yr)	3.80
Number of TOAs	218
RMS timing residual (μs)	1655.7
Weighted fit	Y
Reduced χ^2	1.23
Measured Quantities	
Right ascension, α (hh:mm:ss)	18:38:46.78(1)
Declination, δ (dd:mm:ss)	+15:23:24.9(1)
Galactic longitude, l (deg)	45.3472(4)
Galactic latitude, b (deg)	+9.69394(3)
Pulse frequency, ν (s^{-1})	1.82096092905(2)
First derivative of pulse frequency, $\dot{\nu}$ (s^{-2})	$-6.71(5)\times10^{-17}$
Dispersion measure, DM ($cm^{-3}pc$)	68.26(3)
Set Quantities	
Epoch (MJD)	56675
Derived Quantities	
$\log_{10}$(Characteristic age, yr)	8.6
$\log_{10}$(Surface magnetic field strength, G)	11.0
$\log_{10}$($\dot{E}$, ergs/s)	30.7
Assumptions	
Clock correction procedure	TT(TAI)
Solar system ephemeris model	DE405
Binary model	NONE
Model version number	5.00

the ORT observations. Out of these, one source had a continuum counterpart in the NRAO VLA Sky Survey (NVSS) maps at 1.4 GHz. The NVSS denomination for this source was NVSS J183850+152214. The other source, which was centred at RA: 18 h 38 m 47 s, DEC: +15° 23' 27" with an error circle of about 10" at 325 MHz. This source showed a steep spectrum and did not have any counterpart in the NVSS maps. NVSS J183850+152214 showed an essentially flat spectrum (see Chapter 8 for more details). The first conclusion was then, to associate the steep spectrum source with PSR J1838+1523. This claim was corroborated by 4 non-detections at 610 and 2 at 1170 MHz, wherein NVSS J183850+152214 was

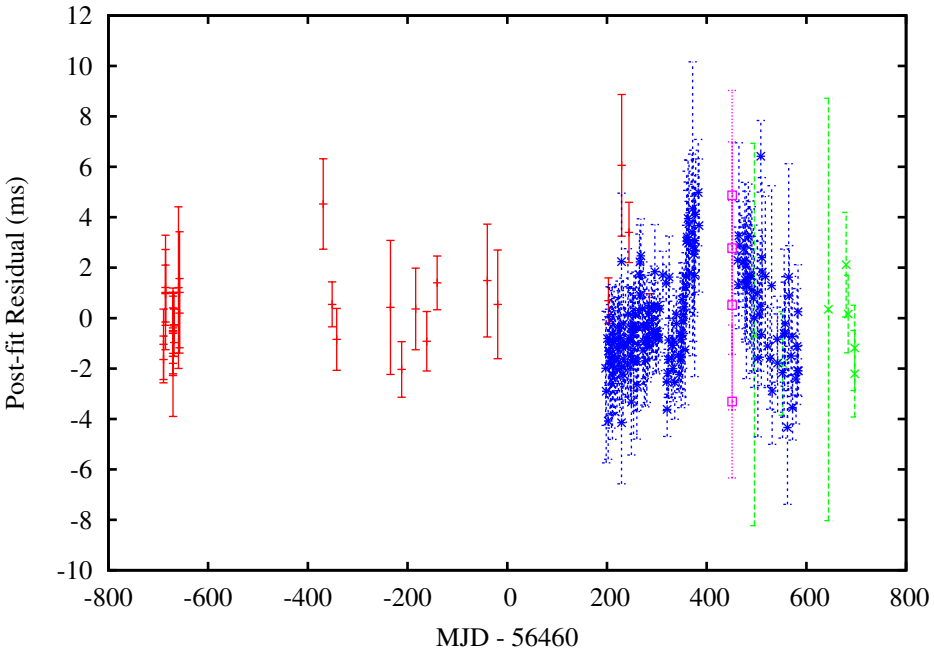

FIGURE 6.5: Post-fit timing residuals obtained for PSR J1838+1523. The RMS post-fit residual is 1655.7 μs. The red crosses indicate TOAs measured at 325 MHz, while green crosses indicate TOAs measured at 610 MHz with the GMRT. Blue asterisks indicate TOAs measured with the ORT at 326 MHz and magenta squares indicate TOAs measured with the GBT at 820 MHz. The gap in ORT TOAs is due to the telescope being down due to maintenance work.

visible in the radio maps. Another supporting evidence was provided by an image made at MJD 56381, which resulted in a non-detection of both the continuum as well as pulsed source. This image is shown in Figure 6.7. With the full timing solution, one can clearly see that the position obtained from timing observations (which is more accurate) is consistent with the interferometric position. Once the continuum counterpart was identified, its flux density was measured in all the images. These flux densities are listed in Table 6.1.

The flux densities of PSR J1838+1523, measured in images made with the GMRT and time series observations with the GMRT and ORT at 325 MHz, are shown in Figure 6.9. The mean flux density of PSR J1838+1523 as estimated from all the measurements at different frequencies is listed in Table 6.3.

All the measurements at a given frequency are consistent with each other with the mean flux density of 4.3 $\pm$ 1.8 mJy at 325 MHz and 1.2 $\pm$ 0.7 mJy at 610

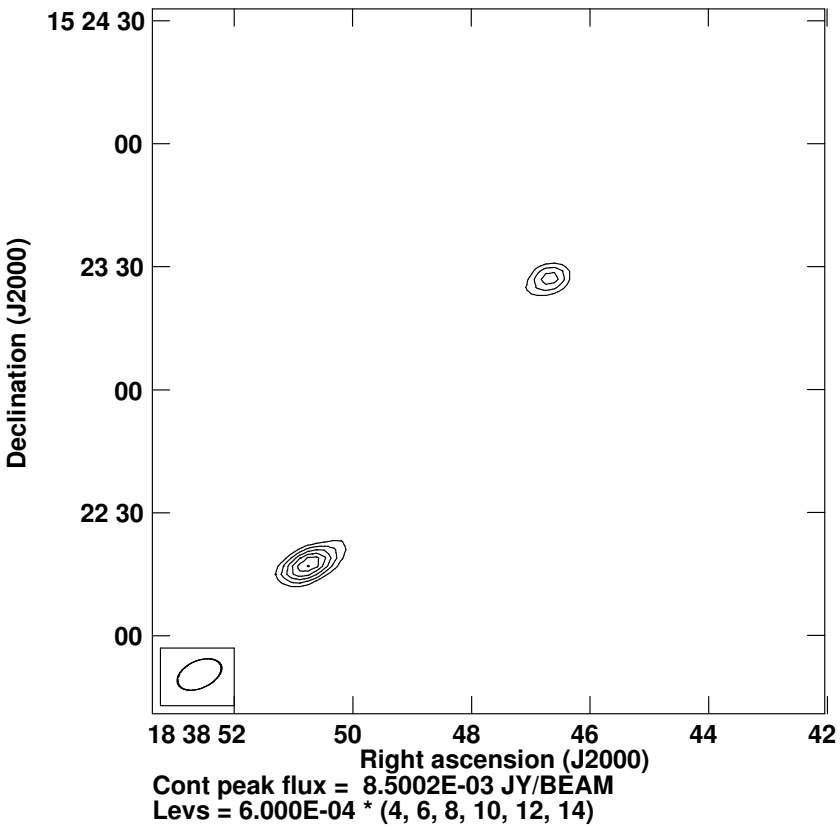

FIGURE 6.6: Interferometric image made at 325 MHz showing NVSS J183850+152214 (towards bottom left, flux density 9.7 mJy) and PSR J1838+1523 (flux density 5.2 mJy) for a time series detection. The image RMS is 0.6 mJy. The contours are at 2.4, 3.6, 4.8, 6.0, 7.2 and 8.4 mJy. The epoch of observation is MJD 56262. The synthesized beam is plotted in bottom left corner.

MHz. This implies a spectral index of -2. Extrapolating the spectral index to a frequency of 1170 MHz gives a predicted flux density of about 0.3 mJy, which is much lower than the detection limit of 2.5 mJy for NVSS (Condon et al. 1998). The RMS noise in the 1170 MHz maps made with the GMRT imaging data were of the same order. Thus, the non-detection in the NVSS maps and 1170 MHz GMRT observations is consistent with the implied spectral index. In fact, given the level of uncertainties in the imaging measurements at 610 MHz (Table 6.1), the non-detections are not surprising considering the fact that the flux density of the pulsar is very close to the detection limit.

As expected with a series of non-detections at 325 MHz, the flux variation is quite a lot. In fact, in all the weak time series detections, the estimated flux densities

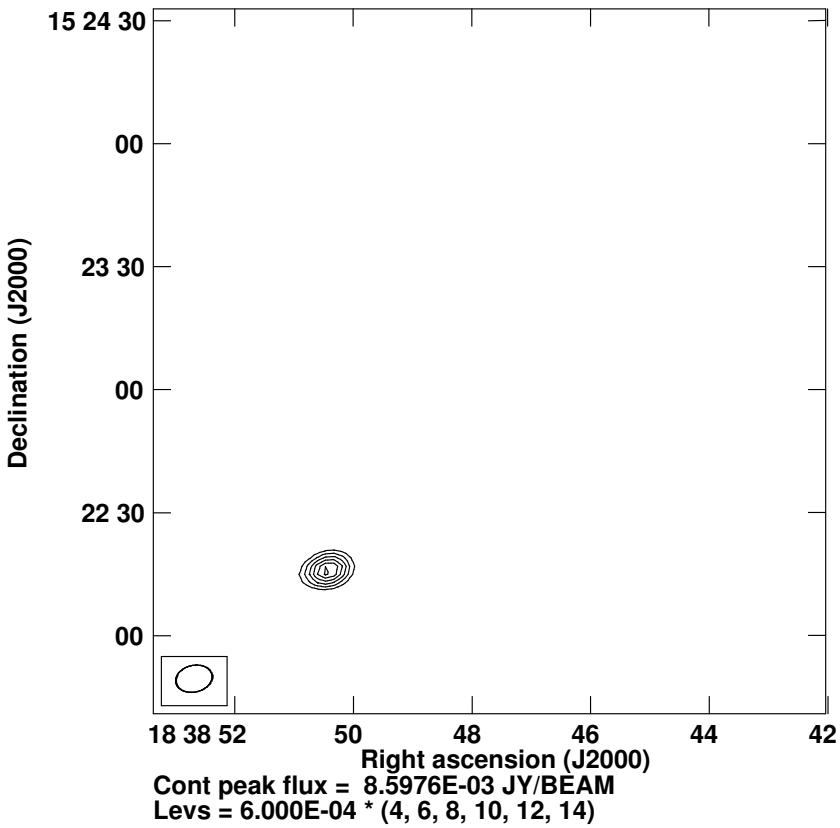

FIGURE 6.7: Interferometric image made at 325 MHz showing NVSS J183850+152214 (towards bottom left, flux density 9.6 mJy) and PSR J1838+1523 for a non-detection. The image RMS is 0.6 mJy. The contours are at 2.4, 3.6, 4.8, 6.0, 7.2 and 8.4 mJy. The epoch of observation is MJD 56381. The synthesized beam is plotted in bottom left corner.

Type of Measurement	Observing Frequency (MHz) 325	610
Time Series (GMRT)	4.0 ± 1.8 mJy	1.0 ± 0.4 mJy
Time Series (ORT)	4.2 ± 1.6 mJy	-
Imaging (GMRT)	4.7 ± 1.2 mJy	1.4 ± 0.7 mJy

TABLE 6.3: Mean flux densities of PSR J1838+1523 at different frequencies. The uncertainties come from the systematic variation across time rather than measurement uncertainties, which are smaller.

are very close to the detection limit. This is more evident in the time series flux density histogram as shown in Figure 6.10. The kurtosis of the time series flux distribution is 3.03, while the kurtosis of the imaging flux density distribution is 0.82. This implies that the time series flux distribution is nearly Gaussian, while the the imaging flux density distribution is almost uniform (Westfall 2014).

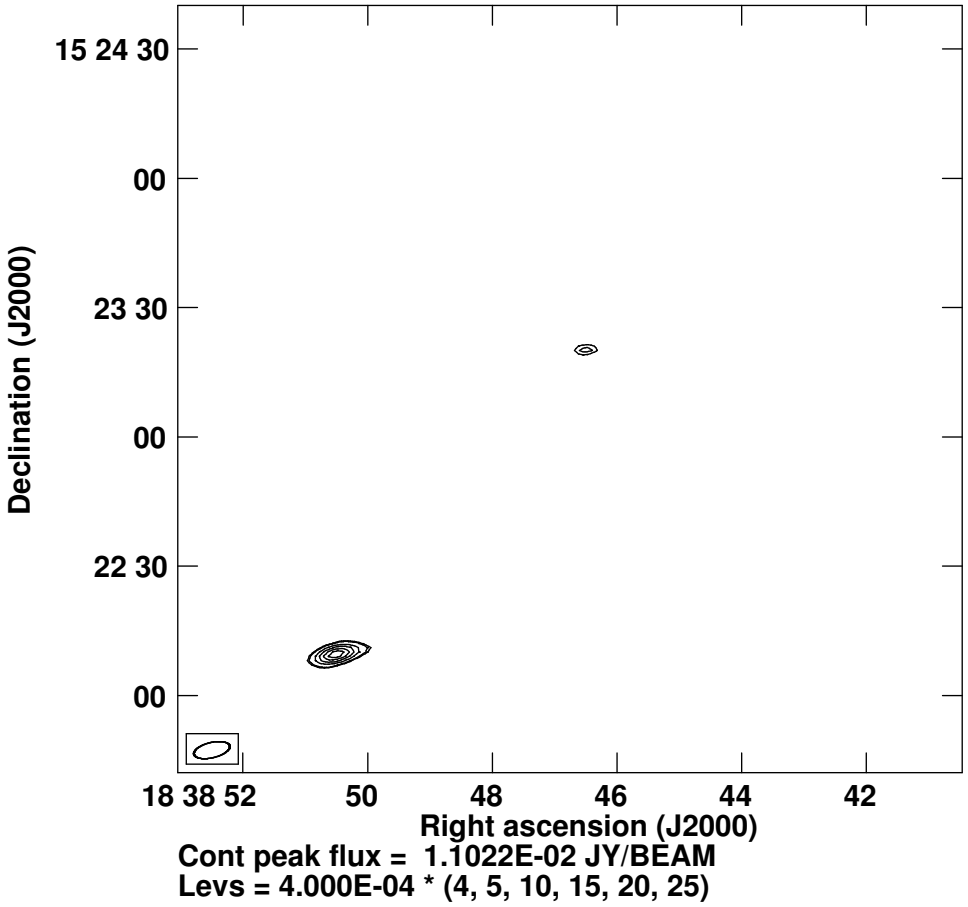

FIGURE 6.8: Interferometric image made at 610 MHz showing NVSS J183850+152214 (towards bottom left, flux density 10 mJy) and PSR J1838+1523 (flux density 1.5 mJy). The image RMS is 0.2 mJy. The contours are at 1.6, 2.0, 4.0, 6.0, 8.0 and 10.0 mJy. The epoch of observation is MJD 57012. The synthesized beam is plotted in bottom left corner.

Although, it should be noted that the 3σ detection limit for imaging is of the order of 1.8 mJy with a typical map RMS of 0.6 mJy and the 8σ detection limit for time series is about 0.5 mJy. With these folded in, there is a noticeable clustering of flux densities in the bin next to the detection limit in both histograms (Figure 6.10 and 6.11).

The dynamic spectra generated from the GBT data are shown in Figure 6.12. The frequency and time resolution roughly correspond to the predicted scintillation bandwidth (0.24 MHz) and time scale (232 s). As is evident, the pulsar is too weak to show considerable scintels. Thus, no concrete conclusion could be drawn from these dynamic spectra. A similar result was obtained from the ORT data

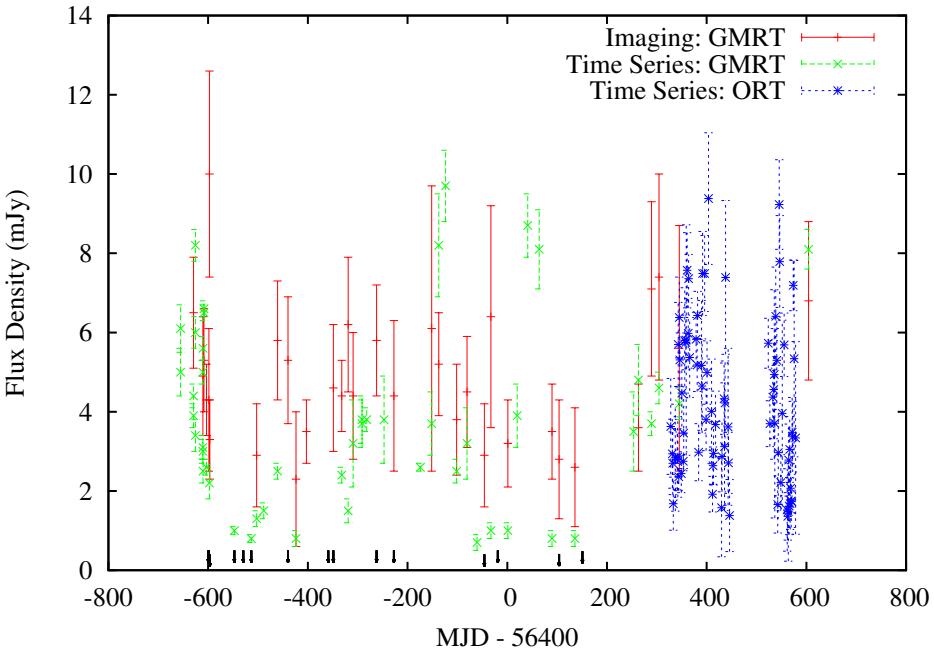

FIGURE 6.9: Flux densities of PSR J1838+1523 measured at different epochs. The observing frequency is 325 MHz. Red crosses indicate flux densities measured from GMRT images. Green crosses indicate flux densities measured from GMRT time series data and blue asterisks indicate flux densities measured from ORT time series data. Black arrows indicate 8σ upper limits on the flux density for a pulsed source in time series non-detections.

with better S/N at 326 MHz (Figure 6.13) and hence, no conclusion could be drawn regarding the presence of DISS as a cause for non-detections. Though, we believe that DISS could not be the cause of complete non-detection but could account for the flux density variation seen in epoch to epoch measurements.

6.7 Discussion

The follow-up observations for PSR J1838+1523 and the subsequent analysis provides a good example of how different types of measurements provide unique aspects of pulsar science. The time series observations using gridding technique provided the first position refinement. The initial timing observations provided further constraints on the position. The position uncertainty in right ascension thus obtained was smaller than that in declination. The unique beam shape of

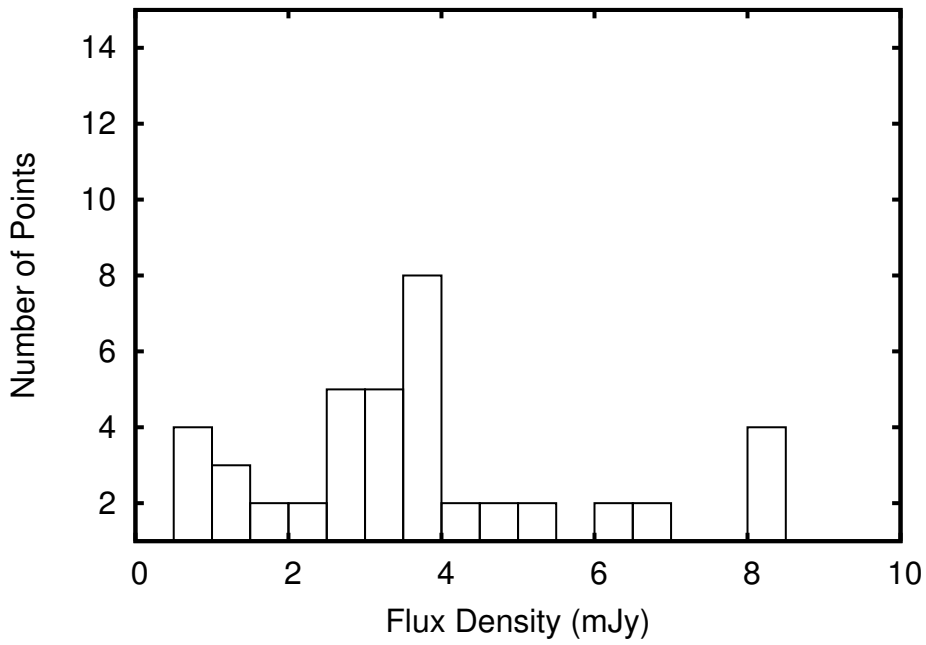

FIGURE 6.10: Time series flux density histogram for PSR J1838+1523 at 325 MHz. The bin size on the horizontal axis is 0.5 mJy. Apart from a few outliers, there is a clear clustering in the distribution the detection limit of about 0.5 mJy.

ORT allowed the uncertainty on the declination position to be reduced. A detection with the GBT, which has a much narrower beam (∼12') at 820 MHz, provided an independent confirmation for this. Further detections using PA mode of GMRT at 325 and 610 MHz built more confidence. Multi-frequency imaging data provided the final association with a continuum source. With this input, long term timing observations with ORT resulted in a much more refined pulsar position with other parameters. Once these parameters were obtained, the same observations provided further constraints on the flux density, spectral index and flux density variations. Together, all of these provided a consistent picture of the source under study. The radio images, which were made using simultaneous data obtained with the time series data, provided a faster localization of the pulsar. This helped in constraining the timing solution even with the patchy timing coverage, which resulted due to multiple non-detections. This demonstrates beyond doubt that simultaneous imaging capability is a powerful addition for low frequency pulsar searches. This has also been demonstrated by Roy et al. (2012) wherein, the same

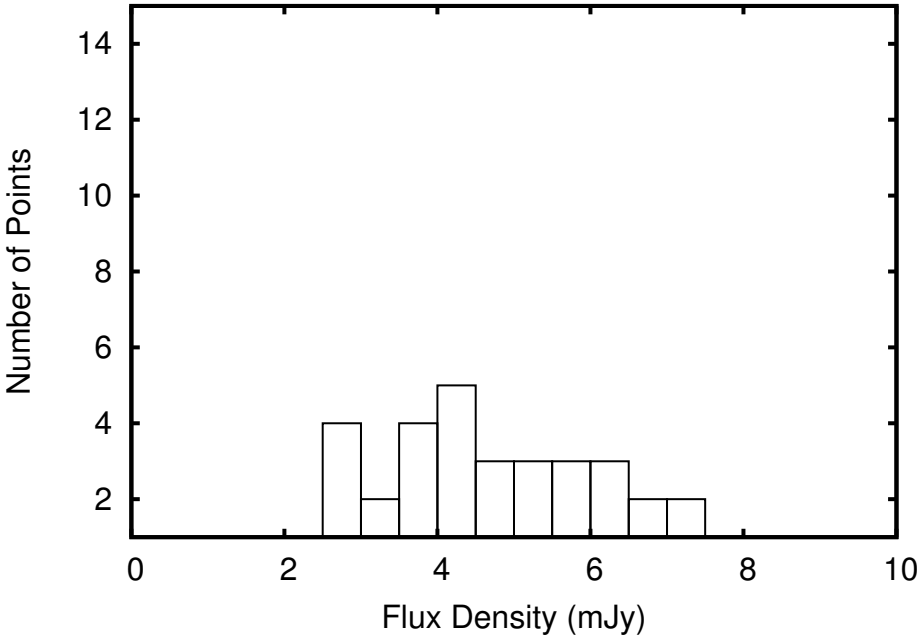

FIGURE 6.11: Imaging flux density histogram for PSR J1838+1523 at 325 MHz. The bin size on the horizontal axis is 0.5 mJy. There is an increased number of flux densities near the 3σ detection limit of about 1.8 mJy.

instrument was used to localize the pulsar much faster using the gated imaging technique. Such precise measurements of pulsar position are very helpful for doing astrometry of pulsars having high spatial velocities.

We firmly believe that diffractive scintillations could be responsible only for the variability in detected flux densities and would not make the pulsar undetectable. with this assumption, the clustering near detection limits in the flux density histograms could point to one of two possibilities. The first possibility is that PSR J1838+1523 has two different emission states (modes) and the mean flux density in the low emission state is below the detection threshold. The other possibility is that the clustering near detection limits is introduced by a combination of RISS and the detection limit of the telescope. The integrated profile bears no evidence of a mode change and essentially remains unchanged during the low emission state. There is no prima facie change in $\dot{P}$ as was seen by Lyne et al. (2010) in their study. In addition, the pulsar was detected in all of the observations at the ORT. The initial GMRT follow-up observations were spaced by 2 weeks. Thus, if there was a change in the $\dot{P}$ during that time, the time scale of a month or two was not

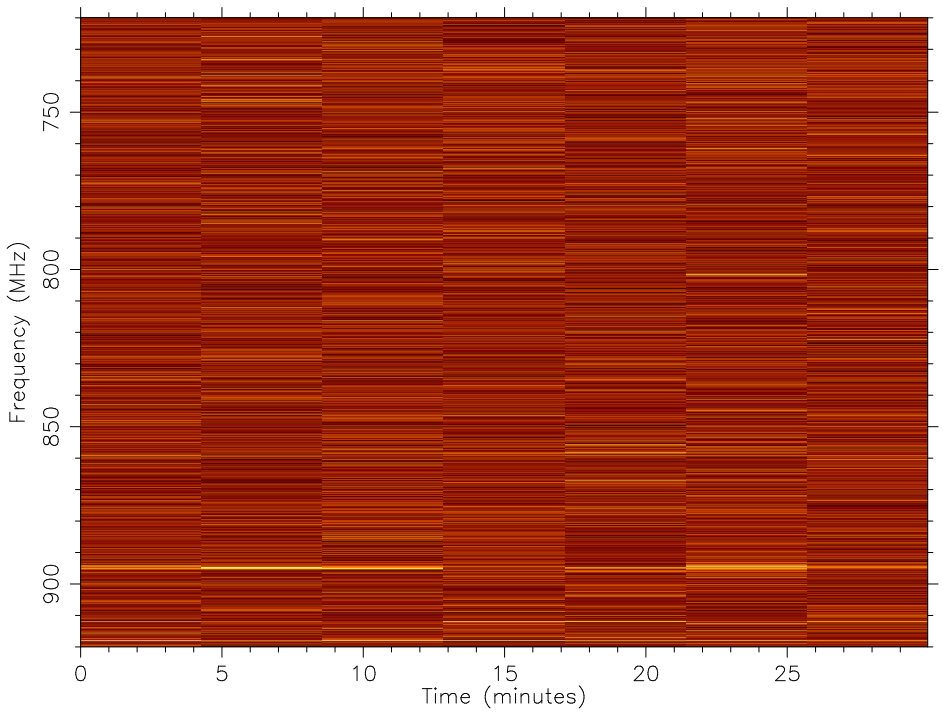

FIGURE 6.12: Dynamic spectra obtained for PSR J1838+1523 from GBT data at 820 MHz. The channel resolution is 0.25 MHz and the time resolution is 230 s.

well sampled by our observations. Thus, such a change would have to be lower than what could be reliably measured. There is also no evidence for nulling in this pulsar as far as the observational evidence is concerned. A single pulse search done on the detections as well as non-detections does not indicate the presence of strong transient pulses. This makes the mode changing scenario less likely. The mean flux density of PSR J1838+1523 is about 8−10 times the nominal detection limit of GMRT. Refractive scintillations could easily bring about a change of this magnitude in the flux density of the pulsar. This makes refractive scintillations as a more likely cause of low flux densities as well as non-detections. In this case, the inherent flux density distribution could be modified by a combination of varying levels of RFI, calibration errors as well as scintillations.

Additionally, in most of the time series non-detections, imaging data still shows a continuum source with lower flux density. In this case, another scenario (although much less likely) could be that the radio emission from this pulsar has a continuum component. As can be seen in Table 6.1 and 6.3, the imaging flux density in the

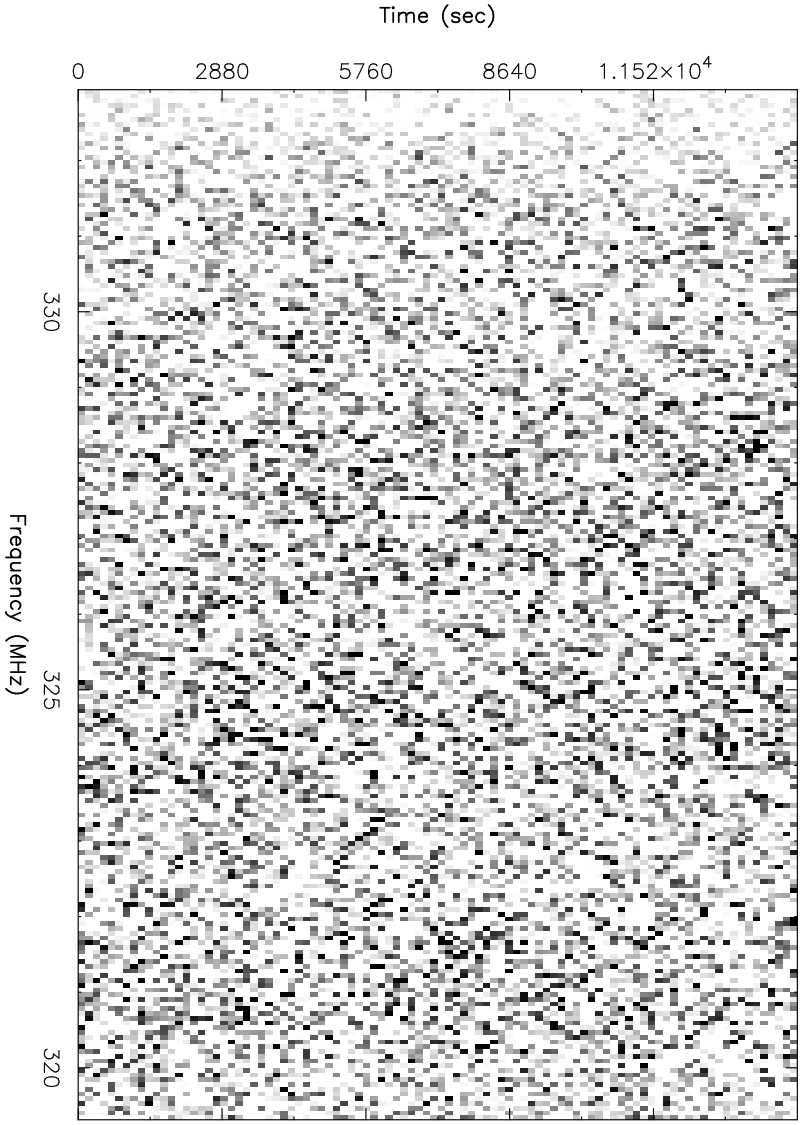

FIGURE 6.13: Dynamic spectra obtained for PSR J1838+1523 from ORT data at 326 MHz. The channel resolution is 62.5 KHz and the time resolution is 140 s.

GMRT data is almost always slightly higher than the time series flux density. Although, the errors on both these numbers are such that they prevent from drawing any firm conclusions, there is still a possibility that the un-pulsed emission might be always present. In this case, the variation in the time series flux density as well as the compactness of the imaging flux density histogram could be explained by the continuum component remaining more or less steady, while the pulsed component having a large, inherent variation due to non-stationary plasma flow in the magnetosphere. Using the detection limits as mentioned in Section 6.6, we can

put a lower limit of 3.6 on the ratio of pulsed to un-pulsed emission. This is slightly higher than the ratio of 2 obtained by (Navarro et al. 1995). No such un-pulsed emission is seen at 610 MHz but it could just be due to the fact that the expected flux density of the pulsar at 610 MHz is much closer to the detection limit. In the time series data, the absence of a pulse even after the addition of 9 non-detections coherently, implies that the pulsed flux density for the time series non-detections could be lower than 0.17 mJy (3 times lower than 0.5 mJy). This puts additional constraints on the pulsed to un-pulsed emission ratio, giving an upper limit of about 11.8 for the ratio. In case the pulsed emission does really switch off during these non-detections, we get a lower limit on the ON to OFF pulsed emission ratio of 23.5, much less than what was estimated for other intermittent pulsars (Kramer et al. 2006; Camilo et al. 2012; Lorimer et al. 2012). Continued long term timing observations interlaced with multi-frequency imaging observations could help in determining the actual cause of the flux density variation with much more robust statistics.

Chapter 7

Follow-up Timing of Three GMRT Pulsars

7.1 Introduction

In a blind survey carried out with the GMRT at 610 MHz, Joshi et al. (2009) discovered three new pulsars, PSR J2208+5500, PSR J2217+5733 and PSR J0026+6320. The survey was carried out at 610 MHz to exploit the steep spectra of pulsars as well as the larger beam size to cover the sky fairly fast with a good sensitivity afforded by the large collecting area of the interferometric array. After bringing down the position uncertainty with the gridding observations, the initial follow-up timing observations were carried out with the GMRT (610 MHz) and the Lovell telescope at Jodrell Bank (1400 MHz). The new pulsars belonged to the normal pulsar population with rotation periods of 318, 933 and 1056 ms. Joshi et al. (2009) also reported on the nulling behaviour of one of the pulsars, PSR J2208+5500 but could not quantify it due to poor S/N of single pulses at 610 MHz. Out of the three, two pulsars, PSR J2208+5500 and PSR J2217+5733 have very steep spectra with the spectral index greater than -2 while PSR J0026+6320 has a much flatter spectrum with a spectral index of -0.8 (Joshi et al. 2009). Given the well known

timing solutions and an interesting mix of very steep and very flat spectrum pulsars, a timing follow-up at 325 MHz with the GMRT PA mode seemed reasonable. As all of these pulsars (together with PSR J1838+1523, see Chapter 6 for details) are GMRT discoveries, it is the most suitable instrument for the follow-up timing observations. GMRT also has a unique capability to provide simultaneous imaging data, which would be helpful to constrain the mean flux density and hence, spectral indices of these pulsars. In addition, given the very steep spectral index of PSR J2208+5500, the GMRT PA data taken at 325 MHz would have enough single pulse S/N to study nulling in this pulsar much better. Regular timing observations over long durations may reveal interesting phenomena like nulling, mode changing and intermittency. This provides a very good motivation to do follow-up timing observations for these pulsars. Thus, when the follow-up timing observations of the newly discovered PSR J1838+1523 were commencing, these three pulsar were also added to the list with a known pulsar, PSR B1937+21 as a test pulsar to check for consistency in the timing solutions obtained for the other pulsars. The results from these follow-up observations are described in this chapter.

7.2 Observations

The timing observations were performed with the GMRT at 325 MHz between MJD 56051−56745 with a cadence of about 2 weeks. The timing observations were moved to 610 MHz after this (see Chapter 6 for more details) and were performed between MJD 56955−57282 with a similar cadence. The observations at the ORT were started on MJD 56653 with almost daily cadence and were continuing at the time of writing the thesis with a cadence of about a week. More details on the observational parameters as well as typical observational set-up is described in Section 3.3. The list of epochs of observation for these pulsars and some more details are given in Table 6.1 in Chapter 6.

7.3 Data Analysis

The GMRT data analysis started with flagging the RFI infected channels as explained in Section 4.1.1. The resultant data were then converted to SIGPROC filterbank format. This was then dedispersed to the DM of the pulsar to produce a time series file, which was subsequently folded to get a time stamped integrated profile. At the ORT, the pulsar back-end, with the help of predictive polyco files produced by TEMPO2, produced coherently dedispersed, time stamped integrated profile (see Naidu et al. 2015, for details). The integrated profiles were added coherently to produce a high S/N template, which was used to estimate the TOAs for all the observations following the procedure described in Section 4.3.1. The timing analysis was done using the timing package TEMPO2. Observations for PSR B1937+21 were carried out with the follow-up observations. This pulsar was treated as a control pulsar and was analysed in a manner similar to other pulsars. During the data analysis of the initial 325 MHz GMRT data, it was noticed that PSR J2217+5733 and J0026+6320 were detected with a much lower S/N than the expected value in only some of the data. In order to investigate this further, a local DM search was undertaken for both the pulsars. This analysis is described in the next section.

7.3.1 Local Search

As the name suggests, local search runs over a local range of trial DMs centred over the best known DM of the pulsar wherein the filterbank file is dedispersed to each of the trial DM and is searched for periodicities using the harmonic search (as described in Section 4.1.3). A manual inspection of the candidate list is then done in order to find out the harmonic S/N of the pulsar periodicity. At the end of the local search, the output is a file containing the harmonic S/N as a function of trial DM. An example plot of such a file is shown in Figure 7.1. The initial local search done for PSR J2217+5733 spanned a DM range of 100−200 pc-cm^{-3}, with a DM step of 0.2, while the local search for PSR J0026+6320 spanned a DM

range of 200−280 pc-cm^{-3}, with a DM step of 0.5. The DM steps were chosen to be slightly finer than otherwise done in order to get a better estimate of the true DM of the pulsar. The results on PSR J2217+5733 indicated the true DM to be near 130 pc-cm^{-3} and hence, the trial DM range was reduced to 100−160 pc-cm^{-3}, while the range for PSR J0026+6320 remained the same. The local search analysis was done on four data sets each for PSR J2217+5733 and J0026+6320.

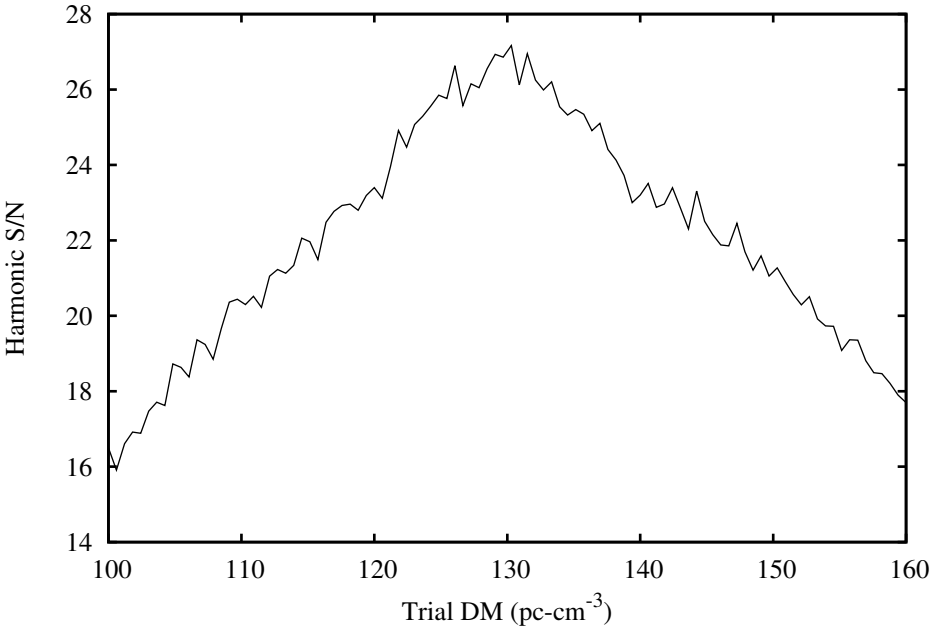

FIGURE 7.1: Harmonic S/N as a function of trial DM obtained from a local search analysis done for PSR J2217+5733.

The harmonic S/N obtained as a function of trial DM was then fit with a Gaussian function to obtain the DM corresponding to the peak S/N. This represents the approximate true DM of the pulsar. This DM estimate is very crude as can be seen from the plot shown in Figure 7.1. Also, the error in DM depends on the amount of low level RFI present in the data, which has a different effect at different trial DMs. This results, sometimes, in a broad peak (Figure 7.1), increasing the error on the location of the peak. In order to get a much better estimate of the true DM of the pulsar, one must do a multi-frequency timing analysis, which is described in the next section.

7.3.2 Timing Analysis

Once the true DMs were determined for PSR J2217+5733 and J0026+6320, the GMRT data were dedispersed to the true DM and folded. Time stamped profiles were obtained from the dedispersed time-series using SIGPROC. The TOAs were then calculated using the template matching technique as described in Section 4.3.1.1. A separate template was used for each frequency and was generated by co-adding the observed profiles at that frequency. The timing analysis was done using the pulsar timing package TEMPO2 (refer to Section 4.3.4 for more details). The average profiles obtained for all the pulsars observed are shown in Figures 7.3, 7.4 and 7.5. While doing the timing analysis, it was realised that the TOA uncertainties estimated from the cross-correlation technique were underestimated. Thus, an additional multiplicative factor (EFAC) was used to scale the TOA uncertainties so as to get a good fit to the TOAs. The value of EFAC was estimated independently for TOAs at each telescope and frequency by doing timing analysis so as to obtain a reduced χ^2 between 0.9−1.1. The EFACs thus obtained are shown in Table 7.1. The EFACs for GMRT TOAs of PSR B1937+21 were very large because of two reasons. The first was that the scatter-broadening was changing across epochs. The second, most dominant effect was due to the fact that Taylor's template matching algorithm almost always underestimates TOA errors. In fact, the TOA errors reduce as the S/N of the template and the observed profile increase. In the case of PSR B1937+21, the GMRT time series data were incoherently dedispersed and folded with 32 bins across the profile. This provided only 2 bins of OFF pulse region, effectively reducing the noise drastically. This resulted in very high profile S/N even in individual observations. Thus, the TOA errors obtained from Taylor's program were grossly underestimated. The nominal errors reported by the template matching routine were of the order of a few μs, while the bin size was of the order of 50 μs. At 610 MHz, the large EFAC value was seen due to low S/N of the template profile in addition to above mentioned effects. At ORT, the time and frequency system was configured such that it was using the falling edge of the GPS signal to derive timestamps. Typically, the rising edge should have been taken as the standard, as the falling edge has a large amount of

jitter. Figure 7.2 shows how changing the clock to derive the timestamp from the rising edge of the GPS signal reduced the jitter drastically. This added jitter in the ORT TOAs was responsible for large EFACs. In addition, as the final timing solution was a joint solution, some part of the jitter in ORT TOAs were absorbed in the EFACs for GMRT TOAs. This fact is mirrored in the timing residuals at 610 MHz as well (see Figure 7.6).

Telescope	Frequency (MHz)	Pulsar			
		B1937+21	J2208+5500	J2217+5733	J0026+6320
ORT	325	40.0	1.3	-	-
GMRT	325	35.0	3.5	2.0	3.0
GMRT	610	25.0	4.2	5.5	4.8
GMRT	1170	-	1.0	3.0	-

TABLE 7.1: EFAC values for different telescopes and observing frequencies for all the observed pulsars. Dashes indicate unavailability of TOAs.

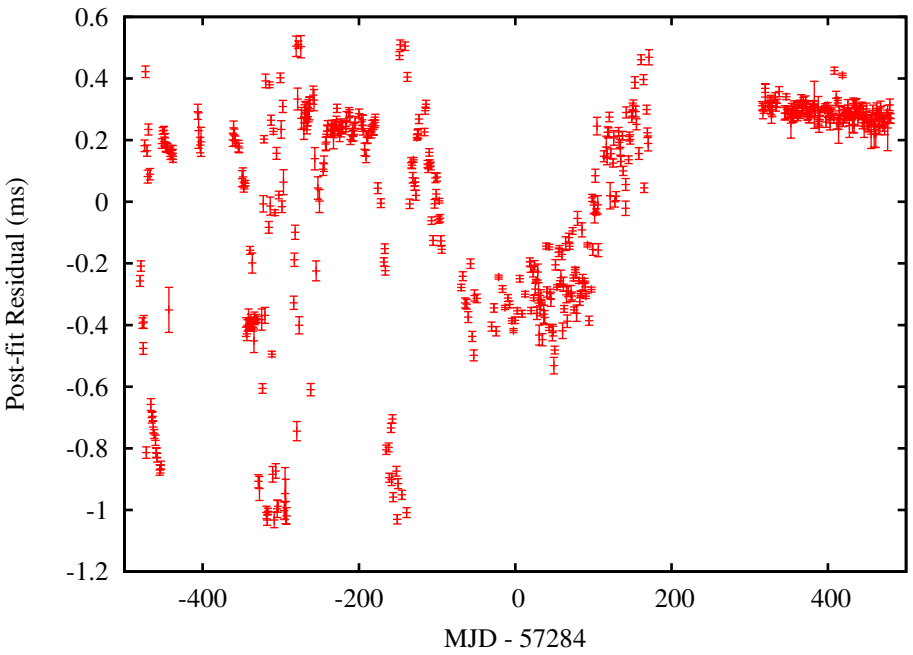

FIGURE 7.2: A plot showing how clock jitter introduces timing irregularities for PSR B1937+21. As can be clearly seen, the timing residuals with the clock using falling edge of the GPS signal show random jitter as compared to a clock using the rising edge of the GPS for timstamp. The clock was changed from MJD 57589.

As the observations were done at different telescopes and frequencies, constant phase offsets were also fit to the TOAs along with other relevant pulsar parameters.

This enabled a much better estimate of the true DMs for these pulsars. Although this procedure seems straightforward, it is more involved. Let us assume that the instrumental phase offset (which is constant for all pulsars) is denoted by $\delta\phi_{\rm off}$ and the extra delay introduced by the DM at low frequencies is denoted by $\delta\phi_{\rm DM}$. The total phase offset thus introduced at each different frequency and/or telescope ($\delta\phi$) would then be given by

$$\delta\phi = \delta\phi_{DM} + \delta\phi_{off} \tag{7.1}$$

Now as stated earlier, $\delta\phi_{\rm off}$ is the same for all pulsars, while $\delta\phi_{\rm DM}$ is not. Thus, in order to obtain a better DM estimate, some kind of joint solution is required. This solution however, is not unique. Thus, a systematic error in one quantity will lead to an error in the other and vice versa. This problem can be partly solved by doing the timing analysis of many pulsars with well known timing solutions (especially well determined DM and its variation). In our case, there were 4 pulsars available for the determination of the phase offset between 325 and 610 MHz, while only 2 pulsars had timing data at 1170 MHz. As explained in Section 7.3.1, the DMs of these pulsars were not very accurately known. To avoid the confusion due to coarse DM estimates in fitting the constant offsets, a controlled experiment was used to estimate the instrumental offsets. In the experiment, a modulated version of the 1 pulse per second (PPS) and 1 pulse per minute (PPM) signal (one at a time) of the GPS with a duty cycle of 50% were emitted at the observing frequency (326.5 MHz at ORT and 325, 610 and 1170 MHz at GMRT) using a broad-band antenna. This signal was then recorded through the regular data recording pipelines at ORT and GMRT. The data were then dedispersed at 0 DM and the time series out put was obtained. The recorded time of the rising edge of the 1 PPS (and 1 PPM) signal was compared with the expected time to obtain the instrumental offsets. While doing timing analysis, the EFACs were determined separately first. In the final analysis, all the TOAs were considered together. The constant phase offsets were then put in and held fixed, while the DM was determined later. Given the different values of EFAC at different telescopes and frequencies (as shown in Table

7.1) and the availability of only two TOAs at 1170 MHz, the actual accuracy of DM determination would be dependent on how accurately the 325−1170 MHz phase offset was calculated. Putting the value of f_1 = 325 MHz and f_2 = 1170 MHz in Equation 1.8, we get

$$\triangle DM = \frac{\triangle t}{36} \tag{7.2}$$

where △DM is expressed in pc-cm^{-3} and △t is expressed in ms. Thus, the systematic uncertainty in the DM, which could be larger than what the timing analysis provides, would be given by the above equation when △t is replaced by the uncertainty in the 325−1170 MHz phase offset. Similarly, putting f_2 = 610 MHz in Equation 1.8 gives,

$$\triangle DM = \frac{\triangle t}{28} \tag{7.3}$$

The uncertainty in the DM for PSR J2208+5500 and J2217+5733 was estimated using Equation 7.2. For PSR B1937+21, J1838+1523 and J0026+6320, the DM uncertainty was estimated using Equation 7.3. These were then compared with the uncertainties reported by TEMPO2. The dominant uncertainty was then reported as the actual uncertainty on the estimated DM.

7.3.3 Nulling Analysis for PSR J2208+5500

In the discovery paper, Joshi et al. (2009) suspected that PSR J2208+5500 may be a nulling pulsar. Their observations were carried out at frequencies higher than 600 MHz. Due to the steep spectral index of this pulsar, they did not have good S/N for single pulses and hence, could put only a lower limit of 7.5% on the nulling fraction. Our data were taken at 325 MHz with PA mode. This implied a good single pulse S/N and enabled us to estimate the nulling fraction. The nulling analysis was performed using the method devised by Ritchings (1976). Data taken at 10 separate epochs were selected for the nulling analysis as these had a good

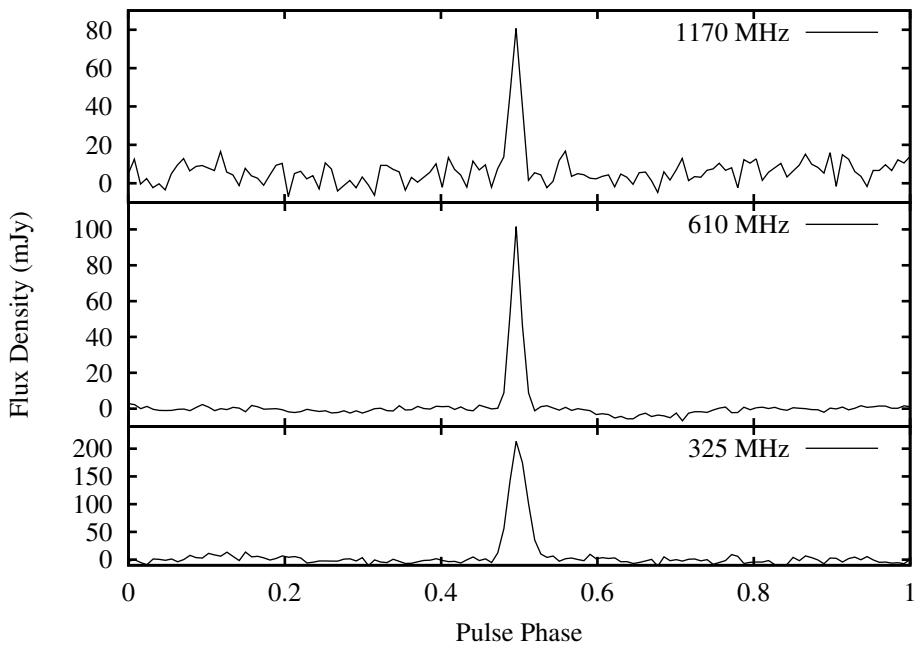

FIGURE 7.3: Average profiles for PSR J2208+5500 at different observing frequencies. All the profiles were obtained using data taken with the GMRT.

single pulse S/N and low RFI level. The analysis was performed on data taken at each epoch independently. The dedispersed time series was folded modulo the pulse period and dumped every period into a single pulse file. The ON and OFF pulse regions of equal width were then identified using a visualising tool based on PGPLOT. The ON pulse region window was selected such that it equalled the pulse width at 10% peak intensity in the integrated profile. The same program provided the integrated energies in ON and OFF windows in two separate files (see Gajjar et al. 2012, for more details on the analysis technique). The normalized pulse energy streams were then formed using the procedure as described in Ritchings (1976). The normalized ON and OFF pulse energies formed for each epoch were then combined to form a single distribution of normalized ON and OFF pulse energies. The combined data provided an ensemble of about 6000 pulse periods. The nulling fraction was then estimated using these distributions.

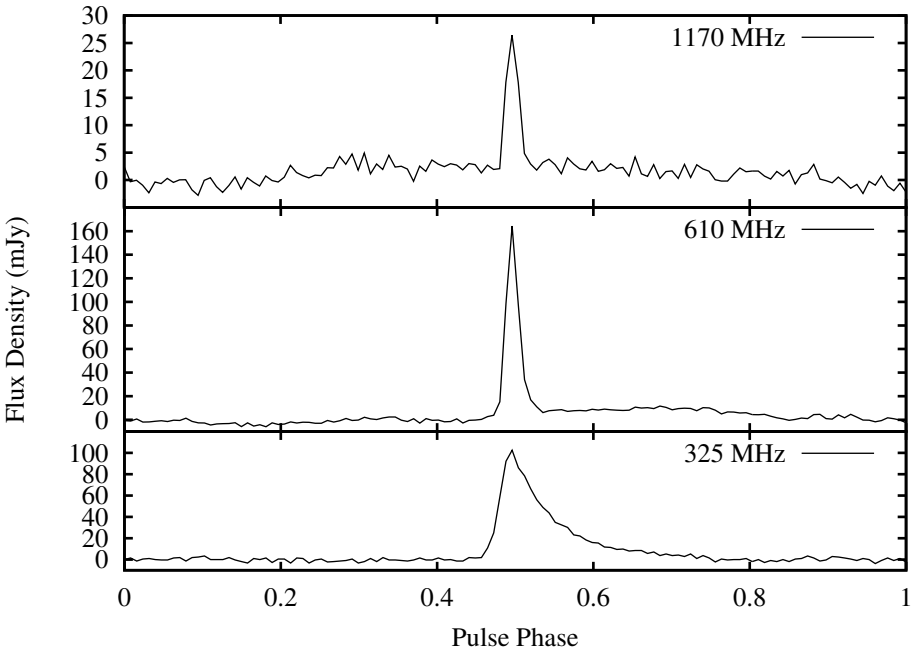

FIGURE 7.4: Average profiles for PSR J2217+5733 at different observing frequencies. All the profiles were obtained using data taken with the GMRT.

7.3.4 Modulation Index for PSR J2208+5500

Individual pulses emitted by pulsars vary in integrated intensity as well as the intensity distribution over the pulse phase. One way to estimate this variation and possibly connect it to the emission mechanism (Jenet and Gil 2003) is through estimating the modulation index (m). In order to obtain the phase resolved modulation index for PSR J2208+5500, the same data sets, which were used to estimate the nulling fraction were used. The dedispersed time series for each observation was folded modulo the topocentric period into 256 phase bins. This resulted in 11 phase bins across the pulse. The intensities for the selected phase bin [I(ϕ)] were then obtained by using a PGPLOT based program. The modulation index for each phase bin was calculated by

$$m(\phi) = \frac{\sqrt{\langle I(\phi)^2 \rangle - \langle I(\phi) \rangle^2}}{\langle I(\phi) \rangle} \tag{7.4}$$

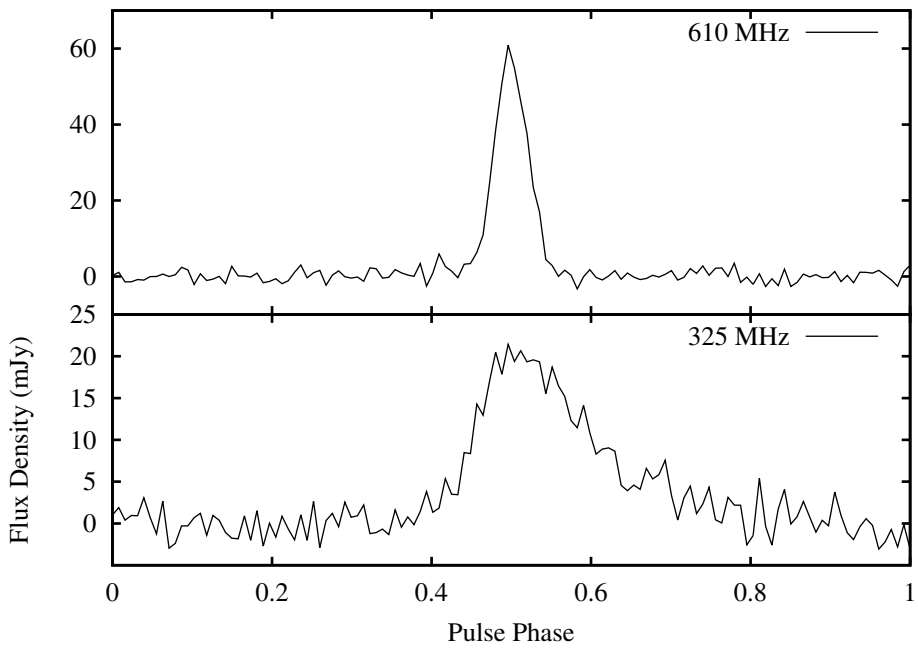

FIGURE 7.5: Average profile for PSR J0026+6320 at different observing frequencies. All the profiles were obtained using data taken with the GMRT.

Finally, the modulation indices for each bin across the 10 observations were averaged and the resulting RMS was used as an error bar on individual measurement.

7.3.5 Scattering Analysis for PSR J2217+5733 and J0026+6320

PSR J2217+5733 and J0026+6320 show scattering tails in their profiles obtained at 325 MHz as can be seen in Figures 7.4 and 7.5. At low frequencies, the observed profile is scatter-broadened due to multi-path propagation. The broad scattering tail has a characteristic exponential form (see Section 1.2.3.2 for more details), which allows the measurement of the characteristic scatter-broadening time scale ($\tau_{\rm sc}$). The scattering analysis for PSR J2217+5733 and J0026+6320 was done using the method and code described in Krishnakumar et al. (2015). The fitting routine assumes that the observed low frequency profile is a convolution of a scatter-free Gaussian profile and an exponential scatter function, which is proportional to exp (-t/$\tau_{\rm sc}$). The estimation of $\tau_{\rm sc}$, thus requires a scatter-free template profile. For PSR J2217+5733, the data were present for observing frequencies of

325, 610 and 1170 MHz. For PSR J0026+6320, the data were present only at 325 and 610 MHz. The template profiles for both PSR J2217+5733 and J0026+6320 were taken to be single component Gaussian profiles with widths equal to w_{50} (i.e. the pulse width at 50% of peak intensity) as given in Joshi et al. (2009). There is some amount of error involved in assuming that a single Gaussian model at high frequency specifies the profile shape correctly at low frequencies. According to various studies of profile evolution with frequency for normal as well as millisecond pulsars (Thorsett 1991; Kramer et al. 1999), the largest variation in profile shape follows a power law $w_{50} \propto \lambda^{0.3}$. With this index, the typical increase in the profile width was smaller than the bin width of the integrated profiles and hence, the frequency evolution does not hamper the estimation of τ_{sc}.

7.3.6 Imaging Analysis

The imaging data, which were acquired simultaneously with time series observations carried out at the GMRT, were flagged and calibrated using FLAGCAL. The images were then made using AIPS with three rounds of self calibration. The imaging analysis is explained with greater details in Section 4.4. The flux densities were then measured by using the task JMFIT. Additionally, flux densities for PSR B1937+21 at 700, 1400 and 3100 MHz were obtained from Manchester et al. (2013). A search in the TIFR GMRT Sky Survey alternate data release (TGSS ADR; Intema et al. 2016)[1] provided 150 MHz flux density for PSR B1937+21, while resulting in non-detection of all the GMRT pulsars. The 6σ upper limit on the flux density from TGSS ADR was estimated to be 21 mJy for all three pulsars.

7.4 Results

The results of the data analysis obtained for the pulsars are listed below in different sections with each section dedicated for one pulsar.

[1] http://tgssadr.strw.leidenuniv.nl/doku.php

7.4.1 PSR B1937+21

The timing solution obtained for the control pulsar, PSR B1937+21 is shown in Table 7.2, while the resultant timing residuals are shown in Figure 7.6. Given the large scattering tail seen in this pulsar at 325 MHz, the timing solution obtained is reasonably accurate. This can be confirmed from the parameters recently obtained by Verbiest et al. (2016) in the first IPTA data release (shown in Table 7.3). Also note that only a single DM value was used throughout the fit, rather than a time-varying DM. This has reduced the accuracy of the timing solution. A method similar to the one used for PSR B1937+21, was used for the timing analysis of other pulsars. The constant offset between GMRT−ORT was estimated to be 769 ± 1 ms, while no offsets were seen at GMRT between 325−610 and 325−1170 MHz down to a level of 0.05 ms. The GMRT−ORT offset was found to be consistent for all relevant pulsars (PSR J1838+1523 and J2208+5500). Putting the value of $\triangle$t in Equation 7.2 as 0.05 ms, we get the uncertainty in DM determination to be 0.0014 pc-cm^{-3}. For $\triangle$t = 0.05 ms in Equation 7.3, we get the uncertainty in DM determination to be 0.0018 pc-cm^{-3}. Given that the RMS residuals obtained in all the pulsars except PSR B1937+21, were of the order of 1–2 ms, the uncertainties from fitting were more dominant and they are the ones that are reported in the results. For PSR B1937+21, the DM uncertainty from the offsets was dominant, which is reflected in the value reported in Table 7.2.

The average flux density obtained for PSR B1937+21 along with all the other pulsars at different observing frequencies are shown in Table 7.4. Additionally, flux density measurements of B1937+21 were obtained from Manchester et al. (2013) and Intema et al. (2016). The resultant spectrum of PSR B1937+21 is shown in Figure 7.7.

TABLE 7.2: Timing solution obtained for PSR B1937+21. For the measured quantities except DM, numbers in brackets indicate 1σ errors in the last significant digit as reported by TEMPO2. The DM uncertainty was determined from the uncertainty in the determination of instrumental offsets at different frequencies. For the set quantities, numbers in brackets indicate 1σ errors in the last significant digit as obtained from the ATNF pulsar catalog (version 1.51).

Fit and data-set	
Pulsar name	B1937+21
MJD range	56068.0—57282.6
Data span (yr)	3.33
Number of TOAs	119
RMS timing residual (μs)	172.4
Weighted fit	Y
Reduced χ^2	1.2
Measured Quantities	
Pulse frequency, ν (s^{-1})	641.9282183123(5)
First derivative of pulse frequency, $\dot{\nu}$ (s^{-2})	$-4.326(3)\times10^{-14}$
Dispersion measure, DM (pc-cm^{-3})	71.06(1)
Set Quantities	
Right ascension, α (hh:mm:ss)	19:39:38.56220(7)
Declination, δ (dd:mm:ss)	+21:34:59.120(3)
Galactic longitude, l (deg)	57.5088601(3)
Galactic latitude, b (deg)	−0.2894995(8)
Epoch (MJD)	56675
First derivative of dispersion measure, $\dot{DM}$ (pc-cm^{-3} yr^{-1})	−0.0012(1)
Proper motion in right ascension, $\mu_\alpha \cos\delta$ (mas yr^{-1})	−0.46(2)
Proper motion in declination, μ_δ (mas yr^{-1})	−0.66(2)
Derived Quantities	
$\log_{10}$(Characteristic age, yr)	11.4
$\log_{10}$(Surface magnetic field strength, G)	8.6
$\log_{10}$($\dot{E}$, ergs/s)	36.0
Assumptions	
Clock correction procedure	TT(TAI)
Solar system ephemeris model	DE405
Binary model	NONE
Model version number	5.00

TABLE 7.3: Timing solution obtained for PSR B1937+21 from the first IPTA data release (Verbiest et al. 2016) with combination A. The value of $\dot{DM}$ is from Reardon et al. (2016). The numbers in brackets indicate 1σ errors in the last significant digit. The numbers have been adjusted to epoch 56675 for comparison.

Fit and data-set	
Pulsar name	B1937+21
MJD range	46024.8—55924.4
Data span (yr)	27.1
Number of TOAs	3905
RMS timing residual (μs)	69.8
Weighted fit	Y
Reduced χ^2	1.0
Measured Quantities	
Right ascension, α (hh:mm:ss)	19:39:38.56122(1)
Declination, δ (dd:mm:ss)	+21:34:59.1257(1)
Galactic longitude, l (deg)	57.5088595(3)
Galactic latitude, b (deg)	−0.2894955(8)
Pulse frequency, ν (s^{-1})	641.92821831382(2)
First derivative of pulse frequency, $\dot{\nu}$ (s^{-2})	$-4.331278(8)\times10^{-14}$
Dispersion measure, DM (pc-cm^{-3})	71.026(1)
First derivative of dispersion measure, $\dot{DM}$ (pc-cm^{-3} yr^{-1})	−0.00059(3)
Proper motion in right ascension, $\mu_\alpha \cos\delta$ (mas yr^{-1})	0.06(1)
Proper motion in declination, μ_δ (mas yr^{-1})	−0.41(1)
Epoch (MJD)	56675
Derived Quantities	
$\log_{10}$(Characteristic age, yr)	11.37
$\log_{10}$(Surface magnetic field strength, G)	8.61
$\log_{10}$($\dot{E}$, ergs/s)	36.04
Assumptions	
Clock correction procedure	TT(BIPM2013)
Solar system ephemeris model	DE421
Binary model	NONE
Model version number	5.00

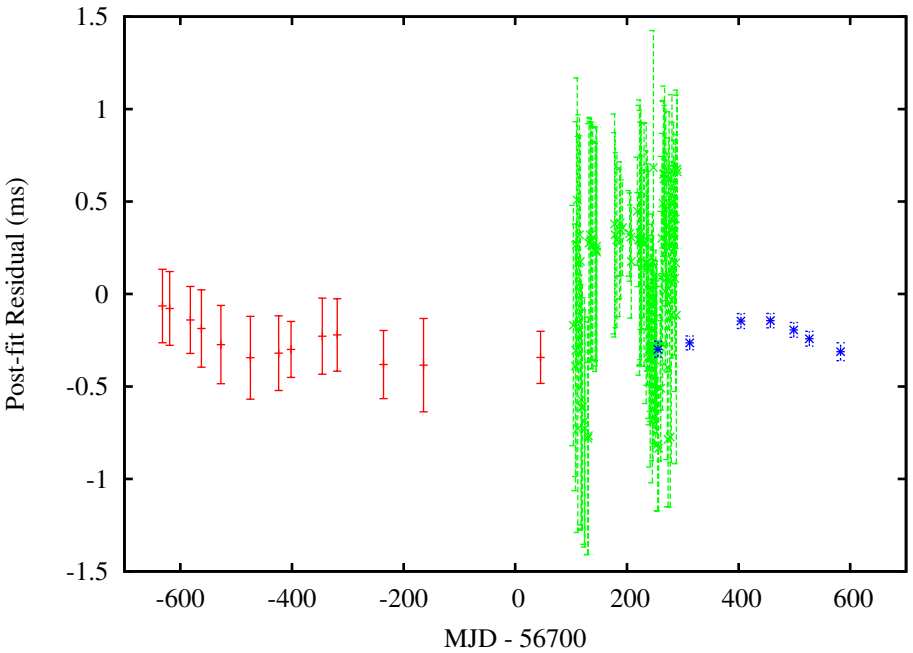

FIGURE 7.6: Post-fit timing residuals obtained for PSR B1937+21. The RMS post-fit residual obtained was 172.4 μs. The GMRT TOA measurements are indicated by red crosses (325 MHz) and blue asterisks (610 MHz), while the ORT TOA measurements are indicated by green crosses (326 MHz).

Pulsar	$S_{1170\ \mathrm{MHz}}$ (mJy)	$\sigma_{1170\ \mathrm{MHz}}$ (mJy)	$S_{610\ \mathrm{MHz}}$ (mJy)	$\sigma_{610\ \mathrm{MHz}}$ (mJy)	$S_{325\ \mathrm{MHz}}$ (mJy)	$\sigma_{325\ \mathrm{MHz}}$ (mJy)	α
B1937+21	-	-	134	16	443	48	-2.4 ± 0.2
J2208+5500	0.4	0.1	2.0	0.4	5.8	1.5	-2.4 ± 0.4
J2217+5733	0.5	0.1	4.6	1.1	10	3	-2.4 ± 0.3
J0026+6320	-	-	2.9	0.8	8.0	4.0	-0.9 ± 0.4

TABLE 7.4: Flux densities of the four observed pulsars at different observing frequencies. The error bars at 325 MHz were obtained from the flux variation, while the error bars at other frequencies were dominated by measurement errors. Spectral indices reported for pulsars other than PSR B1937+21 were obtained by using these measurements along with the ones obtained by Joshi et al. (2009). The flux density measurements for PSR B1937+21 at 700, 1400 and 3100 MHz were obtained by Manchester et al. (2013) and at 150 MHz were obtained by Intema et al. (2016).

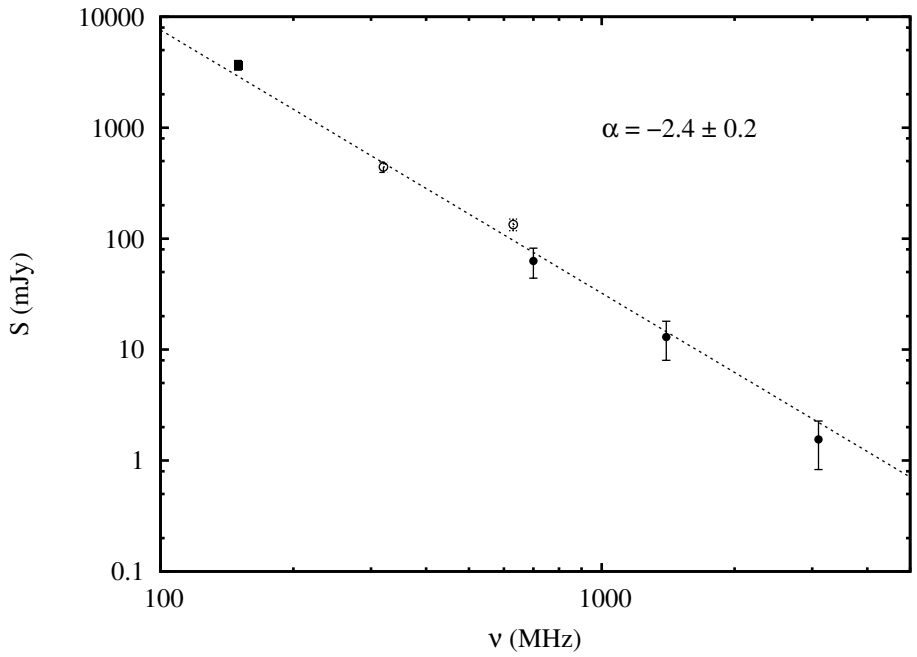

FIGURE 7.7: Spectrum of PSR B1937+21. The filled circles indicate the measurements obtained by Manchester et al. (2013), filled square indicates the measurement obtained by Intema et al. (2016), while the open circles indicate the measurements using images made at 325 and 610 with GMRT data.

7.4.2 PSR J2208+5500

The analysis of the sensitive PA data taken at 325 MHz with the GMRT indicated that PSR J2208+5500 indeed undergoes nulling. This is demonstrated in a single pulse plot shown in Figure 7.8. The pulse energy histograms obtained from 6000 pulses in ON and OFF pulse region are shown in Figure 7.9. The ON pulse energy histogram shows a clear excess at zero mean, which corresponds to the null pulses, which essentially contribute noise. After subtracting a fraction of the OFF pulse histogram from the ON pulse histogram, the estimated pulse nulling fraction is 50 ± 5%.

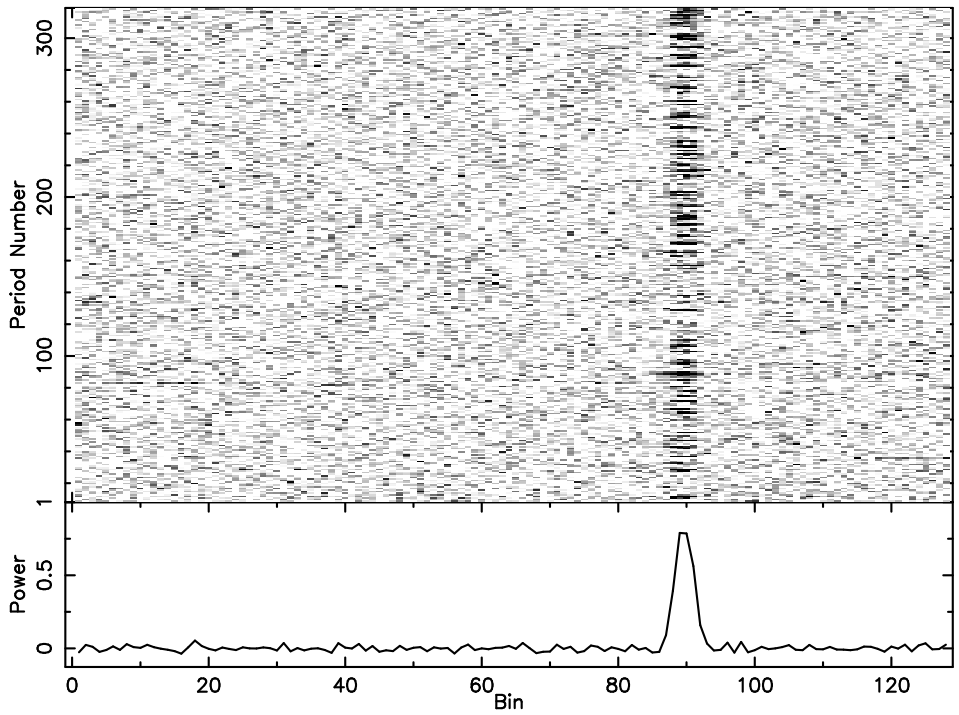

FIGURE 7.8: Pulse nulling seen in PSR J2208+5500 at 325 MHz. The upper panel shows a grayscale plot of pulse number as ordinate and pulse phase as abscissa. The bottom panel is the integrated pulse profile. Pulse nulling is clearly seen near periods 110−150.

The average phase resolved modulation index is plotted in Figure 7.10. It shows a minimum of 1.8 at the profile peak and increases towards both the edges of the profile. The average value of the modulation index was found to be 2.5 ± 0.6.

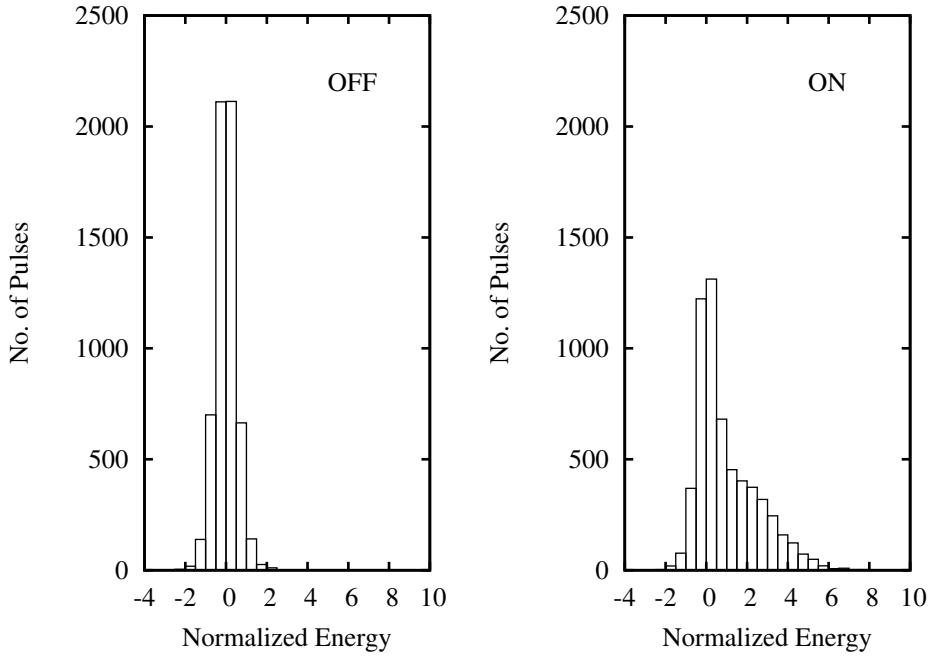

FIGURE 7.9: Histograms of normalized OFF and ON pulse energy for PSR J2208+5500.

No prima facie evidence for drifting of the pulses was seen in any data taken on J2208+5500. This remains to be the case even after analysing the fluctuation spectra of individual pulse bins as well as the fluctuation spectra obtained by averaging spectra of individual bins in all of the 10 observational epochs (independently). One such fluctuation spectrum is shown in Figure 7.11. As can be clearly seen in the figure, there is no obvious periodicity indicating the presence of sub-pulse drifting.

The phase coherent timing solution obtained after the timing analysis is listed in Table 7.5. In the analysis, the values that were held fixed, were obtained from the timing solution from Joshi et al. (2009). Overall, the timing solution obtained by this analysis is consistent with the one obtained by Joshi et al. (2009), with the only difference being the changed value of DM, which was possible because of multi-frequency timing analysis. The post-fit timing residuals obtained are shown in Figure 7.12. As is clearly seen in Figure 7.12, the simultaneous TOA measurements obtained at GMRT and ORT agree well with each other.

The image of PSR J2208+5500 at 325 MHz made at one epoch is shown in Figure

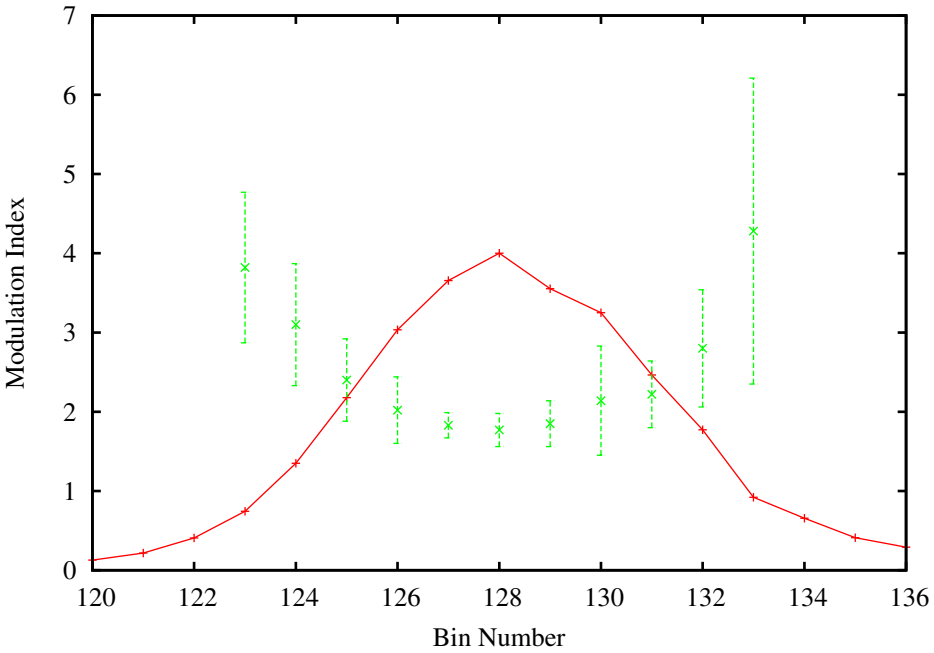

FIGURE 7.10: Average phase resolved modulation index for PSR J2208+5500. The modulation index for each phase bin (denoted by green crosses with errors) was calculated from 10 individual observations and the error bar represents the RMS of the 10 measurements. The red crosses with line represent a scaled version (for representative purpose) of the average pulse profile for the same set of observations.

7.13. The mean flux density measured at 325 MHz from the images is 5.8 ± 1.5 mJy. Flux density measurements at other frequencies are given in Table 7.4. Using these flux densities with the ones measured by Joshi et al. (2009), the spectral index was calculated to be −2.4 ± 0.4 (as shown in Figure 7.14), which is steeper but consistent with the value of −2.09, which was obtained by Joshi et al. (2009). The upper limit from TGSS ADR (shown by an arrow in Figure 7.14) may indicate a spectral break or a turnover below 300 MHz.

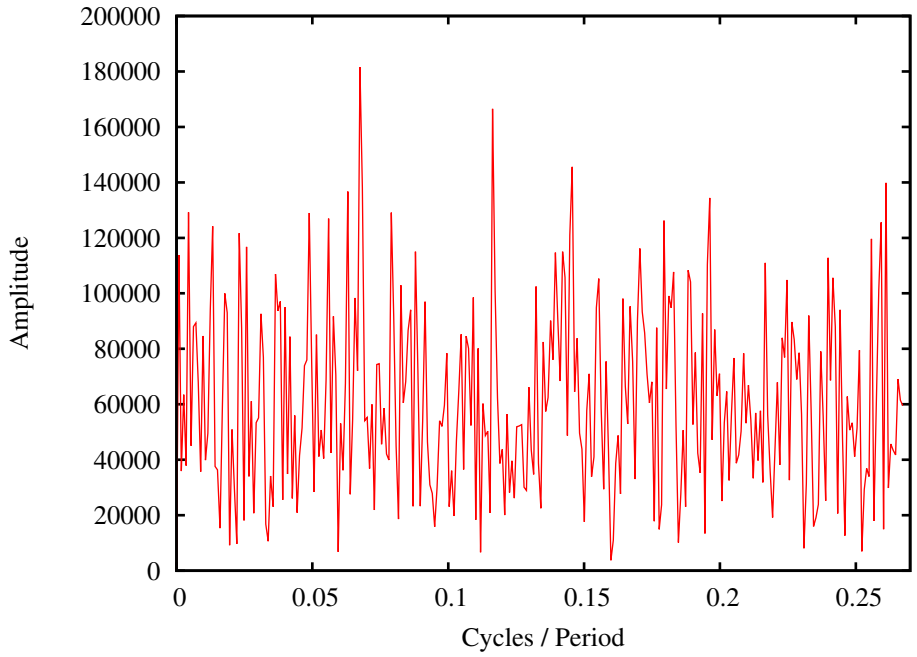

FIGURE 7.11: Fluctuation spectrum of intensities of single pulses of PSR J2208+5500 for one observation epoch (MJD 56298). This spectrum is the sum of fluctuation spectra of individual bins in the pulse region. There is no clear periodicity indicating the presence of pulse drifting.

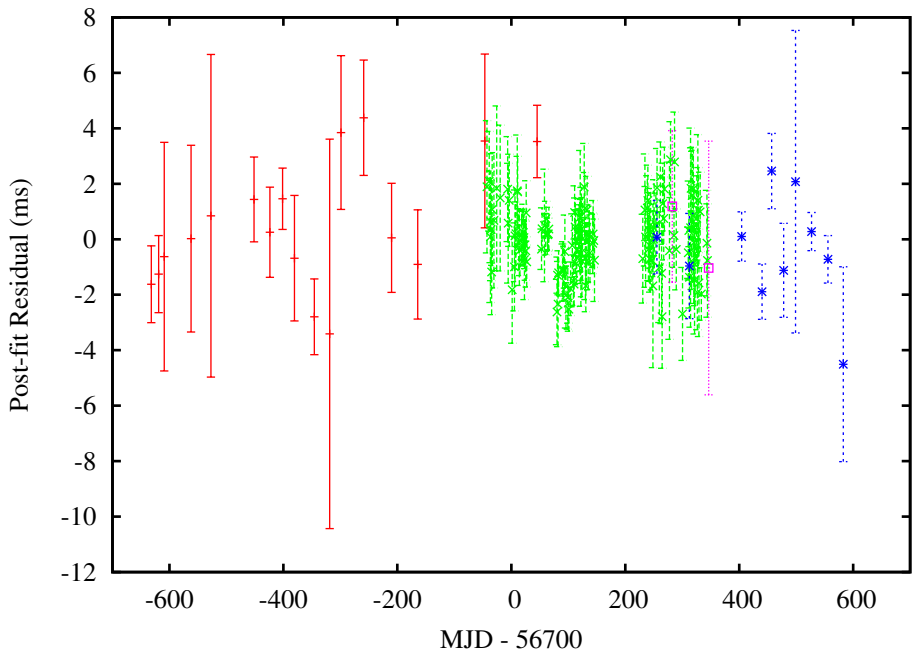

FIGURE 7.12: Post-fit timing residuals obtained for PSR J2208+5500. The RMS post-fit residual obtained was 1132.0 μs. The GMRT TOA measurements are indicated by red crosses (325 MHz), blue asterisks (610 MHz) and magenta squares (1170 MHz), while the ORT TOA measurements are indicated by green crosses (326 MHz).

TABLE 7.5: Timing solution obtained for PSR J2208+5500. For the measured quantities, numbers in brackets indicate 1σ errors in the last significant digit as reported by TEMPO2. For the set quantities, numbers in brackets indicate 1σ errors in the last significant digit as reported by Joshi et al. (2009).

Fit and data-set	
Pulsar name	J2208+5500
MJD range	56068.0—57282.6
Data span (yr)	3.33
Number of TOAs	164
RMS timing residual (μs)	1132.0
Weighted fit	Y
Reduced χ^2	0.94
Measured Quantities	
Pulse frequency, ν (s^{-1})	1.071624701064(8)
First derivative of pulse frequency, $\dot{\nu}$ (s^{-2})	$-8.0246(5)\times10^{-15}$
Dispersion measure, DM (pc-cm^{-3})	105.04(2)
Set Quantities	
Right ascension, α (hh:mm:ss)	22:08:23.72(1)
Declination, δ (dd:mm:ss)	+55:00:08.42(5)
Galactic longitude, l (deg)	100.93858(4)
Galactic latitude, b (deg)	$-0.75066(1)$
Epoch (MJD)	56675
Derived Quantities	
$\log_{10}$(Characteristic age, yr)	6.33
$\log_{10}$(Surface magnetic field strength, G)	12.41
$\log_{10}$($\dot{E}$, ergs/s)	32.53
Assumptions	
Clock correction procedure	TT(TAI)
Solar system ephemeris model	DE405
Binary model	NONE
Model version number	5.00

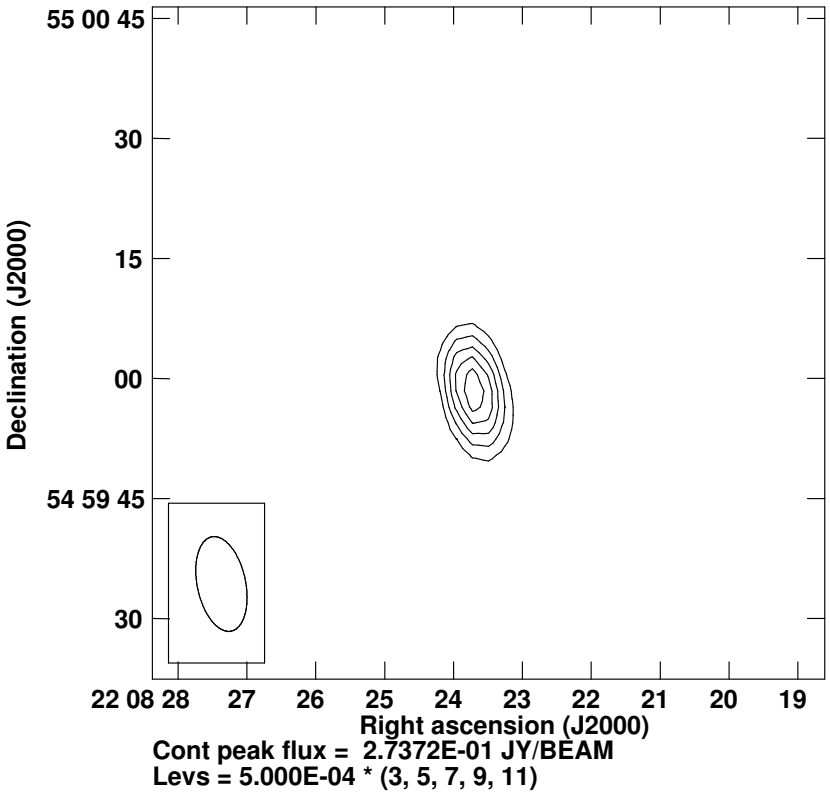

FIGURE 7.13: Interferometric image of PSR J2208+5500 at 325 MHz. The image RMS is 0.5 mJy. The contours are at 1.5, 2.5, 3.5, 4.5 and 5.5 mJy. The epoch of observation is MJD 56081. The synthesized beam is plotted in bottom left corner.

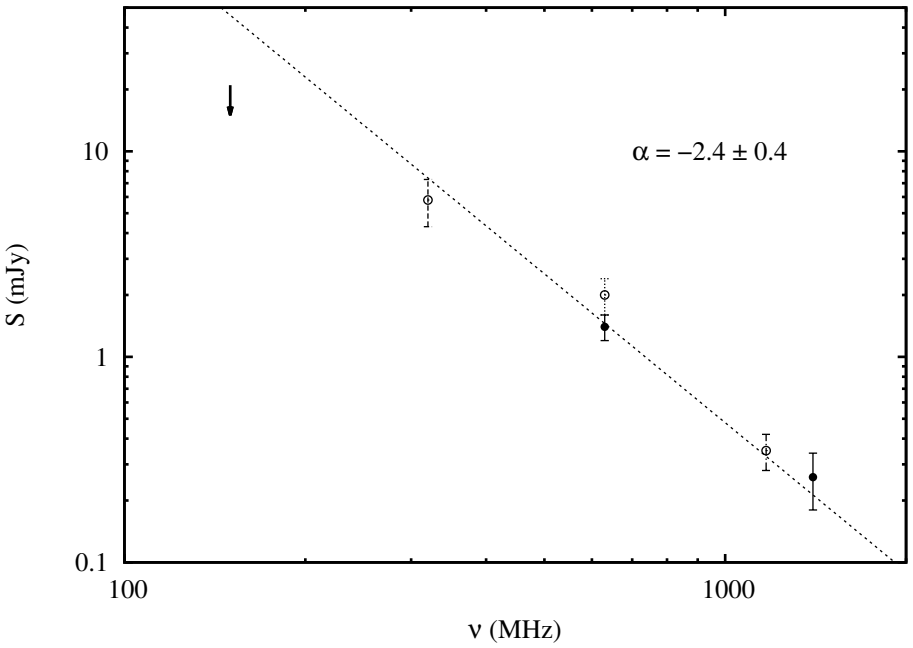

FIGURE 7.14: Spectrum of PSR J2208+5500. The filled circles indicate the measurements obtained by Joshi et al. (2009), while the open circles indicate the measurements using images made at 325, 610 and 1170 MHz with GMRT data. The arrow indicates 6σ flux density upper limit from the TGSS ADR (Intema et al. 2016).

7.4.3 PSR J2217+5733

As was mentioned in Section 7.3.1, the true DM of PSR J2217+5733 was found to be different from the value of 162.75 pc-cm^{-3} quoted by Joshi et al. (2009). The true DM was found to be 131 $\pm$ 10 pc-cm^{-3}, where the error indicates the DM range over which, the harmonic S/N degrades by 3σ. A much better DM estimate was obtained using the multi-frequency timing analysis as mentioned below. The scatter-broadening analysis resulted in $\tau_{\rm sc}$ of 9.7 $\pm$ 0.4 ms at 610 MHz and 61.9 $\pm$ 1.1 ms at 325 MHz. The analysis also returned a $\tau_{\rm sc}$ value much less than the bin width in the pulse profile at 1170 MHz. The results at other two frequencies with reduced χ^2 and number of degrees of freedom (DoF) are shown in Figure 7.15. The results imply a scattering spectral index of -2.9, which is much smaller than -4.4, which is expected for a Kolmogorov spectrum of ISM density perturbations.

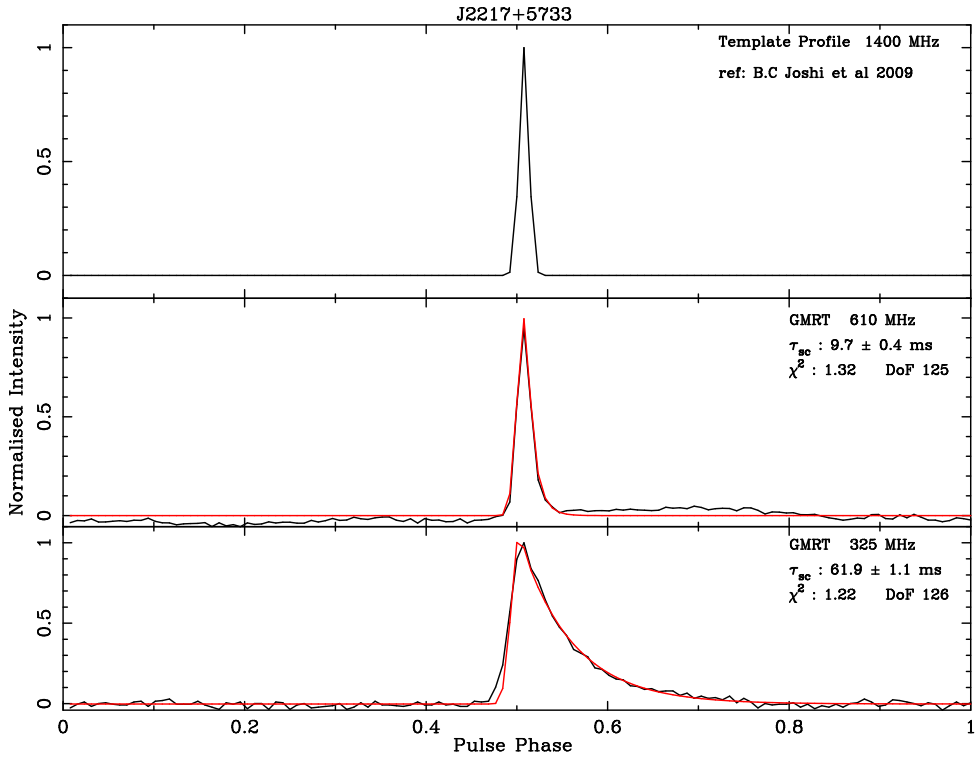

FIGURE 7.15: Estimates of scatter-broadening in PSR J2217+5733. Observed profiles are shown in black and the best fit scattering models are shown in red. The observation frequencies as well as $\tau_{\rm sc}$ estimates with reduced χ^2 and DoF are shown in the top right corner of each panel.

The pulsar, given the large scattering at 325 MHz (as seen in Figure 7.4) combined with the reduced sensitivity of ORT at high declinations, was not detected at ORT even with an integration of 1800 s. Thus, the timing analysis of this pulsar contained TOAs measured only with GMRT. The phase coherent timing solution thus obtained is listed in Table 7.6. The parameters held fixed while performing the fit were obtained from Joshi et al. (2009) with the exception of DM, which was fitted using the timing data. The post-fit residuals thus obtained are shown in Figure 7.16. As is clear from Figure 7.16, the phase connection remains intact even with a gap of more than 250 days.

TABLE 7.6: Timing solution obtained for PSR J2217+5733. For the measured quantities, numbers in brackets indicate 1σ errors in the last significant digit as reported by TEMPO2. For the set quantities, numbers in brackets indicate 1σ errors in the last significant digit as reported by Joshi et al. (2009).

Fit and data-set	
Pulsar name	J2217+5733
MJD range	56081.1—57282.6
Data span (yr)	3.29
Number of TOAs	29
RMS timing residual (μs)	2243.3
Weighted fit	Y
Reduced χ^2	1.20
Measured Quantities	
Pulse frequency, ν (s^{-1})	0.94621311330(3)
First derivative of pulse frequency, $\dot{\nu}$ (s^{-2})	$-5.79(1)\times10^{-16}$
Dispersion measure, DM (pc-cm^{-3})	131.54(3)
Set Quantities	
Right ascension, α (hh:mm:ss)	22:17:55.03(2)
Declination, δ (dd:mm:ss)	57:33:04.0(2)
Galactic longitude, l (deg)	103.47196(8)
Galactic latitude, b (deg)	+0.59943(6)
Epoch (MJD)	56675
Derived Quantities	
$\log_{10}$(Characteristic age, yr)	7.41
$\log_{10}$(Surface magnetic field strength, G)	11.92
$\log_{10}$($\dot{E}$, ergs/s)	31.34
Assumptions	
Clock correction procedure	TT(TAI)
Solar system ephemeris model	DE405
Binary model	NONE
Model version number	5.00

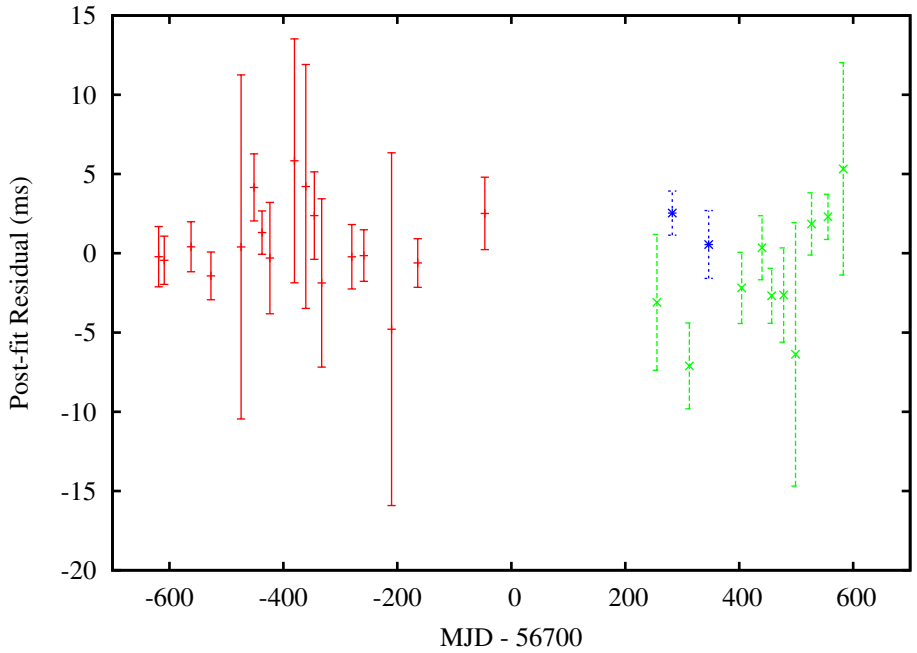

FIGURE 7.16: Post-fit timing residuals obtained for PSR J2217+5733 using data obtained with the GMRT. The RMS post-fit residual obtained was 2243.3 μs. The red crosses indicate TOAs measured at 325 MHz, green crosses indicate TOAs measured at 610 MHz, while blue asterisks indicate TOAs measured at 1170 MHz.

The image of PSR J2217+5733 at 325 MHz made at one epoch is shown in Figure 7.17. The mean flux density measured at 325 MHz from the images is 10 ± 3 mJy. Flux density measurements at other frequencies are given in Table 7.4. Using these flux densities with the ones measured by Joshi et al. (2009), the spectral index was calculated to be -2.4 ± 0.3 (as shown in Figure 7.18), which is shallower but consistent with the value of -2.65 which was obtained by Joshi et al. (2009). The upper limit from TGSS ADR (shown by an arrow in Figure 7.18) may indicate a spectral break or a turnover below 300 MHz.

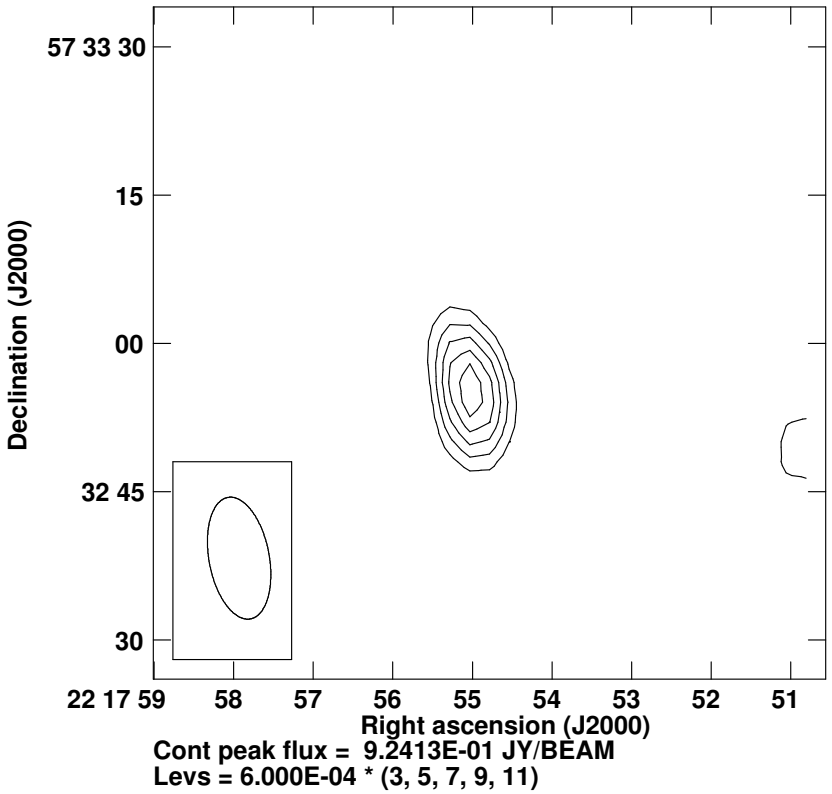

FIGURE 7.17: Interferometric image of PSR J2217+5733 at 325 MHz. The image RMS is 0.6 mJy. The contours are at 1.8, 3.0, 4.2, 5.4 and 6.6 mJy. The epoch of observation is MJD 56081. The synthesized beam is plotted in bottom left corner.

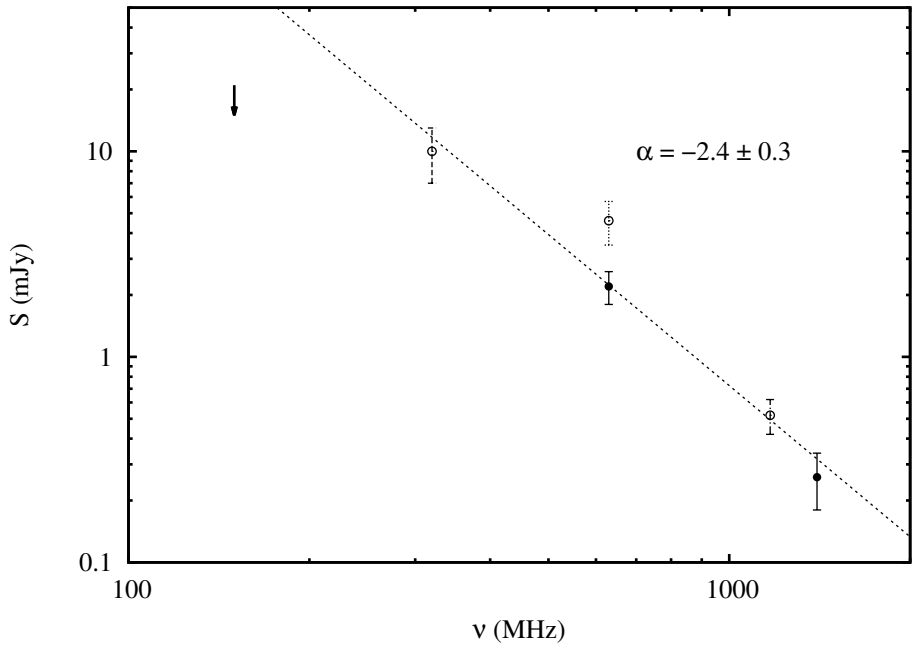

FIGURE 7.18: Spectrum of PSR J2217+5733. The filled circles indicate the measurements obtained by Joshi et al. (2009), while the open circles indicate the measurements using images made at 325, 610 and 1170 MHz with GMRT data. The arrow indicates 6σ flux density upper limit from the TGSS ADR (Intema et al. 2016).

7.4.4 PSR J0026+6320

As was mentioned in Section 7.3.1, the true DM of PSR J0026+6320 was found to be different from the value of 230.31 pc-cm^{-3} quoted by Joshi et al. (2009). The true DM was found to be 244 $\pm$ 10 pc-cm^{-3}, where the error indicates the DM range over which, the harmonic S/N degrades by 3σ. A much better DM was obtained through multi-frequency timing analysis as shown below. This pulsar has so much scatter-broadening that even with the true DM, the profile at 325 MHz is almost unrecognisable from noise. This is shown in Figure 7.20, which shows a very faint detection. This meant that the possibility of detecting the pulsar with ORT was very low. This was corroborated by the actual data. The scattering analysis resulted in $\tau_{\rm sc}$ of 7.5 $\pm$ 0.9 ms at 610 MHz and 47.6 $\pm$ 4.7 ms at 325 MHz. These results along with reduced χ^2 and DoF are shown in Figure 7.19. The very faint nature of the pulse profile at 325 MHz is very well demonstrated by the fact that the profile used for doing the scattering analysis was formed by adding integrated profiles at many epochs. The results imply a scattering spectral index of -2.9, which is much smaller than what is expected for a Kolmogorov spectrum of ISM density perturbations.

The timing solution obtained from 15 TOAs is shown in Table 7.7. The timing residuals obtained are shown in Figure 7.21.

The image of PSR J0026+6320 at 325 MHz made at one epoch is shown in Figure 7.22. The mean flux density measured at 325 MHz from the images is 8 $\pm$ 4 mJy. The large error bar stems from the fact that the image RMS was very large due to RFI. This is also clearly seen in the image shown in Figure 7.22. Flux density measurements at other frequencies are given in Table 7.4. Using these flux densities with the ones measured by Joshi et al. (2009), the spectral index was calculated to be -0.9 ± 0.4 (as shown in Figure 7.23), which is steeper but consistent with the value of -0.8, which was obtained by Joshi et al. (2009). Although the images at 325 MHz did show a point source, the flat spectral index implies low flux density and the uncertainty on the measurement mirrors the same fact. The upper limit from TGSS ADR (shown by an arrow in Figure 7.23) is fairly above the expected

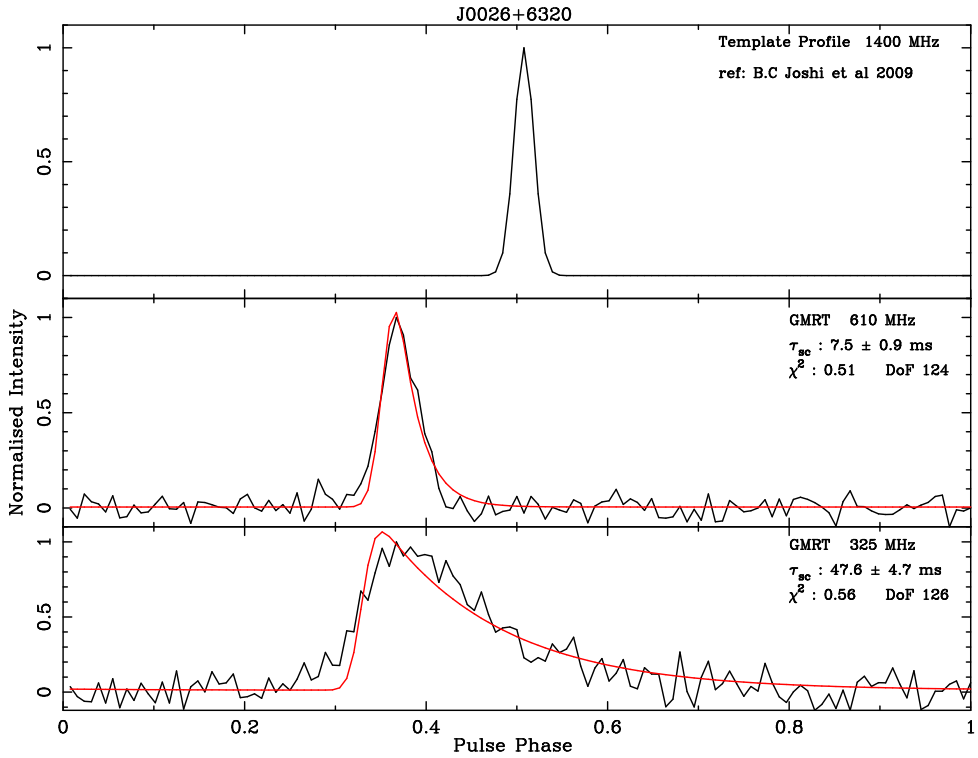

FIGURE 7.19: Estimates of scatter-broadening in PSR J0026+6320. Observed profiles are shown in black and the best fit scattering models are shown in red. The observation frequencies as well as $\tau_{\rm sc}$ estimates with reduced χ^2 and DoF are shown in the top right corner of each panel.

flux density for this pulsar at 150 MHz. Thus, the non-detection at 150 MHz is consistent with expectations.

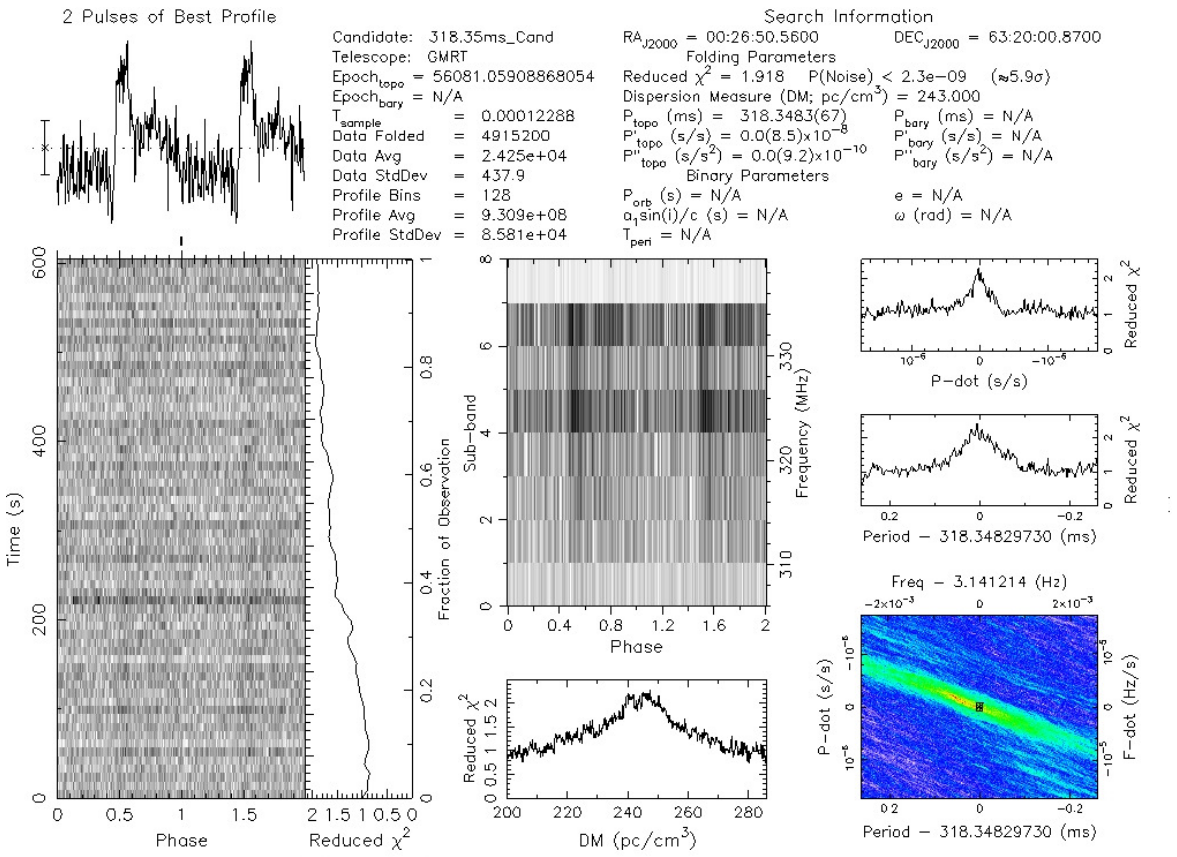

FIGURE 7.20: PRESTO plot showing a very faint detection of PSR J0026+6320 at 325 MHz.

TABLE 7.7: Timing solution obtained for PSR J0026+6320. For the measured quantities, numbers in brackets indicate 1σ errors in the last significant digit as reported by TEMPO2. For the set quantities, numbers in brackets indicate 1σ errors in the last significant digit as reported by Joshi et al. (2009).

Fit and data-set	
Pulsar name	J0026+6320
MJD range	56051.1—57282.6
Data span (yr)	3.37
Number of TOAs	15
RMS timing residual (μs)	1411.9
Weighted fit	Y
Reduced χ^2	1.03
Measured Quantities	
Pulse frequency, ν (s^{-1})	3.1411201226(2)
First derivative of pulse frequency, $\dot{\nu}$ (s^{-2})	$-1.486(5)\times10^{-15}$
Dispersion measure, DM (pc-cm^{-3})	245.06(6)
Set Quantities	
Right ascension, α (hh:mm:ss)	00:26:50.561(8)
Declination, δ (dd:mm:ss)	63:20:00.87(5)
Galactic longitude, l (deg)	120.17644(3)
Galactic latitude, b (deg)	+0.59367(1)
Epoch (MJD)	56675
Derived Quantities	
$\log_{10}$(Characteristic age, yr)	7.52
$\log_{10}$(Surface magnetic field strength, G)	11.35
$\log_{10}$($\dot{E}$, ergs/s)	32.27
Assumptions	
Clock correction procedure	TT(TAI)
Solar system ephemeris model	DE405
Binary model	NONE
Model version number	5.00

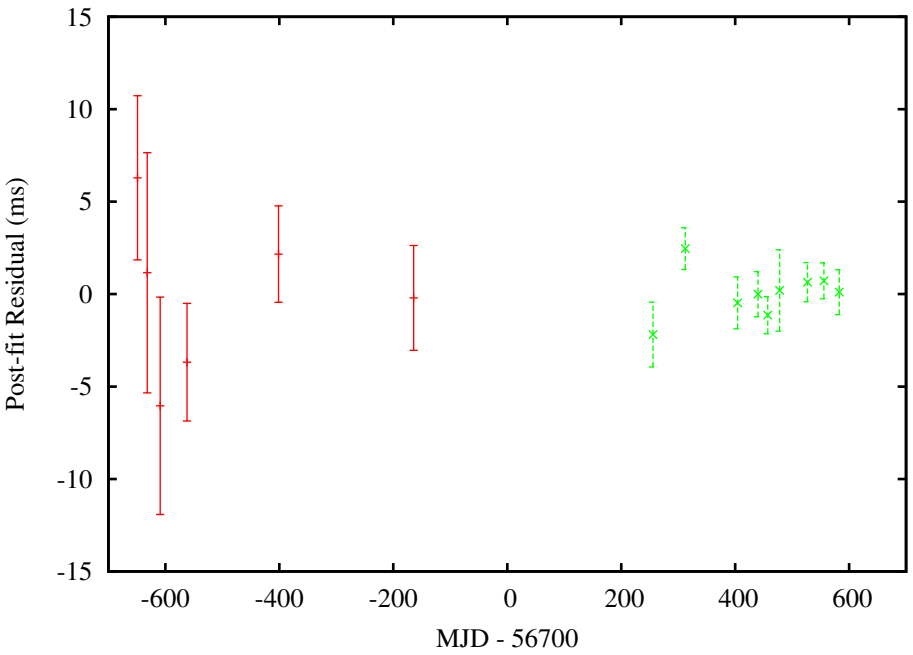

FIGURE 7.21: Post-fit timing residuals obtained for PSR J0026+6320 using data obtained with the GMRT. The RMS post-fit residual is 1411.9 μs. The red crosses indicate TOAs measured at 325 MHz, while green crosses indicate TOAs measured at 610 MHz.

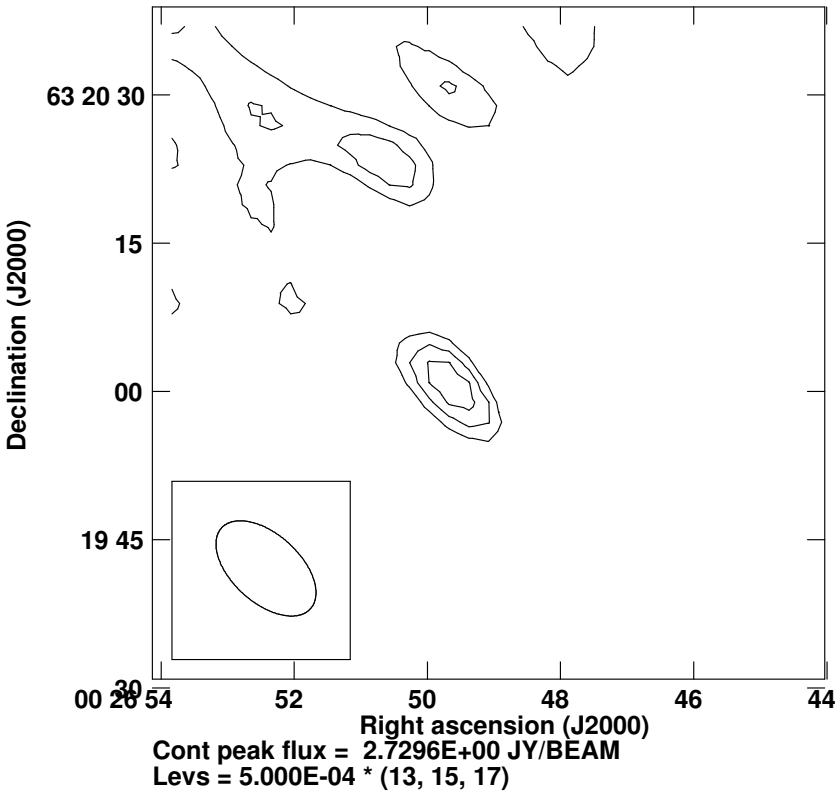

FIGURE 7.22: Interferometric image of PSR J0026+6320 at 325 MHz. The image RMS is 1.4 mJy. The contours are at 6.5, 7.5 and 8.5 mJy. The epoch of observation is MJD 56298.5. The synthesized beam is plotted in bottom left corner.

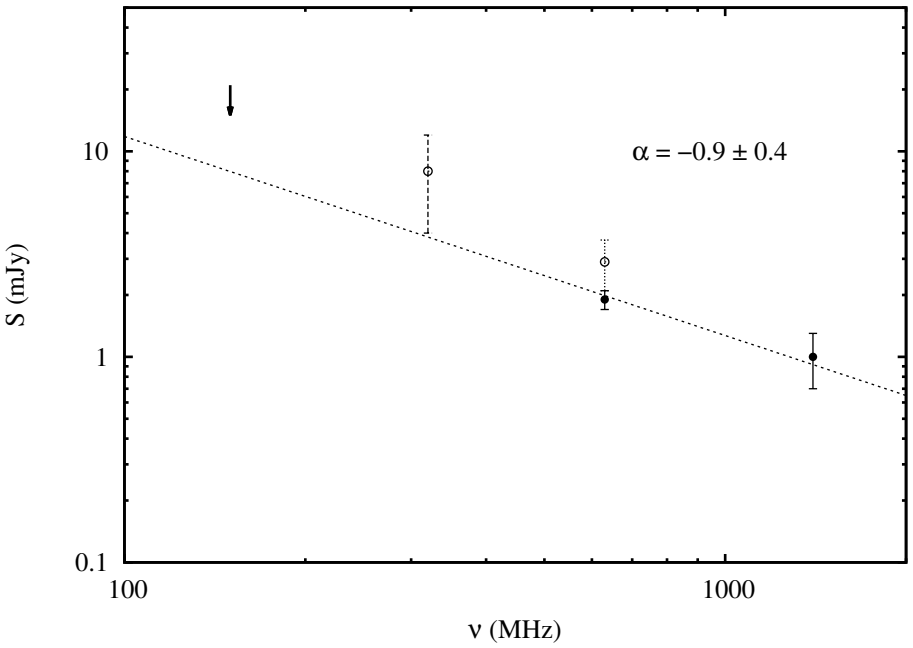

FIGURE 7.23: Spectrum of PSR J0026+6320. The filled circles indicate the measurements obtained by Joshi et al. (2009), while the open circles indicate the measurements using images made at 325 and 610 MHz with GMRT data. The arrow indicates 6σ flux density upper limit from the TGSS ADR (Intema et al. 2016).

7.5 Discussion

Joshi et al. (2009) suspected that PSR J2208+5500 shows nulls but did not have enough S/N for single pulses to estimate the true nulling fraction. They could only put a lower limit of 7.5% from their data. With steep spectral index and sensitive PA data at 325 MHz with the GMRT, the single pulse S/N was sufficient to show that this pulsar indeed shows nulls. In fact, the estimated nulling fraction of 50% indicates very significant nulling. The apparent lack of drifting subpulses in this pulsar is interesting and worth following-up further. Drifting subpulses typically denote conal component and core only pulsars typically do not show nulling (Rankin 1986). The case of PSR J2208+5500 is interesting in this regard because it shows a large nulling fraction but no apparent drifting subpulse structure. Thus, polarization profiles obtained at low radio frequencies would help in determining if the pulse component seen in this pulsar is from the core or cone or a mixture of both.

All of these pulsars were discovered at 610 MHz, where the pulse smearing due to dispersion is much less severe. This led to a coarse estimate of the pulsar DM using search data only. With 325 MHz observations, the inverse square dependence of the dispersion smearing with frequency, allowed for a much better measurement of the pulsar DM for two of the three pulsars. This underlines the importance of low frequency follow-up observations for a complementary study of pulsars discovered at high radio frequencies. The scatter-broadening spectral indices for PSR J2217+5733 and PSR J0026+6320 indicate that, despite higher scattering percentage (with respect to the rotation period), these pulsars lie in a region of significantly low scattering.

Simultaneous multi-frequency observations done with the GMRT and ORT have proven to be very useful in determining the coherent timing solution as well as demonstrate that even with a single polarization detector, ORT is capable of providing high quality timing data for practical applications. This is demonstrated by the very precise DM determination of the order of 0.01 pc-cm^{-3}. This accuracy was achieved with a very few TOAs obtained at frequencies higher than 325 MHz.

In fact, the DM correction for PSR J2208+5500 could be obtained only after multi-frequency timing analysis and not otherwise. The natural extension of this experiment would be to have a timing follow-up program for some of the MSPs, which are a part of the IPTA. The success of such an experiment would prove to be very useful for the timing array experiments as ORT can provide timing data at a much higher cadence and provide complementary data at low radio frequency, which will be really helpful to keep a track of the DM variations. The only point to note in this regard is the need for determining the instrumental offsets to an accuracy much better than the currently estimated value of 0.5 ms.

Simultaneous imaging observations carried out at the GMRT were helpful in determining the spectral index through well calibrated flux densities. This demonstrates that simultaneous multi-frequency imaging and time series follow-up observations of known pulsars help in precise determination of their parameters.

Chapter 8

Imaging Study of a Pulsar Field

8.1 Introduction

During the follow-up timing observations of the GMRT pulsar, PSR J1838+1523 done with the GMRT, data were acquired with the beamformer as well as the correlator. The full analysis of the time series data as well as some imaging data is described in detail in Chapter 6. The follow-up observations at 325 MHz carried out with the GMRT spanned over three years with more or less uniform cadence of about two weeks. Each of the observations consisted of a 30 minute scan on the pulsar. This allowed a snapshot image of the full field (about a degree across) to be made using the simultaneous imaging data. As explained in Section 4.4.4, 4.4.5 and 4.4.6, the requisite flagging and calibration was done using FLAGCAL. The imaging was done using AIPS. The continuum source corresponding to PSR J1838+1523 was identified with the help of images as well as the position obtained from the timing analysis of the ORT data (see Section 6.5 and 6.6 for more details). In the time series analysis of the GMRT data, it was noticed that PSR J1838+1523 was not detectable in a few scans. However, it was still present as a point source in the images made on the same epoch. This demanded very careful measurement of the flux density of the continuum source corresponding to the pulsar. These were done using the AIPS task JMFIT as described in Section 6.5. As the flux

and phase calibration was done with multiple calibrator sources over the full data set, the consistency of the calibration across all the observations needed to be established. To do this, 29 point sources having a range of flux densities were selected from the field and their flux densities were also measured from images made in each epoch. In this chapter, we describe the unique dataset thus obtained and present variability study of these point sources at 325 MHz.

8.2 Observations

The observations were done at 325 and 610 MHz with the GMRT. These spanned about three years between MJD 55744−56745 at 325 MHz and between MJD 56955−57282 at 610 MHz. The cadence was about two weeks. The rationale as well as typical flow of observations are described in detail in Section 3.3.1.2. Basic observational characteristics are listed in Table 3.2. Detailed information about each epoch can be found in Table 6.1. The flux calibrators observed during the observations were 3C48 and 3C286, while J1822−096, J1829+487, J1924+334, J1859+129 and J1830−360 were observed as phase calibrators.

8.3 Data Analysis

The 29 sources selected for this study were chosen such that they had counterparts at 1.4 GHz in the NVSS. The flux densities and their uncertainties at 1.4 GHz and were obtained from the NVSS catalog[1]. The flux densities at 325 MHz were obtained by fitting an elliptical Gaussian to the point sources using the AIPS task JMFIT. The smallest Gaussian to be fit was defined by the synthesized beam for the particular data set. The total flux density contained inside the best-fit elliptical Gaussian region with the centroid at the peak intensity was recorded as the flux density of the source at 325 MHz. This flux density was corrected for the telescope primary beam response. This was done for an image at each epoch independently.

[1]The catalog is available at: www.vizier.u-strasbg.fr/viz-bin/VizieR?-source=%20NVSS

In all, 32 "good" images were obtained in which, the flux and phase calibration was reliable and the RMS in the image did not vary much over the beam area. These measurements provided a type of "time series" for the selected 29 sources in the form of flux densities measured repeatedly over a time span of about 1000 days. In order to quantify the variability of the sources, their mean flux densities were obtained by calculating a mean of the respective time series and the uncertainty due to variation (if any) was estimated from the RMS of this time series. The errors in flux densities were fixed at 15%, which was the maximum percentage of random variation seen in the 325 MHz data (see Figure 8.4 for more details). The percentage of flux density variation was calculated by converting the RMS into percentage of the mean flux density of the particular source. The comparison of this uncertainty to the uncertainty on each measurement allowed a robust estimate of the variability of the source as well as establishing the calibration for all the images independently. Due to a much smaller data set at 610 MHz (6 epochs), such a determination of variability was not reliable. In addition, due to a much smaller field of view (4 times smaller in area), flux densities for only 12 out of 29 sources could be measured at 610 MHz.

Five of these 29 NVSS sources had flux densities measured at other radio frequencies. They were J183751+152616, J183551+151546, J184057+150655, J183853+145514 and J184241+152134. These flux densities were obtained from the NASA[2]/IPAC[3] extragalactic database (NED)[4]. While choosing the flux densities from the NED, only those measurements were considered, which had reported uncertainties. The measurements without uncertainties were not considered for analysis. NVSS J183751+152616 and 11 more sources had flux densities measured at 610 MHz. For these 16 sources, spectral indices were calculated by straight line fits to the log(S)−log(ν) plot using a single power law model. These fits included flux densities measured with the GMRT. The resultant spectra are shown in Figure 8.1 and 8.2.

[2]National Aeronautics and Space Administration
[3]Infrared Processing and Analysis Center
[4]The database is available at www.ned.ipac.caltech.edu

8.4 Results

The 1.4 GHz flux densities with uncertainties obtained from the NVSS catalog and the flux densities with uncertainties obtained from the GMRT data at 325 and 610 MHz for the 29 sources under study are listed in Table 8.1.

TABLE 8.1: The flux densities and uncertainties for the NVSS sources included in this study. The NVSS denominations denote the positions of the sources with an error of 45" on both RA and DEC.

Sr. No.	NVSS Denomination	$S_{1.4\ GHz}$ (mJy)	$\sigma_{1.4\ GHz}$ (mJy)	$S_{610\ MHz}$ (mJy)	$\sigma_{610\ MHz}$ (mJy)	$S_{325\ MHz}$ (mJy)	$\sigma_{325\ MHz}$ (mJy)	α^*	Flux Variation at 325 MHz (%)	Distance from phase center (deg)
1	184114+154308	28.5	1.0	-	-	82.5	9.8	−0.72	12	0.85
2	183823+154458	52.2	2.0	76.2	11.4	156.6	19.8	−0.7 ± 0.1	13	0.68
3	184046+153342	22.5	1.2	-	-	51.2	6.5	−0.56	13	0.66
4	183729+153210†	9.5	0.6	8.6	1.3	20.5	4.3	−0.1 ± 0.4	21	0.59
5	183708+153141	12.1	0.6	15.1	2.3	25.7	6.6	−0.4 ± 0.1	26	0.64
6	183715+153015	8.4	0.5	13.4	2.0	20.8	3.5	−0.61 ± 0.03	17	0.60
7	184241+152134††	202.4	6.1	-	-	627.4	72.8	−0.69 ± 0.05	12	0.97
8	184028+152236	71.7	2.2	189.9	28.5	228.0	19.3	−0.8 ± 0.1	8	0.48
9	183909+152512	18.3	0.7	38.3	5.7	45.4	4.4	−0.64 ± 0.09	10	0.34
10	183820+152713	32.6	1.4	37.5	5.6	46.7	6.2	−0.23 ± 0.03	13	0.40
11	183751+152616††	63.4	2.0	154.8	23.2	249.8	19.5	−0.94 ± 0.03	8	0.45
12	183850+152214	7.0	0.5	9.2	1.4	8.3	1.5	−0.2 ± 0.1	18	0.29
13	183658+152318	6.6	0.5	-	-	21.8	2.8	−0.81	13	0.59
14	184024+151211	22.1	0.8	63.2	9.5	80.9	6.1	−0.9 ± 0.1	8	0.38
15	183637+151830	8.2	0.5	-	-	31.9	4.8	−0.93	15	0.63
16	183551+151644	86.4	2.6	-	-	652.5	73.6	−1.38	11	0.80
17	183551+151546††	965.6	31.5	-	-	3444.2	395.4	−0.80 ± 0.04	11	0.80
18	184057+150655††	37.1	1.5	-	-	72.8	6.2	−0.4 ± 0.1	9	0.50
19	183959+150529	9.7	1.0	15.6	2.3	14.9	1.7	−0.3 ± 0.1	11	0.25
20	183858+150451	6.2	0.5	14.2	2.1	17.8	1.2	−0.72 ± 0.09	7	0.001
21	184023+145929	57.3	2.1	-	-	160.2	13.3	−0.70	8	0.37
22	183923+145820	5.0	0.5	-	-	17.5	1.5	−0.86	9	0.15
23	183853+145514††	88.8	2.7	-	-	267.8	19.3	−0.76 ± 0.01	7	0.16

Continued on next page

Table 8.1 – continued from previous page

Sr. No.	NVSS Denomination	$S_{1.4\ \mathrm{GHz}}$ (mJy)	$\sigma_{1.4\ \mathrm{GHz}}$ (mJy)	$S_{610\ \mathrm{MHz}}$ (mJy)	$\sigma_{610\ \mathrm{MHz}}$ (mJy)	$S_{325\ \mathrm{MHz}}$ (mJy)	$\sigma_{325\ \mathrm{MHz}}$ (mJy)	α^*	Flux Variation at 325 MHz (%)	Distance from phase center (deg)
24	184100+144858	9.6	0.6	-	-	29.4	3.5	−0.77	12	0.57
25	184038+144825	22.4	1.1	-	-	79.8	7.8	−0.86	10	0.50
26	184033+144215	43.3	1.4	-	-	139.3	11.5	−0.80	8	0.55
27	183914+144106	43.8	1.4	-	-	106.8	7.3	−0.61	7	0.40
28	184114+143644	32.7	1.1	-	-	110.7	11.1	−0.83	10	0.74
29	184115+143536	17.6	0.7	-	-	60.0	8.4	−0.84	14	0.75

* α is reliable only if flux densities were measured at more than two frequencies.

† The 610 MHz flux density for this source was much lower than expected, leading to a very uncertain α.

†† Flux densities at frequencies other than listed here were obtained from NED.

Figure 8.1 and 8.2 also show the best-fit power law model as well as the spectral indices obtained for all 16 sources. 11 out of the 16 sources have measured flux densities at two frequencies in our study and spectral indices are being reported for these sources for the first time. The spectral indices are also listed in Table 8.1. The GMRT measurements agree well with the overall spectral trends for the five sources having multiple flux density measurements. This implies that the flux density measurements obtained with the GMRT data do not have offsets or scaling errors and are reliable. Another method to establish the reliability of the measured flux densities is to plot the systematic variation as a function of the flux densities. This is shown in Figure 8.3. As is expected for reliable calibration, the scatter in the plot goes down for sources having higher flux density.

With the reliability of the flux density measurements established through spectra and scatter in the systematic variations, one can now quantify the variability of these sources. The measurement errors on the flux densities were typically around 15% for all the maps. This number arises from the average of uncertainty provided by JMFIT for each measurement. The measurement error for very strong sources (with S/N of more than 20 or so) would be smaller than this. The flux density scale used for calibration was given by Baars et al. (1977). This scale has an absolute error of 5%. Thus, the maximum uncertainty provided by the measurement error for the flux density measurements was 15%. Figure 8.4 shows a histogram of systematic variations in the flux densities for all the 29 sources under study. As is clearly visible, 25 out of 29 sources have systematic variation, which is less than or equal to the maximum measurement error. This implies that the variation of flux densities for these sources is definitely less than 15%. On the other hand, the histogram also reveals that for two sources, the variability is slightly higher than the measurement error. These sources are NVSS J183715+153015 with a variability of 17% and NVSS J183850+152214 with a variability of 18%. Two more sources show much more variability than all of these sources. These sources are NVSS J183729+153210 with a variability of 21% and NVSS J183708+153141 with a variability of 26%. Now considering the fact that the uncertainties reported by JMFIT are typically at least 2−3 times the RMS in the region adjacent to the

particular source, the 15% measurement error reported by the task is already a robust estimate of the variability. Thus, the variabilities of 17% and 18% are somewhat on the borderline of high variability and hence, NVSS J183715+153015 and J183850+152214 can not be reliably called as variable sources. With a similar argument, NVSS J183729+153210 and J183708+153141 can definitely be classified as variable sources.

In addition to variability, the maps were also scrutinized for the presence of transient sources. No such source was detected. Apart from PSR J1838+1523, no source was seen to switch off or on at any epoch. Given that the map RMS did not vary much from epoch to epoch, we are confident that there are no transient sources upto a flux density level of 1.5 mJy.

8.5 Discussion

Pulsar timing observations are typically carried out using large single dish telescopes. Thus, the timing follow-up carried out with the GMRT, which also allowed simultaneous imaging data to be recorded, forms a unique data set. Such imaging observations would usually be carried out for fields having particular sources of interests. While this field does not have such objects, the presence of a newly discovered pulsar enabled the variability study to be carried out. The flux density measurements done for 29 point sources have enabled us to put stringent constraints on the variability of radio frequency flux densities for all of them. Another such long term study of variability at low radio frequencies was carried out by Salgado et al. (1999). In their campaign, which ran over 14 years, they studied 33 known extragalactic radio sources simultaneously at 318 and 430 MHz with the Arecibo telescope. While most of the sources studied by Salgado et al. (1999) showed variability, our study shows that most of the sources are not variable. Salgado et al. (1999) chose known extragalactic sources, mostly active galactic nuclei (AGN) because they were either known or suspected to be variable sources. Our sources were were not subject to any such criteria. This might explain the low

number of variable sources in our study.

There were two very closely spaced pairs of sources in the field of view. They were NVSS J183551+151644 − J183551+151546 and NVSS J184114+143644 − J184115+143536. Out of these, the second pair of sources show almost identical spectral indices with a flux ratio of 1.85 while the first pair of sources show very different spectral indices. In fact, these sources are separated by only about 1'. Thus, the flux density measurements for NVSS J183551+151546 could be contaminated by the flux of NVSS J183551+151644 at lower radio frequencies due to large telescope beams. The implied spectral index of −1.38 for NVSS J183551+151644 could mean that the contamination at radio frequencies lower than 300 MHz would be even more. In this case, the flat spectral index of −0.8 for NVSS J183551+151546 could have resulted from flux density contamination at low radio frequencies. If the contamination from NVSS J183551+151644 is removed, there is a possibility that NVSS J183551+151546 may have a spectral turnover at frequencies lower than 300 MHz.

Three of the four variable sources mentioned above have flat spectra. These are implied by using the flux density measurements at only two frequencies. The most variable sources, NVSS J183729+153210 and J183708+153141 have spectral indices of about −0.5, while the next most variable source, NVSS J183850+152214 has a spectral index of nearly zero within the measurements errors. None of these have counterparts at any other electromagnetic band as seen through the Set of Identifications, Measurements and Bibliography for Astronomical Data (SIMBAD)[5], which is a database for astronomical data for all electromagnetic bands. The amount of variability (15% to 25%) of these sources matches well with the range of variability shown by radio loud quasars and BL Lac objects (see Salgado et al. 1999; Barvainis et al. 2005, for example). Additionally, the implied flat spectra indicate that these sources could be potential flat spectrum radio quasars (FSRQ). FSRQs are radio quasars in which, the line of sight goes very close to the

[5]simbad.u-strasbg.fr/simbad/

axis of the radio jet. As the flow in the radio jet is not stationary, these sources typically show a lot of variability as well as occasional outbursts. This happens due to the inherent clumpy nature of the gas clouds falling in the central supermassive black hole. Such sources are identified through optical variability as well as the broad optical spectral lines. The lack of optical counterparts in the current archival data prevents straight forward confirmation but our findings make such observations very prudent.

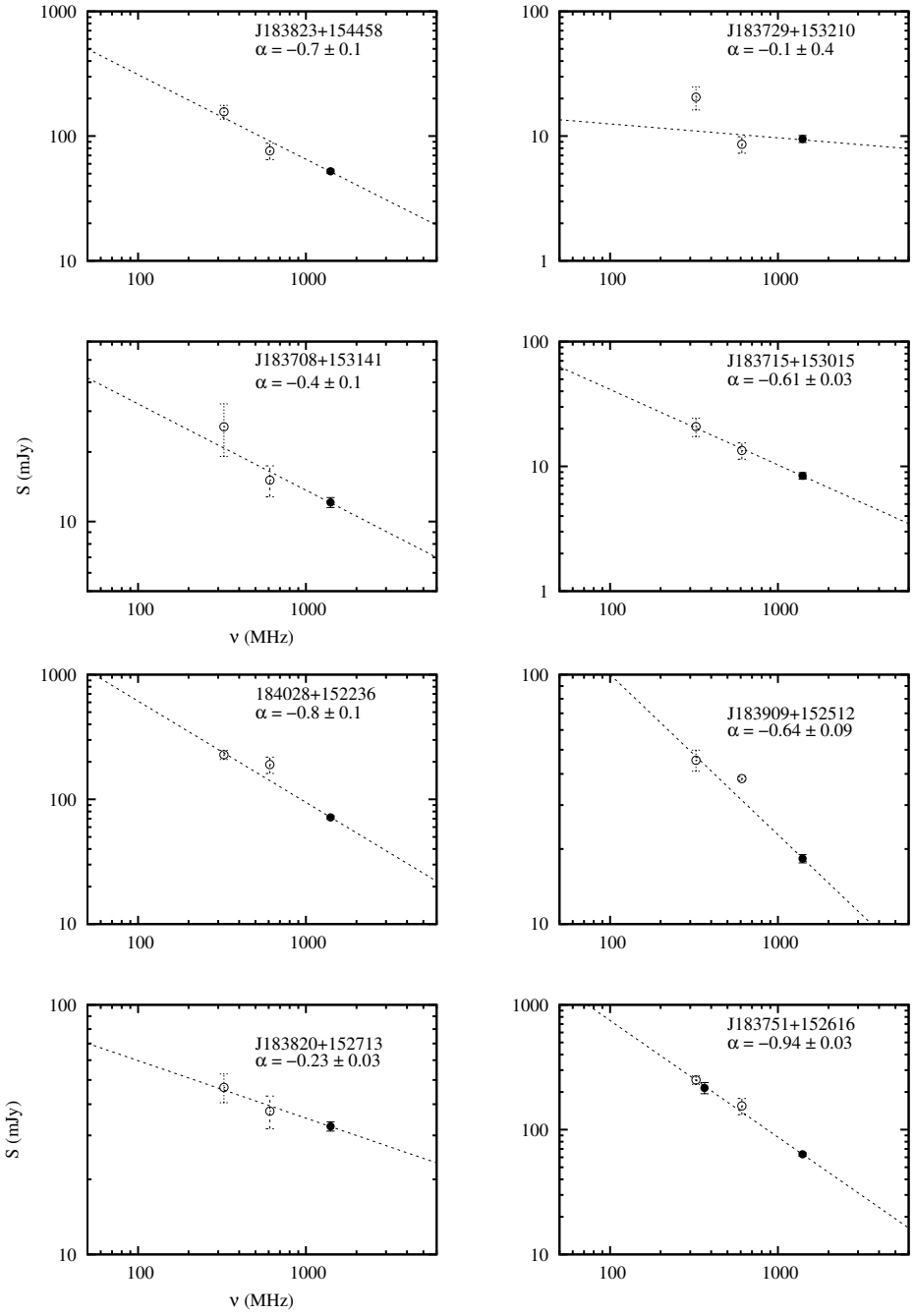

FIGURE 8.1: Spectra of the NVSS sources under study. For all the plots, abscissa is frequency in MHz and ordinate is flux density in mJy. In each plot, filled circles represent measurements obtained from NED, while open circles represent GMRT measurements at 325 and 610 MHz. Dashed line represents best-fit power law model. The NVSS denomination and best fit spectral index is mentioned towards the top right corner of each plot.

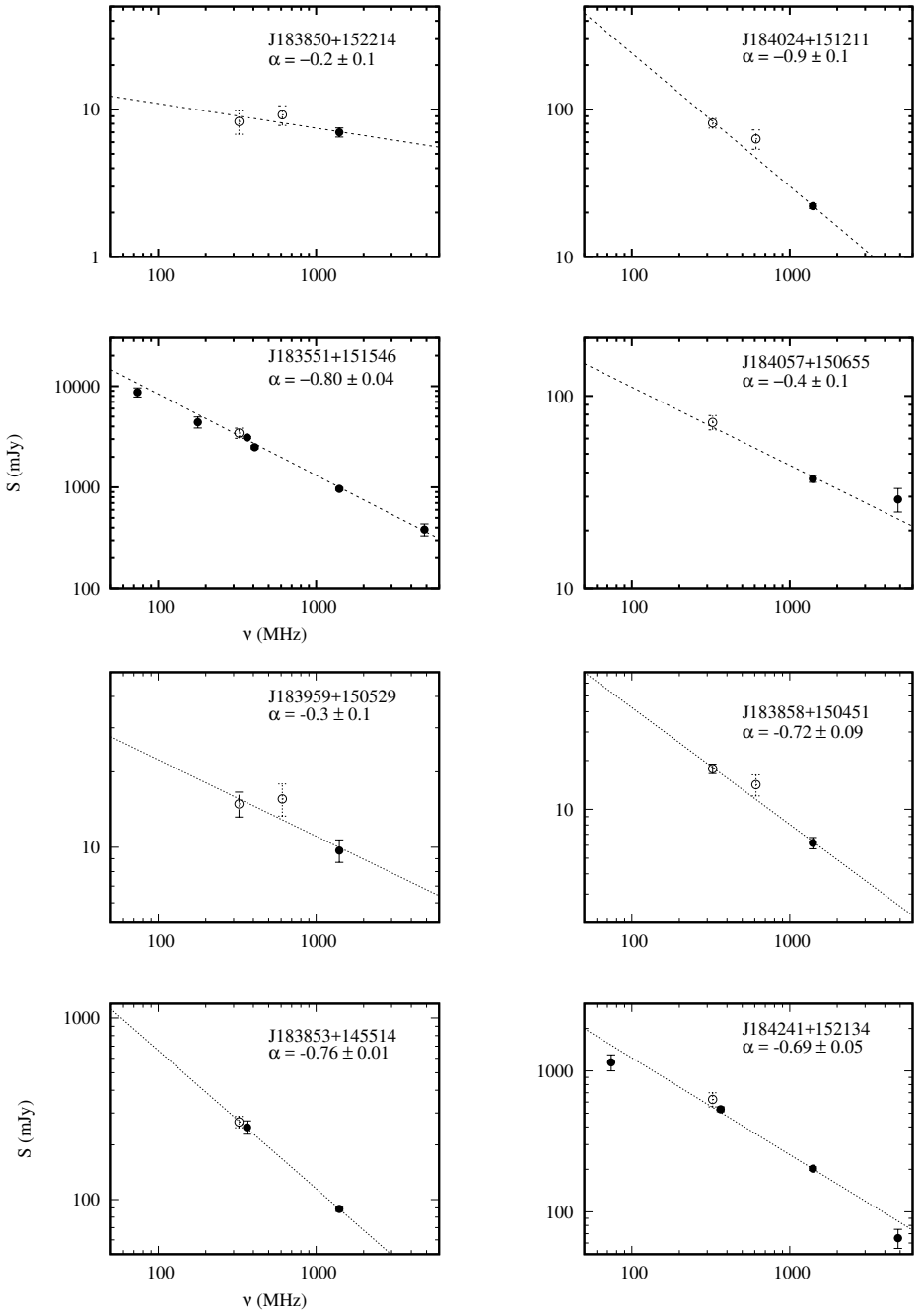

FIGURE 8.2: Spectra of the NVSS sources under study. For all the plots, abscissa is frequency in MHz and ordinate is flux density in mJy. In each plot, filled circles represent measurements obtained from NED, while open circles represent GMRT measurements at 325 and 610 MHz. Dashed line represents best-fit power law model. The NVSS denomination and best fit spectral index is mentioned towards the top right corner of each plot.

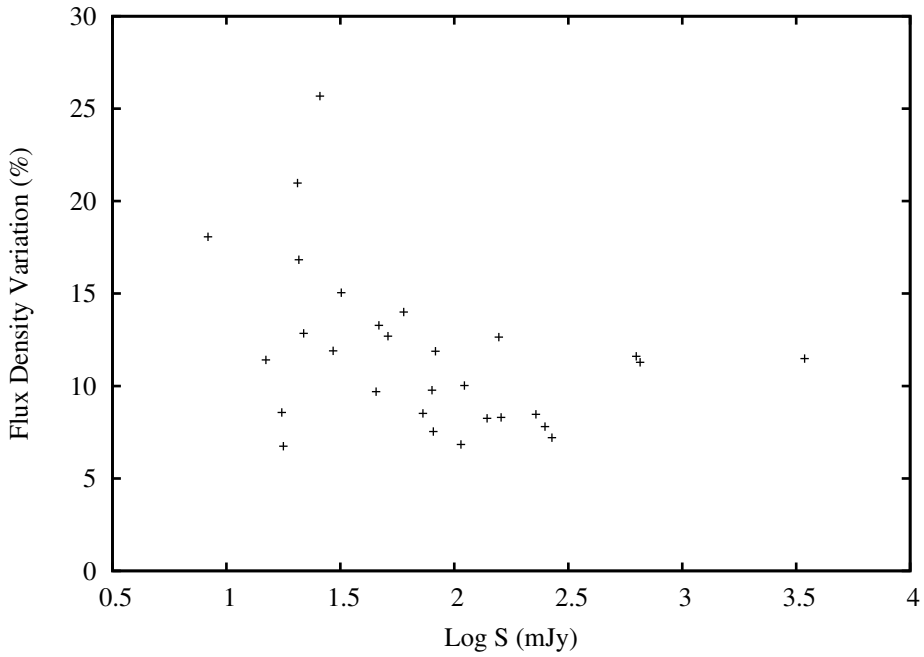

FIGURE 8.3: Flux density variation as a function of source flux density. As expected, the scatter in the plot goes down for higher flux densities.

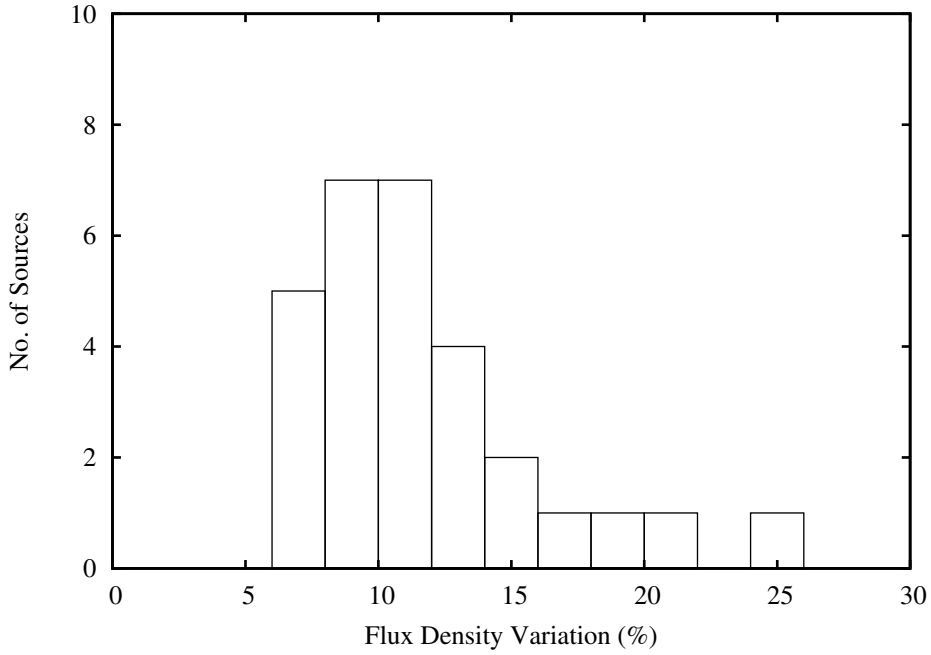

FIGURE 8.4: A histogram of systematic flux density variation.

Chapter 9

Radio Observations of HESS J1818–154/SNR G15.4+0.1

9.1 Introduction

TeV γ-rays were detected recently by many instruments such as HESS, Major Atmospheric Gamma Imaging Cherenkov Telescopes (MAGIC), Very Energetic Radiation Imaging Telescope Array System (VERITAS), from many Galactic SNRs. Some of these SNRs were found to harbour PWNs in their central regions. Such SNRs have come to be known as *composite SNRs*. These places are excellent cosmic particle accelerators. The correlation between extended high energy emission and SNRs and/or PWNs is currently very poorly identified. A broad band observational approach involving careful, multi-frequency observations have the potential to reveal the underlying mechanism powering these sources. This may, in turn, help in understanding the origin of some fraction of the cosmic rays.

The VHE γ-ray emission in SNRs can be explained by two different types of mechanisms. One of them is the interaction of molecular gas with the supernova shock front. In this interaction, cosmic rays, accelerated through the Fermi acceleration mechanism (i.e. energy gained through multiple crossings of the supersonic shock

wave front), collide with the molecules in the cloud. This interaction produces π^0 mesons. They decay further, to produce the VHE γ-rays. As this interaction involves molecules, which are formed from hadrons, this model is called as the *hadronic* model. The second mechanism is the inverse Compton scattering of the cosmic microwave background (CMB) photons by the highly energetic positrons and electrons present in the particle wind produced by a rotating neutron star. As the particles responsible for γ-ray emission are electrons and positrons, which are leptons, this model is called as the *leptonic* model. Out of the two, the second mechanism is of more interest to us as it entails the presence of a rotating neutron star. In addition to providing an opportunity to detect radio pulsations, the particle wind of the neutron star may power a PWN, which may be detected from the continuum imaging of the SNR, as a central, diffuse patch of radio emission. The GMRT, with its unique ability to perform simultaneous imaging and pulsar mode observations at multiple frequencies, is therefore, the most obvious choice for doing radio frequency observations of such composite SNRs. With this motivation, we observed a suspected composite SNR G15.4+0.1 (Hofverberg et al. 2011) with the GMRT.

The source G15.4+0.1 was first discovered and identified as an SNR in a Galactic survey carried out with the VLA at 90 cm (Brogan et al. 2006). It was also detected at 20 cm by Helfand et al. (2006) in their Multi-Array Galactic Plane Imaging Survey (MAGPIS). It has an almost circular shell with a diameter of about 15′ with a brighter northern side. The southern side is less bright with a break-out morphology clearly visible (see Figure 9.1). Hofverberg et al. (2011) detected TeV γ-ray emission from an extended source inside the radio shell of SNR G15.4+0.1 with the HESS, which is an array of atmospheric Cherenkov telescopes. The source was identified as HESS J1818−154. The extent of the γ-ray emission was about 8.5′ and was totally contained within the radio shell of the SNR. This led Hofverberg et al. (2011) to propose that the VHE γ-ray emission (with photon energy > 100 GeV) may be originating from a PWN, powered by a yet un-detected, rotating neutron star. While the image obtained by Helfand

et al. (2006) at 20 cm, shows[1] some evidence for central emission supporting a PWN, spurious emission from a very strong nearby source makes the identification somewhat uncertain. The lack of good quality images at multiple frequencies, combined with the possibility of an associated rotating neutron star, made this an interesting source. The detection of the putative pulsar would confirm the source of the VHE γ-rays to be the PWN. Even non-detection of the pulsar combined with imaging observations would provide a complete picture of the SNR in terms of its energetics and help in putting better constrains on the source of the VHE emission. This led us to propose simultaneous imaging and pulsar mode observations at 610 and 1420 MHz at the GMRT. These are described in the next section. Based on the 1420 MHz imaging data from GMRT, our collaborators produced the first high resolution image of G15.4+0.1 at 1420 MHz (Castelletti et al. 2013).

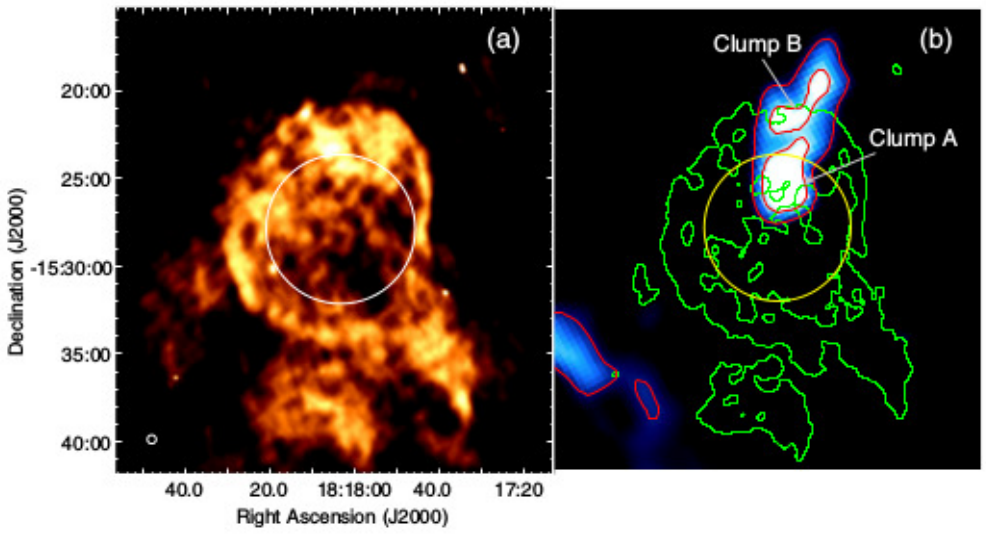

FIGURE 9.1: (a) First high resolution image of SNR G15.4+0.1 at 1420 MHz. The resolution of the image is about 15" and the synthesized beam size is shown in the bottom left corner. (b) Integrated channel map of ^{13}CO (J = 1−0) from Galactic Ring Survey (GRS) data over a velocity range of 46−50.3 km-s^{-1}. The 0.45 mJy-beam^{-1} contour of the GMRT 1420 MHz image is plotted in green. The circle in both images marks the position and extent of HESS J1818−154. Image taken from Castelletti et al. (2013).

Using the HI absorption features from the Southern Galactic Plane Survey (SGPS; McClure-Griffiths et al. 2005) data, we estimated the distance to the SNR to be 4.8 ± 1.0 kpc. We also used the molecular ^{13}CO (J = 1−0) data obtained from

[1]image available at http://third.ucllnl.org/gps/paper1/images.html

the Galactic Ring Survey (GRS; Jackson et al. 2006) to identify a molecular cloud, about 5′ in size, with two bright clumps (named clump A and B in Figure 9.1), with densities of $(1.5 \pm 0.4) \times 10^3$ cm^{-3} and $(1.1 \pm 0.3) \times 10^3$ cm^{-3}, respectively. These clumps were positionally coincident with HESS J1818−154 and their kinematic distance estimate of 4.2 ± 1.2 kpc is consistent with them being at physically the same location as SNR G15.4+0.1. Our calculations showed that the matter and density in clump A was sufficient to produce the observed VHE γ-ray emission, thus favouring a hadronic scenario for the origin of the VHE γ-rays. In X-ray follow-up observations of HESS J1818−154 done with the X-ray Multi-mirror Mission (XMM)-Newton space telescope, Abramowski et al. (2014) discovered compact, diffuse emission, positionally associated with HESS J1818−154. This emission was totally contained within the radio shell of the remnant. They interpreted the emission as non-thermal emission originating from a PWN. They also detected five point-like sources out of which, two sources turned out to be of Galactic origin. Although they did not detect any significant X-ray pulsations from these, they postulated that one of them may be the putative pulsar powering the X-ray PWN.

In this chapter, we describe the results of the radio pulsation search. The radio imaging and spectral analysis was performed by our collaborators. This work was published recently (Supan et al. 2015) and contains the first ever, detailed multi-frequency study carried out for SNR G15.4+0.1/HESS J1818−154 composite system.

9.2 Observations

The radio observations of G15.4+0.1 were taken with the GMRT at 610 and 1420 MHz (Project code 22_015). The 1420 MHz data were acquired on 10th and 11th May 2012, while 610 MHz data were acquired on 16th and 17th June 2012. The data were taken with a bandwidth of 33 MHz, divided in to 512 spectral channels, which is the maximum bandwidth with the highest spectral resolution. The imaging data

were recorded with a sampling time of 16 s (default), while the pulsar data were recorded with a time resolution of 61 μs. The pulsar data were recorded with both the IA and the PA mode. The IA mode data were recorded by combining the 26 available antennae, which resulted in a beam with diameter of 43′ and 24′, respectively at 610 and 1420 MHz. The higher sensitivity PA mode data were recorded by combining the signals from 15 central square antennae (see Section 3.1.1 for details), resulting in a much narrower beam of 100″ and 40″ diameter, respectively at 610 and 1420 MHz. The centroid of HESS J1818−154 (RA: 18 h 18 m 03.40 s, DEC: −15° 27′ 54.00″ in the J2000 epoch) was used as a phase centre for the observations. The five point-like sources discovered by Abramowski et al. (2014) were within 2′−5′ from this position. The IA beams covered these sources as well as the full radio shell of the SNR with a lower sensitivity. The total on-source time was 240 (12 scans) and 260 (13 scans) minutes at 610 and 1420 MHz, respectively. 3C286 was observed as the flux density calibrator, while J1822−096 was the phase calibrator. It was observed after every 20 minutes for a 4 minute scan, while simultaneously re-phasing the PA mode output. We also observed three known pulsars: B1642−03, B1937+21 and J1901−0906 to asses the sensitivity of the radio pulsation search as well as to get flux density estimates for the pulsar mode data.

9.3 Data Analysis

The pulsar mode data were analysed by using the data analysis pipeline developed for a broken search analysis as described in Section 4.2.1. The narrow band RFI channels as well as non-flat portions towards the band edges were manually flagged so that, the final available bandwidth was around 26 MHz at both observing frequencies. The actual number of channels flagged were different for different individual scans as well as modes (IA and PA). The trial DM range chosen for the 610 MHz pulsation search was 0−815 pc-cm^{-3}. According to the NE2001 model (Cordes and Lazio 2002), the maximum DM of 815 pc-cm^{-3} corresponds to a model distance of 9 kpc in this line of sight. Considering the DM smear and

scattering time scales along this line of sight, the full trial DM range was divided into 6 sub-ranges, each with different number of samples added together to avoid computational effort. This resulted in 1792 trial DMs across the trial DM range. They are shown in Table 9.1.

Trial DM range (pc-cm^{-3})	DM step (pc-cm^{-3})	No. of samples added	Effective sampling time (ms)
0−102	0.05	1	0.061
102−204	0.40	2	0.122
204−306	0.80	8	0.488
306−408	0.80	32	1.952
408−611	1.60	128	7.808
611−815	1.60	256	15.616

TABLE 9.1: The number of adjacent samples added and effective sampling time for the different trial DM ranges used for the 610 MHz pulsation search.

The trial DM range chosen for the 1420 MHz search was 0−1218 pc-cm^{-3}. It was divided further into 5 different sub-ranges. This resulted in 360 trial DMs across the trial DM range. These are shown in Table 9.2. The difference in the DM step is very large at the higher frequency. This is because of the DM smear being very small at higher radio frequencies. This is also manifested in Equation 4.6, where t_{samp} is replaced by the effective sampling time for that particular trial DM range. This allowed us to search at higher trial DMs than in the 610 MHz search. This was done because the pulsar observations were very deep and there was always a possibility of detecting an un-associated pulsar. This chance would be maximised by searching over a larger trial DM range. In case any periodicity was discovered at 1420 MHz with a DM higher than 815 pc-cm^{-3}, the 610 MHz data could be easily dedispersed in a much finer DM mesh around this DM to get a much better estimate of the candidate DM.

The resultant dedispersed data were then searched for periodic signals using the broken search technique as described in Section 4.2.3. This was followed by single pulse search analysis, which was run on each scan separately. In order to check whether the search pipeline was working properly, the known pulsar data were analysed through it to see if the known pulsar was detected. The diagnostic plot

Trial DM range (pc-cm^{-3})	DM step (pc-cm^{-3})	No. of samples added	Effective sampling time (ms)
0−152	0.60	1	0.061
152−227	1.19	2	0.122
227−304	4.76	8	0.488
304−609	19.03	32	1.952
609−1218	76.10	128	7.808

TABLE 9.2: The number of adjacent samples added and effective sampling time for the different trial DM ranges used for the 1420 MHz pulsation search.

for the known pulsar PSR J1901−0906 thus produced from the 610 MHz PA data is shown in Figure 9.2.

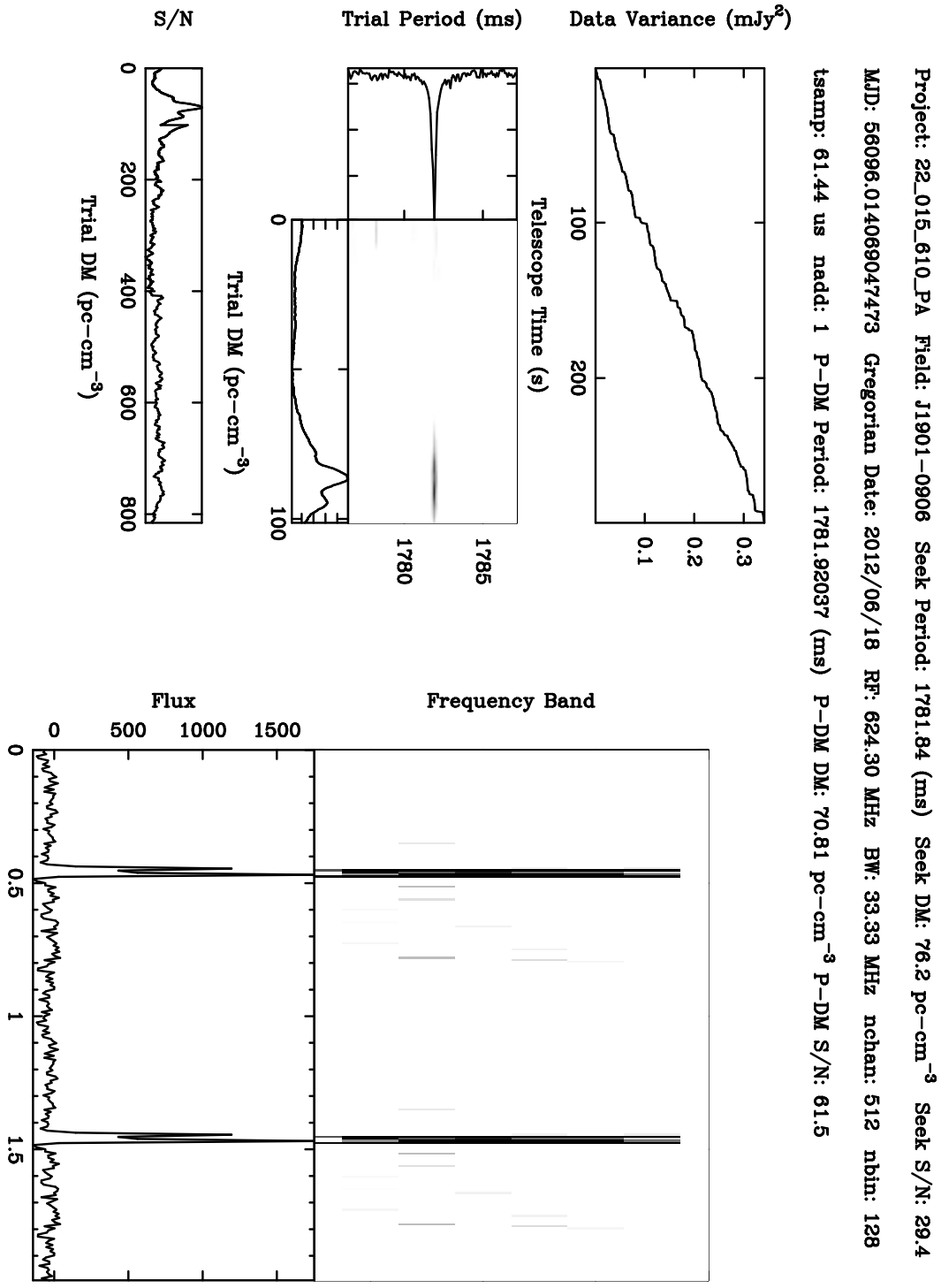

FIGURE 9.2: The diagnostic plot produced using the broken search pipeline for known pulsar PSR J1901−0906. The plot is similar to the one shown in Figure 4.7 without the period refinement by timing as the known pulsar had only one scan. This has resulted in the post-fit RMS error plot missing from this figure.

The known pulsars were observed in order to estimate the sensitivity of the pulsar mode observations. This estimate was derived in the following way:

1. Dedisperse the known pulsar filterbank data at its true DM to get the time series.

2. Fold this time series at the improved period obtained from the search pipeline.

3. Calculate the profile S/N using the following expression (Lorimer and Kramer 2005)

$$S/N = \frac{1}{\sigma_p \sqrt{W_{eq}}} \sum_{i=1}^{N} (p_i - \bar{p}) \tag{9.1}$$

   where $\bar{p}$ and σ_p are profile mean and RMS, respectively, calculated in the off pulse region, W_{eq} is the equivalent width of a top hat pulse having the same area as that of the pulse profile and there are N bins in the profile.

4. Calculate the expected profile S/N using the radiometer equation for pulsed emission (Lorimer and Kramer 2005)

$$S/N = \frac{S_{mean} G \sqrt{n_p t_{obs} \triangle f}}{T_{sys}} \sqrt{\frac{P - W}{W}} \tag{9.2}$$

   where S_{mean} is the pulse averaged flux density of the pulsar in mJy, G is the gain of the system in K/Jy, n_p is the number polarizations summed, t_{obs} is the integration time, $\triangle$f is the bandwidth in MHz, T_{sys} is the system temperature in K and P and W, both in s, are the period and pulse width at 10% of the peak. It should be noted that the above equation applies to a single antenna. When calculating this for an array, use should be made of Equations 3.1 and 3.2 for IA and PA mode, respectively.

5. Divide the expected S/N by the profile S/N. This number can be greater than or equal to 1. In practice, it is always greater than 1 because of non-ideal observing system as well as presence of RFI. Call this the correction factor, κ.

6. Calculate average flux density corresponding to a threshold S/N of 8 by inverting Equation 9.2 for the target source.

7. Multiply this number by κ to get the observed, minimum detectable flux density or sensitivity.

The known pulsar parameters required to calculate the expected S/N were obtained from the web interface of the ATNF pulsar catalogue (Manchester et al. 2005). The correction factor κ denotes how much worse the actual data is, as compared to the expected theoretical sensitivity.

9.4 Results

The broken search pipeline typically produced 60 to 70 candidates for the PA data, while the number of candidates for the IA data was around 180 to 200 at both the frequencies. The scrutiny of the diagnostic plots resulted in non-detection of any pulsation more significant than a S/N of 8 at both frequencies. The upper limits were calculated as described in the last section. As can be seen in Equation 9.2, the minimum detectable flux density depends on the pulse duty cycle (δ = W/P). Thus, it makes sense to report the upper limits on the flux density of the putative pulsar as a function of the pulse duty cycle. These are shown in Figure 9.3 for different frequencies and observing modes. In addition to the non-detection of any significant pulsation in the time series data, there are no point-like radio sources at the positions of the point-like sources discovered by Abramowski et al. (2014) (see Castelletti et al. 2013 for the 1420 MHz image and Supan et al. 2015 for the 610 MHz image). The canonical duty cycle of 10% for the putative pulsar gives upper limits of 250 and 300 μJy at 610 and 1420 MHz, respectively, for the PA data, while the limits for IA data turn out to be 700 and 500 μJy at 610 and 1420 MHz, respectively. These limits also rule out any un-associated pulsar along the line of sight at the same flux density levels.

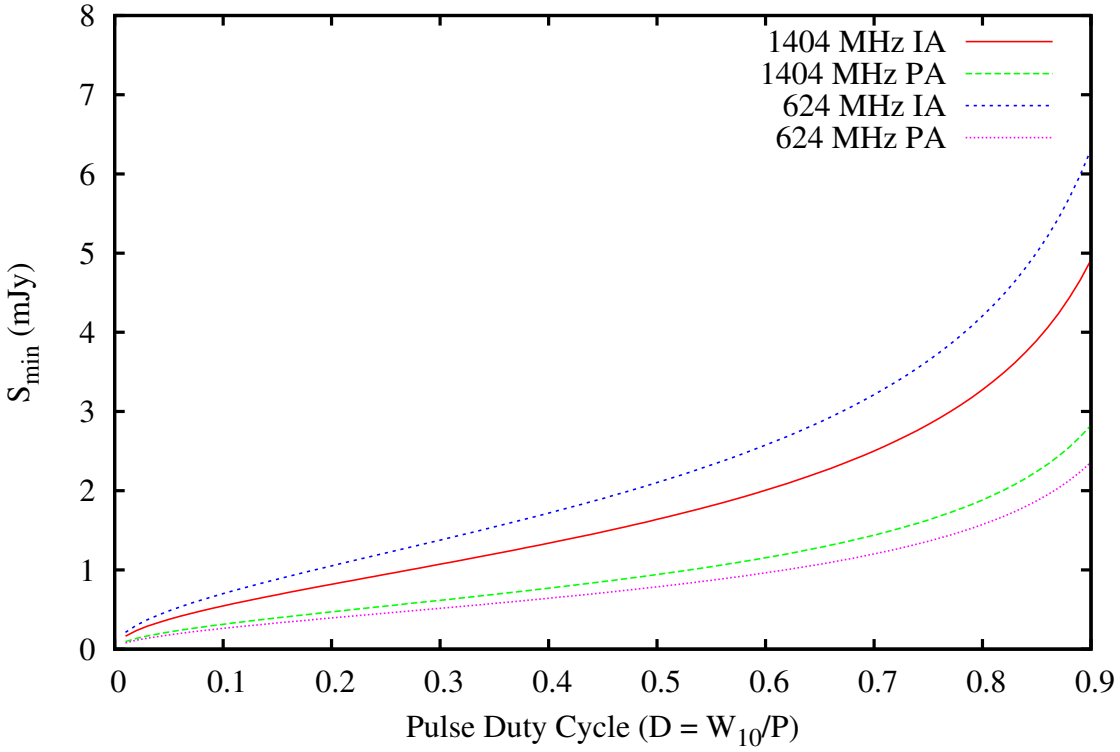

FIGURE 9.3: 8σ upper limits on the flux density of a putative pulsar as a function of the pulse duty cycle.

9.5 Discussion

The spectral studies performed by our collaborators using the 90-cm image obtained from Brogan et al. (2006) and the 610 MHz image from the GMRT data, reveals that the overall spectral index of the SNR is -0.62 ± 0.03, which is consistent with the observation made by Brogan et al. (2006). In the spectral tomography, the spectral index was found to become steeper (starting from -0.5) towards the shell from the inside. This is consistent with most shell type SNRs (Supan et al. 2015). The HI emission studies on the data obtained from McClure-Griffiths et al. (2005) showed that the HI gas distribution shows disruption due to the shock driven by the SNR shell. This goes very well with the overall expectation of a bubble formed in the ISM by the supernova shock and the molecular gas may be sitting on the edge towards the observer. The estimated ambient gas densities from the HI maps helped in calculating the age of the SNR by using the dynamic

model. The age turned out to be 8.2×10^3 years as compared to the age of 2.5×10^3 years estimated by Abramowski et al. (2014), based on the assumption of the SNR being in the Sedov-Taylor phase. Abramowski et al. (2014) also discovered diffuse X-ray emission in the interior of the radio shell of the SNR and note that it does not significantly overlap the molecular cloud region and hence it could still come from the PWN. However, the complete absence of any point-like or diffuse emission in our GMRT images combined with non-detection of pulsed emission in both the radio (this work) as well as X-ray (Abramowski et al. 2014), makes the case of a putative pulsar and a PWN unlikely. Apart from that, the limits on the flux density of the putative pulsar imposed by the non-detection in pulsed emission are much better as compared to the ones imposed by non-detection in the images. This is because of the duty cycle of pulsars are typically of the order of 10%. In the work described in Supan et al. (2015), we also modelled the broad band spectral energy distribution (SED) of the SNR using the flux densities measured at 610 and 1420 MHz with the GMRT observations. The data were fit using a hadronic model for the Gev and TeV emission and synchrotron emission for the radio band. This model produced a very good fit for the available data. Abramowski et al. (2014) used one zone leptonic model in which the radio emission was modelled as synchrotron, while the Gev and TeV emission was modelled using the inverse Compton scattering model. This model assumes explicitly that the leptons are supplied by the putative pulsar through its particle wind. Their radio data points were the VLA flux densities, considered as upper limits, as the SNR was detected as a weak source. We have re-fit the data with our much more sensitive measurements with the GMRT and we get a better fit because of it. Given the complete lack of pulsed radio emission in the time series as well as absence of a point source in the imaging data, we are fairly confident that our model for the SED is more robust. The real problem in this case is the lack of very good quality data in the MeV-GeV range. The current Fermi large area telescope (LAT) data does not show any considerable emission from this SNR and hence, gives only upper limits which are not sufficient to constrain the model. This leaves the issue of the correct emission model in a fix, as both hadronic and leptonic model describe the data

fairly well. If there is still a hidden neutron star in the interior of this SNR, it may still be detected in high energy γ-rays because of the much wider emission beam as compared to the beam of radio emission. Thus, better data, especially at MeV-GeV energies, would help settle this issue, making such observations very prudent.

Chapter 10

Radio Pulsation Search in SGR Sources

10.1 Introduction

SGRs are sources that produce repeating bursts of γ-rays and are usually discovered through either γ-ray or X-ray bursts followed by pulsations. Together with Anomalous X-ray Pulsars (AXPs), they form a rare, distinct class of pulsars, which have transient, highly variable emission in the high energy electromagnetic band. Duncan and Thompson (1992) proposed that the object powering the high energy bursts could be a neutron star with the magnetic field strength in the range $10^{14}-10^{15}$ G (hence the adopted name of magnetar) and the bursts are powered by the release of magnetic energy in a short time scale. The resultant emission is basically in the soft X-ray and γ-ray bands. The typical magnetar spin periods are of the order of a few seconds. This prevents them from emitting pulsed radio emission (Ruderman and Sutherland 1975). In addition, it was thought that the soft X-ray flux of the magnetars is relatively constant, given the fixed magnetic field decay rate which is responsible for the radiation (Thompson and Duncan 1996). The only foreseeable scenario when the flux varies, was thought to be during a burst because of the release of large amount of magnetic energy. This perception

was changed after the detection of transient high energy emission without any SGR-like burst from XTE J1810−197 (Ibrahim et al. 2004). In follow-up radio observations, it also showed radio pulsations (Camilo et al. 2006). This opened up another window to study magnetars, which was through radio observations following a burst. According to the McGill online magnetar catalogue[1], there are 4 such SGR/AXP sources, which show pulsed radio emission. The sources showing radio pulsations, have a large variability in their emission, spectral index as well as integrated profile shapes at radio frequencies (Serylak et al. 2009; Camilo et al. 2007, 2016). On the other hand, PSR J1622−4950, which was discovered through its radio emission (Levin et al. 2010, 2012), is at the other end of the spectrum. It has many properties like profile variation, flux density variation along with quenching of radio emission altogether. All of these were seen while the source was in X-ray quiescence. It turned out to be a magnetar when its magnetic field was estimated using the measured period derivative from radio timing observations. Such diverse properties make AXPs and SGRs very interesting targets. In addition, a high energy burst from these sources is typically followed by radio pulsations. The radio emission usually fades away with the burst energy. Multi-frequency measurements of the flux density during the burst may be useful in order to identify the mechanism of radio emission from these sources. In case the radio emission is detected at some radio frequencies and not at other frequencies or even otherwise, upper limits on the flux density are also useful inputs in modelling the broad band SED. This makes SGRs with a on-going burst, very good candidates for targeted radio pulsation search at GMRT, as target of opportunity (TOO) observations. During the thesis period, we did TOO observations on four SGR sources. We describe them in the following sections.

[1]http://www.physics.mcgill.ca/∼pulsar/magnetar/main.html

10.2 SGR J1745–2900

10.2.1 Introduction

A large X-ray flare was reported by Swift from the direction of the Galactic center (Sgr A*) during regular monitoring observations on 24th April 2013 (Degenaar et al. 2013). Another SGR-like flare was detected by Swift Burst Alert Telescope (BAT) from near Sgr A* on 25th April 2013 (Kennea et al. 2013). The duration of the burst was about 30 ms and based on the position, duration of the burst, persistence of the emission and many other factors, the authors concluded that it might be an SGR. On the next day, Mori et al. (2013) detected a 3.76 second periodicity in their Nuclear Spectroscopic Telescope Array (NuSTAR) data in the 3−10 KeV X-ray band, indicating that the underlying source was a rotating neutron star. This triggered many follow-up observations in the X-ray band. Observations performed with the Chandra X-ray telescope narrowed down the position of the X-ray source (RA: 17 h 45 m 40.19 s, DEC: −29° 00' 30.37" with a 1σ statistical error of 0.3") to conclusively establish a source different than the Galactic center black hole (Rea et al. 2013). These observations also confirmed the 3.76 s periodicity seen by NuSTAR. The X-ray flare and SGR-like properties of this source encouraged follow-up radio observations to search for pulsations, with non-detections resulting from observations done at 1.4 GHz at Jodrell Bank observatory (Bassa et al. 2013) and at 4.85 and 14.6 GHz at Effelsberg radio telescope (Eatough et al. 2013). The non-detections were attributed to the low elevation of the source at the two sites. The observations continued with better observing conditions and the search finally succeeded when Burgay et al. (2013) detected radio pulsations with a periodicity of 3.76 s, at 1.4 and 3 GHz with Parkes radio telescope and at 2 GHz with the GBT in the observations performed on 27th and 29th April 2013. Curiously, the DM of the pulsar appeared to be 50 pc-cm^{-3}, with a duty cycle approaching 100%. The pulse shape varied with time and frequency and the source was strongly detected only for just about a minute in the whole observation. The possible RFI association, however, was ruled out given the detection at different

locations, at different sidereal times and non-detections in off source scans taken 1° and 2° away, respectively at Parkes and GBT. Eatough et al. (2013) detected the source again at 8.35 GHz in a 2.5 hour observation made with the Effelsberg telescope on 2nd May 2013. The pulse profile this time, had a duty cycle of just 2% with the DM of 4000 pc-cm^{-3}. The DM estimate had a large error as very small delays can change the DM by a large amount at high radio frequencies. Nonetheless, the high DM indicated that the pulsar could be very close to the Galactic center. This made the pulsar even more interesting because it opened up a very unique laboratory for gravitational physics. In addition, there was a puzzle regarding the DM of the pulsar. Eatough et al. (2013) detected the pulsar again using observations from Effelsberg telescope at 8.35 and 4.85 GHz. The estimated DMs from these observations were 1300 $\pm$ 200 pc-cm^{-3} and 1000 $\pm$ 600 pc-cm^{-3}, respectively. This put the pulsar very close to the Galactic center (the distance calculated using NE2001 model of Cordes and Lazio (2002), turns out to be 8.4 kpc as compared to the Galactic center distance of 8.5 kpc) While the duty cycle remained at around 2%, the measured period differed somewhat from the expected period. The estimated flux densities were 0.2 and 0.1 mJy, respectively at 8.35 and 4.85 GHz. On 4th May 2013, Gotthelf et al. (2013) made a $\dot{P}$ measurement from preliminary X-ray timing data, which resulted in an estimated magnetic field strength of 3×10^{14} G, confirming that the underlying neutron star was indeed a magnetar. This established very clearly that SGR J174−2900 was indeed a radio loud magnetar in outburst. Given that the 1.4 GHz detection made at Parkes by Burgay et al. (2013), showed a large pulse broadening of the order of the pulsar period combined with the large DM uncertainty, we decided to undertake GMRT observations at 1 GHz, which was the lowest radio frequency where it was expected to be detected. The low frequency detection would also constrain the DM much better. Even a non-detection with the GMRT would confirm the pulse broadening time scale and put an upper limit on the flux density of the pulsar.

10.2.2 Observations

We performed GMRT observations on 9th May 2013, at 1 GHz in the imaging as well as PA mode consisting of 14 central square antennae. The observation was performed using the time allocated through a director's discretionary time (DDT) request (DDTB086), which was promptly approved. We used the Chandra position as the phase center for our observations. The data were recorded with a 33 MHz bandwidth, divided into 512 spectral channels, which provided a spectral resolution of 65 kHz. This was needed in order to determine the DM of the pulsar with a higher accuracy. The imaging data were sampled every 16 s (default sampling time) and the pulsar data were sampled every 1 ms. The sampling time was chosen to be coarse because of the large spin period of the pulsar as well as the expected, large pulse broadening. The integration time was 1 hour.

10.2.3 Data Analysis

Given the fact that SGR J1745−2900 was <3" (within 1 synthesized beam of GMRT at 1 GHz) to Sgr A* (Galactic center), which is a very bright source at radio frequencies, it was impossible to resolve them as two different sources due to confusion in the imaging data. The imaging data were hence, not analysed. The pulsar data were analysed using an analysis pipeline developed for the NCRA HPC based on SIGPROC pulsar data analysis package, which is described in Section 4.2.1. Given the uncertainty on the DM of the pulsar, the time series data were dedispersed to trial DMs in the range 0−2000 pc-cm^{-3}. The full range was divided into 476 DM steps. The DM step was decided based on the effective time resolution provided by the data as well as to make sure excessive computation was avoided given the expected scatter broadening time scale in the direction of the source (the factors affecting the choice of trial DM step are discussed in detail in Section 4.1.2). The dedispersed time series data were then searched using harmonic search and single pulse search. The resultant candidate plots were manually scrutinised for the presence of pulsar signatures.

10.2.4 Results

We did not detect any significant pulsation from this source. The data were subsequently folded at the periodicity detected by NuSTAR (Mori et al. 2013), resulting in a non-detection. The 8σ upper limit on the average pulsed emission from our observation was estimated to be 0.4 mJy for a duty cycle of 30%. We also did not detect any significant RRAT-like burst emission with a 6σ upper limit of 37 mJy. The non-detection is consistent with the high scattering expected along the line of sight. Due to the expected confusion in the radio image because of the proximity to the Galactic center as stated in the previous section, we can not put an upper limit on the continuum flux density of SGR J1745−2900 from our imaging observations. The results were reported in Astronomer's telegram (Surnis et al. 2013).

10.2.5 Discussion

The follow-up radio observations as well as archival searches continued at higher radio frequencies. Palaniswamy et al. (2013) detected radio pulsations at 22 GHz in 2011 archival observations made with the 26 m radio telescope at the Mount Pleasant radio observatory near Hobart. The observed profile duty cycle was about 25%. They estimated the flux density to be 4 ± 1 mJy, which indicated that the radio pulsations were stronger in the past. Mori et al. (2013) published the first comprehensive record of the observational efforts in the X-ray band with a modified magnetic field strength of 1.6×10^{14} G. It showed no detectable X-ray emission in the archival search of Chandra data. Based on the observational evidence for the other radio loud magnetars XTE J1810−197 (Camilo et al. 2006), 1E 1547−5408 (Camilo et al. 2007) and J1622−4950 (Levin et al. 2010), it seems that they all have transient emission and very low X-ray emission during quiescence. The radio emission was detected only during on-going burst activity. This defines a new sub-class of magnetars, which are radio loud when transient, indicating that other radio pulsars having very high magnetic fields may well be magnetars.

Multi frequency radio observations of SGR J1745−2900 (Eatough et al. 2013) indicated that, apart from flux variation common to transient magnetars, it has a flat spectrum, similar to the other radio loud magnetars. This hints towards a common origin of the radio emission. Together with the burst mechanism, it may help to constrain the possible coherent emission mechanisms in such sources. Eatough et al. (2013) also noted, that this pulsar has the highest measured rotation measure (RM), $(-6.696 \pm 0.005) \times 10^4$ rad-m^{-2} and DM, 1778±3 pc-cm^{-3}, of all the known radio pulsars. This, with the projected distance of less than a parsec from the Galactic center, means that continued follow-up could help map the changes in the RM. With the help of precise astrometric observations made using VLBI imaging, the RM changes could help in mapping the magnetic field near the Galactic center. This will be helpful in understanding the accretion mechanism of the central super-massive black hole very well. According to the NE2001 model (Cordes and Lazio 2002), the expected DM in the direction of SGR J1745−2900, at a distance of 8.5 kpc, is about 2000 pc-cm^{-3}. The fact that the pulsar was detected at radio frequencies with variable DMs and scatter-broadening (Eatough et al. 2013; Pennucci et al. 2015), gives rise to a possibility that the ionized medium near the Galactic center may have holes. This notion was compounded with the scatter broadening time scale of 1.3 ± 0.2 s at 1 GHz (Spitler et al. 2014) and a much lower angular broadening than the expected value (Bower et al. 2014), putting the effective scattering screen at a distance of 5.9 ± 0.3 kpc from the Earth.

This source has an almost flat radio spectrum (Eatough et al. 2013; Yusef-Zadeh et al. 2015). The mean radio flux density measured at 8.7 GHz using the GBT is around 3 mJy (Lynch et al. 2015). Assuming a spectral index of −0.9 for low radio frequencies as indicated by Yusef-Zadeh et al. (2015), the estimated flux density at 1 GHz would be about 21 mJy. Even with a spectral index of −0.54 for the global fit obtained by Yusef-Zadeh et al. (2015), the estimated flux density at 1 GHz would be about 9 mJy, which is much more than the upper limit of 0.4 mJy obtained by us. This implies that a detection was possible at the GMRT. Pennucci et al. (2015) have also observed this source in the X band, closer to our

observation epoch. It is clear from Figure 6 in Pennucci et al. (2015) that the radio flux density of the magnetar was lower initially and it increased over time. Also, looking at Figure 7 again from Pennucci et al. (2015), there appears to be a turnover in the radio spectrum around a frequency of 2 GHz. These observational evidences combined with the scatter-broadening estimate of about 35% of the pulse period and the variations in the observed DM and pulse duty cycle, our non-detection at 1 GHz implies a highly varying nature of the radio emission caused due to patchy nature of the ISM along this line of sight. This implies that one can detect normal pulsars near the Galactic center at radio frequencies above 1.4 GHz and millisecond pulsars at radio frequencies above 10 GHz. Such pulsars, if detected, would be very important for studying the very strong gravitational field near the Galactic center and will open up new windows into the understanding of how gravity actually bends space-time.

10.3 SGR J1935+2154

10.3.1 Introduction

The Swift BAT detected an X-ray burst from SGR J1935+2154 on 5th July 2014. The duration of the burst was 0.1 s with a double peaked structure (Cummmings et al. 2014). Swift X-Ray Telescope (XRT) started observing the field shortly after the BAT trigger. The XRT and Ultraviolet and Optical Telescope (UVOT) imaging helped in localizing the source (RA: 19 h 34 m 55.68 s, DEC: +21° 53' 48.2"). The initial burst was followed by three more short, soft bursts out of which, the first two were of a duration of 30 μs, while the third was of a duration of 70 μs. Cummings and Campana (2014) later reported non-detection in archival BAT data but they also reported serendipitous detection of the same source in Swift XRT data in 2010 and 2011. Brian Gaensler noted that the SGR lies very close to the geometric center of SNR G057.2+0.8 and there is a good chance of association as that part of the Galaxy is relatively less populated[2]. Chandra observations

[2]http://gcn.gsfc.nasa.gov/gcn3/16533.gcn3

done on 28th July 2014 detected pulsations with >10σ significance with a period of 3.2 s (Israel et al. 2014). The data taken between the BAT trigger and these observations also show the presence of pulsations with a lower significance. The SGR was observed from Parkes telescope at 10 and 20 cm wavelength by Burgay et al. (2014). The observations were done on 1st and 3rd August 2014. The analysis resulted in non-detection with 8σ upper limits of 0.07 and 0.1 mJy at 10 and 20 cm, respectively. As was seen for the other SGR sources (see Section 10.2.1), the radio flux is highly variable. This means that one needs to keep looking for a radio counterpart till the source is in the burst stage. The suspected association with an SNR provided a unique opportunity to detect a radio loud magnetar associated with an SNR. For a distance of 8.5 kpc (to SNR G057.2+0.8) the NE2001 model (Cordes and Lazio 2002) provided very low line of sight scatter broadening estimates of 180 μs and 2.2 ms at 610 and 325 MHz, respectively. In addition, the SNR G057.2+0.8 did not have any published radio image at 610 MHz. Thus, at GMRT, in addition to the pulsar search, it was possible to make a snapshot image of the SNR. A simultaneous 325 MHz detection at the ORT would also have helped to constrain its DM to a high accuracy besides providing a flux density measurement to constrain the spectral index of radio emission. This led us to propose simultaneous observations at the GMRT and the ORT.

10.3.2 Observations

We performed ORT observations at 326.5 MHz on 9th and 14th July 2014 using 16 MHz bandwidth in the pulsar mode. The data were recorded using the PONDER (Naidu et al. 2015) back-end (see Section 3.1.2.2), employing 1024 filterbank channels with a sampling time of 1 ms. The sampling time was chosen so as to reduce data size, owing to the estimated [from NE2001 model of Cordes and Lazio (2002), assuming a distance of 8.5 kpc to SNR G057.2+0.8] scattering time scale of 2.2 ms. The total integration time was 4 and 3 hours, respectively. The GMRT observations were performed using the DDT allocation (ddtB134). The observations were performed on 14th July 2014 at 610 MHz with 33 MHz band spread

across 512 filterbank channels. The imaging data were recorded with a sampling time of 16 s (default), while the pulsar data were recorded in the IA and PA mode with a sampling time of 61 μs. The PA data would provide high sensitivity pulsar data with a small beam, while the IA data would provide a slightly less sensitive search data over a larger region of sky. This is helpful as an independent check in case of a detection and may also bring out un-associated sources sometimes. The total integration time was 2 hours out of which, on-source time was 1.25 hours. The initial Swift position was used as a phase center. For imaging mode, 3C48 and J1822−096 were observed as flux density and phase calibrator, respectively. PSR B1937+21 was observed as a test pulsar to estimate the sensitivity of the pulsar mode data.

10.3.3 Data Analysis

The pulsar data from both GMRT and ORT were analysed using an analysis pipeline developed for the NCRA HPC based on SIGPROC pulsar data analysis package (see Section 4.2.1 for details). The expected low scattering along the line of sight and the high time resolution of the data implied that the DM step used for the pulsar search be very fine. The data were thus, dedispersed to 2240 trial DMs in the range 0−1500 pc-cm^{-3}. Such a DM limit was imposed keeping in mind the very high DM measured for the Galactic centre magnetar, PSR J1745−2900 (Eatough et al. 2013) and the fact that patchy nature of ionised plasma structures along the line of sight may produce a DM which may be much more than the model prediction. The dedispersed time series data were then searched using both harmonic and single pulse search. The resultant candidate plots were manually scrutinised for the presence of pulsar signatures.

The imaging data were flagged and calibrated using FLAGCAL and the image was made using multi-facet imaging technique (see Section 4.4.8 for details) in AIPS with 19 facets spread across the primary beam area of about 0.3 square degree. The CLEAN image obtained after de-convolution was further improved

by self calibration (see Section 4.4.9 for details). The time scales for calculating the phase solutions were 5, 1 and 0.5 minutes, respectively for the three rounds of self calibration. The resultant high resolution image is shown in Figure 10.1. We made another image of SNR G057.2+0.8 from the archival VLA data at 1365 MHz. The data were acquired using the VLA on 6th April 1995 in the D configuration over a bandwidth of 25 MHz, giving a maximum baseline of 5 Kλ, resulting in an angular resolution of ∼60" (Project code: AH0535, PI: Mark Holdaway). This image was made using the standard steps followed for imaging analysis as explained in Section 4.4. In order to compare the GMRT image with the VLA image, it was convolved with a circular Gaussian beam with an FWHM of 60". This was achieved using the AIPS task CONVL[3]. The resultant images having equal resolution are shown in Figure 10.2.

Additionally, publicly available archival spectral cubes were downloaded from the VLA Galactic Plane Survey (VGPS; Stil et al. 2006) to obtain HI spectra towards the SNR. Spectra from the bright northern portion of SNR as well as a blank region just above it were extracted at 5 pixels each (marked by boxes in Figure 10.3), to form the ON and OFF spectra. These were then used to obtain the emission and absorption spectra towards the source using a procedure similar to that described in Castelletti et al. (2013). The average emission spectrum obtained towards the direction of SGR J1935+2154 was used to calculate the HI column density (N_H) along this line of sight. This was done as follows. First, the moment zero map was generated from the spectral cube. The RMS was determined in this map over an area roughly equal to that of the diffuse emission seen in X-ray image (which was found to be 2.7 K). N_H was then calculated assuming an optically thin medium, implying (Verschuur et al. 1974)

$$N_H\ (cm^{-2}) = 1.823 \times 10^{18} \int T_B dV \tag{10.1}$$

[3]http://www.aips.nrao.edu/cgi-bin/ZXHLP2.PL?CONVL

where T_B is the brightness temperature in Kelvin, and V is the radial velocity in km s^{-1}. In the emission profile obtained towards the SGR, all the bins having brightness temperature more than 2.7 K were averaged and then multiplied by the total range of velocity bins to get an estimate of N_H (total area under the emission profiles).

The public archival data (obtained by Israel et al. 2016) from the PN charge coupled device (CCD) instrument (Strüder et al. 2001) of the European Photon Imaging Camera (EPIC) on board the XMM-Newton mission for all but one observation (as the latest observational data were not public) were added together to make a 98 ks exposure image of the region around SGR J1935+2154. This image is shown in Figure 10.3. More details about the XMM-Newton observations are given in Table 1 of Israel et al. (2016). The diffuse emission around SGR J1935+2154, which was reported by Israel et al. (2016), is seen clearly in this image.

10.3.4 Results

The time-series observations, both from the ORT and the GMRT, did not show the presence of significant pulsations. The flux density upper limits for a putative radio pulsar (associated or otherwise) were then calculated for both GMRT (IA and PA) and ORT data using the radiometer formula. The flux density limits thus derived, are applicable to the highest DM searched for normal pulsars at both frequencies. With an assumed 10% duty cycle, these limits for the high resolution GMRT data are applicable to millisecond pulsars only upto a DM of 100 pc-cm^{-3}. For periodic pulsed emission, the 8σ upper limits on average flux density assuming 10% duty cycle are 0.4 and 0.2 mJy at 326.5 and 610 MHz, respectively. The GMRT PA data were subsequently folded at the period detected by Israel et al. (2014) and it also resulted in a non-detection. The preliminary results for the pulsation search were reported earlier in the Astronomer's Telegram (Surnis et al. 2014). We also did not detect significant bursts with 6σ upper limits on flux density (assuming 10 ms burst duration) of 0.5 Jy and 63 mJy at 326.5 and 610 MHz, respectively.

The corresponding flux density upper limits from GMRT IA data at 610 MHz are 0.8 mJy (8σ) for pulsed emission (with an assumed duty cycle of 10%) and 244 mJy (6σ) for isolated bursts (assuming 10 ms burst duration).

We have made the first high resolution image of SNR G057.2+0.8 at 610 MHz. It is shown in Figure 10.1. The synthesized beam size is 18.5"×9.9" with a parallactic angle of 85° (as indicated in the bottom left corner of the image), while the RMS noise in the map is 0.4 mJy. As can be clearly seen, there is no associated point source at the position of SGR J1935+2154, with a 3σ upper limit of 1.2 mJy, as indicated by a cross in Figure 10.1. Thus, the time series non-detection is consistent with the absence of a continuum source in the radio map. No diffuse radio emission, associated with a putative wind nebula with an extent similar to the diffuse X-ray emission reported by Israel et al. (2016) (in radii of 15", and 70"), was detected with a 3σ flux density upper limit of about 4.5 mJy over a circular area with a radius of 70".

The HI emission spectra along with the absorption profiles are shown in Figure 10.4. The average spectrum shows a broad emission feature upto a velocity of 61.2 km-s^{-1}, which is the maximum velocity at the tangent point. As there are clear absorption features present at negative radial velocities, the continuum source (the SNR in this case) lies outside the solar orbit, much beyond the tangent point. The absorption features appear upto the maximum negative velocity of -63.3 km-s^{-1}. This translates to a kinematic distance of 11.7 ± 2.8 kpc, using the circular rotation curve of the Milky Way given by Fich et al. (1989) (assuming $\Theta = 220$ km-s^{-1}, $R_{\odot} = 8.5$ kpc).

From HI emission profile obtained in the direction of SGR J1935+2154, we calculate the HI column density in this line of sight to be $(1.1 \pm 0.1) \times 10^{22}$ cm^{-2}.

10.3.5 Discussion

SGR J1935+2154 emitted many short, soft bursts which triggered a TOO observation on 27th February 2015 (Younes et al. 2015). The observations detected

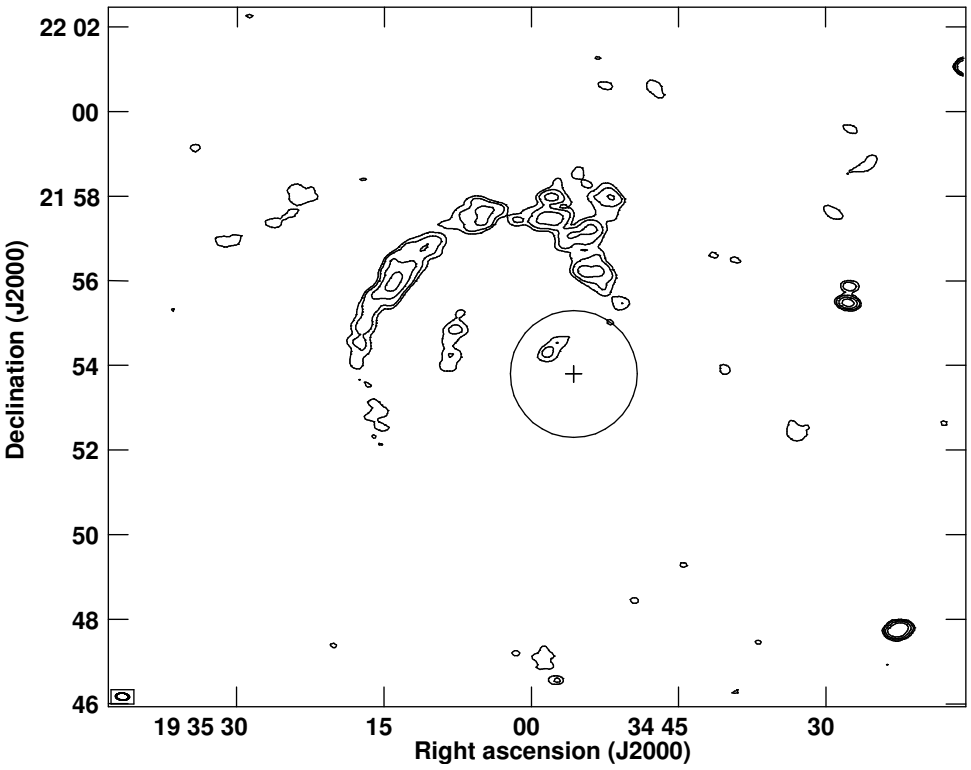

FIGURE 10.1: High resolution GMRT Image of SNR G057.2+0.8 at 610 MHz. The synthesized beam size is 18.5"×9.9" with a parallactic angle of 85° as indicated in the bottom left corner. The RMS noise in the map is 0.4 mJy. The contour levels are at 3, 5, 10 and 20σ. The cross indicates the position of SGR J1935+2154 with the size of the cross indicating 10σ position uncertainty. The solid circle represents the extent of diffuse X-ray emission reported by Israel et al. (2016).

X-ray pulsations which allowed them to measure the spin-down rate. The inferred magnetic field strength turns out to be 7×10^{14} G, making this another magnetar. This SGR has shown very similar characteristics like SGR J1745−2900 but for the absence of radio pulses. This makes SGR J1935+2154 a very unique transient magnetar with no detectable emission (neither continuum nor pulsed) down to about 100 μJy at 20 cm (Burgay et al. 2014).

The first high resolution image of SNR G057.2+0.8 at 610 MHz (Figure 10.1) shows an incomplete, filamentary radio shell, which is brighter towards the north-eastern edge. The south-western radio shell is not detectable with the sensitivity afforded by our observations. This could be due to very high ambient density in the ISM towards the north-eastern region wherein, the interaction with the shock

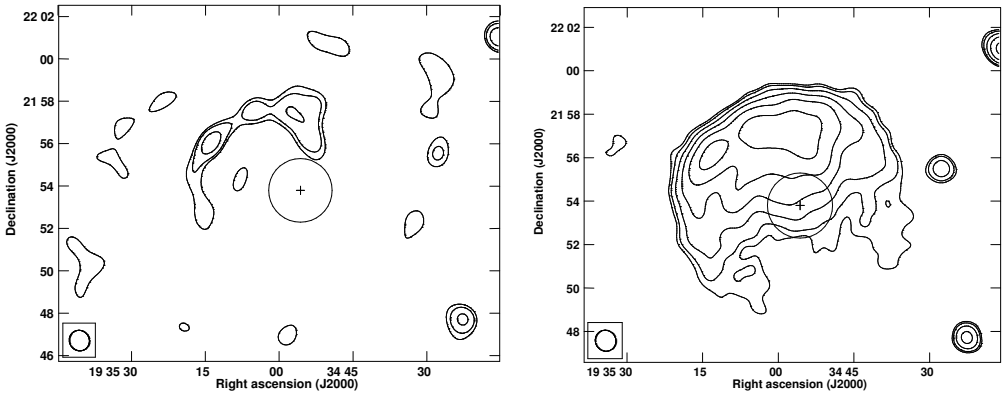

FIGURE 10.2: Left: GMRT Image of SNR G057.2+0.8 at 610 MHz, convolved with a circular Gaussian having an FWHM of 60". The RMS noise in the map is 4 mJy. The contour levels are at 3, 5, 10 and 20σ. Right: VLA Image of SNR G057.2+0.8 at 1365 MHz, obtained in the D configuration. The RMS noise in the map is 0.6 mJy. The contour levels are at 3, 5, 10, 20, 40 and 80σ. In both images, the cross indicates the position of SGR J1935+2154 with the size of the cross indicating 10σ position uncertainty. The solid circle represents the extent of diffuse X-ray emission reported by Israel et al. (2016).

wave is responsible for the radio emission. The south-western region may not have enough density to emit strong electromagnetic radiation in the radio band. There is a hint of some point-like radio emission just north-east of SGR J1935+2154, but the extent of the 10 σ position error on SGR J1935+2154 rules out any possible association. The low resolution GMRT and VLA images (Figure 10.2) both show a bright north-eastern shell dominating the emission. The radio emission in the VLA image, however, shows much larger spatial extent than the GMRT image. Given the drastically lower sensitivity in the GMRT image (imaging RMS of 4 mJy against 0.6 mJy), the lowest contour in the GMRT image is comparable to the highest contour in the VLA image. Although this prevents us from drawing any firm conclusions about the spectral index using the GMRT image, the VLA image probably indicates towards a fully filled radio SNR (emission coming from edges as well as central part of the shell) with over dense ISM towards the north-eastern border and under dense ISM towards the south-western end.

The SGR J1935+2154 lies close to the centroid of SNR G57.2+0.8. An approximate estimate of distance to the magnetar can be made as follows. The spectral analysis by Israel et al. (2016) obtained a value of N_H as 2×10^{22} and 1.6×10^{22}

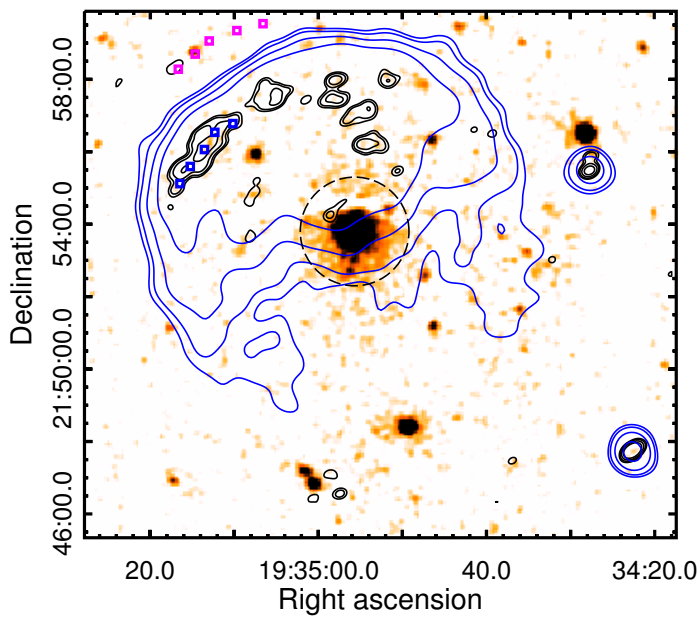

FIGURE 10.3: 98 ks integrated XMM-Newton EPIC-PN image of the region around SGR J1935+2154. The publicly available archival data were obtained by G. L. Israel (Israel et al. 2016) and the observation details are given in Table 1 therein. The resultant map has been smoothed using a Gaussian function with a radius of 4". The blue contours are plotted from the 1365 MHz VLA map of SNR G57.2+0.8 (as shown in the right panel of Figure 10.2), while black contours are plotted from the high resolution GMRT image at 610 MHz (as shown in Figure 10.1). The pixels used for obtaining the ON and OFF spectra are marked by blue and magenta boxes, respectively. The dashed circle represents a region of radius 90", which includes the diffuse X-ray emission (see text for more details).

cm^{-2} from their spectral fits using Chandra and XMM-Newton data, respectively towards the magnetar and 3.8 $\times$ 10^{22} cm^{-2} for the diffuse emission from XMM-Newton data. If we assume that the N$_H$-DM correlation (He et al. 2013) holds for this line of sight, we can obtain an estimate of associated DM for the magnetar. Adopting the value of N$_H$ as 1.8 $\times$ 10^{22} cm^{-2}, we get a DM of 600 $^{+260}_{-180}$ pc-cm^{-3} for the magnetar, and 1300 $^{+500}_{-400}$ pc-cm^{-3} for the diffuse emission. Using NE2001 model (Cordes and Lazio 2002) towards this line of sight, we get a distance estimate for both the magnetar and the diffuse emission to be much higher than the extent of the Galaxy (>50 kpc). However, it is to be noted that the NE2001 model saturates beyond a DM of 540 pc cm^{-3} in this line of sight. Also the distance estimates from the N$_H$-DM correlation can have a large uncertainty beyond

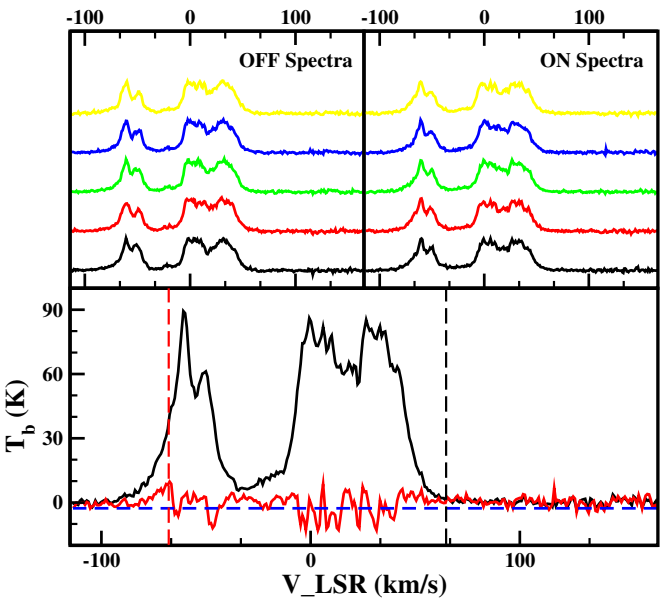

FIGURE 10.4: Emission spectra and absorption profile extracted from VGPS archival data (Stil et al. 2006). The top two panels show the extracted spectra from 5 pixels each for the OFF (left panel) and the ON source region (right panel; as indicated in Figure 10.3). The bottom panel shows the averaged ON source emission spectrum (black) and the absorption profile (red) towards the northern filament of SNR G57.2+0.8. The black dashed line shows the maximum velocity at the tangent point, the dashed red line indicates the absorption feature with the highest negative velocity and the dashed blue line indicates −2.7 K below which, absorption features are believable.

a DM of 100 pc cm^{-3} or a distance greater than 3 kpc (He et al. 2013). He et al. (2013) also note that the N_H value inferred from X-ray observations of pulsars at low Galactic latitudes may be higher than that inferred from HI emission profiles. This happens due to absorption of X-rays by molecular clouds rather than neutral Hydrogen. With this caveat, the N_H values measured by Israel et al. (2016) for the magnetar and our own measurements along the same line of sight are consistent with each other. Considering the spiral structure of the HI in our Galaxy (Levine et al. 2006) and the N_H values obtained from the Leiden Argentine Bonn (LAB) survey[4] (Kalberla et al. 2005) along different lines of sight in the Galactic latitude range of 40°−80°, which are all nearly around 1−1.5 × 10^{22} cm^{-2}, the magnetar (and the diffuse emission) could be located in or beyond the Perseus arm. With all these (uncertain) estimates of the magnetar distance, it can be argued that SGR J1935+2154 and SNR G057.2+0.8 may be physically associated.

[4]https://www.astro.uni-bonn.de/hisurvey/profile/

Israel et al. (2016) estimated the quiescent X-ray luminosity of the magnetar, L_X as 5×10^{33} ergs-s^{-1} assuming a distance of 9 kpc. This distance was derived assuming an association between the magnetar and the SNR. Even with our revised estimate for the SNR distance, such an association is possible. As discussed by Israel et al. (2016) assuming a distance of 9 kpc, the SGR is somewhat under-luminous during a burst as compared to a typical magnetar. It may be noted that this luminosity is still larger than 10 out of 22 magnetars listed in online McGill magnetar catalog[5] (Olausen and Kaspi 2014). The SGR was observed from Parkes telescope at 10 and 20 cm wavelength by Burgay et al. (2014), resulting in a non-detection with 8σ upper limits of 0.07 and 0.1 mJy at 10 and 20 cm, respectively, which is consistent with our non-detection at 610 and 326.5 MHz. With a typical flat spectrum emission expected from radio-loud magnetars (e.g. Yusef-Zadeh et al. 2015), our upper limits for the pulsed radio emission along with the high frequency limits may imply a spectral index less steeper than -0.8. Assuming an association between the SGR and the SNR and considering the upper limit on the distance of the magnetar to be 14.5 kpc (from 1σ error on the SNR distance), the X-ray luminosity of the SGR turns out to be 1.3×10^{34} ergs-s^{-1}. Even with a slightly increased distance estimate, the ratio $L_{X,qui}/L_{sd}$ is still about 0.65, which is much less than unity. Thus, the SGR falls into the "radio-loud" class (Rea et al. 2012) and the non-detection of radio pulsations are puzzling, but could be due to the radio beam pointing away from the line-of-sight.

No radio counterpart of diffuse X-ray emission reported by Israel et al. (2016) was detected in the high resolution image at 610 MHz. The diffuse X-ray emission could be due to the scattering of X-rays from the magnetar by a dust halo (Esposito et al. 2013; Israel et al. 2016) or a wind nebula powered by the magnetar (Younes et al. 2012; Israel et al. 2016). In the former case, one does not expect diffuse radio emission, which is consistent with our non-detection. In case of a wind nebula, synchrotron radio emission is expected. As a PWN is powered by the loss of rotational kinetic energy from the central pulsar, one can expect its radio luminosity to be related to its spin-down luminosity. Assuming this proportionality

[5]http://www.physics.mcgill.ca/∼pulsar/magnetar/main.html

to be in the form S = K × $\dot{E}$ / d^2 for an order of magnitude calculation, where S is the flux density in Jy at 1 GHz, $\dot{E}$ is the spin-down luminosity in ergs-s^{-1} and d the distance to the PWN in kpc, one can estimate the value of proportionality constant K for some typical PWNs such as Crab, Vela and Kes75. With the spin-down luminosities from Australia Telescope National Facility (ATNF) pulsar catalog[6](Manchester et al. 2005) and distances and 1 GHz flux density from available literature (Crawford et al. 2001; Dodson et al. 2003; Green 2014; Leahy and Tian 2008; Milne 1968), we obtain an average value of K as 1.6×10^{-15}. With our distance estimate of 11.7 kpc and spin-down luminosity of SGR J1935+2154 of 2×10^{34} ergs-s^{-1} (Israel et al. 2016), we expect a flux density of 2.4 mJy at 610 MHz (assuming a spectral index of −0.3) for any associated PWN. As the upper limit on the flux density of diffuse emission from our observations is higher than this, we can not rule out the presence of such an emission. We would like to caution that this conclusion is based on the assumption that the radio luminosity is proportional to spin-down luminosity. Such a relation is uncertain as it would depend upon many factors, such as integrated spin-down history of pulsar, nature of confining reverse shock and pulsar velocity. The nature of a wind nebula around a magnetar is also likely to be different from usual PWNs. In the light of the uncertainty in the distance estimate of the SGR and the diffuse X-ray emission, as well as the lower expected radio PWN flux density than our upper limits, it is difficult for us to comment on the plausibility of a PWN and we can not rule out any of these two scenarios based on the currently available data.

10.4 SWIFT J174540.7–290015

10.4.1 Introduction

During the regular Galactic center monitoring observations, the Swift XRT detected an X-ray transient source, J174540.7−290015, on 6th February 2016. Its position was narrowed down to RA: 17 h 45 m 40.74 s, DEC: −29° 00' 14.7"

[6]http://www.atnf.csiro.au/people/pulsar/psrcat/

with a 90 % confidence uncertainty radius of 2.2" (Reynolds et al. 2016). The spectrum obtained from the same observation implied that the source could be either an accreting neutron star or a magnetar. Given a sampling time of 2.5 s, Reynolds et al. (2016) were unable to search for coherent X-ray pulsations. In a follow-up The International Gamma-Ray Astrophysics Laboratory (INTEGRAL) observation done on 11$^{\rm th}$ February 2016, Esposito et al. (2016) estimated the photon index over an energy range of 20−80 keV to be 2.7 ± 0.2. Detection of radio pulsations from this source would have clearly established this transient source as a magnetar. This prompted radio follow-up observations with ORT and GMRT.

10.4.2 Observations

The ORT observations were carried out on 10$^{\rm th}$ February 2016 at 326.5 MHz in pulsar mode with a 16 MHz band spread over 1024 channels using PONDER (Naidu et al. 2015). The data were sampled every 4 ms over an observing session lasting 3.5 hours. The GMRT observations were carried out on 15$^{\rm th}$ February 2016 at 1390 MHz with a 33 MHz band spread over 512 channels (proposal code ddtB210). The data were recorded in the PA mode over 2.7 hours with a sampling time of 123 μs. Imaging data were simultaneously recorded with a sampling time of 4 s. The swift position (Reynolds et al. 2016) was used as the phase center for both the observations. 3C48 and J1712−281 were observed as flux density and phase calibrator, respectively.

10.4.3 Data Analysis

Both the ORT and GMRT data were analysed for periodic signals using two different pipelines using PRESTO and SIGPROC, respectively. The SIGPROC pipeline simultaneously searched for isolated dispersed bursts. The search was carried out over a DM range of 0−3000 pc-cm^{-3}. Given that the position of the transient was just 16" away from the Galactic center (Reynolds et al. 2016), the radio image

would be limited in dynamic range due to the strong emission from the Galactic center. The imaging data were thus, not analysed.

10.4.4 Results

The analysis did not yield any significant pulsed or bursty radio emission in both ORT and GMRT data. The 5σ flux density upper limits at 326.5 MHz were estimated to be 4.5 mJy (assuming 10% duty cycle) for harmonic search and 15 Jy (assuming a pulse width of 10 ms) for single pulse search. The corresponding limits at 1390 MHz were 70 μJy (assuming 10% duty cycle) and 0.2 Jy (assuming a pulse width of 10 ms), respectively. These results were posted on the Astronomer's telegram (Maan et al. 2016).

10.4.5 Discussion

Based on our non-detection, we could not rule out either magnetar or accreting X-ray binary origin for the X-ray burst. This region was observed with Chandra (Baganoff et al. 2016) on 13th and 14th February 2016. These observations confirmed the transient as a new source, different from any catalogued source in this region (Baganoff et al. 2016). The pulsation search using the Chandra data also yielded negative results. More follow-up radio observations were performed with the VLA at 6 and 15 GHz on 25th February 2016 (Bower et al. 2016). These data were recorded simultaneously in PA and imaging mode. The analysis yielded negative results for pulsation and burst search (Bower et al. 2016). The upper limits on flux density at 10σ level were 30 and 45 μJy at 6 and 8 GHz, respectively. These limits were more stringent than our reported upper limits assuming a flat spectral index seen for PSR J1745−2900 (Eatough et al. 2013; Yusef-Zadeh et al. 2015). Due to contamination from the Galactic center, the RMS in the images were 6 and 53 mJy at 6 and 8 GHz, respectively. Bower et al. (2016) estimate the expected radio flux density to be around 1 mJy for an accreting source in the low-hard state. Thus, all the observational constraints can not rule out any scenario for the

source origin. Interestingly, the addition of this transient near the Galactic center implies a rate of 0.37 ± 0.15 transient sources per year in this region (Baganoff et al. 2016). This implies that continued monitoring of this region may uncover many more transient sources in the near future.

10.5 SGR J0755–2933

10.5.1 Introduction

Swift BAT detected an SGR-like burst on 16th March 2016. The burst duration was less than 128 ms with a count rate of ∼1900 counts per second (Barthelmy et al. 2016). Swift XRT started observing this field ∼75 seconds after the BAT trigger. With the XRT data, the position of the source was narrowed down to RA: 07 h 55 m 42.48 s, DEC: −29° 33' 49.2" with a 90 % confidence uncertainty radius of 2" (Barthelmy et al. 2016). It was tentatively named as SGR J0755−2933. UVOT image did not reveal any optical counterpart upto a limiting magnitude of 18. The estimated HI column density was much higher than the typical Galactic contribution. The short time scale of the burst together with an enhanced column density hinted towards an SGR origin for the X-ray burst. Also, the X-ray emission was variable but not fading. This made radio follow-up observations imminent.

10.5.2 Observations

The observations at the ORT were performed on 17th March 2016 at 326.5 MHz with 8 ms sampling over a band of 16 MHz, spread over 1024 channels using PONDER (Naidu et al. 2015). The total integration time was 3 hours. The observations at the GMRT were performed on 25th March 2016 (proposal code ddtB216) at 1390 MHz wherein, the data were recorded simultaneously in imaging and PA mode, over a bandwidth of 33 MHz, spread over 512 channels. The PA data were recorded with a sampling time of 123 μs, while the imaging data

were recorded with a sampling time of 16 s for a duration of 1 hour. For the imaging observations, 3C147 and J0828−375 were observed as flux density and phase calibrator, respectively.

10.5.3 Data Analysis

Pulsar mode data from both ORT and GMRT were analysed using search pipelines using PRESTO and SIGPROC. The SIGPROC based pipeline also provided single pulse candidates. The pulsation search ran over a DM range of 0−2000 pc-cm^{-3}. The imaging data were flagged and calibrated using FLAGCAL. The final image was made using standard imaging techniques with self calibration in AIPS.

10.5.4 Results

No significant pulsations were detected from either GMRT or ORT data. The 8 σ flux density upper limits at 326.5 MHz were estimated to be 0.89 mJy (assuming 10% duty cycle) for harmonic search and 2.8 Jy (assuming a width of 10 ms) for isolated bursts. Corresponding limits at 1390 MHz were estimated to be 0.12 mJy (assuming 10% duty cycle) for harmonic search and 220 mJy (assuming a width of 10 ms) for isolated bursts. From the radio maps, the absence of a continuum source implies a 3σ flux density upper limit of 0.3 mJy. These results were posted on the Astronomer's telegram (Surnis et al. 2016).

10.5.5 Discussion

The X-ray flux of SGR J0755−2933 fell by a factor of 5 in about half a day after the initial burst as seen by Archibald et al. (2016) in the ∼18 ks Swift XRT data. They also did not detect significant pulsations with a 3σ upper limit of 15% on the pulse duty cycle. Although this source emitted a short-hard X-ray burst, which was very powerful, the apparent lack of X-ray and radio pulsations makes the case for a neutron star origin very unlikely. The other scenario is that the neutron star,

if present, may not be beaming towards the Earth. Given the high X-ray flux, further deep X-ray follow-up observations may still be able to detect pulsations to establish magnetar nature of this source.

Chapter 11

Summary

The thesis work involved blind and targeted radio pulsation searches as well as follow-up timing observations. The search data were obtained with the GMRT, while the timing data were obtained with the GMRT as well as the ORT. Apart from these data sets, the simultaneous imaging data taken from GMRT provided an opportunity to perform variability study on the point sources detected in the field containing the newly discovered pulsar, PSR J1838+1523. In the following sections, we will summarize the main results of the thesis and their implications.

11.1 Main Results

- **Blind Pulsar Survey with the GMRT**
  - The blind Galactic pulsar survey resulted in the detection of 28 pulsars out of which, PSR J1838+1523 was a new discovery.
  - The overall survey sensitivity for an 8σ detection threshold was estimated to be 2.7 mJy for harmonic search (assuming 10% duty cycle) and 2.3 Jy for single pulse search (assuming a pulse width of 10 ms).
  - The rate of discovery in the survey was found to be consistent with the current population models.

- **Discovery and Follow-up Timing of PSR J1838+1523**
  - The newly discovered pulsar PSR J1838+1523 has a period of 549 ms and a DM of 68 pc-cm^{-3}. It belongs to the normal pulsar population.
  - During the follow-up timing observations, it showed random ON–OFF states lasting 1–2 months.
  - A coherent timing solution was obtained for this pulsar from daily follow-up observations with the ORT at 325 MHz and bi-weekly timing observations with the GMRT at 325 and 610 MHz.
  - The continuum counterpart of this pulsar was identified from the images made with simultaneously recorded imaging data taken with the GMRT.
  - The mean flux density of this pulsar at 325 MHz is 4.3 ± 1.8 mJy and 1.2 ± 0.7 mJy at 610 MHz, implying a spectral index of −2.
  - Flux density histograms at 325 MHz indicate towards RISS as a probable cause for the ON–OFF nature of this pulsar.

- **Follow-up of 3 GMRT Pulsars**
  - **PSR J2208+5500**
    - The nulling fraction for this pulsar was estimated to be 50 ± 5%, while the phase averaged modulation index was estimated to be 2.5 ± 0.6. The phase resolved modulation index was seen to show a minimum at the peak bin, while increasing towards the edges, indicating towards a core only profile.
    - Multi-frequency timing observations were used to determine the DM for this pulsar to be 105.04 ± 0.02 pc-cm^{-3}, while the spectral index was estimated to be −2.4 ± 0.4.
  - **PSR J2217+5733**
    - $\tau_{\rm sc}$ for this pulsar was estimated to be 9.7 ± 0.4 ms at 610 MHz and 61.9 ± 1.1 ms at 325 MHz. These imply a scattering spectral

index of -2.9, which is much smaller than -4.4, which is expected for a Kolmogorov spectrum of non-uniformities in the ISM.

  * Multi-frequency timing observations were used to determine the DM for this pulsar to be 131.54 ± 0.03 pc-cm^{-3}, while the spectral index was estimated to be -2.4 ± 0.3.

- **PSR J0026+6320**

  * $\tau_{\rm sc}$ for this pulsar was estimated to be 7.5 ± 0.9 ms at 610 MHz and 47.6 ± 4.7 ms at 325 MHz. These imply a scattering spectral index of -2.9, which is much smaller than a what is expected for a Kolmogorov spectrum of non-uniformities in the ISM.
  * Multi-frequency timing observations were used to determine the DM for this pulsar to be 245.06 ± 0.06 pc-cm^{-3}, while the spectral index was estimated to be -0.9 ± 0.4.

- **Imaging Study of a Known Pulsar Field**

  - Flux densities of 29 point sources in the field containing PSR J1838+1523 were measured at 325 MHz to establish the reliability of the calibration of the imaging data.
  - Flux densities of 12 of the above 29 point sources were measured at 610 MHz, resulting in the estimation of the spectral indices of 11 of them for the first time.
  - at 325 MHz, NVSS J183715+153015 (17%) and J183850+152214 (18%) were found to be mildly variable, while NVSS J183729+153210 (21%) and J183708+153141 (26%) were found to be moderately variable.
  - J183850+152214 was found to be a flat spectrum source (spectral index almost 0) with mild variability.

- **Pulsation Search towards HESS J1818−154 / SNR G15.4+0.1**

  - No associated or un-associated pulsar was discovered in this search. The canonical duty cycle of 10% for the putative pulsar gives 8σ upper

limits of 250 and 300 μJy at 610 and 1420 MHz, respectively, for the PA data, while the limits for IA data turn out to be 700 and 500 μJy at 610 and 1420 MHz, respectively.

- The origin of the VHE emission was attributed to the interaction of the SNR shell with local molecular clouds.

- **Radio Pulsation Search towards Soft Gamma-ray Repeaters**
  - **SGR J1745−2900**
    - No significant pulsations were detected with 8σ flux density upper limit (assuming a 30% duty cycle) of 0.4 mJy.
  - **SGR J1935+2154**
    - No significant pulsations were detected in the GMRT PA data with 8σ flux density upper limits (assuming a 10% duty cycle) of 0.4 and 0.2 mJy at 326.5 and 610 MHz, respectively for harmonic search. The corresponding IA limits from GMRT data turn out to be 0.8 mJy at 610 MHz.
    - No significant bursty emission was detected in the PA data with 6σ flux density upper limits (assuming a burst duration of 10 ms) of 0.5 Jy and 63 mJy at 326.5 and 610 MHz, respectively. The corresponding IA limits from GMRT data turn out to be 244 mJy at 610 MHz.
    - No continuum radio emission was seen in the radio maps with a 3σ flux density upper limit of 1.2 and 4.5 mJy for the SGR and the associated diffuse X-ray emission, respectively.
    - The kinematic distance of SNR G057.2+0.8 was estimated to be 11.7 $\pm$ 2.8 kpc, while the HI column density along the line of sight was estimated to be $(1.1 \pm 0.1) \times 10^{22}$ cm^{-2}.
  - **SWIFT J174540.7−290015**
    - The analysis resulted in non-detection of radio pulsations with 5σ flux density upper limits at 326.5 MHz of 4.5 mJy (assuming 10%

duty cycle) for harmonic search and 15 Jy (assuming a pulse width of 10 ms) for single pulse search. The corresponding limits at 1390 MHz were 70 μJy (assuming 10% duty cycle) and 0.2 Jy (assuming a pulse width of 10 ms), respectively.

– **SGR J0755−2933**

  * No significant pulsations were detected with 8 σ flux density upper limits at 326.5 MHz to be 0.89 mJy (assuming 10% duty cycle) for harmonic search and 2.8 Jy (assuming a width of 10 ms) for isolated bursts. Corresponding limits at 1390 MHz were estimated to be 0.12 mJy (assuming 10% duty cycle) for harmonic search and 220 mJy (assuming a width of 10 ms) for isolated bursts. From the radio maps, the absence of a continuum source implies a 3σ flux density upper limit of 0.3 mJy.

11.2 Discussion

11.2.1 Blind Pulsar Survey with the GMRT

Pulsar surveys are typically carried out with large single dish telescopes at high radio frequencies. Although such telescopes provide good sensitivity due to large collecting area, a small beam size makes them slow in sky coverage. A multi-element telescope like the GMRT offers a large collecting area of about 30,000 m^2 (Swarup et al. 1991) with a field of view of about 85' (Lal 2013) at 325 MHz, making it a sensitive pulsar survey instrument with a good survey speed. In order to exploit the sensitivity and survey speed of GMRT, we proposed a blind pulsar survey to cover the region between Galactic longitude $45° < l < 135°$ and Galactic latitude $1° < |b| < 10°$ at 325 MHz. This survey was titled "GMRT Galactic Plane Pulsar and Transient Survey". Over two observation cycles of the GMRT, about 10% of the region was covered. Out of the 152 fields observed, data for 30 fields had to be ignored due to the presence of large amount of RFI. The simulated

survey analysis using PSRPOP[1] using the post-analysis parameters indicates a detection of 96 normal pulsars and 5 millisecond pulsars (known plus new) for the full survey region. Thus, the detection of 28 pulsars including 2 MSPs and the discovery of 1 new pulsar in the 10% region that was covered in a non-uniform manner, is much more than what the current population models predict, but it is not alarming given the non-uniform survey coverage.

The steep spectral index of PSR J1838+1523 (see Chapter 6 for details) reiterates the need for low frequency pulsar searches in order to discover very steep spectrum pulsars. The overall survey sensitivity of 2.7 mJy (8σ for 10% duty cycle) translates to a detection limit of 0.35 mJy at 1.4 GHz [assuming an average spectral index of -1.4 as has been derived by Bates et al. (2013)]. This is comparable to the limit of 0.25 mJy (which assumes a 5% duty cycle) for the mid-latitude HTRU survey (Keith et al. 2010). Thus, even with degraded sensitivity due to presence of RFI, our low frequency survey was complementary to the high frequency surveys. The presence of RFI not only degrades the overall sensitivity of the survey but some particular types of RFI like power line RFI produce spurious periodicities in harmonic searches. This can be avoided by suppressing the harmonics of power line frequency but it drastically reduces the detectability of periodicities near these harmonics. As an example, the newly discovered pulsar, PSR J1838+1523 was detected only after RFI mitigation using the zero DM filtering technique (Eatough et al. 2009). This makes RFI mitigation very important in low frequency blind surveys. Any future low frequency surveys should have well developed and tested RFI mitigation techniques in order to make these surveys more effective.

11.2.2 Discovery and Follow-up Timing of PSR J1838+1523

The discovery and timing of PSR J1838+1523 has provided a good example of how dedicated multi-frequency follow-up observations combined with radio imaging can help constrain the timing solution of pulsars discovered in low frequency surveys. Low frequency searches cover the sky faster because of their large field of view

[1] http://www.psrpop.phys.wvu.edu/index.php

but this also implies that the position of the newly discovered pulsar is poorly known. It can be mitigated by using the gated imaging technique (e. g. Roy et al. 2012) to localize the pulsar faster. This in turn provides a better timing solution much faster than traditional timing only technique, which requires at least one year worth of follow-up observations to fit for the Doppler effect due to Earth's revolution. An additional advantage provided by simultaneous imaging data is the ability to monitor the flux density of the pulsar and compare it with the flux density of its pulsed emission. It would help in identifying un-pulsed (Navarro et al. 1995) or OFF-pulse emission (Basu et al. 2011) if it is present. It would also help to identify scintillation effects (like in the case of PSR J1838+1523) and spectral index using the same multi-frequency data as is used for timing analysis. This is really important for current telescopes like GMRT, LOFAR, Australian Square Kilometre Array Pathfinder (ASKAP), MEERKAT and SKA in future.

11.2.3 Follow-up of 3 GMRT pulsars

In these follow-up observations, multi-frequency data allowed many more aspects of the pulsars and the ISM to be studied apart from obtaining better timing solutions. Well calibrated imaging data allowed spectral indices to be estimated for these pulsars. The values of $\tau_{\rm sc}$ obtained for PSR J2217+5733 and J0026+6320 turned out to be very different than the ones predicted by the NE2001 model of Cordes and Lazio (2002). This reinforces the variable and patchy nature of the ISM along different lines of sight. The implied spectral indices of $\tau_{\rm sc}$ were also found to be very different than what were expected from a Kolmogorov spectrum for the density fluctuations in the ISM. This indicates that PSR J2217+5733 and PSR J0026+6320 both lie in a region with significantly low scattering. Recently, Krishnakumar et al. (2015) published scattering measurements for 124 pulsars using data obtained with the ORT. Such studies along different lines of sight would shed more light on the patchy nature of the ISM. In fact it will also act as a feedback into the Galactic free electron density models and make them more robust over time.

11.2.4 Imaging Study of a Known Pulsar Field

Multi-epoch timing observations providing simultaneous imaging data would be useful not only to provide an independent assessment of the calibration procedure but would also be helpful for studying variability of many radio sources simultaneously. As these observations are typically spaced regularly, such observations would also be helpful in discovering transient radio sources. In addition, these observations would provide much better constraints on the radio flux density of these sources as compared to single epoch observations. Many of the continuum point sources are discovered and catalogued by large scale imaging surveys. Thus, multi-epoch imaging observations at the same frequency would provide a better flux density constraint. Similar observations at a different frequency would provide a handle on the spectral index of these sources. A radio spectral index allows an observer to determine which type of source it is. Once the source type is known, follow-up observations at other frequencies (like optical, X-rays and γ-rays) would provide a complete view of such sources and helps us understand the physics of such systems. Such off-shoot scientific studies would be possible only with simultaneous imaging data.

11.2.5 Pulsation Search towards HESS J1818–154 / G15.4+0.1

The PWN surrounding the Crab pulsar provides a good example of high energy emission powered by the wind of particles generated by a spin powered radio pulsar. The Crab PWN lacks an SNR and hence, is not a composite SNR. In the source that we studied, we found that molecular cloud interaction was more plausible as an origin of VHE emission. Recently, Kilpatrick et al. (2016) did a systematic molecular line survey of Galactic SNRs and found no significant association between VHE sources and molecular clouds. This favours PWNs as one of the more dominant origin of the VHE emission from Galactic sources. This makes an association between VHE sources and PWNs more likely than not. In

a broader scheme of things, this implies that composite SNRs may be one of the primary sites of cosmic ray acceleration.

11.2.6 Radio Pulsation Search towards Soft Gamma-ray Repeaters

During the thesis period, we carried out TOO observations on four SGR candidate sources. We did not detect radio pulsation in any of these. In general, SGRs can be broadly categorized as either radio-loud or radio-quiet based on the ratio of their quiescent X-ray luminosity to spin-down luminosity inferred from timing analysis (Rea et al. 2012). While the Galactic center magnetar did show radio pulsations (it also falls in the radio-loud class), our non-detection was consistent with the reported scattering time scale of almost 35% of the pulse period (Spitler et al. 2014). In the case of SGR J1935+2154, no radio pulsations were seen even from Parkes telescope with more stringent limits (Burgay et al. 2014). Surprisingly, Israel et al. (2016) found that SGR J1935+2154 should ideally fall in the radio-loud class. From our analysis, we obtain similar results (Surnis et al. 2016) but the radio non-detections could just be because our line of sight does not intersect the radio beam. The other two sources, SWIFT J174540.7−290015 and SGR J0755−2933 showed SGR-like X-ray bursts but did not even show X-ray pulsations. This makes their case as SGRs much weaker. In general, detection or non-detection of radio pulsations from SGR candidates provides crucial information while studying these objects.

11.3 Future Work

Although most of the work presented in the thesis is almost complete, there are some additional aspects, which we would like to explore in order to obtain better results or more scientific output from our data. These are listed below.

- To do much better RFI mitigation on the GMGPPTS data and re-run the harmonic and acceleration search.
- Keep timing PSR J1838+1523 with ORT once a week in order to catch a change in its $\dot{P}$ if it takes place in the future.
- To follow-up more on the possible FSRQs which were observed in the images of the field containing PSR J1838+1523 and look for any faint transient sources.
- To carry out polarization observations on PSR J1838+1523, J2208+5500, J2217+5733 and J0026+6320 using the upgraded GMRT.
- Repeat the variability study for fields containing PSR B1937+21, J2208+5500, J2217+5733 and J0026+6320.
- Study the variability of PSR B1937+21 and its spatially associated HII region.

Appendix A

The NCRA HPC

The most important part of any pulsar search analysis is the computational platform used. This was provided at NCRA by IBM® inc. and implemented by Locuz Enterprise Solutions Ltd. The cluster has 32 compute nodes[1] and 2 management nodes. Each compute node has 2 Intel® Sandy Bridge™ processors (16 cores) and 2 hard disks with a storage capacity of 500 GB each. The cluster also has a NAS of 100 TB capacity. The NAS is connected to the cluster through an Infiniband (IB) network with a total bandwidth of 2 GB/s out of which, 1.5 GB/s is for reading and 500 MB/s is for writing. The theoretical throughput of the cluster is 10 TFlops. Once the HPC was commissioned, we ran benchmark tests for processing throughput as well as input/output performance of the memory. They are briefly described below.

A.1 Processor Performance

In order to check and tune various performance related issues, a cluster program suite, Intel® Cluster Studio XE 2013, was installed on the HPC. It contained an inbuilt program for evaluating processor performance called LINPACK. It is basically a linear equation solver that uses matrix inversion as its method. It

[1] The compute nodes are numbered as n0 . . . n31

solves the system of equations for different number of matrix dimensions and reports average and maximum flops[2] rating of each processor.

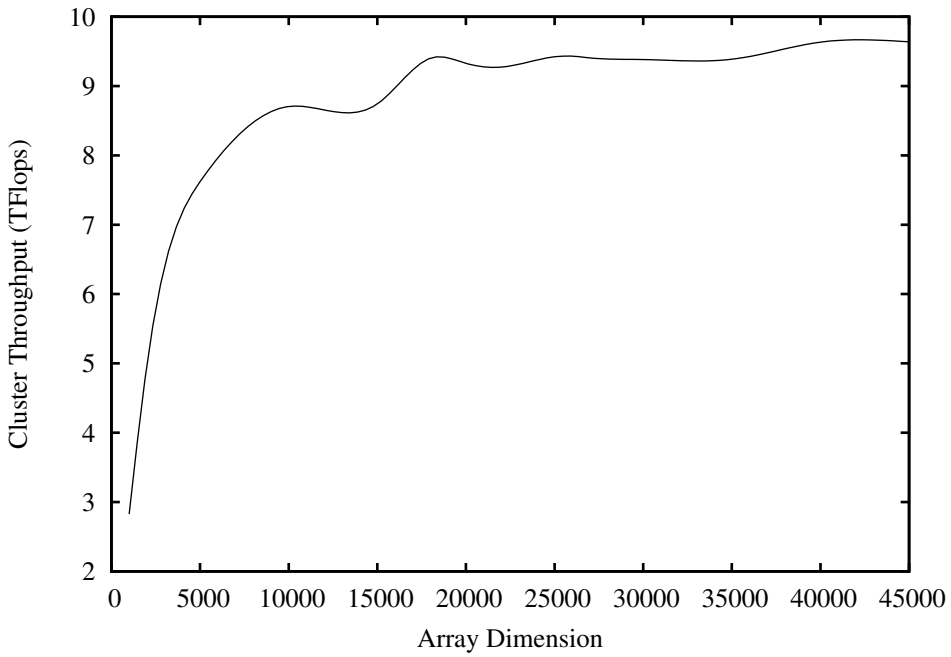

FIGURE A.1: Cluster throughput as a function of array dimension in the LINPACK solver.

This test was run on all the nodes using open source version of the MPI[3]. The MPI was configured so as to run the same LINPACK solver independently on all the cores (512 of them) simultaneously (the embarrassingly parallel model). The cluster throughput was calculated by adding the ratings obtained for all the processors. The tests were concluded with a sustained maximum throughput of 9.6 TFlops (see Figure A.1) as compared to the theoretical maximum of 10 TFlops.

A.2 Disk Performance

The expected bandwidths for simultaneous reading and writing from all nodes to NAS were 1.5 GB/s and 500 MB/s, respectively. The IOR[4] benchmark suite can be used to test this. It was used with a sample file of 512 MB, block size of 1

[2]short for floating point operations per second
[3]http://www.open-mpi.org
[4]http://www.sourceforge.net/projects/ior-sio/

MB for two transfer sizes of 512 KB and 1 MB. The IOR benchmark has different application program interfaces (APIs) to do the tests. Overall, two tests each were done using POSIX[5] and MPIIO[6] API. The maximum transfer speeds seen were as follows:

API	POSIX	MPIIO
Max read	248964.97 MB/s	216964.27 MB/s
Max write	822.17 MB/s	921.03 MB/s

These numbers were consistent with the ones obtained by the Locuz team (239706.18 MB/s for read and 489.13 MB/s for write) during their performance testing.

This estimate, however, suffers from the caching of files before being actually written to the disks. The cache memory on each node is 1 GB. The random access memory (RAM) of each node is 64 GB. Thus, each processor has 4 GB of RAM available for intense input/output operations. The test done above does not take care of these issues and hence gives a very high value for both read and write performance. In fact, the numbers obtained are the read/write speed for the cache, which is much faster. To avoid getting such unreal numbers, the IOR tests were run again with a file size of 9.4 GB (to avoid the RAM being used for input/output) and a block size of 1 GB (to avoid the cache being used for input/output). This time, only the MPIIO API was used with transfer sizes of 1 and 2 MB. The numbers obtained were as follows:

Transfer Size	1 MB	2 MB
Max read	940.83 MB/s	951.71 MB/s
Max write	203.58 MB/s	203.80 MB/s

From the above numbers, we concluded that the actual read and write speeds were about 60 % and 40 % respectively, of the theoretical values. As the search

[5]Portable Operating System Interface
[6]MPI-input/output

analysis was run on a local copy of the data, the lower performance of the disk speed was not a major concern for search analysis. In fact the near expected processor performance was a much desired result given the embarrassingly parallel implementation of the pulsar search algorithm.

Bibliography

Abramowski, A., F. Aharonian, F. Ait Benkhali, A. G. Akhperjanian, E. Angüner, G. Anton, S. Balenderan, A. Balzer, A. Barnacka, and et al. (2014, February). HESS J1818-154, a new composite supernova remnant discovered in TeV gamma rays and X-rays. *A&A 562*, A40.

Archibald, R. F., P. Scholz, and V. Kaspi (2016, March). Swift XRT Observations of SGR J0755-2933. *The Astronomer's Telegram 8868*.

Baade, W. and F. Zwicky (1934a, May). Cosmic Rays from Super-novae. *Proceedings of the National Academy of Science 20*, 259–263.

Baade, W. and F. Zwicky (1934b, May). On Super-novae. *Proceedings of the National Academy of Science 20*, 254–259.

Baars, J. W. M., R. Genzel, I. I. K. Pauliny-Toth, and A. Witzel (1977, October). The absolute spectrum of CAS A - an accurate flux density scale and a set of secondary calibrators. *A&A 61*, 99–106.

Backer, D. C. (1970, October). Pulsar Nulling Phenomena. *Nature 228*, 42–43.

Backer, D. C., S. R. Kulkarni, C. Heiles, M. M. Davis, and W. M. Goss (1982, December). A millisecond pulsar. *Nature 300*, 615–618.

Backer, D. C., T. Wong, and J. Valanju (2000, November). A Plasma Prism Model for an Anomalous Dispersion Event in the Crab Pulsar. *ApJ 543*, 740–753.

Baganoff, F. K., L. R. Corrales, J. Neilsen, M. A. Nowak, N. Rea, F. C. Zelati, D. Haggard, S. Markoff, G. Ponti, G. C. Bower, and G. P. Garmire (2016, February). Chandra Position of Galactic Center X-ray Transient Swift J174540.7-290015. *The Astronomer's Telegram 8746*.

Barr, E. D., D. J. Champion, M. Kramer, R. P. Eatough, P. C. C. Freire, R. Karuppusamy, K. J. Lee, J. P. W. Verbiest, C. G. Bassa, A. G. Lyne, B. Stappers, D. R. Lorimer, and B. Klein (2013, November). The Northern High Time Resolution Universe pulsar survey - I. Setup and initial discoveries. *MNRAS 435*, 2234–2245.

Barthelmy, S. D., V. D'Elia, N. Gehrels, L. Izzo, J. A. Kennea, H. A. Krimm, D. M. Palmer, M. H. Siegel, and T. N. Ukwatta (2016, March). Swift detection of a likely new SGR: SGR 0755-2933. *The Astronomer's Telegram 8831*.

Barvainis, R., J. Lehár, M. Birkinshaw, H. Falcke, and K. M. Blundell (2005, January). Radio Variability of Radio-quiet and Radio-loud Quasars. *ApJ 618*, 108–122.

Bassa, C. G., C. A. Jordan, E. F. Keane, A. G. Lyne, B. W. Stappers, and P. Weltevrede (2013, May). Searches for Dispersed Radio Pulsar Emission from the Sag A* SGR. *The Astronomer's Telegram 5033*, 1.

Basu, R., R. Athreya, and D. Mitra (2011, February). Detection of Off-pulse Emission from PSR B0525+21 and PSR B2045-16. *ApJ 728*, 157.

Bates, S. D., D. R. Lorimer, and J. P. W. Verbiest (2013, May). The pulsar spectral index distribution. *MNRAS 431*, 1352–1358.

Bhattacharya, D. and E. P. J. van den Heuvel (1991). Formation and evolution of binary and millisecond radio pulsars. *Phys. Rep. 203*, 1–124.

Bhattacharyya, B., S. Cooper, M. Malenta, J. Roy, J. Chengalur, M. Keith, S. Kudale, M. McLaughlin, S. M. Ransom, P. S. Ray, and B. W. Stappers (2016, February). The GMRT High Resolution Southern Sky Survey for Pulsars and Transients. I. Survey Description and Initial Discoveries. *ApJ 817*, 130.

Bower, G. C., A. Deller, P. Demorest, A. Brunthaler, R. Eatough, H. Falcke, M. Kramer, K. J. Lee, and L. Spitler (2014, January). The Angular Broadening of the Galactic Center Pulsar SGR J1745-29: A New Constraint on the Scattering Medium. *ApJ 780*, L2.

Bower, G. C., P. Demorest, F. Baganoff, L. Corrales, A. Deller, J. Dexter, D. Haggard, S. Markoff, N. Rea, and F. C. Zelati (2016, March). A Search for a Radio Counterpart to Swift J174540.7-290015. *The Astronomer's Telegram 8793*.

Boyles, J., R. S. Lynch, S. M. Ransom, I. H. Stairs, D. R. Lorimer, M. A. McLaughlin, J. W. T. Hessels, V. M. Kaspi, V. I. Kondratiev, A. Archibald, A. Berndsen, R. F. Cardoso, A. Cherry, C. R. Epstein, C. Karako-Argaman, C. A. McPhee, T. Pennucci, M. S. E. Roberts, K. Stovall, and J. van Leeuwen (2013, February). The Green Bank Telescope 350 MHz Drift-scan survey. I. Survey Observations and the Discovery of 13 Pulsars. *ApJ 763*, 80.

Bracewell, R. (1965). *The Fourier Transform and its applications*.

Briggs, D. S., F. R. Schwab, and R. A. Sramek (1999). Imaging. In G. B. Taylor, C. L. Carilli, and R. A. Perley (Eds.), *Synthesis Imaging in Radio Astronomy II*, Volume 180 of *Astronomical Society of the Pacific Conference Series*, pp. 127.

Brogan, C. L., J. D. Gelfand, B. M. Gaensler, N. E. Kassim, and T. J. W. Lazio (2006, March). Discovery of 35 New Supernova Remnants in the Inner Galaxy. *ApJ 639*, L25–L29.

Burgay, M., N. D'Amico, A. Possenti, R. N. Manchester, A. G. Lyne, B. C. Joshi, M. A. McLaughlin, M. Kramer, J. M. Sarkissian, F. Camilo, V. Kalogera, C. Kim, and D. R. Lorimer (2003, December). An increased estimate of the merger rate of double neutron stars from observations of a highly relativistic system. *Nature 426*, 531–533.

Burgay, M., G. L. Israel, N. Rea, A. Possenti, F. C. Zelati, P. Esposito, S. Mereghetti, and A. Tiengo (2014, August). Parkes upper limits on the pulsed radio emission of SGR 1935+2154. *The Astronomer's Telegram 6371*, 1.

Burgay, M., B. C. Joshi, N. D'Amico, A. Possenti, A. G. Lyne, R. N. Manchester, M. A. McLaughlin, M. Kramer, F. Camilo, and P. C. C. Freire (2006, May). The Parkes High-Latitude pulsar survey. *MNRAS 368*, 283–292.

Burgay, M., M. J. Keith, D. R. Lorimer, T. E. Hassall, A. G. Lyne, F. Camilo, N. D'Amico, G. B. Hobbs, M. Kramer, R. N. Manchester, M. A. McLaughlin, A. Possenti, I. H. Stairs, and B. W. Stappers (2013, February). The Perseus Arm Pulsar Survey. *MNRAS 429*, 579–588.

Burgay, M., M. Kramer, and M. A. McLaughlin (2014, September). The Double Pulsar J0737-3039A/B: a decade of surprises. *Bulletin of the Astronomical Society of India 42*, 101–119.

Burgay, M., R. Shannon, A. Possenti, M. Keith, J. Sarkissian, G. Israel, S. Johnston, N. Rea, and P. Esposito (2013, May). Detection of radio pulsations from the direction of the Galactic center Soft Gamma-ray Repeater with Parkes and the GBT. *The Astronomer's Telegram 5035*, 1.

Burns, W. R. and B. G. Clark (1969, July). Pulsar Search Techniques. *A&A 2*, 280–287.

Camilo, F., I. Cognard, S. M. Ransom, J. P. Halpern, J. Reynolds, N. Zimmerman, E. V. Gotthelf, D. J. Helfand, P. Demorest, G. Theureau, and D. C. Backer (2007, July). The Magnetar XTE J1810-197: Variations in Torque, Radio Flux Density, and Pulse Profile Morphology. *ApJ 663*, 497–504.

Camilo, F., D. R. Lorimer, P. Freire, A. G. Lyne, and R. N. Manchester (2000, June). Observations of 20 Millisecond Pulsars in 47 Tucanae at 20 Centimeters. *ApJ 535*, 975–990.

Camilo, F., D. J. Nice, J. A. Shrauner, and J. H. Taylor (1996, October). Princeton-Arecibo Declination-Strip Survey for Millisecond Pulsars. I. *ApJ 469*, 819.

Camilo, F., S. M. Ransom, S. Chatterjee, S. Johnston, and P. Demorest (2012, February). PSR J1841-0500: A Radio Pulsar That Mostly is Not There. *ApJ 746*, 63.

Camilo, F., S. M. Ransom, J. P. Halpern, J. A. J. Alford, I. Cognard, J. E. Reynolds, S. Johnston, J. Sarkissian, and W. van Straten (2016, April). Radio Disappearance of the Magnetar XTE J1810-197 and Continued X-ray Timing. *ApJ 820*, 110.

Camilo, F., S. M. Ransom, J. P. Halpern, and J. Reynolds (2007, September). 1E 1547.0-5408: A Radio-emitting Magnetar with a Rotation Period of 2 Seconds. *ApJ 666*, L93–L96.

Camilo, F., S. M. Ransom, J. P. Halpern, J. Reynolds, D. J. Helfand, N. Zimmerman, and J. Sarkissian (2006, August). Transient pulsed radio emission from a magnetar. *Nature 442*, 892–895.

Castelletti, G., L. Supan, G. Dubner, B. C. Joshi, and M. P. Surnis (2013, September). A hadronic scenario for HESS J1818-154. *A&A 557*, L15.

Chengalur, J. N. (2013, April). FLAGCAL: A flagging and calibration pipeline for GMRT data. Technical report, National Centre for Radio Astrophysics, Ganeshkhind, Pune.

Clark, B. G. (1980, September). An efficient implementation of the algorithm 'CLEAN'. *A&A 89*, 377.

Clark, B. G. (1999). Coherence in Radio Astronomy. In G. B. Taylor, C. L. Carilli, and R. A. Perley (Eds.), *Synthesis Imaging in Radio Astronomy II*, Volume 180 of *Astronomical Society of the Pacific Conference Series*, pp. 1.

Clifton, T. R. and A. G. Lyne (1986, March). High-radio-frequency survey for young and millisecond pulsars. *Nature 320*, 43–45.

Clifton, T. R., A. G. Lyne, A. W. Jones, J. McKenna, and M. Ashworth (1992, January). A high-frequency survey of the galactic plane for young and distant pulsars. *MNRAS 254*, 177–184.

Condon, J. J., W. D. Cotton, E. W. Greisen, Q. F. Yin, R. A. Perley, G. B. Taylor, and J. J. Broderick (1998, May). The NRAO VLA Sky Survey. *AJ 115*, 1693–1716.

Cordes, J. M., P. C. C. Freire, D. R. Lorimer, F. Camilo, D. J. Champion, D. J. Nice, R. Ramachandran, J. W. T. Hessels, W. Vlemmings, J. van Leeuwen, S. M. Ransom, N. D. R. Bhat, Z. Arzoumanian, M. A. McLaughlin, V. M. Kaspi, L. Kasian, J. S. Deneva, B. Reid, S. Chatterjee, J. L. Han, D. C. Backer, I. H. Stairs, A. A. Deshpande, and C. Faucher-Giguère (2006, January). Arecibo Pulsar Survey Using ALFA. I. Survey Strategy and First Discoveries. *ApJ 637*, 446–455.

Cordes, J. M. and T. J. W. Lazio (2002, July). NE2001.I. A New Model for the Galactic Distribution of Free Electrons and its Fluctuations. *ArXiv Astrophysics e-prints*.

Cordes, J. M. and M. A. McLaughlin (2003, October). Searches for Fast Radio Transients. *ApJ 596*, 1142–1154.

Cornwell, T. and E. B. Fomalont (1999). Self-Calibration. In G. B. Taylor, C. L. Carilli, and R. A. Perley (Eds.), *Synthesis Imaging in Radio Astronomy II*, Volume 180 of *Astronomical Society of the Pacific Conference Series*, pp. 187.

Crawford, F., B. M. Gaensler, V. M. Kaspi, R. N. Manchester, F. Camilo, A. G. Lyne, and M. J. Pivovaroff (2001, June). A Radio Supernova Remnant Associated with the Young Pulsar J1119-6127. *ApJ 554*, 152–160.

Cummings, J. R. and S. Campana (2014, July). SGR 1935+2154 Swift-BAT archival data search. *The Astronomer's Telegram 6299*, 1.

Cummmings, J. R., S. D. Barthelmy, M. M. Chester, and K. L. Page (2014, July). Newly discovered SGR 1935+2154: Swift observations. *The Astronomer's Telegram 6294*, 1.

Damashek, M., J. H. Taylor, and R. A. Hulse (1978, October). Parameters of 17 newly discovered pulsars in the northern sky. *ApJ 225*, L31–L33.

Davies, J. G. and M. I. Large (1970). A single-pulse search for pulsars. *MNRAS 149*, 301.

Davies, J. G., M. I. Large, and A. C. Pickwick (1970, September). Five New Pulsars. *Nature 227*, 1123–1124.

Davies, J. G., A. G. Lyne, and J. H. Seiradakis (1972, November). Pulsar Associated with the Supernova Remnant IC 443. *Nature 240*, 229–230.

Davies, J. G., A. G. Lyne, and J. H. Seiradakis (1973, August). Thirteen New Pulsars. *Nature Physical Science 244*, 84–85.

Degenaar, N., M. T. Reynolds, J. M. Miller, J. A. Kennea, and R. Wijnands (2013, April). Large Flare from Sgr A* Detected by Swift. *The Astronomer's Telegram 5006*, 1.

Demorest, P. B., T. Pennucci, S. M. Ransom, M. S. E. Roberts, and J. W. T. Hessels (2010, October). A two-solar-mass neutron star measured using Shapiro delay. *Nature 467*, 1081–1083.

Deneva, J. S., K. Stovall, M. A. McLaughlin, S. D. Bates, P. C. C. Freire, J. G. Martinez, F. Jenet, and M. Bagchi (2013, September). Goals, Strategies and First Discoveries of AO327, the Arecibo All-sky 327 MHz Drift Pulsar Survey. *ApJ 775*, 51.

Dewey, R. J., J. H. Taylor, J. M. Weisberg, and G. H. Stokes (1985, July). A search for low-luminosity pulsars. *ApJ 294*, L25–L29.

Dodson, R., D. Legge, J. E. Reynolds, and P. M. McCulloch (2003, October). The Vela Pulsar's Proper Motion and Parallax Derived from VLBI Observations. *ApJ 596*, 1137–1141.

Duncan, R. C. and C. Thompson (1992, June). Formation of very strongly magnetized neutron stars - Implications for gamma-ray bursts. *ApJ 392*, L9–L13.

DuPlain, R., S. Ransom, P. Demorest, P. Brandt, J. Ford, and A. L. Shelton (2008, August). Launching GUPPI: the Green Bank Ultimate Pulsar Processing Instrument. In *Society of Photo-Optical Instrumentation Engineers (SPIE)*

Conference Series, Volume 7019 of *Society of Photo-Optical Instrumentation Engineers (SPIE) Conference Series*, pp. 1.

Eatough, R., R. Karuppusamy, M. Kramer, B. Klein, D. Champion, E. Keane, A. Kraus, C. Bassa, A. Lyne, P. Lazarus, J. Verbiest, P. Freire, A. Brunthaler, H. Falcke, L. Spitler, and B. Stappers (2013, May). Further radio pulsations from the direction of the NuSTAR 3.76-second X-ray pulsar, and a dispersion measure estimate. *The Astronomer's Telegram 5043*, 1.

Eatough, R., R. Karuppusamy, M. Kramer, B. Klein, D. Champion, A. Kraus, E. Keane, C. Bassa, A. Lyne, P. Lazarus, J. Verbiest, P. Freire, A. Brunthaler, and H. Falcke (2013, May). Detection of radio pulsations from the direction of the NuSTAR 3.76 second X-ray pulsar at 8.35 GHz. *The Astronomer's Telegram 5040*, 1.

Eatough, R., R. Karuppusamy, M. Kramer, A. Kraus, B. Klein, D. Champion, J. Verbiest, P. Lazarus, P. Freire, A. Brunthaler, and H. Falcke (2013, April). Searches for radio pulsations from the 3.76 second NuSTAR X-ray pulsar in the Galactic centre. *The Astronomer's Telegram 5027*, 1.

Eatough, R. P., H. Falcke, R. Karuppusamy, K. J. Lee, D. J. Champion, E. F. Keane, G. Desvignes, D. H. F. M. Schnitzeler, L. G. Spitler, M. Kramer, B. Klein, C. Bassa, G. C. Bower, A. Brunthaler, I. Cognard, A. T. Deller, P. B. Demorest, P. C. C. Freire, A. Kraus, A. G. Lyne, A. Noutsos, B. Stappers, and N. Wex (2013, September). A strong magnetic field around the supermassive black hole at the centre of the Galaxy. *Nature 501*, 391–394.

Eatough, R. P., E. F. Keane, and A. G. Lyne (2009, May). An interference removal technique for radio pulsar searches. *MNRAS 395*, 410–415.

Eatough, R. P., M. Kramer, A. G. Lyne, and M. J. Keith (2013, May). A coherent acceleration search of the Parkes multibeam pulsar survey - techniques and the discovery and timing of 16 pulsars. *MNRAS 431*, 292–307.

Edwards, R. T., M. Bailes, W. van Straten, and M. C. Britton (2001, September). The Swinburne intermediate-latitude pulsar survey. *MNRAS 326*, 358–374.

Esposito, P., A. Tiengo, N. Rea, R. Turolla, A. Fenzi, A. Giuliani, G. L. Israel, S. Zane, S. Mereghetti, A. Possenti, M. Burgay, L. Stella, D. Götz, R. Perna, R. P. Mignani, and P. Romano (2013, March). X-ray and radio observations of the magnetar Swift J1834.9-0846 and its dust-scattering halo. *MNRAS 429*, 3123–3132.

Esposito, V., E. Kuulkers, A. Bazzano, V. Beckmann, T. Bird, A. Bodaghee, J. Chenevez, M. Del Santo, A. Domingo, P. Jonker, P. Kretschmar, C. Markwardt, A. Paizis, K. Pottschmidt, C. Sánchez-Fernández, R. Wijnands, E. Bozzo, and C. Ferrigno (2016, February). INTEGRAL observations of Swift J174540.7-290015. *The Astronomer's Telegram 8684*.

Fich, M., L. Blitz, and A. A. Stark (1989, July). The rotation curve of the Milky Way to 2 R(0). *ApJ 342*, 272–284.

Folkner, W. M., J. G. Williams, D. H. Boggs, R. S. Park, and P. Kuchynka (2014, February). The Planetary and Lunar Ephemerides DE430 and DE431. *Interplanetary Network Progress Report 196*, C1.

Fomalont, E. B. and R. A. Perley (1999). Calibration and Editing. In G. B. Taylor, C. L. Carilli, and R. A. Perley (Eds.), *Synthesis Imaging in Radio Astronomy II*, Volume 180 of *Astronomical Society of the Pacific Conference Series*, pp. 79.

Foster, R. S. and D. C. Backer (1990, September). Constructing a pulsar timing array. *ApJ 361*, 300–308.

Foster, R. S., B. J. Cadwell, A. Wolszczan, and S. B. Anderson (1995, December). A High Galactic Latitude Pulsar Survey of the Arecibo Sky. *ApJ 454*, 826.

Freire, P. C., F. Camilo, M. Kramer, D. R. Lorimer, A. G. Lyne, R. N. Manchester, and N. D'Amico (2003, April). Further results from the timing of the millisecond pulsars in 47 Tucanae. *MNRAS 340*, 1359–1374.

Gajjar, V., B. C. Joshi, and M. Kramer (2012, August). A survey of nulling pulsars using the Giant Meterwave Radio Telescope. *MNRAS 424*, 1197–1205.

Gold, T. (1968, May). Rotating Neutron Stars as the Origin of the Pulsating Radio Sources. *Nature 218*, 731–732.

Gotthelf, E. V., K. Mori, J. P. Halpern, N. M. Barriere, M. Nynka, C. J. Hailey, F. A. Harrison, J. A. Kennea, V. M. Kaspi, C. B. Markwardt, J. A. Tomsick, and S. Zhang (2013, May). Spin-down Measurement of PSR J1745-2900: a New Magnetar. *The Astronomer's Telegram 5046*, 1.

Green, D. A. (2014, June). A catalogue of 294 Galactic supernova remnants. *Bulletin of the Astronomical Society of India 42*, 47–58.

Haslam, C. G. T., C. J. Salter, H. Stoffel, and W. E. Wilson (1982, January). A 408 MHz all-sky continuum survey. II - The atlas of contour maps. *A&AS 47*, 1.

He, C., C.-Y. Ng, and V. M. Kaspi (2013, May). The Correlation between Dispersion Measure and X-Ray Column Density from Radio Pulsars. *ApJ 768*, 64.

Helfand, D. J., R. H. Becker, R. L. White, A. Fallon, and S. Tuttle (2006, May). MAGPIS: A Multi-Array Galactic Plane Imaging Survey. *AJ 131*, 2525–2537.

Helfand, D. J., R. N. Manchester, and J. H. Taylor (1975). Observations of pulsar radio emission. iii. stability of integrated profiles. *Astrophys. J. 198*, 661–670.

Hessels, J. W. T., S. M. Ransom, I. H. Stairs, P. C. C. Freire, V. M. Kaspi, and F. Camilo (2006, March). A Radio Pulsar Spinning at 716 Hz. *Science 311*, 1901–1904.

Hessels, J. W. T., M. S. E. Roberts, M. A. McLaughlin, P. S. Ray, P. Bangale, S. M. Ransom, M. Kerr, F. Camilo, and M. E. Decesar (2011, August). A 350-MHz GBT Survey of 50 Faint Fermi γ-ray Sources for Radio Millisecond Pulsars. In M. Burgay, N. D'Amico, P. Esposito, A. Pellizzoni, and A. Possenti (Eds.), *American Institute of Physics Conference Series*, Volume 1357 of *American Institute of Physics Conference Series*, pp. 40–43.

Hewish, A., S. J. Bell, J. D. H. Pilkington, P. F. Scott, and R. A. Collins (1968, February). Observation of a Rapidly Pulsating Radio Source. *Nature 217*, 709–713.

Hobbs, G., W. Coles, R. N. Manchester, M. J. Keith, R. M. Shannon, D. Chen, M. Bailes, N. D. R. Bhat, S. Burke-Spolaor, D. Champion, A. Chaudhary, A. Hotan, J. Khoo, J. Kocz, Y. Levin, S. Oslowski, B. Preisig, V. Ravi, J. E. Reynolds, J. Sarkissian, W. van Straten, J. P. W. Verbiest, D. Yardley, and X. P. You (2012, December). Development of a pulsar-based time-scale. *MNRAS 427*, 2780–2787.

Hobbs, G., R. Edwards, and R. Manchester (2006, December). TEMPO2: a New Pulsar Timing Package. *Chinese Journal of Astronomy and Astrophysics Supplement 6*(2), 189–192.

Hofverberg, P., R. C. G. Chaves, J. Méhault, and M. de Naurois (2011). Discovery of VHE gamma-ray emission from the shell-type SNR G15.4+0.1 with H.E.S.S. *International Cosmic Ray Conference 7*, 248.

Högbom, J. A. (1974, June). Aperture Synthesis with a Non-Regular Distribution of Interferometer Baselines. *A&AS 15*, 417.

Holdaway, M. A. and T. T. Helfer (1999). Interferometric Array Design. In G. B. Taylor, C. L. Carilli, and R. A. Perley (Eds.), *Synthesis Imaging in Radio Astronomy II*, Volume 180 of *Astronomical Society of the Pacific Conference Series*, pp. 537.

Huguenin, G. R., J. H. Taylor, L. E. Goad, A. Hartai, G. S. F. Orsten, and A. K. Rodman (1968, August). New Pulsating Radio Source. *Nature 219*, 576–577.

Hulse, R. A. and J. H. Taylor (1974, July). A High-Sensitivity Pulsar Survey. *ApJ 191*, L59.

Hulse, R. A. and J. H. Taylor (1975a, October). A deep sample of new pulsars and their spatial extent in the galaxy. *ApJ 201*, L55–L59.

Hulse, R. A. and J. H. Taylor (1975b, January). Discovery of a pulsar in a binary system. *ApJ 195*, L51–L53.

Ibrahim, A. I., C. B. Markwardt, J. H. Swank, S. Ransom, M. Roberts, V. Kaspi, P. M. Woods, S. Safi-Harb, S. Balman, W. C. Parke, C. Kouveliotou, K. Hurley, and T. Cline (2004, July). Discovery of a Transient Magnetar: XTE J1810-197. *ApJ 609*, L21–L24.

Intema, H. T., P. Jagannathan, K. P. Mooley, and D. A. Frail (2016, March). The GMRT 150 MHz All-sky Radio Survey: First Alternative Data Release TGSS ADR1. *ArXiv e-prints*.

Israel, G. L., P. Esposito, N. Rea, F. Coti Zelati, A. Tiengo, S. Campana, S. Mereghetti, G. A. Rodriguez Castillo, D. Götz, M. Burgay, A. Possenti, S. Zane, R. Turolla, R. Perna, G. Cannizzaro, and J. Pons (2016, April). The discovery, monitoring and environment of SGR J1935+2154. *MNRAS 457*, 3448–3456.

Israel, G. L., N. Rea, F. C. Zelati, P. Esposito, M. Burgay, S. Mereghetti, A. Possenti, and A. Tiengo (2014, August). Chandra discovery of 3.2s X-ray pulsations from SGR 1935+2154. *The Astronomer's Telegram 6370*, 1.

Jackson, J. M., J. M. Rathborne, R. Y. Shah, R. Simon, T. M. Bania, D. P. Clemens, E. T. Chambers, A. M. Johnson, M. Dormody, R. Lavoie, and M. H. Heyer (2006, March). The Boston University-Five College Radio Astronomy Observatory Galactic Ring Survey. *ApJS 163*, 145–159.

Jacoby, B. A., M. Bailes, S. M. Ord, R. T. Edwards, and S. R. Kulkarni (2009, July). A Large-Area Survey for Radio Pulsars at High Galactic Latitudes. *ApJ 699*, 2009–2016.

Jenet, F. A. and J. Gil (2003, October). Using the Intensity Modulation Index to Test Pulsar Radio Emission Models. *ApJ 596*, L215–L218.

Johnston, S., A. G. Lyne, R. N. Manchester, D. A. Kniffen, N. D'Amico, J. Lim, and M. Ashworth (1992, April). A high-frequency survey of the southern Galactic plane for pulsars. *MNRAS 255*, 401–411.

Johnston, S., R. N. Manchester, A. G. Lyne, M. Bailes, V. M. Kaspi, G. Qiao, and N. D'Amico (1992, March). PSR 1259-63 - A binary radio pulsar with a Be star companion. *ApJ 387*, L37–L41.

Joshi, B. C., M. A. McLaughlin, A. G. Lyne, D. A. Ludovici, N. A. Pawar, A. J. Faulkner, D. R. Lorimer, M. Kramer, and M. L. Davies (2009, September). Discovery of three new pulsars in a 610-MHz pulsar survey with the GMRT. *MNRAS 398*, 943–948.

Kalberla, P. M. W., W. B. Burton, D. Hartmann, E. M. Arnal, E. Bajaja, R. Morras, and W. G. L. Pöppel (2005, September). The Leiden/Argentine/Bonn (LAB) Survey of Galactic HI. Final data release of the combined LDS and IAR surveys with improved stray-radiation corrections. *A&A 440*, 775–782.

Keane, E. F., B. Bhattacharyya, M. Kramer, B. W. Stappers, S. D. Bates, M. Burgay, S. Chatterjee, D. J. Champion, R. P. Eatough, J. W. T. Hessels, G. Janssen, K. J. Lee, J. van Leeuwen, J. Margueron, M. Oertel, A. Possenti, S. Ransom, G. Theureau, and P. Torne (2015). A Cosmic Census of Radio Pulsars with the SKA. *Advancing Astrophysics with the Square Kilometre Array (AASKA14)*, 40.

Keane, E. F., M. Kramer, A. G. Lyne, B. W. Stappers, and M. A. McLaughlin (2011, August). Rotating Radio Transients: new discoveries, timing solutions and musings. *MNRAS 415*, 3065–3080.

Keith, M. J., A. Jameson, W. van Straten, M. Bailes, S. Johnston, M. Kramer, A. Possenti, S. D. Bates, N. D. R. Bhat, M. Burgay, S. Burke-Spolaor, N. D'Amico, L. Levin, P. L. McMahon, S. Milia, and B. W. Stappers (2010, December). The High Time Resolution Universe Pulsar Survey - I. System configuration and initial discoveries. *MNRAS 409*, 619–627.

Kennea, J. A., H. Krimm, S. Barthelmy, N. Gehrels, C. Markwardt, J. Cummings, F. Marshall, T. Sakamoto, N. Degenaar, M. T. Reynolds, J. M. Miller, and C. Kouveliotou (2013, April). Swift/BAT detection of an SGR-like flare from near Sgr A*. *The Astronomer's Telegram 5009*, 1.

Kilpatrick, C. D., J. H. Bieging, and G. H. Rieke (2016, January). A Systematic Survey for Broadened CO Emission toward Galactic Supernova Remnants. *ApJ 816*, 1.

Kramer, M., C. Lange, D. R. Lorimer, D. C. Backer, K. M. Xilouris, A. Jessner, and R. Wielebinski (1999, December). The Characteristics of Millisecond Pulsar Emission. III. From Low to High Frequencies. *ApJ 526*, 957–975.

Kramer, M., A. G. Lyne, J. T. O'Brien, C. A. Jordan, and D. R. Lorimer (2006, April). A Periodically Active Pulsar Giving Insight into Magnetospheric Physics. *Science 312*, 549–551.

Krishnakumar, M. A., D. Mitra, A. Naidu, B. C. Joshi, and P. K. Manoharan (2015, May). Scatter Broadening Measurements of 124 Pulsars At 327 Mhz. *ApJ 804*, 23.

Lal, D. V. (2013, November). *GMRT Observer's Manual*. NCRA-TIFR.

Large, M. I., A. E. Vaughan, and R. Wielebinski (1968, November). Pulsar Search at the Molonglo Radio Observatory. *Nature 220*, 753–756.

Leahy, D. A. and W. W. Tian (2008, March). The distance of the SNR Kes 75 and PWN PSR J1846-0258 system. *A&A 480*, L25–L28.

Levin, L., M. Bailes, S. Bates, N. D. R. Bhat, M. Burgay, S. Burke-Spolaor, N. D'Amico, S. Johnston, M. Keith, M. Kramer, S. Milia, A. Possenti, N. Rea, B. Stappers, and W. van Straten (2010, September). A Radio-loud Magnetar in X-ray Quiescence. *ApJ 721*, L33–L37.

Levin, L., M. Bailes, S. D. Bates, N. D. R. Bhat, M. Burgay, S. Burke-Spolaor, N. D'Amico, S. Johnston, M. J. Keith, M. Kramer, S. Milia, A. Possenti,

B. Stappers, and W. van Straten (2012, May). Radio emission evolution, polarimetry and multifrequency single pulse analysis of the radio magnetar PSR J1622-4950. *MNRAS 422*, 2489–2500.

Levine, E. S., L. Blitz, and C. Heiles (2006, June). The Spiral Structure of the Outer Milky Way in Hydrogen. *Science 312*, 1773–1777.

Lorimer, D. and M. Kramer (2005). *Handbook of Pulsar Astronomy*. Cambridge University Press.

Lorimer, D. R., F. Camilo, and M. A. McLaughlin (2013, September). Timing of pulsars found in a deep Parkes multibeam survey. *MNRAS 434*, 347–351.

Lorimer, D. R., A. G. Lyne, M. A. McLaughlin, M. Kramer, G. G. Pavlov, and C. Chang (2012, October). Radio and X-Ray Observations of the Intermittent Pulsar J1832+0029. *ApJ 758*, 141.

Lynch, R. S., R. F. Archibald, V. M. Kaspi, and P. Scholz (2015, June). Green Bank Telescope and Swift X-Ray Telescope Observations of the Galactic Center Radio Magnetar SGR J1745-2900. *ApJ 806*, 266.

Lyne, A., G. Hobbs, M. Kramer, I. Stairs, and B. Stappers (2010, July). Switched Magnetospheric Regulation of Pulsar Spin-Down. *Science 329*, 408–.

Lyne, A. G., M. Burgay, M. Kramer, A. Possenti, R. N. Manchester, F. Camilo, M. A. McLaughlin, D. R. Lorimer, N. D'Amico, B. C. Joshi, J. Reynolds, and P. C. C. Freire (2004, February). A Double-Pulsar System: A Rare Laboratory for Relativistic Gravity and Plasma Physics. *Science 303*, 1153–1157.

Lyne, A. G., R. N. Manchester, D. R. Lorimer, M. Bailes, N. D'Amico, T. M. Tauris, S. Johnston, J. F. Bell, and L. Nicastro (1998, April). The Parkes Southern Pulsar Survey - II. Final results and population analysis. *MNRAS 295*, 743–755.

Lyne, A. G., R. N. Manchester, and J. H. Taylor (1985, April). The galactic population of pulsars. *MNRAS 213*, 613–639.

Maan, Y., M. Surnis, M. A. Krishnakumar, B. C. Joshi, and P. K. Manoharan (2016, February). Search for pulsed radio emission from SWIFT J174540.7-290015. *The Astronomer's Telegram 8729*.

Magro, A., A. Karastergiou, S. Salvini, B. Mort, F. Dulwich, and K. Zarb Adami (2011, November). Real-time, fast radio transient searches with GPU de-dispersion. *MNRAS 417*, 2642–2650.

Manchester, R. N., N. D'Amico, and I. R. Tuohy (1985, February). A search for short-period pulsars. *MNRAS 212*, 975–986.

Manchester, R. N., G. Hobbs, M. Bailes, W. A. Coles, W. van Straten, M. J. Keith, R. M. Shannon, N. D. R. Bhat, A. Brown, S. G. Burke-Spolaor, D. J. Champion, A. Chaudhary, R. T. Edwards, G. Hampson, A. W. Hotan, A. Jameson, F. A. Jenet, M. J. Kesteven, J. Khoo, J. Kocz, K. Maciesiak, S. Oslowski, V. Ravi, J. R. Reynolds, J. M. Sarkissian, J. P. W. Verbiest, Z. L. Wen, W. E. Wilson, D. Yardley, W. M. Yan, and X. P. You (2013, January). The Parkes Pulsar Timing Array Project. *PASA 30*, e017.

Manchester, R. N., G. B. Hobbs, A. Teoh, and M. Hobbs (2005, April). The Australia Telescope National Facility Pulsar Catalogue. *AJ 129*, 1993–2006.

Manchester, R. N., A. G. Lyne, F. Camilo, J. F. Bell, V. M. Kaspi, N. D'Amico, N. P. F. McKay, F. Crawford, I. H. Stairs, A. Possenti, M. Kramer, and D. C. Sheppard (2001, November). The Parkes multi-beam pulsar survey - I. Observing and data analysis systems, discovery and timing of 100 pulsars. *MNRAS 328*, 17–35.

Manchester, R. N., A. G. Lyne, N. D'Amico, M. Bailes, S. Johnston, D. R. Lorimer, P. A. Harrison, L. Nicastro, and J. F. Bell (1996, April). The Parkes Southern Pulsar Survey. I. Observing and data analysis systems and initial results. *MNRAS 279*, 1235–1250.

Manchester, R. N., A. G. Lyne, C. Robinson, M. Bailes, and N. D'Amico (1991, July). Discovery of ten millisecond pulsars in the globular cluster 47 Tucanae. *Nature 352*, 219–221.

Manchester, R. N., A. G. Lyne, J. H. Taylor, J. M. Durdin, M. I. Large, and A. G. Little (1978, November). The second Molonglo pulsar survey - discovery of 155 pulsars. *MNRAS 185*, 409–421.

Maron, O., J. Kijak, M. Kramer, and R. Wielebinski (2000, December). Pulsar spectra of radio emission. *A&AS 147*, 195–203.

McClure-Griffiths, N. M., J. M. Dickey, B. M. Gaensler, A. J. Green, M. Haverkorn, and S. Strasser (2005, June). The Southern Galactic Plane Survey: H I Observations and Analysis. *ApJS 158*, 178–187.

McLaughlin, M. A., A. G. Lyne, D. R. Lorimer, M. Kramer, A. J. Faulkner, R. N. Manchester, J. M. Cordes, F. Camilo, A. Possenti, I. H. Stairs, G. Hobbs, N. D'Amico, M. Burgay, and J. T. O'Brien (2006, February). Transient radio bursts from rotating neutron stars. *Nature 439*, 817–820.

Milne, D. K. (1968, April). Radio emission from the supernova remnant Vela-X. *Australian Journal of Physics 21*, 201.

Mori, K., E. V. Gotthelf, N. M. Barriere, C. J. Hailey, F. A. Harrison, V. M. Kaspi, J. A. Tomsick, and S. Zhang (2013, April). NuSTAR discovery of a 3.76 second pulsar in the Sgr A* region. *The Astronomer's Telegram 5020*, 1.

Mori, K., E. V. Gotthelf, S. Zhang, H. An, F. K. Baganoff, N. M. Barrière, A. M. Beloborodov, S. E. Boggs, F. E. Christensen, W. W. Craig, F. Dufour, B. W. Grefenstette, C. J. Hailey, F. A. Harrison, J. Hong, V. M. Kaspi, J. A. Kennea, K. K. Madsen, C. B. Markwardt, M. Nynka, D. Stern, J. A. Tomsick, and W. W. Zhang (2013, June). NuSTAR Discovery of a 3.76 s Transient Magnetar Near Sagittarius A*. *ApJ 770*, L23.

Naidu, A., B. C. Joshi, P. K. Manoharan, and M. A. Krishnakumar (2015, March). PONDER - A Real time software backend for pulsar and IPS observations at the Ooty Radio Telescope. *Experimental Astronomy*.

Navarro, J., A. G. de Bruyn, D. A. Frail, S. R. Kulkarni, and A. G. Lyne (1995, December). A Very Luminous Binary Millisecond Pulsar. *ApJ 455*, L55.

Nice, D. J., A. S. Fruchter, and J. H. Taylor (1995, August). A Search for Fast Pulsars along the Galactic Plane. *ApJ 449*, 156.

Nice, D. J., J. H. Taylor, and A. S. Fruchter (1993, January). Two newly discovered millisecond pulsars. *ApJ 402*, L49–L52.

Olausen, S. A. and V. M. Kaspi (2014, May). The McGill Magnetar Catalog. *ApJS 212*, 6.

Palaniswamy, D., N. D. R. Bhat, S. J. Tingay, S. P. Ellingsen, R. B. Wayth, and C. M. Trott (2013, May). Detection of radio pulsations at 22 GHz from the Magnetar PSR J1745-2900 in the archival data from 2011. *The Astronomer's Telegram 5076*, 1.

Papitto, A., C. Ferrigno, E. Bozzo, N. Rea, L. Pavan, L. Burderi, M. Burgay, S. Campana, T. di Salvo, M. Falanga, M. D. Filipović, P. C. C. Freire, J. W. T. Hessels, A. Possenti, S. M. Ransom, A. Riggio, P. Romano, J. M. Sarkissian, I. H. Stairs, L. Stella, D. F. Torres, M. H. Wieringa, and G. F. Wong (2013, September). Swings between rotation and accretion power in a binary millisecond pulsar. *Nature 501*, 517–520.

Pennucci, T. T., A. Possenti, P. Esposito, N. Rea, D. Haggard, F. K. Baganoff, M. Burgay, F. Coti Zelati, G. L. Israel, and A. Minter (2015, July). Simultaneous Multi-band Radio and X-Ray Observations of the Galactic Center Magnetar SGR 1745-2900. *ApJ 808*, 81.

Pound, R. V. and G. A. Rebka (1959, November). Gravitational Red-Shift in Nuclear Resonance. *Physical Review Letters 3*, 439–441.

Press, W. H., B. P. Flannery, and S. A. Teukolsky (1986). *Numerical recipes. The art of scientific computing.*

Rankin, J. M. (1986, February). Toward an empirical theory of pulsar emission. III - Mode changing, drifting subpulses, and pulse nulling. *ApJ 301*, 901–922.

Ransom, S. M., I. H. Stairs, A. M. Archibald, J. W. T. Hessels, D. L. Kaplan, M. H. van Kerkwijk, J. Boyles, A. T. Deller, S. Chatterjee, A. Schechtman-Rook, A. Berndsen, R. S. Lynch, D. R. Lorimer, C. Karako-Argaman, V. M. Kaspi, V. I. Kondratiev, M. A. McLaughlin, J. van Leeuwen, R. Rosen, M. S. E. Roberts, and K. Stovall (2014, January). A millisecond pulsar in a stellar triple system. *Nature 505*, 520–524.

Rea, N., P. Esposito, G. L. Israel, A. Papitto, A. Tiengo, F. Baganoff, D. Haggard, S. Mereghetti, M. Burgay, A. Possenti, and S. Zane (2013, April). Chandra localization of the soft gamma repeater in the Galactic Center region. *The Astronomer's Telegram 5032*, 1.

Rea, N., J. A. Pons, D. F. Torres, and R. Turolla (2012, March). The Fundamental Plane for Radio Magnetars. *ApJ 748*, L12.

Reardon, D. J., G. Hobbs, W. Coles, Y. Levin, M. J. Keith, M. Bailes, N. D. R. Bhat, S. Burke-Spolaor, S. Dai, M. Kerr, P. D. Lasky, R. N. Manchester, S. Osłowski, V. Ravi, R. M. Shannon, W. van Straten, L. Toomey, J. Wang, L. Wen, X. P. You, and X.-J. Zhu (2016, January). Timing analysis for 20 millisecond pulsars in the Parkes Pulsar Timing Array. *MNRAS 455*, 1751–1769.

Reynolds, M., J. Kennea, N. Degenaar, R. Wijnands, and J. Miller (2016, February). New Galactic Center X-ray Transient Detected by Swift: SWIFT J174540.7-290015. *The Astronomer's Telegram 8649*.

Rickett, B. J. (1977). Interstellar scattering and scintillation of radio waves. *ARA&A 15*, 479–504.

Ridley, J. P., F. Crawford, D. R. Lorimer, S. R. Bailey, J. H. Madden, R. Anella, and J. Chennamangalam (2013, July). Eight new radio pulsars in the Large Magellanic Cloud. *MNRAS 433*, 138–146.

Ritchings, R. T. (1976, August). Pulsar single pulse intensity measurements and pulse nulling. *MNRAS 176*, 249–263.

Roy, J., B. Bhattacharyya, and Y. Gupta (2012, November). A multi-pixel beamformer using an interferometric array and its application to the localization of newly discovered pulsars. *MNRAS 427*, L90–L94.

Roy, J., Y. Gupta, U.-L. Pen, J. B. Peterson, S. Kudale, and J. Kodilkar (2010, August). A real-time software backend for the GMRT. *Experimental Astronomy 28*, 25–60.

Ruderman, M. A. and P. G. Sutherland (1975, February). Theory of pulsars - Polar caps, sparks, and coherent microwave radiation. *ApJ 196*, 51–72.

Ryle, M., A. Hewish, and J. Shakeshaft (1959, December). The synthesis of large radio telescopes by the use of radio interferometers. *IEEE Transactions on Antennas and Propagation 7*, 120–124.

Salgado, J. F., D. R. Altschuler, T. Ghosh, B. K. Dennison, K. J. Mitchell, and H. E. Payne (1999, January). 14-YEAR Program Monitoring the Flux Densities of 33 Radio Sources at Low Frequencies. *ApJS 120*, 77–93.

Sayer, R. W., D. J. Nice, and J. H. Taylor (1997, January). The Green Bank Northern Sky Survey for Fast Pulsars. *ApJ 474*, 426–432.

Scheuer, P. A. G. (1968, June). Amplitude Variations in Pulsed Radio Sources. *Nature 218*, 920–922.

Seiradakis, J. H. and R. Wielebinski (2004, December). Morphology and characteristics of radio pulsars. *A&A Rev. 12*, 239–271.

Serylak, M., B. W. Stappers, P. Weltevrede, M. Kramer, A. Jessner, A. G. Lyne, C. A. Jordan, K. Lazaridis, and J. A. Zensus (2009, March). Simultaneous multifrequency single-pulse properties of AXP XTE J1810-197. *MNRAS 394*, 295–308.

Shannon, R. M., V. Ravi, W. A. Coles, G. Hobbs, M. J. Keith, R. N. Manchester, J. S. B. Wyithe, M. Bailes, N. D. R. Bhat, S. Burke-Spolaor, J. Khoo, Y. Levin, S. Oslowski, J. M. Sarkissian, W. van Straten, J. P. W. Verbiest, and J.-B.

Wang (2013, October). Gravitational-wave limits from pulsar timing constrain supermassive black hole evolution. *Science 342*, 334–337.

Spitler, L. G., K. J. Lee, R. P. Eatough, M. Kramer, R. Karuppusamy, C. G. Bassa, I. Cognard, G. Desvignes, A. G. Lyne, B. W. Stappers, G. C. Bower, J. M. Cordes, D. J. Champion, and H. Falcke (2014, January). Pulse Broadening Measurements from the Galactic Center Pulsar J1745-2900. *ApJ 780*, L3.

Staveley-Smith, L., W. E. Wilson, T. S. Bird, M. J. Disney, R. D. Ekers, K. C. Freeman, R. F. Haynes, M. W. Sinclair, R. A. Vaile, R. L. Webster, and A. E. Wright (1996, November). The Parkes 21 CM multibeam receiver. *PASA 13*, 243–248.

Stil, J. M., A. R. Taylor, J. M. Dickey, D. W. Kavars, P. G. Martin, T. A. Rothwell, A. I. Boothroyd, F. J. Lockman, and N. M. McClure-Griffiths (2006, September). The VLA Galactic Plane Survey. *AJ 132*, 1158–1176.

Stokes, G. H., D. J. Segelstein, J. H. Taylor, and R. J. Dewey (1986, December). Results of two surveys for fast pulsars. *ApJ 311*, 694–700.

Stokes, G. H., J. H. Taylor, J. M. Welsberg, and R. J. Dewey (1985, October). A survey for short-period pulsars. *Nature 317*, 787.

Stovall, K., R. S. Lynch, S. M. Ransom, A. M. Archibald, S. Banaszak, C. M. Biwer, J. Boyles, L. P. Dartez, D. Day, A. J. Ford, J. Flanigan, A. Garcia, J. W. T. Hessels, J. Hinojosa, F. A. Jenet, D. L. Kaplan, C. Karako-Argaman, V. M. Kaspi, V. I. Kondratiev, S. Leake, D. R. Lorimer, G. Lunsford, J. G. Martinez, A. Mata, M. A. McLaughlin, M. S. E. Roberts, M. D. Rohr, X. Siemens, I. H. Stairs, J. van Leeuwen, A. N. Walker, and B. L. Wells (2014, August). The Green Bank Northern Celestial Cap Pulsar Survey. I. Survey Description, Data Analysis, and Initial Results. *ApJ 791*, 67.

Strüder, L., U. Briel, K. Dennerl, R. Hartmann, E. Kendziorra, N. Meidinger, E. Pfeffermann, C. Reppin, B. Aschenbach, W. Bornemann, H. Bräuninger, W. Burkert, M. Elender, M. Freyberg, F. Haberl, G. Hartner, F. Heuschmann,

H. Hippmann, E. Kastelic, S. Kemmer, G. Kettenring, W. Kink, N. Krause, S. Müller, A. Oppitz, W. Pietsch, M. Popp, P. Predehl, A. Read, K. H. Stephan, D. Stötter, J. Trümper, P. Holl, J. Kemmer, H. Soltau, R. Stötter, U. Weber, U. Weichert, C. von Zanthier, D. Carathanassis, G. Lutz, R. H. Richter, P. Solc, H. Böttcher, M. Kuster, R. Staubert, A. Abbey, A. Holland, M. Turner, M. Balasini, G. F. Bignami, N. La Palombara, G. Villa, W. Buttler, F. Gianini, R. Lainé, D. Lumb, and P. Dhez (2001, January). The European Photon Imaging Camera on XMM-Newton: The pn-CCD camera. *A&A 365*, L18–L26.

Supan, L., G. Castelletti, B. C. Joshi, M. P. Surnis, and D. Supanitsky (2015, April). A complete radio study of SNR G15.4+0.1 from new GMRT observations. *A&A 576*, A81.

Surnis, M. P., B. C. Joshi, and S. Roy (2013, May). Search for pulsed radio emission from PSR J1745-2900 at 1 GHz with the GMRT. *The Astronomer's Telegram 5070*, 1.

Surnis, M. P., M. A. Krishnakumar, Y. Maan, B. C. Joshi, and P. K. Manoharan (2014, August). Upper limits on the pulsed radio emission of SGR 1935+2154 from the Ooty Radio Telescope and the Giant Meterwave Radio Telescope. *The Astronomer's Telegram 6376*, 1.

Surnis, M. P., Y. Maan, B. C. Joshi, M. A. Krishnakumar, P. K. Manoharan, and A. Naidu (2016). Radio Pulsation Search and Imaging Study of SGR J1935+2154. *ApJ submitted*.

Surnis, M. P., Y. Maan, B. C. Joshi, and P. K. Manoharan (2016, April). Upper limits on the pulsed radio emission from SGR candidate SGR 0755-2933. *The Astronomer's Telegram 8943*.

Swarup, G., S. Ananthakrishnan, V. K. Kapahi, A. P. Rao, C. R. Subrahmanya, and V. K. Kulkarni (1991, January). The Giant Metre-Wave Radio Telescope. *Current Science, Vol. 60, NO.2/JAN25, P. 95, 1991 60*, 95.

Taylor, J. H. (1992, October). Pulsar Timing and Relativistic Gravity. *Royal Society of London Philosophical Transactions Series A 341*, 117–134.

Taylor, J. H. and J. M. Weisberg (1989, October). Further experimental tests of relativistic gravity using the binary pulsar PSR 1913 + 16. *ApJ 345*, 434–450.

Thompson, A. R., J. M. Moran, and G. W. Swenson, Jr. (2001). *Interferometry and Synthesis in Radio Astronomy, 2nd Edition.*

Thompson, C. and R. C. Duncan (1996, December). The Soft Gamma Repeaters as Very Strongly Magnetized Neutron Stars. II. Quiescent Neutrino, X-Ray, and Alfven Wave Emission. *ApJ 473*, 322.

Thorsett, S. E. (1991, August). Frequency dependence of pulsar integrated profiles. *ApJ 377*, 263–267.

Thorsett, S. E., W. T. S. Deich, S. R. Kulkarni, J. Navarro, and G. Vasisht (1993, October). A Search for Pulsars at High Galactic Latitudes. *ApJ 416*, 182.

Turtle, A. J. and A. E. Vaughan (1968, August). Discovery of Two Southern Pulsars. *Nature 219*, 689–690.

Verbiest, J. P. W., L. Lentati, G. Hobbs, R. van Haasteren, P. B. Demorest, G. H. Janssen, J.-B. Wang, G. Desvignes, R. N. Caballero, M. J. Keith, D. J. Champion, Z. Arzoumanian, S. Babak, C. G. Bassa, N. D. R. Bhat, A. Brazier, P. Brem, M. Burgay, S. Burke-Spolaor, S. J. Chamberlin, S. Chatterjee, B. Christy, I. Cognard, J. M. Cordes, S. Dai, T. Dolch, J. A. Ellis, R. D. Ferdman, E. Fonseca, J. R. Gair, N. E. Garver-Daniels, P. Gentile, M. E. Gonzalez, E. Graikou, L. Guillemot, J. W. T. Hessels, G. Jones, R. Karuppusamy, M. Kerr, M. Kramer, M. T. Lam, P. D. Lasky, A. Lassus, P. Lazarus, T. J. W. Lazio, K. J. Lee, L. Levin, K. Liu, R. S. Lynch, A. G. Lyne, J. Mckee, M. A. McLaughlin, S. T. McWilliams, D. R. Madison, R. N. Manchester, C. M. F. Mingarelli, D. J. Nice, S. Osłowski, N. T. Palliyaguru, T. T. Pennucci, B. B. P. Perera, D. Perrodin, A. Possenti, A. Petiteau, S. M. Ransom, D. Reardon, P. A. Rosado, S. A. Sanidas, A. Sesana, G. Shaifullah, R. M. Shannon, X. Siemens, J. Simon, R. Smits, R. Spiewak, I. H. Stairs, B. W. Stappers, D. R. Stinebring, K. Stovall, J. K. Swiggum, S. R. Taylor, G. Theureau, C. Tiburzi, L. Toomey, M. Vallisneri, W. van Straten, A. Vecchio, Y. Wang, L. Wen, X. P. You, W. W.

Zhu, and X.-J. Zhu (2016, May). The International Pulsar Timing Array: First data release. *MNRAS 458*, 1267–1288.

Verschuur, G. L., K. I. Kellermann, and V. van Brunt (1974). *Galactic and Extra-Galactic Radio Astronomy.*

Weisberg, J. M., R. W. Romani, and J. H. Taylor (1989, December). Evidence for geodetic spin precession in the binary pulsar 1913 + 16. *ApJ 347*, 1030–1033.

Westfall, P. H. (2014, August). Kurtosis as Peakedness, 1905 – 2014. R.I.P. *Am Stat 68*, 191–195.

Will, C. M. (2014, June). The Confrontation between General Relativity and Experiment. *Living Reviews in Relativity 17*, 4.

Williamson, I. P. (1972). Pulse broadening due to multiple scattering in the interstellarmedium. *MNRAS 157*, 55.

Wolszczan, A. and D. A. Frail (1992, January). A planetary system around the millisecond pulsar PSR1257 + 12. *Nature 355*, 145–147.

Younes, G., E. Gogus, C. Kouveliotou, and A. J. van der Hors (2015, March). NuSTAR observations of the magnetar candidate SGR 1935+2154. *The Astronomer's Telegram 7213*, 1.

Younes, G., C. Kouveliotou, O. Kargaltsev, G. G. Pavlov, E. Göğüş, and S. Wachter (2012, September). XMM-Newton View of Swift J1834.9-0846 and Its Magnetar Wind Nebula. *ApJ 757*, 39.

Young, M. D., R. N. Manchester, and S. Johnston (1999, August). A radio pulsar with an 8.5-second period that challenges emission models. *Nature 400*, 848–849.

Yusef-Zadeh, F., R. Diesing, M. Wardle, L. O. Sjouwerman, M. Royster, W. D. Cotton, D. Roberts, and C. Heinke (2015, October). Radio Continuum Emission from the Magnetar SGR J1745-2900: Interaction with Gas Orbiting Sgr A*. *ApJ 811*, L35.

Zhang, B., A. K. Harding, and A. G. Muslimov (2000, March). Radio Pulsar Death Line Revisited: Is PSR J2144-3933 Anomalous? *ApJ 531*, L135–L138.